UNIVERSITY OF CALIFORNIA SAN DIEGO

Utilizing Extractive Electrospray Ionization Mass Spectrometry to Probe the Composition of Sea Spray Aerosol and the Photochemical Reaction Kinetics of Aerosol-Phase Bisphenol-A

A Dissertation submitted in partial satisfaction of the requirements
for the degree Doctor of Philosophy

in

Chemistry

by

Samantha Marie Kruse

Committee in charge:

Professor Jonathan H. Slade, Chair
Professor Lihini Aluwihare
Professor Vicki H. Grassian
Professor Francesco Paesani
Professor Amitabha Sinha

2024

The Dissertation of Samantha Marie Kruse is approved, and it is acceptable in quality and form for publication on microfilm and electronically.

University of California San Diego

2024

DEDICATION

To my Mama and Papa,

Pix, Uli, Eddie, and Einzee,

I love you

TABLE OF CONTENTS

LIST OF FIGURES

LIST OF TABLES

LIST OF ABBREVIATIONS

AFM	Atomic Force Microscopy
AMS	Aerosol Mass Spectrometer
BPA	Bisphenol-A
CAICE	Center for Aerosol Impacts on Chemistry of the Environment
CCN	Cloud Condensation Nuclei
Chl-a	Chlorophyll-a
CPC	Condensation Particle Counter
D	Diffusion Coefficient
DMA	Differential Mobility Analyzer
EESI	Extractive Electrospray Ionization
ELPI	Electrical Low-Pressure Impactor
IN	Ice Nucleation
INP	Ice Nucleating Particle
κ	Hygroscopicity Parameter
K	Degree Kelvin
L	Liter
LPM	Liters per Minute
MART	Marine Aerosol Reference Tank
mb	Millibar
MW	Molecular Weight
η	Viscosity
ρ	Density

Pa s	Pascal Seconds
PAM-OFR	Potential Aerosol Mass-Oxidative Flow Reactor
RH	Relative Humidity
RID	Relative Indentation Depth
SeaSCAPE	Sea Spray Chemistry and Particle Evolution Experiment
SEMS	Scanning Electrical Mobility Spectrometer
SIO	Scripps Institution of Oceanography
SMA	Secondary Marine Aerosol
SMPS	Scanning Mobility Particle Sizer
SOA	Secondary Organic Aerosol
SSA	Sea Spray Aerosol
SSML	Sea Surface Microlayer
T	Temperature
T_{amb}	Ambient Temperature
T_g	Glass Transition Temperature
µm	Micrometer
UV	Ultra-Violet
V	Volume
VOC	Volatile Organic Compound

ACKNOWLEDGEMENTS

I would first like to thank Professor Nate Slade for all his mentorship, help, and advice while pursuing my PhD. I still remember entering his office in the middle of the summer, having almost dropped out of graduate school, and after hearing about his project on microplastics decided to join his lab the same day. I truly would not be here without him. I'm sure it was not easy training a graduate student while teaching them the basics of atmospheric chemistry, but I feel honored to have had the opportunity to be his first PhD student.

I would also like to thank my committee, Professor Lihini Aluwihare, Professor Vicki H. Grassian, Professor Francesco Paesani, and Professor Amitabha Sinha for their guidance during my PhD, and a special thank you to Professor Grassian for her additional mentorship through the Center for Aerosol Impacts on Chemistry of the Environment.

I'd like to thank all past and current members of the Slade lab for their continued support throughout my PhD and helping shape me into the kind of chemist I want to be. Specifically, I want to thank Dr. (Paul) Ryan Tumminello for going far above and beyond the expectations of a lab mate.

Thank you to Dr. Stephanie Hurst, my undergraduate mentor, for putting in so much work to make sure I got into graduate school, I hope that we can catch up eventually over some beers and pool.

I'm very thankful for the friends I've made along the way. Dr. Max Bernbeck, you were the primary reason I decided to stick around long enough to meet Professor Slade, and for that and all your support during my (brief) stint as an inorganic chemist I will always be grateful. Dr. Elizabeth Porto, thank you for all our co-working sessions and late-night trips to Target, I will

always have fond memories of our hunt for Christmas décor. Allison Kawasaki, going to future Twice concerts will never be as fun as going with you (Twice!).

Thank you to all the friends and family who supported me throughout my education, even though I was near impossible to reach at times. Nathan Diefenderfer, Loren Reichsfeld, and Amanda Robinson, thank you for all your patience and grace during this process. Lastly but certainly not least, I'd like to thank my parents for their love and support during this challenging process.

Chapter 3, in full, is a reprint of the material as it appears in the Journal of Physical Chemistry A. "Heterogeneous and Photosensitized Oxidative Degradation Kinetics of the Plastic Additive Bisphenol-A in Sea Spray Aerosol Mimics" Kruse, Samantha M., Slade, Jonathan H., 2023. The dissertation author was the primary researcher and author of this paper.

Chapter 4, in full, has been submitted to Analytical Chemistry. Kruse, Samantha M., Tumminello, Paul R. Slade, Jonathan H. The dissertation author was the primary researcher and author of this paper.

Chapter 5, in full, is currently being prepared for submission for publication in American Chemical Society Environmental Science & Technology Air. Kruse, Samantha M., Slade, Jonathan H. The dissertation author was the primary researcher and author of this paper.

VITA

2015 Bachelor of Science in Chemistry, Northern Arizona University

2019 Master of Science in Chemistry, University of California San Diego

2024 Doctor of Philosophy in Chemistry, University of California San Diego

PUBLICATIONS

Kruse, S.M.; Tumminello, P.R.; Slade, J. H. "Effects of Relative Humidity and Phase on the Molecular Detection of Nascent Sea Spray Aerosol using Extractive Electrospray Ionization", Anal. Chem., Submitted

Kruse, S.M.; Slade, J. H. "Heterogeneous and Photosensitized Oxidative Degradation Kinetics of the Plastic Additive Bisphenol-A in Sea Spray Aerosol Mimics", J. Phys. Chem. A 2023 127 (21), 4724–4733, 10.1021/acs.jpca.3c00127

Tumminello, P. R.; James, R. C.; **Kruse, S.M.**; Kawasaki, A.; Cooper, A. W.; Guadalupe-Diaz, I.; Lopo-Zepeda, K.; Crocker, D. R.; Mayer, K. J.; Sauer, J. S.; Lee, C.; Prather, K. A.; Slade, J. H. "Evolution of Sea Spray Aerosol Particle Phase State Across a Phytoplankton Bloom" ACS Earth and Space Chemistry 2021 5 (11), 2995-3007, 10.1021/acsearthspacechem.1c00186

Hasenecz, E. S.; Jayarathne, T.; Pendergraft, M. A.; Santander, M. V.; Mayer, K. J.; Sauer, J. S.; Lee, C.; Gibson, W. S.; **Kruse, S.M.**; Malfatti, F.; Prather, K. A.; Stone, E. A. "Marine Bacteria Affect Saccharide Enrichment in Sea Spray Aerosol during a Phytoplankton Bloom" ACS Earth Space Chemistry 2020 4 (9), 1638-1649, 10.1021/acsearthspacechem.0c00167

Kruse, S.M.; Hurst, S. K. "Rapid One-Pot Synthesis of Cycloheptatriene-Phosphonium Derivatives" Tetrahedron Letters 2015 56 (46), 6319-6322, 10.1016/j.tetlet.2015.06.097

FIELD OF STUDY

Major Field: Chemistry

Studies in Atmospheric Chemistry
Studies in Analytical Chemistry

ABSTRACT OF THE DISSERTATION

Utilizing Extractive Electrospray Ionization Mass Spectrometry to Probe the Composition of Sea Spray Aerosol and the Photochemical Reaction Kinetics of Aerosol-Phase Bisphenol-A

by

Samantha Marie Kruse

Doctor of Philosophy in Chemistry

University of California San Diego, 2024

Professor Jonathan H. Slade, Chair

Plastics have become ubiquitous in the world's oceans, and recent work indicates that they can transfer from the ocean to the atmosphere in sea spray aerosol (SSA). SSA is the largest contributor to annual aerosol mass load and is a significant source of plastic to the atmosphere. Plastic additives, including bisphenol-A (BPA), represent a sizable fraction of consumer plastics and have been measured consistently in air over both terrestrial and marine environments. However, the chemical lifetimes of BPA and mechanisms by which it degrades with respect to

photochemical and heterogeneous oxidation processes in aerosols are unknown. The work in this dissertation utilized an extractive electrospray ionization time-of-flight mass spectrometer (EESI-TOF) to monitor changes in aerosol composition with high time resolution. In Chapter 3, the photosensitized and OH- initiated heterogeneous oxidation kinetics of BPA in the aerosol phase consisting of pure-component BPA and internal mixtures of BPA, NaCl, and dissolved photosensitizing organic matter are presented. OH-initiated degradation is enhanced in the presence of chloride, likely due to the enhanced mobility of BPA in the more liquid-like particle due to the hygroscopicity of NaCl increasing the liquid water content within the aerosol. In contrast, photosensitized reactions were limited in the presence of chloride, which was attributed to quenching of triplet state formation by dissolved Cl^- in the less viscous aqueous aerosol mixtures. In Chapter 4, the composition changes in SSA during a phytoplankton bloom are determined, including the temporal variability and trends dependent on specific biological processes occurring in seawater. Through this study, it was also established that EESI-TOF sensitivity is critically dependent on the sample's relative humidity after adjusting for pressure variations at the inlet and normalization to the reagent ion. In Chapter 5, the photosensitized degradation of BPA at high and low pH is investigated. At pH 3 and pH 11, the photosensitized degradation of BPA is inhibited, and the potential causes are discussed. This dissertation highlights important heterogeneous and photosensitized reactions which BPA undergoes, as well as the role of particle viscosity. Ultimately, this work contributes to our understanding of the lifetimes of hazardous plastic pollutants in SSA with implications for pollutant transport and exposure risks in coastal marine environments.

Chapter 1 Introduction

1.1 Plastic Waste in Oceans

The problem with plastic waste in our oceans was identified as early as the 1980s[1], and the problem continues to grow today. It was estimated in 2014 that the ocean contained over 5 trillion pieces of plastic, weighing more than 250,000 tonnes.[2] In a 2023 study, it was estimated that the number of plastic pieces in the ocean had grown to over 170 trillion, a 34x increase in less than a decade, and it is anticipated to increase exponentially.[3] Plastic waste enters the ocean by mismanaging plastic waste due to littering or inadequate disposal, such as open landfills.[4] While there are attempts to mitigate these problems in many countries, those same countries will ship their waste to other countries to mask the problem.[5] Plastic waste can lead to the distribution of harmful organic and inorganic chemicals to the environment, the transfer of diseases, and the spread of invasive species.[6] Additionally, plastics can cause a massive increase in the death of marine animals due to entanglement, ingestion, or laceration, all caused by plastic waste.[7] Beyond concerns for the environment, it was estimated in 2021 that the damage to our oceans would cause economic losses of 1.5 trillion USD.[8]

Microplastics

One cause for the exponential increase in plastic waste in the ocean is the generation of microplastics and nanoplastics from the aging and breakdown of larger plastics (i.e., photochemical, thermal, and microbial wear) and direct inputs of engineered nano- and micro-particles. Although definitions vary between fields, microplastics are generally defined as plastics with its largest diameter between 1-1000 μm and nanoplastics are defined as plastics <1 μm.[9, 10] Plastics are manufactured to resist biodegradation and, therefore, are not completely removed in nature. Instead, they tend to fragment into smaller and smaller pieces.[11] Due to their small size and generally low density, microplastics tend to accumulate at the surface of the ocean,[12] and from

there are susceptible to transfer into the atmosphere. It has been found that due to this enhancement at the surface of the ocean, plastics can get aerosolized through wave breaking activity, and this leads to an estimated annual global flux of 24 quintillion pieces, or 773 tons, of plastic into the atmosphere.[13]

Plastic Leaching

The problem with plastics goes beyond their sheer numbers in the ocean. As plastics become smaller, their surface area increases, which can lead to the leaching of chemical additives in the plastics.[14, 15] Plastic additives have a number of different qualities, including dyes, lubricants, light stabilizers, plasticizers, and flame retardants.[16] The overall quantity of these additives depend on the function that is desired for the plastic, and have a large range, from 10-70% w/w for plasticizers, 3-25% for flame retardants, and 0.001-10% for dyes.[17] The rate of plastic leaching is dependent on factors such as the properties of the plastic (size and polymeric structure),[18] properties of the surrounding water (salinity and pH),[19, 20] ambient temperature,[21] solar irradiation,[22] contact time,[21] and age of the plastics.[23] These leachates are not easily dissolved in water,[14] and therefore concentrate in the sea surface microlayer (SSML). The sea surface microlayer is a thin layer at the surface of the ocean, which is a complex mixture of bacteria, microalgae, small invertebrates, dissolved organic carbon (DOC), and organic and inorganic molecules.[24] Anthropogenic contaminants, due to their hydrophobicity, tend to accumulate in the SSML at concentrations up to 500x higher than within the water column.[25]

Bisphenol-A

One of the most widely used plastic additives is Bisphenol-A (BPA). BPA was first synthesized in 1981 and is one of the most highly produced chemicals worldwide.[26] It is used in the production of polycarbonate plastics as a co-monomer and additive,[27] as well as a plastic

additive in dental sealants[28] and thermal paper (i.e. receipts).[29] The chemical structure of BPA is shown in Figure 1.1.

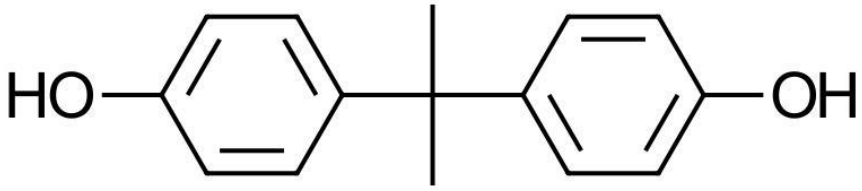

Figure 1.1 Two-dimensional chemical structure of bisphenol-A (BPA)

In July 2012, the US Food and Drug Administration restricted the use of BPA in baby bottles, sippy cups, and infant formula packaging.[30] The reason for this regulation is the finding that exposure to BPA was leading to altered growth and behavioral problems in children.[31] The leading reason for these problems was the activity of BPA as an endocrine disruptor, where in the body, BPA is recognized as estrogen, and causes an uptick in hormonal processes.[32] While BPA has been regulated in baby products, these policies have not extended to other food products. However, the effects on adults can be just as severe as the effects on children. Beyond the effects as an endocrine disruptor, BPA is a known carcinogen,[33] and it has been associated with type 2 diabetes,[34, 35] obesity,[36] and heart disease.[37, 38] It was estimated in 2014 that if BPA exposure were limited, 22,000 cases of coronary heart disease would be prevented.[39] Aside from the health effects of BPA, it is also one of the most common environmental pollutants. BPA has been found to leach from plastic at rates up to 6x higher than other endocrine disrupting chemicals.[22] BPA has been found in concentrations up to 17 mg/L in seawater, even when far away from wastewater effluent,[40, 41] and BPA is known to concentrate at the SSML due to its hydrophobicity.[42] Due to this concentration at the sea surface, one of the predicted routes of airborne exposure is from transfer of BPA into sea spray aerosol.

1.2 Importance of Aerosols

Aerosols, which are solids, semisolids, and/or liquids suspended in gas, typically ranging in size from 0.001-10μm, at concentrations ranging from 4.8μg/m^3 in remote areas to 88 μg/m^3 and higher in more polluted areas.[43] Primary sources of aerosols include biomass burning, dust, sea spray, pollen, and volcanic emissions. Aerosols can also be generated through the oxidation of volatile organic compounds (VOCs), which creates lower-volatility species that partition into the condensed phase, called secondary organic aerosols (SOA).[44] Individual aerosols are so small that they cannot generally be seen with the naked eye, but large collections of aerosols can be, such as smoke plumes, pollution haze, and fog.

Radiative Forcing

Aerosols influence the atmosphere through their impact on radiative forcing. Radiative forcing is the net warming or cooling of the atmosphere caused by the interactions between different atmospheric constituents and incoming solar radiation, generally in units of W/m^2. A summary of atmospheric constituents and their impact on radiative forcing from the Intergovernmental Panel on Climate Change (IPCC) 6th Assessment Report is shown in Figure 1.2.

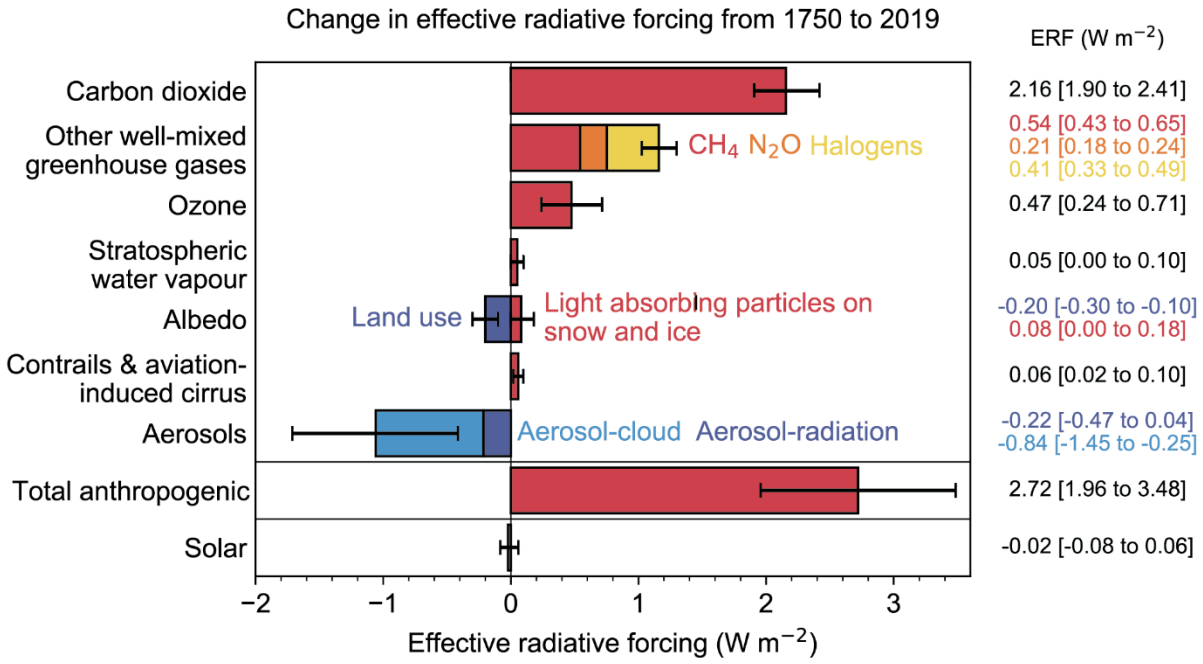

Figure 1.2 Plot of the change in effective radiative forcing for nine different atmospheric constituents from 1750 to 2019 from the IPCC 6th Assessment Report.[45]

Aerosols can interact directly with incoming solar radiation by absorbing or scattering light, however the degree of this impact is dependent on the type of the aerosol. For example, sulfate aerosols have a generally cooling effect while brown carbon has a generally warming effect.[46, 47] Aerosols can also impact the Earth's climate indirectly by acting as cloud condensation nuclei (CCN). When a particle is a CCN, it absorbs water from the surrounding air and becomes a liquid water droplet, which then can seed clouds.[48] Aerosols and clouds scatter and absorb incoming solar radiation. The degree to which clouds have a positive or negative radiative forcing is dependent on the droplet size in the cloud, i.e. darker clouds with larger droplets tend to absorb radiation, whereas light clouds with smaller droplets are more likely to scatter radiation. Darker colored aerosol particles, including brown and black carbon (e.g., soot) absorb radiation causing a warming influence in the atmosphere, whereas lighter colored aerosol particles (e.g., ammonium

sulfates and salts) cause a cooling influence in the atmosphere. Understanding how aerosols interact with light directly and indirectly in the atmosphere is critical and the indirect effects represent the greatest uncertainty in global temperature predictions, largely due to their variety in composition and CCN activity.[45]

Health Effects

The negative health impacts of aerosols have been well documented for their effect on the pulmonary and vascular systems. Larger aerosols generally deposit higher in the pulmonary system, such as the throat and thorax, and smaller aerosols can penetrate deeper into the lungs, into the bronchi and alveoli.[49] These smaller lung structures are utilized by the body to transfer gases like oxygen into the bloodstream and push carbon dioxide out, and damage to these structures can inhibit their function.[50] Once inside the body, these aerosols can cause irritation and inflammation. On the shorter timescale, this can look like coughing after inhaling smoke or the initiation of asthma attacks.[51, 52] However, over longer timescales, these effects compound, and disease such as heart disease due to prolonged vascular inflammation can take root.[53, 54] These impacts disproportionately affect lower and middle income countries due to increased pollution.[55]

1.3 Sea Spray Aerosols

Sea spray aerosol (SSA) is one of the largest contributors to global aerosol mass per year, and are the primary aerosol system of focus in this dissertation.[56] SSA is generated by wave breaking activity in the ocean. There are three known types of primary SSA: spume droplets, jet droplets, and film droplets, which decrease in size, respectively. Spume droplets are generated from mechanical shearing of waves by winds and their concentrations increase with higher wind speeds.[57] They are much larger than both film and jet droplets, with the size range starting at 140μm and increasing to as large as millimeters, and therefore have extremely short atmospheric lifetimes due to gravitational settling.[58] The primary mechanism for the generation of both film droplets and

jet droplets is bubble bursting at the ocean's surface, as shown in Figure 1.3. When a wave breaks, bubbles are entrained underneath the surface of the water. As they rise to the surface and the bubble cap pops, the thin film on the surface fragments, which generates small film droplets less than 1μm in diameter.[59] Collapse of the bubble cavity creates a slight vacuum, and the force of water into the cavity creates a jet, ejecting small droplets (0.1-25μm) known as jet droplets into the atmosphere.[60] These size ranges are approximations; notably, the size of both film and jet droplets depend on the bubble's size and the surface tension of the rupturing bubble.[61, 62] Additionally, research has found that in number concentration, up to 43% of sub-micrometer SSA is comprised of jet droplets.[63]

Figure 1.3 Illustration of the bubble bursting process. From left to right, first the bubble rises to the surface, then the bubble pops creating film droplets, and then as the bubble cavity collapses, jet droplets are formed.

SSA Chemical Composition and pH

It is critical to discuss the differences between film and jet droplets because their composition can vary wildly due to their respective production mechanisms, even though they may overlap in size.[63-65] Atmospheric models parameterize SSA as sea salt,[66, 67] however the chemical composition of SSA is highly complex, mirroring the chemical complexity of the ocean. Broadly,

SSA can contain whole cells, bacterium, and viruses,[68] different organic molecules including hydrophobic molecules like surfactants[69] and lipids[70] and hydrophilic molecules like saccharides,[71, 72] dissolved organic matter,[73-75] and inorganic salts (primarily NaCl).[72, 76, 77] SSA composition also depends significantly on size. Several studies show a large number of film droplets are primarily composed of organic carbon mimicking the SSML, whereas jet droplets contain a greater fraction of sea salt.[63-65] Greater biological activity in the water increases the organic carbon fraction in SSA during phytoplankton blooms.[72, 78-80] The greater organic carbon fraction modulates SSA's ability to act as CCN[81-83] and ice nuclei (IN).[84]

Particle pH is a difficult process to study, due to rapid changes in acidity from evaporation and reactions with ambient gases.[85, 86] Recent work has shown that SSA rapidly acidifies once it is emitted from the water, from the bulk water pH of 8.1 to a pH of 2, and this pH is also size dependent, with smaller aerosols being more acidic, independent of reactive gaseous species.[87] The presence of pollutants generally increases the acidity of ambient aerosols from the presence of nitric or sulfuric acid, leading to potentially worsening health impacts.[88] Furthermore, there is evidence that plastic waste can contribute to ocean acidification via the release of organic acids, which could further acidify SSA.[89] Studies have shown that increased particle acidity leads to higher rates of reactivity, as well as the production of larger molecular weight species from acid-catalyzed reactions.[90-92] Particle pH also influences phase separation within aerosol particles. As molecules are deprotonated at higher pH, they are more water-soluble due to water-ion interactions, and therefore can change the extent of liquid-liquid phase separation dependent on the composition of the aerosol.[86]

SSA Morphology and Phase

SSA has been shown to have multiple distinct morphologies wherein the particle is not well mixed and has different types of phase separation. Some examples of these morphologies that

have been identified in SSA are (i) prism-like, where there is a high amount of inorganic salt and low organic content, (ii) core-shell, where a primarily inorganic core is surrounded by an organic shell of varying thickness, (iii) rounded, which are comprised primarily of different organic compounds, and (iv) rod-like, which are primarily composed of inorganic sulfate, shown in Figure 1.4.[93, 94] The ratios of these particle types in SSA depend significantly on the biological activity of the water.[93, 94] Beyond these broad particle types, SSA can also exhibit different types of phase separation, including liquid-liquid phase separation,[95, 96] and the creation of "islands" of monolayers of hydrophobic material at the surface of the particle.[97]

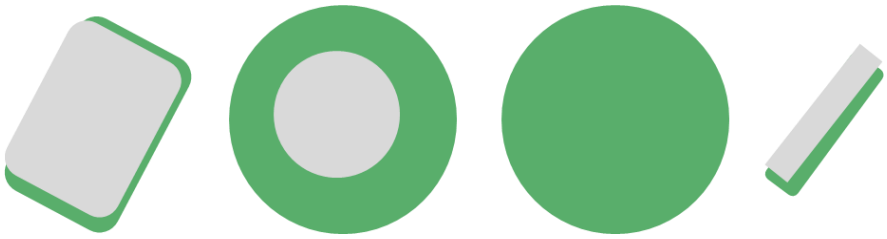

Figure 1.4 Illustration of SSA particle types at low relative humidity (20% RH). From left to right: prism-like, core-shell, rounded, and rod-like particles, with the inorganic portion in grey and the organic portion in green.

Particle viscosity is another important parameter of SSA. Viscosity, colloquially known as "thickness", is the ability of a substance to resist deformation. A higher viscosity means the substance requires more force to deform. Solids are defined as >1012 Pa·s, semi-solids as 10^2-10^{12} Pa·s, and liquids as $<10^2$ Pa·s.[98] For example, water has a viscosity of 10^{-3} Pa·s whereas honey has a viscosity of 10 Pa·s.[99] Particle viscosity can affect gas diffusion,[100] reactivity,[101] and lifetime of aerosol particles.[102, 103] Particle viscosity is also impacted by temperature and RH, where higher temperatures and higher RH reduce particle viscosity.[104] Prior work has shown that SSA viscosity is dependent on biological activity, with a higher amount of biological activity leading to more viscous particles.[93, 94, 105] When there is phase separation within a particle, each separate phase can have a different viscosity, increasing the complexity of aerosol processes.[106-108] A higher particle

viscosity can lead to increased lifetimes of anthropogenic contaminants, where the surface of the aerosol becomes heavily reacted but the reactive gases are unable to penetrate into the unreacted core of the aerosol.[102]

1.4 Aerosol Aging in the Atmosphere

Aging in the atmosphere can influence both the climate properties[109-111] and the health effects[112, 113] of aerosols. Broadly, aging can be divided into physical aging and chemical aging. Physical aging includes processes such as (i) coagulation, where two particles collide and fuse, reducing total number concentration and increasing particle mass, (ii) condensation, where water vapor or semi-volatile VOCs absorb/adsorb into/onto a particle, increasing particle mass, and (iii) evaporation, where higher temperatures lead to the loss of volatile and semi-volatile compounds from the aerosol, decreasing particle mass.[43] Chemical aging involves any kind of composition change within the aerosol, either through heterogeneous reactions with gases (OH, O_3, NO_3, etc.), or homogeneous reactions between reactive molecules within the aerosol.[114] Chemical aging is an extremely broad category, so within the scope of this dissertation, the focus will be on heterogeneous oxidation (specific to hydroxyl radicals) and photochemical aging of aerosols.

Heterogeneous Oxidation Processes and Hydroxyl Radicals

Heterogeneous oxidation is a process where a gas phase molecule (e.g., oxidants like OH, O_3, or NO_3) reacts with (oxidizes) components in an aerosol particle either directly at the surface before adsorbing to the surface (known as Eley-Rideal kinetics) or following adsorption (known as Langmuir-Hinshelwood kinetics). Other interactions, including gaseous diffusion, mass accommodation, dissolution and diffusion at the surface or in the particle bulk affect the rate of heterogeneous reaction. These processes are summarized in Figure 1.5.[114] When a gas molecule interacts with the surface of a particle, it can either react at the surface or it can diffuse through the particle following accommodation at the surface. If a gas molecule is taken up by the aerosol, it

can then diffuse through the bulk of the particle and react in the particle phase. The proportion of either of these processes is dependent on the reactivity of the gas molecule, where highly reactive molecules (such as OH) tend to participate in surface reactions, whereas molecules with a lower reactivity (such as O_3) tend to partition into the particle, and participate in bulk reactions.[115, 116]

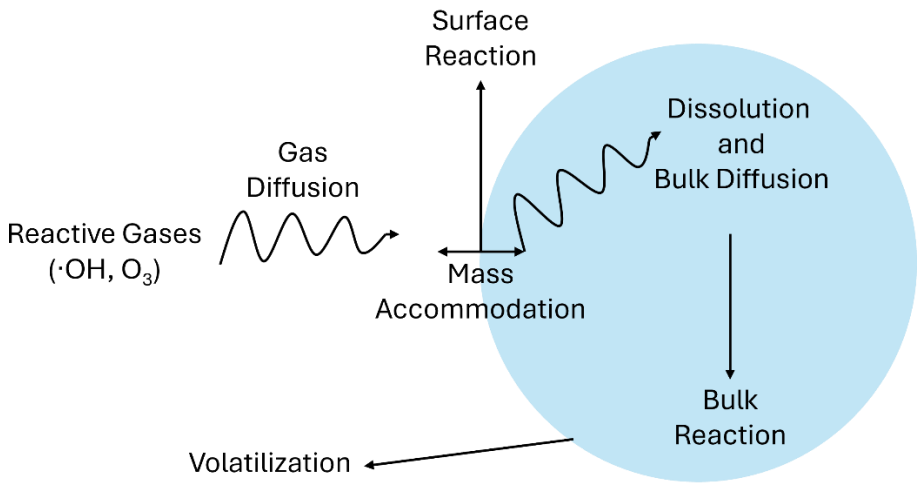

Figure 1.5 Illustration of processes that determine heterogeneous gas uptake by a particle. The surface processes include gas-phase diffusion, mass accommodation, volatilization, and surface reaction, and the bulk processes include dissolution, bulk diffusion, and bulk reaction

Hydroxyl radicals are known as the "detergent of the atmosphere" (coined by Nobel prize winner Paul Krutzen),[117] because they are highly reactive and act as a major sink for other atmospheric gases such as methane and carbon monoxide.[114, 118] Hydroxyl radicals are generated through the photolysis of ozone which generates electronically excited atomic oxygen, and the reaction of electronically excited atomic oxygen and water, as shown in R 1.1 and R 1.2:[43]

$$O_3 + h\nu \rightarrow O_2 + O(^1D) \qquad \text{R 1.1}$$

$$O(^1D) + H_2O \rightarrow 2HO\cdot \qquad \text{R 1.2}$$

Because hydroxyl radicals are dependent on the presence and intensity of light, daytime concentrations are location dependent, but are roughly on the order of 10^6 molecules cm^{-3}.[43, 119, 120] OH radicals have a relatively short reacto-diffusive length in aerosols, meaning that they rapidly

react away with components at the particle surface (within a few nanometers) and less into the particle bulk.[121] When oxidized, reduced organic carbon species can either undergo functionalization, which as defined, adds new functional groups contributing to an increase in particle mass assuming there is appreciable dissolved O_2 in the particle phase, or fragmentation (bond scission resulting in two new molecules from the parent molecule) reactions. Fragmentation increases the particle's volatility and, in some cases, volatilization of the particle and a decrease in particle mass.[116, 122] While this is a broad mechanism, it has been more refined for saturated hydrocarbons. First, the hydrocarbon is deprotonated by OH, creating an alkyl radical, which then reacts with oxygen to form an alkylperoxy radical, and after self-reaction, an alkoxy radical.[114] Beyond this point, the alkoxy radical can undergo functionalization via isomerization or chain propagation, which generates lower volatility species, or fragmentation via decomposition, leading to higher volatility species.[114] These mechanisms make reactive intermediate species, which can react with other particle constituents, accelerating the level of particle oxidation. These processes depend on molecular structure, e.g., cyclic structures fragment less than acyclic molecules because more energy is required to break the chain. As these reactions alter the particle's volatility, they can also impact the particle's viscosity by modulating its molecular weight and water solubility.[101, 122, 123]

Photochemical Aging

Aerosols undergo photochemical aging via direct photolysis or indirectly via photosensitization reactions.[124, 125] The first process is direct photolysis, which only requires the presence of light. Direct photolysis leads to bond-breaking reactions of different chemical compounds in aerosols, and will lead to more volatilization of these chemicals due to their smaller molecular weight, which can decrease aerosol size.[126, 127] The other type of photochemical aging is indirect, caused by the presence of photosensitizing molecules within the aerosol.

Photosensitizers are molecules that absorb light energy, which generally requires the molecule to have large, delocalized π systems. The process of photosensitization is shown in Figure 6, where first, the photosensitizer absorbs a photon from incoming radiation, promoting the photosensitizer to an excited singlet state.[128] After this excitation, the molecule can undergo an intersystem crossing, to an excited triplet state.[128] The excited triplet state is longer lived, which enables the photosensitizer to interact with neighboring molecules.[128]

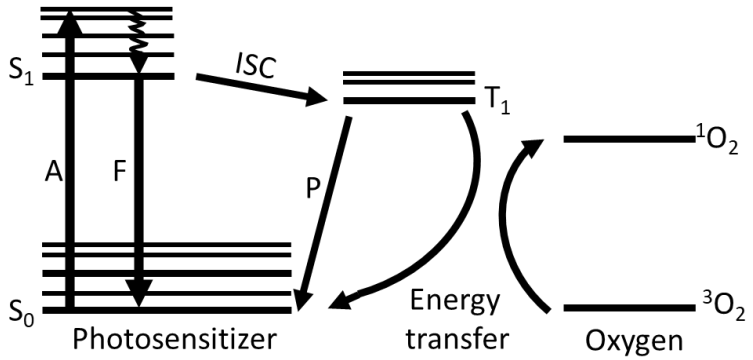

Figure 1.6 Jablonski diagram of the excitation of a photosensitizer from the ground state (S_0) to the excited state (S_1) after absorbance (A) of a photon, after which it may undergo fluorescence (F), or and intersystem crossing (ISC) to the triplet state (T_1) and phosphorescence (P) or energy transfer to a neighboring diatomic oxygen molecule

There are type I and type II photosensitization mechanisms. In type I photosensitization, the photosensitizer reacts with a neighboring molecule that is not diatomic oxygen.[129] In type II photosensitization, the photosensitizer reacts with ground state triplet oxygen to generate excited singlet state oxygen that can react with neighboring molecules, as shown in Figure 1.6.[129] Both processes are extremely important to the atmospheric lifetime of particles, because they can be a source of reactive oxygen species within the bulk of the aerosol, whereas the gaseous species would react before being able to penetrate into the bulk.[130, 131]

1.5 Dissertation Objectives and Research Aims

The primary objective of this dissertation is to advance our understanding of the underlying photochemical aging kinetics and heterogeneous chemical kinetics of OH radicals with SSA constituents including BPA. While there has been a large focus on the lifetimes of plastic additives like BPA in wastewater and other ground-based sources, there have been less studies investigating their lifetimes in aerosols, which have important implications for air quality and airborne exposure to plastic additives in coastal environments impacted by plastic pollution. Specific objectives include determining (1) the effects of particle viscosity on the reactive uptake kinetics of OH with BPA, (2) the role of salt and photosensitizers on both the reactive uptake kinetics of OH with BPA and light degradation in the absence of OH, and (3) the effects of varying pH on the photosensitized degradation of BPA in SSA mimics. To achieve this, several well-controlled experiments involving model SSA generated in the lab and authentic SSA generated from real seawater in the presence of breaking waves were employed. A separate objective of this dissertation involved the online analysis of SSA molecular composition and how it evolved across a phytoplankton bloom via a state-of-the-art extractive electrospray ionization time-of-flight mass spectrometer (EESI-TOF), the first application of this instrument for SSA composition analysis. We discovered fortuitously during the measurements that there is a strong sensitivity dependence on the aerosol phase (viscosity) and relative humidity of the sample aerosol, which had not been reported previously. At the date of publication of this dissertation, my works have been published as a first-author publication in the *Journal of Physical Chemistry A*, co-author publication in *ACS Earth and Space Chemistry*, a first-author manuscript submitted to *Analytical Chemistry*, and a first-author manuscript in prep for submission to *ACS ES&T Air*.

1.6 References

(1) Lang, G. E. Plastics, the marine menace: Causes and cures. *J. Land Use & Envtl. L.* **1989**, *5*, 729.

(2) Cressey, D. Bottles, bags, ropes and toothbrushes: the struggle to track ocean plastics. *Nature* **2016**, *536* (7616), 263-265. DOI: 10.1038/536263a.

(3) Eriksen, M.; Cowger, W.; Erdle, L. M.; Coffin, S.; Villarrubia-Gómez, P.; Moore, C. J.; Carpenter, E. J.; Day, R. H.; Thiel, M.; Wilcox, C. A growing plastic smog, now estimated to be over 170 trillion plastic particles afloat in the world's oceans-Urgent solutions required. *PLoS One* **2023**, *18* (3), e0281596. DOI: 10.1371/journal.pone.0281596.

(4) Jambeck, J. R.; Geyer, R.; Wilcox, C.; Siegler, T. R.; Perryman, M.; Andrady, A.; Narayan, R.; Law, K. L. Plastic waste inputs from land into the ocean. *Science* **2015**, *347* (6223), 768-771. DOI: 10.1126/science.1260352.

(5) Campbell, V. B. Ghost Ships and Recycling Pollution: Sending America's Trash to Europe. *Tulsa J. Comp. & Int'l L.* **2004**, *12*, 189.

(6) Khalid, N.; Aqeel, M.; Noman, A.; Hashem, M.; Mostafa, Y. S.; Alhaithloul, H. A. S.; Alghanem, S. M. Linking effects of microplastics to ecological impacts in marine environments. *Chemosphere* **2021**, *264* (Pt 2), 128541. DOI: 10.1016/j.chemosphere.2020.128541.

(7) Wabnitz, C.; Nichols, W. J. Plastic pollution: An ocean emergency. *Mar. Turtle Newsl.* **2010**, (129), 1.

(8) Watt, E.; Picard, M.; Maldonado, B.; Abdelwahab, M. A.; Mielewski, D. F.; Drzal, L. T.; Misra, M.; Mohanty, A. K. Ocean plastics: environmental implications and potential routes for mitigation - a perspective. *RSC Adv.* **2021**, *11* (35), 21447-21462. DOI: 10.1039/d1ra00353d.

(9) Rochman, C. Microplastics research—from sink to source. *Science* **2018**, *360*, 28-29. DOI: 10.1126/science.aar7734.

(10) Hartmann, N. B.; Hüffer, T.; Thompson, R. C.; Hassellöv, M.; Verschoor, A.; Daugaard, A. E.; Rist, S.; Karlsson, T.; Brennholt, N.; Cole, M.; Herrling, M. P.; Hess, M. C.; Ivleva, N. P.; Lusher, A. L.; Wagner, M. Are We Speaking the Same Language? Recommendations for a Definition and Categorization Framework for Plastic Debris. *Environ. Sci. Technol.* **2019**, *53* (3), 1039-1047. DOI: 10.1021/acs.est.8b05297.

(11) Moita Neto, J. M.; Silva, E. A. d. Sources of Microplastic Generation in the Environment. *Int. J. Environ. Res. Public Health* **2023**, *20* (13). DOI: 10.3390/ijerph20136202.

(12) Anderson, Z. T.; Cundy, A. B.; Croudace, I. W.; Warwick, P. E.; Celis-Hernandez, O.; Stead, J. L. A rapid method for assessing the accumulation of microplastics in the sea surface microlayer (SML) of estuarine systems. *Sci. Rep.* **2018**, *8* (1), 9428. DOI: 10.1038/s41598-018-27612-w.

(13) Yang, S.; Zhang, T.; Gan, Y.; Lu, X.; Chen, H.; Chen, J.; Yang, X.; Wang, X. Constraining Microplastic Particle Emission Flux from the Ocean. *Environ. Sci. Technol. Lett.* **2022**. DOI: 10.1021/acs.estlett.2c00214.

(14) Do, A. T. N.; Ha, Y.; Kwon, J.-H. Leaching of microplastic-associated additives in aquatic environments: A critical review. *Environ. Pollut.* **2022**, *305*, 119258. DOI: 10.1016/j.envpol.2022.119258.

(15) Wiesinger, H.; Wang, Z.; Hellweg, S. Deep Dive into Plastic Monomers, Additives, and Processing Aids. *Environ. Sci. Technol.* **2021**, *55* (13), 9339-9351. DOI: 10.1021/acs.est.1c00976.

(16) Qiu, S.-Q.; Huang, G.-Y.; Fang, G.-Z.; Li, X.-P.; Lei, D.-Q.; Shi, W.-J.; Xie, L.; Ying, G.-G. Chemical characteristics and toxicological effects of leachates from plastics under simulated seawater and fish digest. *Water Res.* **2022**, *209*, 117892. DOI: 10.1016/j.watres.2021.117892.

(17) Hahladakis, J. N.; Velis, C. A.; Weber, R.; Iacovidou, E.; Purnell, P. An overview of chemical additives present in plastics: Migration, release, fate and environmental impact during their use, disposal and recycling. *J. Hazard. Mater.* **2018**, *344*, 179-199. DOI: 10.1016/j.jhazmat.2017.10.014.

(18) Szczepańska, N.; Kudłak, B.; Tsakovski, S.; Yotova, G.; Nedyalkova, M.; Simeonov, V.; Dołęga, A.; Namieśnik, J. Modeling and MANOVA studies on toxicity and endocrine potential of packaging materials exposed to different extraction schemes. *Environ. Res.* **2018**, *165*, 294-305. DOI: 10.1016/j.envres.2018.05.004.

(19) Dhavamani, J.; Beck, A. J.; Gledhill, M.; El-Shahawi, M. S.; Kadi, M. W.; Ismail, I. M. I.; Achterberg, E. P. The effects of salinity, temperature, and UV irradiation on leaching and adsorption of phthalate esters from polyethylene in seawater. *Sci. Total Environ.* **2022**, *838* (Pt 1), 155461. DOI: 10.1016/j.scitotenv.2022.155461.

(20) Li, C. T. K. H., Daniel. Effects of pH and Temperature on the Leaching of Di(2- Ethylhexyl) Phthalate and Di-n-butyl Phthalate from Microplastics in Simulated Marine Environment. *Biointerface Research in Applied Chemistry* **2022**, *13* (3), 1-12. DOI: 10.33263/BRIAC133.269.

(21) Zimmermann, L.; Bartosova, Z.; Braun, K.; Oehlmann, J.; Völker, C.; Wagner, M. Plastic Products Leach Chemicals That Induce In Vitro Toxicity under Realistic Use Conditions. *Environ. Sci. Technol.* **2021**, *55* (17), 11814-11823. DOI: 10.1021/acs.est.1c01103.

(22) Chen, Q.; Allgeier, A.; Yin, D.; Hollert, H. Leaching of endocrine disrupting chemicals from marine microplastics and mesoplastics under common life stress conditions. *Environ. Int.* **2019**, *130*, 104938. DOI: 10.1016/j.envint.2019.104938.

(23) Romera-Castillo, C.; Birnstiel, S.; Álvarez-Salgado, X. A.; Sebastián, M. Aged Plastic Leaching of Dissolved Organic Matter Is Two Orders of Magnitude Higher Than Virgin Plastic Leading to a Strong Uplift in Marine Microbial Activity. *Frontiers in Marine Science* **2022**, *9*. DOI: 10.3389/fmars.2022.861557.

(24) Hardy, J. T. The sea surface microlayer: Biology, chemistry and anthropogenic enrichment. *Prog. Oceanogr.* **1982**, *11* (4), 307-328. DOI: 10.1016/0079-6611(82)90001-5.

(25) Wurl, O.; Obbard, J. P. A review of pollutants in the sea-surface microlayer (SML): a unique habitat for marine organisms. *Mar. Pollut. Bull.* **2004**, *48* (11-12), 1016-1030. DOI: 10.1016/j.marpolbul.2004.03.016.

(26) Vandenberg, L. N.; Hauser, R.; Marcus, M.; Olea, N.; Welshons, W. V. Human exposure to bisphenol A (BPA). *Reprod. Toxicol.* **2007**, *24* (2), 139-177. DOI: 10.1016/j.reprotox.2007.07.010.

(27) Pakalin, S. A., K.; Munn, S. Updated European Union risk assessment report 4,4'-isopropylidenediphenol (bisphenol-A)

Human health addendum of February 2008. **2010**. DOI: 10.2788/40195.

(28) Fleisch, A. F.; Sheffield, P. E.; Chinn, C.; Edelstein, B. L.; Landrigan, P. J. Bisphenol A and related compounds in dental materials. *Pediatrics* **2010**, *126* (4), 760-768. DOI: 10.1542/peds.2009-2693.

(29) Schwartz, A. W.; Landrigan, P. J. Bisphenol A in thermal paper receipts: an opportunity for evidence-based prevention. *Environ. Health Perspect.* **2012**, *120* (1), A14-15; author reply A15. DOI: 10.1289/ehp.1104004.

(30) Center for Food, S.; Nutrition, A. Bisphenol A (BPA): Use in Food Contact Application. FDA: 2023.

(31) Erler, C.; Novak, J. Bisphenol a exposure: human risk and health policy. *J. Pediatr. Nurs.* **2010**, *25* (5), 400-407. DOI: 10.1016/j.pedn.2009.05.006.

(32) Rubin, B. S. Bisphenol A: an endocrine disruptor with widespread exposure and multiple effects. *J. Steroid Biochem. Mol. Biol.* **2011**, *127* (1-2), 27-34. DOI: 10.1016/j.jsbmb.2011.05.002.

(33) Seachrist, D. D.; Bonk, K. W.; Ho, S.-M.; Prins, G. S.; Soto, A. M.; Keri, R. A. A review of the carcinogenic potential of bisphenol A. *Reprod. Toxicol.* **2016**, *59*, 167-182. DOI: 10.1016/j.reprotox.2015.09.006.

(34) Wang, T.; Li, M.; Chen, B.; Xu, M.; Xu, Y.; Huang, Y.; Lu, J.; Chen, Y.; Wang, W.; Li, X.; Liu, Y.; Bi, Y.; Lai, S.; Ning, G. Urinary bisphenol A (BPA) concentration associates with obesity and insulin resistance. *J. Clin. Endocrinol. Metab.* **2012**, *97* (2), E223-227. DOI: 10.1210/jc.2011-1989.

(35) Pérez-Bermejo, M.; Mas-Pérez, I.; Murillo-Llorente, M. T. The role of the Bisphenol A in diabetes and obesity. *Biomedicines* **2021**, *9* (6), 666. DOI: 10.3390/biomedicines9060666.

(36) Vom Saal, F. S.; Nagel, S. C.; Coe, B. L.; Angle, B. M.; Taylor, J. A. The estrogenic endocrine disrupting chemical bisphenol A (BPA) and obesity. *Mol. Cell. Endocrinol.* **2012**, *354* (1-2), 74-84. DOI: 10.1016/j.mce.2012.01.001.

(37) Melzer, D.; Rice, N. E.; Lewis, C.; Henley, W. E.; Galloway, T. S. Association of urinary bisphenol a concentration with heart disease: evidence from NHANES 2003/06. *PLoS One* **2010**, *5* (1), e8673. DOI: 10.1371/journal.pone.0008673.

(38) Han, C.; Hong, Y.-C. Bisphenol A, Hypertension, and Cardiovascular Diseases: Epidemiological, Laboratory, and Clinical Trial Evidence. *Curr. Hypertens. Rep.* **2016**, *18* (2), 11. DOI: 10.1007/s11906-015-0617-2.

(39) Trasande, L. Further limiting bisphenol a in food uses could provide health and economic benefits. *Health Aff.* **2014**, *33* (2), 316-323. DOI: 10.1377/hlthaff.2013.0686.

(40) Kang, J.-H.; Kondo, F. Bisphenol A degradation in seawater is different from that in river water. *Chemosphere* **2005**, *60* (9), 1288-1292. DOI: 10.1016/j.chemosphere.2005.01.058.

(41) Yamamoto, T.; Yasuhara, A.; Shiraishi, H.; Nakasugi, O. Bisphenol A in hazardous waste landfill leachates. *Chemosphere* **2001**, *42* (4), 415-418. DOI: 10.1016/s0045-6535(00)00079-5.

(42) Zhang, Z.-M.; Zhang, H.-H.; Zou, Y.-W.; Yang, G.-P. Distribution and ecotoxicological state of phthalate esters in the sea-surface microlayer, seawater and sediment of the Bohai Sea and the Yellow Sea. *Environ. Pollut.* **2018**, *240*, 235-247. DOI: 10.1016/j.envpol.2018.04.056.

(43) Seinfeld, J. H.; Pandis, S. N. *Atmospheric Chemistry and Physics: From Air Pollution to Climate Change*; John Wiley & Sons, 2016.

(44) Hallquist, M.; Wenger, J. C.; Baltensperger, U.; Rudich, Y.; Simpson, D.; Claeys, M.; Dommen, J.; Donahue, N. M.; George, C.; Goldstein, A. H.; Hamilton, J. F.; Herrmann, H.; Hoffmann, T.; Iinuma, Y.; Jang, M.; Jenkin, M. E.; Jimenez, J. L.; Kiendler-Scharr, A.; Maenhaut, W.; McFiggans, G.; Mentel, T. F.; Monod, A.; Prévôt, A. S. H.; Seinfeld, J. H.; Surratt, J. D.; Szmigielski, R.; Wildt, J. The formation, properties and impact of secondary organic aerosol: current and emerging issues. *Atmos. Chem. Phys.* **2009**, *9* (14), 5155-5236. DOI: 10.5194/acp-9-5155-2009.

(45) Lee, H.; Romero, J. IPCC, 2023: Climate Change 2023: Synthesis Report. **2023**, 35-115. DOI: 10.59327/IPCC/AR6-9789291691647.

(46) Charlson, R. J.; Wigley, T. M. L. Sulfate Aerosol and Climatic Change. *Sci. Am.* **1994**, *270* (2), 48-57.

(47) Feng, Y.; Ramanathan, V.; Kotamarthi, V. R. Brown carbon: a significant atmospheric absorber of solar radiation? *Atmos. Chem. Phys.* **2013**, *13* (17), 8607-8621. DOI: 10.5194/acp-13-8607-2013.

(48) Farmer, D. K.; Cappa, C. D.; Kreidenweis, S. M. Atmospheric processes and their controlling influence on cloud condensation nuclei activity. *Chem. Rev.* **2015**, *115* (10), 4199-4217. DOI: 10.1021/cr5006292.

(49) Koullapis, P. G.; Stylianou, F. S.; Sznitman, J.; Olsson, B.; Kassinos, S. C. Towards whole-lung simulations of aerosol deposition: A model of the deep lung. *J. Aerosol Sci.* **2020**, *144*, 105541. DOI: 10.1016/j.jaerosci.2020.105541.

(50) Rupp, G. Aerosol dynamics and health: strategies to reduce exposure and harm. *Biomarkers* **2009**, *14 Suppl 1*, 3-4. DOI: 10.1080/13547500903145458.

(51) Taylor, P. E.; Flagan, R. C.; Valenta, R.; Glovsky, M. M. Release of allergens as respirable aerosols: A link between grass pollen and asthma. *J. Allergy Clin. Immunol.* **2002**, *109* (1), 51-56. DOI: 10.1067/mai.2002.120759.

(52) Jindal, S. K.; Gupta, D. The relationship between tobacco smoke & bronchial asthma. *Indian J. Med. Res.* **2004**, *120* (5), 443-453.

(53) Delfino, R. J.; Staimer, N.; Tjoa, T.; Polidori, A.; Arhami, M.; Gillen, D. L.; Kleinman, M. T.; Vaziri, N. D.; Longhurst, J.; Zaldivar, F.; Sioutas, C. Circulating biomarkers of inflammation, antioxidant activity, and platelet activation are associated with primary combustion aerosols in subjects with coronary artery disease. *Environ. Health Perspect.* **2008**, *116* (7), 898-906. DOI: 10.1289/ehp.11189.

(54) Grunig, G.; Marsh, L. M.; Esmaeil, N.; Jackson, K.; Gordon, T.; Reibman, J.; Kwapiszewska, G.; Park, S.-H. Perspective: ambient air pollution: inflammatory response and effects on the lung's vasculature. *Pulm. Circ.* **2014**, *4* (1), 25-35. DOI: 10.1086/674902.

(55) Seposo, X.; Ueda, K.; Park, S. S.; Sudo, K.; Takemura, T.; Nakajima, T. Effect of global atmospheric aerosol emission change on PM2.5-related health impacts. *Glob. Health Action* **2019**, *12* (1), 1664130. DOI: 10.1080/16549716.2019.1664130.

(56) de Leeuw, G.; Andreas, E. L.; Anguelova, M. D.; Fairall, C. W.; Lewis, E. R.; O'Dowd, C.; Schulzl, M.; Schwartz, S. E. Production Flux Of Sea Spray Aerosol. *Reviews of Geophysics* **2011**, *49*, 1-39. DOI: 10.1029/2010RG000349.

(57) C. W. Fairall; M. L. Banner; W. L. Peirson; W. Asher; Morison, R. P. Investigation of the physical scaling of sea spray spume droplet production. *Journal Of Geophysical Research* **2009**, *114* (C10001), 1-19. DOI: 10.1029/2008JC004918.

(58) F. Veron; C. Hopkins; E. L. Harrison; Mueller, J. A. Sea spray spume droplet production in high wind speeds. *Geophysical Research Letters* **2012**, *39* (16), 1-5. DOI: 10.1029/2012GL052603.

(59) Spiel, D. E. On the births of film drops from bubbles bursting on seawater surfaces. *J. Geophys. Res.* **1998**, *103* (C11), 24907-24918. DOI: 10.1029/98jc02233.

(60) Lewis, E. R.; Schwartz, S. E. *Sea Salt Aerosol Production: Mechanisms, Methods, Measurements, and Models*; American Geophysical Union, 2004.

(61) Stokes, M. D.; Deane, G. B.; Prather, K.; Bertram, T. H.; Ruppel, M. J.; Ryder, O. S.; Brady, J. M.; Zhao, D. A Marine Aerosol Reference Tank system as a breaking wave analogue for the

production of foam and sea-spray aerosols. *Atmos. Meas. Tech.* **2013**, *6* (4), 1085-1094. DOI: 10.5194/amt-6-1085-2013.

(62) Modini, R. L.; Russell, L. M.; Deane, G. B.; Stokes, M. D. Effect of soluble surfactant on bubble persistence and bubble-produced aerosol particles. *J. Geophys. Res.* **2013**, *118* (3), 1388-1400. DOI: 10.1002/jgrd.50186.

(63) Wang, X.; Deane, G. B.; Moore, K. A.; Ryder, O. S.; Stokes, M. D.; Beall, C. M.; Collins, D. B.; Santander, M. V.; Burrows, S. M.; Sultana, C. M.; Prather, K. A. The role of jet and film drops in controlling the mixing state of submicron sea spray aerosol particles. *Proc. Natl. Acad. Sci. U. S. A.* **2017**, *114* (27), 6978-6983. DOI: 10.1073/pnas.1702420114.

(64) Ault, A. P.; Moffet, R. C.; Baltrusaitis, J.; Collins, D. B.; Ruppel, M. J.; Cuadra-Rodriguez, L. A.; Zhao, D.; Guasco, T. L.; Ebben, C. J.; Geiger, F. M.; Bertram, T. H.; Prather, K. A.; Grassian, V. H. Size-dependent changes in sea spray aerosol composition and properties with different seawater conditions. *Environ. Sci. Technol.* **2013**, *47* (11), 5603-5612. DOI: 10.1021/es400416g.

(65) Prather, K. A.; Bertram, T. H.; Grassian, V. H.; Deane, G. B.; Stokes, M. D.; Demott, P. J.; Aluwihare, L. I.; Palenik, B. P.; Azam, F.; Seinfeld, J. H.; Moffet, R. C.; Molina, M. J.; Cappa, C. D.; Geiger, F. M.; Roberts, G. C.; Russell, L. M.; Ault, A. P.; Baltrusaitis, J.; Collins, D. B.; Corrigan, C. E.; Cuadra-Rodriguez, L. A.; Ebben, C. J.; Forestieri, S. D.; Guasco, T. L.; Hersey, S. P.; Kim, M. J.; Lambert, W. F.; Modini, R. L.; Mui, W.; Pedler, B. E.; Ruppel, M. J.; Ryder, O. S.; Schoepp, N. G.; Sullivan, R. C.; Zhao, D. Bringing the ocean into the laboratory to probe the chemical complexity of sea spray aerosol. *Proc. Natl. Acad. Sci. U. S. A.* **2013**, *110* (19), 7550-7555. DOI: 10.1073/pnas.1300262110.

(66) Tsigaridis, K.; Koch, D.; Menon, S. Uncertainties and importance of sea spray composition on aerosol direct and indirect effects. *JGR Atmospheres* **2013**, *118*, 220-235. DOI: 10.1029/2012JD018165.

(67) Ma, X.; Salzen, K.; Li, J. Modelling sea salt aerosol and its direct and indirect effects on climate. *Atmos. Chem. Phys.* **2007**, *8*, 1311-1327. DOI: 10.5194/ACP-8-1311-2008.

(68) Patterson, J. P.; Collins, D. B.; Michaud, J. M.; Axson, J. L.; Sultana, C. M.; Moser, T.; Dommer, A. C.; Conner, J.; Grassian, V. H.; Stokes, M. D.; Deane, G. B.; Evans, J. E.; Burkart, M. D.; Prather, K. A.; Gianneschi, N. C. Sea Spray Aerosol Structure and Composition Using Cryogenic Transmission Electron Microscopy. *ACS Cent Sci* **2016**, *2* (1), 40-47. DOI: 10.1021/acscentsci.5b00344.

(69) Cochran, R. E.; Laskina, O.; Jayarathne, T.; Laskin, A.; Laskin, J.; Lin, P.; Sultana, C.; Lee, C.; Moore, K. A.; Cappa, C. D.; Bertram, T. H.; Prather, K. A.; Grassian, V. H.; Stone, E. A. Analysis of Organic Anionic Surfactants in Fine and Coarse Fractions of Freshly Emitted Sea Spray Aerosol. *Environ. Sci. Technol.* **2016**, *50* (5), 2477-2486. DOI: 10.1021/acs.est.5b04053.

(70) Burdette, T. C.; Bramblett, R. L.; Zimmermann, K.; Frossard, A. A. Influence of Air Mass Source Regions on Signatures of Surface-Active Organic Molecules in Size Resolved Atmospheric Aerosol Particles. *ACS Earth Space Chem.* **2023**. DOI: 10.1021/acsearthspacechem.3c00161.

(71) Schill, S. R.; Burrows, S. M.; Hasenecz, E. S.; Stone, E. A.; Bertram, T. H. The Impact of Divalent Cations on the Enrichment of Soluble Saccharides in Primary Sea Spray Aerosol. *Atmosphere* **2018**, *9* (12), 476. DOI: 10.3390/atmos9120476.

(72) Jayarathne, T.; Sultana, C. M.; Lee, C.; Malfatti, F.; Cox, J. L.; Pendergraft, M. A.; Moore, K. A.; Azam, F.; Tivanski, A. V.; Cappa, C. D.; Bertram, T. H.; Grassian, V. H.; Prather, K. A.; Stone, E. A. Enrichment of Saccharides and Divalent Cations in Sea Spray Aerosol During Two Phytoplankton Blooms. *Environ. Sci. Technol.* **2016**, *50* (21), 11511-11520. DOI: 10.1021/acs.est.6b02988.

(73) Schmitt-Kopplin, P.; Liger-Belair, G.; Koch, B. P.; Flerus, R.; Kattner, G.; Harir, M.; Kanawati, B.; Lucio, M.; Tziotis, D.; Hertkorn, N.; Gebefügi, I. Dissolved organic matter in sea spray: a transfer study from marine surface water to aerosols. *Biogeosci. Discuss.* **2011**, *8* (6), 11767-11793. DOI: 10.5194/bgd-8-11767-2011.

(74) Miyazaki, Y.; Yamashita, Y.; Kawana, K.; Tachibana, E.; Kagami, S.; Mochida, M.; Suzuki, K.; Nishioka, J. Chemical transfer of dissolved organic matter from surface seawater to sea spray water-soluble organic aerosol in the marine atmosphere. *Sci. Rep.* **2018**, *8* (1), 14861. DOI: 10.1038/s41598-018-32864-7.

(75) Quinn, P. K.; Bates, T. S.; Schulz, K. S.; Coffman, D. J.; Frossard, A. A.; Russell, L. M.; Keene, W. C.; Kieber, D. J. Contribution of sea surface carbon pool to organic matter enrichment in sea spray aerosol. *Nat. Geosci.* **2014**, *7* (3), 228-232. DOI: 10.1038/ngeo2092.

(76) Su, B.; Bi, X.; Zhang, Z.; Liang, Y.; Song, C.; Wang, T.; Hu, Y.; Li, L.; Zhou, Z.; Yan, J.; Wang, X.; Zhang, G. Enrichment of calcium in sea spray aerosol: insights from bulk measurements and individual particle analysis during the R/V Xuelong cruise in the summertime in Ross Sea, Antarctica. *Atmos. Chem. Phys.* **2023**, *23* (18), 10697-10711. DOI: 10.5194/acp-23-10697-2023.

(77) Salter, M. E.; Hamacher-Barth, E.; Leck, C.; Werner, J.; Johnson, C. M.; Riipinen, I.; Nilsson, E. D.; Zieger, P. Calcium enrichment in sea spray aerosol particles. *Geophys. Res. Lett.* **2016**, *43* (15), 8277-8285. DOI: 10.1002/2016gl070275.

(78) Pham, D. Q.; O'Brien, R.; Fraund, M.; Bonanno, D.; Laskina, O.; Beall, C.; Moore, K. A.; Forestieri, S.; Wang, X.; Lee, C.; Sultana, C.; Grassian, V.; Cappa, C. D.; Prather, K. A.; Moffet, R. C. Biological Impacts on Carbon Speciation and Morphology of Sea Spray Aerosol. *ACS Earth Space Chem.* **2017**, *1* (9), 551-561. DOI: 10.1021/acsearthspacechem.7b00069.

(79) Ault, A. P.; Zhao, D.; Ebben, C. J.; Tauber, M. J.; Geiger, F. M.; Prather, K. A.; Grassian, V. H. Raman microspectroscopy and vibrational sum frequency generation spectroscopy as probes of the bulk and surface compositions of size-resolved sea spray aerosol particles. *Phys. Chem. Chem. Phys.* **2013**, *15* (17), 6206-6214. DOI: 10.1039/c3cp43899f.

(80) Crocker, D. R.; Hernandez, R. E.; Huang, H. D.; Pendergraft, M. A.; Cao, R.; Dai, J.; Morris, C. K.; Deane, G. B.; Prather, K. A.; Thiemens, M. H. Biological Influence on δ13C and Organic Composition of Nascent Sea Spray Aerosol. *ACS Earth Space Chem.* **2020**, *4* (9), 1686-1699. DOI: 10.1021/acsearthspacechem.0c00072.

(81) Collins, D. B.; Bertram, T. H.; Sultana, C. M.; Lee, C.; Axson, J. L.; Prather, K. A. Phytoplankton blooms weakly influence the cloud forming ability of sea spray aerosol. *Geophys. Res. Lett.* **2016**, *43* (18), 9975-9983. DOI: 10.1002/2016gl069922.

(82) Forestieri, S. D.; Cornwell, G. C.; Helgestad, T. M.; Moore, K. A.; Lee, C.; Novak, G. A.; Sultana, C. M.; Wang, X.; Bertram, T. H.; Prather, K. A.; Cappa, C. D. Linking variations in sea spray aerosol particle hygroscopicity to composition during two microcosm experiments. *Atmos. Chem. Phys. Discuss.* **2016**, 1-35. DOI: 10.5194/acp-2016-36.

(83) Moore, M. J. K.; Furutani, H.; Roberts, G. C.; Moffet, R. C.; Gilles, M. K.; Palenik, B.; Prather, K. A. Effect of organic compounds on cloud condensation nuclei (CCN) activity of sea spray aerosol produced by bubble bursting. *Atmos. Environ.* **2011**, *45* (39), 7462-7469. DOI: 10.1016/j.atmosenv.2011.04.034.

(84) DeMott, P. J.; Hill, T. C. J.; McCluskey, C. S.; Prather, K. A.; Collins, D. B.; Sullivan, R. C.; Ruppel, M. J.; Mason, R. H.; Irish, V. E.; Lee, T.; Hwang, C. Y.; Rhee, T. S.; Snider, J. R.; McMeeking, G. R.; Dhaniyala, S.; Lewis, E. R.; Wentzell, J. J. B.; Abbatt, J.; Lee, C.; Sultana, C. M.; Ault, A. P.; Axson, J. L.; Diaz Martinez, M.; Venero, I.; Santos-Figueroa, G.; Stokes, M. D.; Deane, G. B.; Mayol-Bracero, O. L.; Grassian, V. H.; Bertram, T. H.; Bertram, A. K.; Moffett, B. F.; Franc, G. D. Sea spray aerosol as a unique source of ice nucleating particles. *Proc. Natl. Acad. Sci. U. S. A.* **2016**, *113* (21), 5797-5803. DOI: 10.1073/pnas.1514034112.

(85) Angle, K. J.; Nowak, C. M.; Davasam, A.; Dommer, A. C.; Wauer, N. A.; Amaro, R. E.; Grassian, V. H. Amino Acids Are Driven to the Interface by Salts and Acidic Environments. *J. Phys. Chem. Lett.* **2022**, *13* (12), 2824-2829. DOI: 10.1021/acs.jpclett.2c00231.

(86) Freedman, M. A.; Ott, E.-J. E.; Marak, K. E. Role of pH in Aerosol Processes and Measurement Challenges. *J. Phys. Chem. A* **2019**, *123* (7), 1275-1284. DOI: 10.1021/acs.jpca.8b10676.

(87) Angle, K. J.; Crocker, D. R.; Simpson, R. M. C.; Mayer, K. J.; Garofalo, L. A.; Moore, A. N.; Mora Garcia, S. L.; Or, V. W.; Srinivasan, S.; Farhan, M.; Sauer, J. S.; Lee, C.; Pothier, M. A.; Farmer, D. K.; Martz, T. R.; Bertram, T. H.; Cappa, C. D.; Prather, K. A.; Grassian, V. H. Acidity across the interface from the ocean surface to sea spray aerosol. *Proc. Natl. Acad. Sci. U. S. A.* **2021**, *118* (2), e2018397118. DOI: 10.1073/pnas.2018397118.

(88) Wu, G.; Wang, H.; Zhang, C.; Gong, D.; Liu, X.; Ristovski, Z.; Wang, B. Anthropogenic pollutants induce enhancement of aerosol acidity at a mountainous background atmosphere in southern China. *Sci. Total Environ.* **2023**, 166192. DOI: 10.1016/j.scitotenv.2023.166192.

(89) Romera-Castillo, C.; Lucas, A.; Mallenco-Fornies, R.; Briones-Rizo, M.; Calvo, E.; Pelejero, C. Abiotic plastic leaching contributes to ocean acidification. *Sci. Total Environ.* **2023**, *854*, 158683. DOI: 10.1016/j.scitotenv.2022.158683.

(90) Jang, M.; Czoschke, N. M.; Lee, S.; Kamens, R. M. Heterogeneous atmospheric aerosol production by acid-catalyzed particle-phase reactions. *Science* **2002**, *298* (5594), 814-817. DOI: 10.1126/science.1075798.

(91) Jang, M.; Lee, S.; Kamens, R. M. Organic aerosol growth by acid-catalyzed heterogeneous reactions of octanal in a flow reactor. *Atmos. Environ.* **2003**, *37*, 2125-2138. DOI: 10.1016/S1352-2310(03)00077-3.

(92) Gao, S.; Ng, N. L.; Keywood, M.; Varutbangkul, V.; Bahreini, R.; Nenes, A.; He, J.; Yoo, K. Y.; Beauchamp, J. L.; Hodyss, R. P.; Flagan, R. C.; Seinfeld, J. H. Particle phase acidity and oligomer formation in secondary organic aerosol. *Environ. Sci. Technol.* **2004**, *38* (24), 6582-6589. DOI: 10.1021/es049125k.

(93) Kaluarachchi, C. P.; Or, V. W.; Lan, Y.; Madawala, C. K.; Hasenecz, E. S.; Crocker, D. R.; Morris, C. K.; Lee, H. D.; Mayer, K. J.; Sauer, J. S.; Lee, C.; Dorce, G.; Malfatti, F.; Stone, E. A.; Cappa, C. D.; Grassian, V. H.; Prather, K. A.; Tivanski, A. V. Size-Dependent Morphology, Composition, Phase State, and Water Uptake of Nascent Submicrometer Sea Spray Aerosols during a Phytoplankton Bloom. *ACS Earth Space Chem.* **2022**, *6* (1), 116-130. DOI: 10.1021/acsearthspacechem.1c00306.

(94) Lee, H. D.; Wigley, S.; Lee, C.; Or, V. W.; Hasenecz, E. S.; Stone, E. A.; Grassian, V. H.; Prather, K. A.; Tivanski, A. V. Physicochemical Mixing State of Sea Spray Aerosols: Morphologies Exhibit Size Dependence. *ACS Earth Space Chem.* **2020**, *4* (9), 1604-1611. DOI: 10.1021/acsearthspacechem.0c00153.

(95) You, Y.; Smith, M. L.; Song, M.; Martin, S. T.; Bertram, A. K. Liquid–liquid phase separation in atmospherically relevant particles consisting of organic species and inorganic salts. *Int. Rev. Phys. Chem.* **2014**, *33* (1), 43-77. DOI: 10.1080/0144235X.2014.890786.

(96) Nandy, L.; Liu, S.; Gunsbury, C.; Wang, X.; Pendergraft, M. A.; Prather, K. A.; Dutcher, C. S. Multistep Phase Transitions in Sea Surface Microlayer Droplets and Aerosol Mimics using Microfluidic Wells. *ACS Earth Space Chem.* **2019**, *3* (7), 1260-1267. DOI: 10.1021/acsearthspacechem.9b00121.

(97) Dommer, A. C.; Wauer, N. A.; Angle, K. J.; Davasam, A.; Rubio, P.; Luo, M.; Morris, C. K.; Prather, K. A.; Grassian, V. H.; Amaro, R. E. Revealing the Impacts of Chemical Complexity on Submicrometer Sea Spray Aerosol Morphology. *ACS Cent. Sci.* **2023**. DOI: 10.1021/acscentsci.3c00184.

(98) Shiraiwa, M.; Ammann, M.; Koop, T.; Pöschl, U. Gas uptake and chemical aging of semisolid organic aerosol particles. *Proc. Natl. Acad. Sci. U. S. A.* **2011**, *108* (27), 11003-11008. DOI: 10.1073/pnas.1103045108.

(99) Koop, T.; Bookhold, J.; Shiraiwa, M.; Pöschl, U. Glass transition and phase state of organic compounds: dependency on molecular properties and implications for secondary organic aerosols in the atmosphere. *Phys. Chem. Chem. Phys.* **2011**, *13* (43), 19238-19255. DOI: 10.1039/c1cp22617g.

(100) Marshall, F. H.; Miles, R. E. H.; Song, Y.-C.; Ohm, P. B.; Power, R. M.; Reid, J. P.; Dutcher, C. S. Diffusion and reactivity in ultraviscous aerosol and the correlation with particle viscosity. *Chem. Sci.* **2016**, *7* (2), 1298-1308. DOI: 10.1039/c5sc03223g.

(101) Slade, J. H.; Knopf, D. A. Multiphase OH oxidation kinetics of organic aerosol: The role of particle phase state and relative humidity. *Geophys. Res. Lett.* **2014**, *41* (14), 5297-5306. DOI: 10.1002/2014gl060582.

(102) Reid, J. P.; Bertram, A. K.; Topping, D. O.; Laskin, A.; Martin, S. T.; Petters, M. D.; Pope, F. D.; Rovelli, G. The viscosity of atmospherically relevant organic particles. *Nat. Commun.* **2018**, *9* (1), 956. DOI: 10.1038/s41467-018-03027-z.

(103) Hosny, N. A.; Fitzgerald, C.; Vyšniauskas, A.; Athanasiadis, A.; Berkemeier, T.; Uygur, N.; Pöschl, U.; Shiraiwa, M.; Kalberer, M.; Pope, F. D.; Kuimova, M. K. Direct imaging of changes in aerosol particle viscosity upon hydration and chemical aging. *Chem. Sci.* **2016**, *7* (2), 1357-1367. DOI: 10.1039/c5sc02959g.

(104) DeRieux, W.-S. W.; Li, Y.; Lin, P.; Laskin, J.; Laskin, A.; Bertram, A. K.; Nizkorodov, S. A.; Shiraiwa, M. Predicting the glass transition temperature and viscosity of secondary organic material using molecular composition. *Atmos. Chem. Phys.* **2018**, *18* (9), 6331-6351. DOI: 10.5194/acp-18-6331-2018.

(105) Tumminello, P. R.; James, R. C.; Kruse, S.; Kawasaki, A.; Cooper, A.; Guadalupe-Diaz, I.; Zepeda, K. L.; Crocker, D. R.; Mayer, K. J.; Sauer, J. S.; Lee, C.; Prather, K. A.; Slade, J. H. Evolution of Sea Spray Aerosol Particle Phase State Across a Phytoplankton Bloom. *ACS Earth Space Chem.* **2021**, *5* (11), 2995-3007. DOI: 10.1021/acsearthspacechem.1c00186.

(106) Freedman, M. A. Phase separation in organic aerosol. *Chem. Soc. Rev.* **2017**, *46* (24), 7694-7705. DOI: 10.1039/c6cs00783j.

(107) Ye, Q.; Goss, M. B.; Krechmer, J. E.; Majluf, F.; Zaytsev, A.; Li, Y.; Roscioli, J. R.; Canagaratna, M.; Keutsch, F. N.; Heald, C. L.; Kroll, J. H. Product distribution, kinetics, and aerosol formation from the OH oxidation of dimethyl sulfide under different RO2 regimes. *Atmospheric Chemistry and Physics Discussions* **2022**. DOI: 10.5194/acp-2022-566.

(108) Ciobanu, V. G.; Marcolli, C.; Krieger, U. K.; Weers, U.; Peter, T. Liquid-liquid phase separation in mixed organic/inorganic aerosol particles. *J. Phys. Chem. A* **2009**, *113* (41), 10966-10978. DOI: 10.1021/jp905054d.

(109) Shilling, J. E.; King, S. M.; Mochida, M.; Worsnop, D. R.; Martin, S. T. Mass spectral evidence that small changes in composition caused by oxidative aging processes alter aerosol CCN properties. *J. Phys. Chem. A* **2007**, *111* (17), 3358-3368. DOI: 10.1021/jp068822r.

(110) George, I. J.; Chang, R. Y. W.; Danov, V.; Vlasenko, A.; Abbatt, J. P. D. Modification of cloud condensation nucleus activity of organic aerosols by hydroxyl radical heterogeneous oxidation. *Atmos. Environ.* **2009**, *43* (32), 5038-5045. DOI: 10.1016/j.atmosenv.2009.06.043.

(111) Slade, J. H.; Shiraiwa, M.; Arangio, A.; Su, H.; Pöschl, U.; Wang, J.; Knopf, D. A. Cloud droplet activation through oxidation of organic aerosol influenced by temperature and particle phase state. *Geophysical* **2017**. DOI: 10.1002/2016GL072424.

(112) Petrick, L. M.; Svidovsky, A.; Dubowski, Y. Thirdhand smoke: heterogeneous oxidation of nicotine and secondary aerosol formation in the indoor environment. *Environ. Sci. Technol.* **2011**, *45* (1), 328-333. DOI: 10.1021/es102060v.

(113) Pillar-Little, E. A.; Guzman, M. I. An Overview of Dynamic Heterogeneous Oxidations in the Troposphere. *Environments* **2018**, *5* (9), 104. DOI: 10.3390/environments5090104.

(114) George, I. J.; Abbatt, J. P. D. Heterogeneous oxidation of atmospheric aerosol particles by gas-phase radicals. *Nat. Chem.* **2010**, *2* (9), 713-722. DOI: 10.1038/nchem.806.

(115) Kroll, J. H.; Lim, C. Y.; Kessler, S. H.; Wilson, K. R. Heterogeneous Oxidation of Atmospheric Organic Aerosol: Kinetics of Changes to the Amount and Oxidation State of Particle-Phase Organic Carbon. *J. Phys. Chem. A* **2015**, *119* (44), 10767-10783. DOI: 10.1021/acs.jpca.5b06946.

(116) Kroll, J. H.; Smith, J. D.; Che, D. L.; Kessler, S. H.; Worsnop, D. R.; Wilson, K. R. Measurement of fragmentation and functionalization pathways in the heterogeneous oxidation of oxidized organic aerosol. *Phys. Chem. Chem. Phys.* **2009**, *11* (36), 8005-8014. DOI: 10.1039/b905289e.

(117) Crutzen, P. Lecture: The Importance of the Tropics in Atmospheric Chemistry and Climate Wednesday. **2002**.

(118) Ehhalt, D.; Dorn, H.; Poppe, D. The chemistry of the hydroxyl radical in the troposphere. *Proceedings of The Royal Society B: Biological Sciences* **1990**, *97*, 17-34. DOI: 10.1017/S0269727000005273.

(119) Stone, D.; Whalley, L. K.; Heard, D. E. Tropospheric OH and HO_2 radicals: field measurements and model comparisons. *Chem. Soc. Rev.* **2012**, *41* (19), 6348-6404. DOI: 10.1039/c2cs35140d.

(120) Li, M.; Karu, E.; Brenninkmeijer, C.; Fischer, H.; Lelieveld, J.; Williams, J. Tropospheric OH and stratospheric OH and Cl concentrations determined from CH_4, CH_3Cl, and SF_6 measurements. *npj Climate and Atmospheric Science* **2018**, *1* (1), 1-7. DOI: 10.1038/s41612-018-0041-9.

(121) Davies, J. F.; Wilson, K. R. Nanoscale interfacial gradients formed by the reactive uptake of OH radicals onto viscous aerosol surfaces. *Chem. Sci.* **2015**, *6* (12), 7020-7027. DOI: 10.1039/c5sc02326b.

(122) Donahue, N. M.; Robinson, A. L.; Trump, E. R.; Riipinen, I.; Kroll, J. H. Volatility and aging of atmospheric organic aerosol. *Top. Curr. Chem.* **2014**, *339*, 97-143. DOI: 10.1007/128_2012_355.

(123) George, I. J.; Vlasenko, A.; Slowik, J. G.; Broekhuizen, K.; Abbatt, J. P. D. Heterogeneous oxidation of saturated organic aerosols by hydroxyl radicals: uptake kinetics, condensed-phase products, and particle size change. *Atmos. Chem. Phys.* **2007**, *7* (16), 4187-4201. DOI: 10.5194/acp-7-4187-2007.

(124) Shilling, J. E.; Zawadowicz, M. A.; Liu, J.; Zaveri, R. A.; Zelenyuk, A. Photochemical Aging Alters Secondary Organic Aerosol Partitioning Behavior. *ACS Earth Space Chem.* **2019**, *3* (12), 2704-2716. DOI: 10.1021/acsearthspacechem.9b00248.

(125) Sareen, N.; Moussa, S. G.; McNeill, V. F. Photochemical aging of light-absorbing secondary organic aerosol material. *J. Phys. Chem. A* **2013**, *117* (14), 2987-2996. DOI: 10.1021/jp309413j.

(126) Wu, J.; Bei, N.; Hu, B.; Liu, S.; Wang, Y.; Shen, Z.; Li, X.; Liu, L.; Wang, R.; Liu, Z.; Cao, J.; Tie, X.; Molina, L. T.; Li, G. Aerosol–photolysis interaction reduces particulate matter during wintertime haze events. *Proceedings of the National Academy of Sciences* **2020**, *117* (18), 9755-9761. DOI: 10.1073/pnas.1916775117.

(127) Hodzic, A.; Madronich, S.; Kasibhatla, P.; Tyndall, G.; Aumont, B.; Jimenez, J.; Lee-Taylor, J.; Orlando, J. Organic photolysis reactions in tropospheric aerosols: effect on secondary organic aerosol formation and lifetime. *Atmos. Chem. Phys.* **2015**, *15*, 9253-9269. DOI: 10.5194/ACP-15-9253-2015.

(128) Gómez Alvarez, E.; Wortham, H.; Strekowski, R.; Zetzsch, C.; Gligorovski, S. Atmospheric photosensitized heterogeneous and multiphase reactions: from outdoors to indoors. *Environ. Sci. Technol.* **2012**, *46* (4), 1955-1963. DOI: 10.1021/es2019675.

(129) Baptista, M. S.; Cadet, J.; Di Mascio, P.; Ghogare, A. A.; Greer, A.; Hamblin, M. R.; Lorente, C.; Nunez, S. C.; Ribeiro, M. S.; Thomas, A. H.; Vignoni, M.; Yoshimura, T. M. Type I and Type II Photosensitized Oxidation Reactions: Guidelines and Mechanistic Pathways. *Photochem. Photobiol.* **2017**, *93* (4), 912-919. DOI: 10.1111/php.12716.

(130) Martins-Costa, M. T. C.; Anglada, J. M.; Francisco, J. S.; Ruiz-López, M. F. Photosensitization mechanisms at the air-water interface of aqueous aerosols. *Chem. Sci.* **2022**, *13* (9), 2624-2631. DOI: 10.1039/d1sc06866k.

(131) Woods, E. I.; Harris, O. T.; Leiter, W. E.; Burner, N. E.; Ofosuhene, P.; Krez, A.; Hilton, M. A.; Burke, K. A. Lifetime of Triplet Photosensitizers in Aerosol Using Time-Resolved Photoelectric Activity. *ACS Earth Space Chem.* **2020**, *4* (8), 1424-1434. DOI: 10.1021/acsearthspacechem.0c00141.

Chapter 2 Methods

This chapter will describe the experimental methods and relevant theory utilized in future chapters in more detail. The following chapters will include the details of each method relevant to those specific experiments. Additionally, the method development of the EESI-TOF, which was a large portion of this thesis work, will be covered. The method portion of this chapter will cover (i) aerosol generation methods, (ii) aerosol separation and sizing, (iii) aerosol aging techniques, and (iv) the development of an EESI inlet for enhanced measurements of sea spray aerosols. The theory portion of this chapter will cover (i) reactive uptake coefficient derivation, (ii) gas-particle diffusion correction, and (iii) glass transition temperatures.

2.1 Aerosol Generation Methods

Mesocosm Studies of Sea Spray Aerosol

The same number and size of bubbles generated in the water column following a wave break are required to reproduce SSA accurately in the laboratory. In the absence of winds, SSA is generated from the rupturing of bubble films at the sea surface (known as film droplets) and the jet produced by the displaced water following the bubble's collapse (known as jet droplets). These different SSA generation mechanisms are well characterized, with film droplets producing relatively smaller and more organic carbon-enriched SSA. Methods to generate synthetic SSA include bubbling through glass frits, plunging waterfalls, and wave flumes.[1] Glass frits produce a size distribution that is more narrow and shifted to smaller sizes (<100 nm) than both plunging waterfall and real breaking waves, which have a peak number-weighted aerosol size distribution around 140-180 nm.[2] The synthetic SSA studied in this work was generated from a wave flume developed in the Ocean–Atmosphere Interaction Facility at the Scripps Institution of Oceanography (SIO). This wave flume was described in detail in Sauer et al. 2022[3] and is only briefly covered here. The wave flume is a glass tank (33m in length×0.5m in width×0.8m in height)

and holds 11,800L of water at a depth of 0.56m. Waves are generated inside of the large wave flume by a 0.96 m^2 paddle, operated at 3Hz with an amplitude of 73 cm. These waves then break on an artificial beach midway down the flume, which is 2.4 m long and sits at a 16º angle to the bottom of the channel, with the top edge of the beach ~5 cm from the surface. Near the end of the wave flume, there is a secondary beach to eliminate resonant waves by dissipating the remaining energy after the initial wave break. This setup produces an aerosol sample size distribution similar to that of the real ocean due to the size and persistence of the bubbles entrained by wave breaking.[2, 4]

To probe how SSA properties changed with seawater biological activity, we collaborated with the National Science Foundation - Center for Aerosol Impacts on Chemistry of the Environment (NSF-CAICE) during the Sea Spray Chemistry and Particle Evolution 2019 (SeaSCAPE 2019) study, the focus of Chapter 4.[3, 5-7] One of the major benefits to this study was the ability to compare results from ~50 different methods all sampling from the same aerosol source. In this study, real seawater was sampled off the Scripps Pier in La Jolla, CA (32° 52' 01.0" N, 117° 15' 25.7" W). The water was filtered using 50 µm Nitex nylon mesh (Flystuff; Cat # 57-106) to remove larger biological species. To initiate the bloom, f/2 growth media were added to the wave flume. F/2 growth media was developed by Guillard and Ryther 1962.[8] The f/2 media contains $NaNO_3$, NaH_2PO_4, Na_2CO_3, Na_2SiO_3, trace metals (iron, copper, zinc, cobalt, manganese, and molybdenum salts), and trace vitamins (thiamine, biotin, and B_{12}), which are all critical to the growth of coastal marine algae, especially diatoms.[8] The other critical component to the growth of a phytoplankton bloom is the presence of light. During these studies, fluorescent lights (Spectra 5700K F32-T8, Full Spectrum Solutions, Inc.) were equipped onto either side of the flume. These lamps produced a flux of ~80 µE m^{-2} s^{-1} of photosynthetically active radiation, which is sufficient

for the growth of phytoplankton blooms.[9] To simulate diurnal cycles, the lamps were set on a timer for 15 hours with lights on (07:00-21:59 PST) and 9 hours with lights off (22:00-06:59 PST).

Sea Spray Aerosol Mimics

To perform more mechanistic studies in the lab, models, or so-called "mimics", of SSA were generated in the lab using a commercial atomizer (Model 3076, TSI Inc.).[10, 11] Constant output atomizers such as the TSI model have the benefit of producing large, stable quantities of polydisperse aerosols (~1×10^7 particles cm^{-3}) with known composition based on the bulk solution that is used. The specific Model 3076 has been cited in over 3000 papers (Google Scholar) and is a common way to generate aerosols in the laboratory. This atomizer is a type of Collison nebulizer, where a high-pressure stream of gas creates an area of negative pressure due to Bernoulli's principle.[12] More specifically to the TSI atomizer, a 20 psi stream of zero air (zero-air generator, Sabio, 1001), is sent into the atomizer block, which creates a slight vacuum that pulls the bulk liquid solution up into the block. Once the solution reaches the stream of air, the solution is atomized, as shown in Figure 2.1.[13]

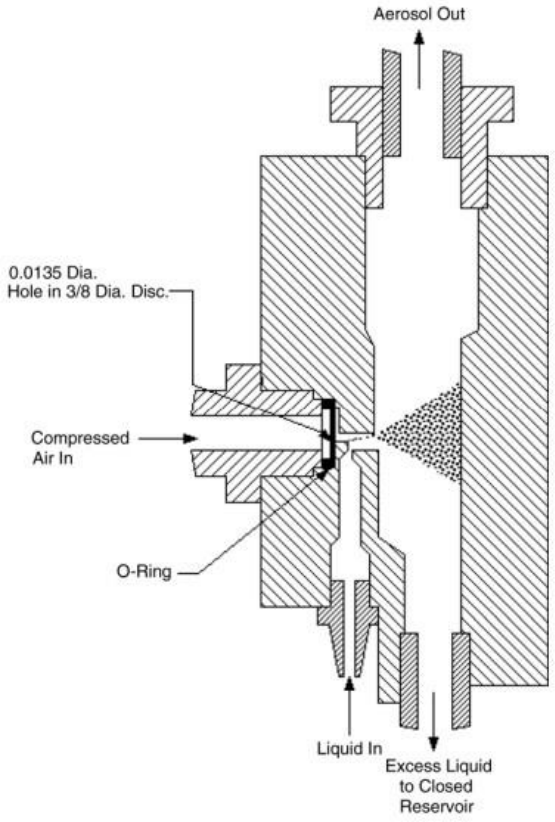

Figure 2.1 Schematic of atomizer assembly block, adapted from TSI Instruments.[13]

The atomizer was run in recirculating mode with bulk solutions containing analytes of interest that were dissolved into 75:25 water/methanol at concentrations between 100-300 ppm. The TSI atomizer has been characterized with solution concentrations up to 400 ppm, and when varying the concentration of analytes within the atomizer, the particle size distribution changes, shifting to larger particle diameter as the solute concentration increases. For example, in the case of sodium chloride particles, a 1ppm solution produces mostly 25 nm particles and a 120 ppm solution produces mostly 50 nm particles.[13] Within these tested parameters, 99% of the large drops (>1um) generated by this process stick onto the side wall of the atomizer, rather than being emitted from the atomizer.[13]

2.2 Aerosol Separation and Sizing

Scanning Electrical Mobility Spectrometer

The scanning electrical mobility spectrometer (SEMS, Brechtel) consists of a differential mobility analyzer (DMA) and a mixing condensation particle counter (MCPC) which takes the incoming aerosol, separates it by size with the DMA, and then counts the number of particles in each size bin with the MCPC.[14, 15] The DMA also serves as a monodisperse aerosol generator.

Differential Mobility Analyzer

Broadly, the DMA works by generating an electric field which, depending on the strength, will separate certain sizes of aerosol. First, the air being sampled is passed through a polonium-210 neutralizer, which reduces static and creates a Gaussian dispersion of charge of about 0 across the aerosol surface, i.e., an equal number of positive and negative charges. Due to their larger surface area, particles with larger diameter can hold more charge. Inside the DMA column, there is an outer wall and an inner wall that are both charged to act as electrodes. The outer wall is held at a constant voltage, and the inner wall has a varying voltage at a constant polarity to create an electrical field of varying strength. Only particles of a certain size with a certain number of charges at a determined electrical field strength will pass through the DMA outlet, as shown in Figure 2.2.[14-16]

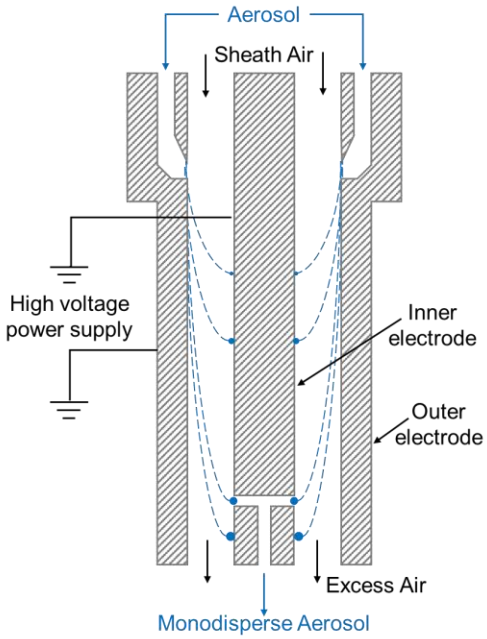

Figure 2.2 Schematic of a differential mobility analyzer[16]

The particle sizes that make it through at a certain voltage are based on their electrical mobility, as defined by Eq. 2.1

$$Z_p = \frac{neC_c}{3\pi\mu D_p} \qquad \text{Eq. 2.1}$$

where Zp is the electrical mobility (V m^{-2} s^{-1}), n is the number of charges carried by the particle, e is the unit of electrical charge (1.6×10^{-19}C), C_c is the Cunningham slip correction factor (unitless), μ is the air dynamic viscosity (kg/m/s), and D_p is the particle diameter (m). The voltage that determines the size of particles that pass through is determined by Eq. 2.2

$$V = \frac{Q_{sheath} ln \frac{R_{outer}}{R_{inner}}}{2\pi L_{DMA} Z_p} \qquad \text{Eq. 2.2}$$

Where V is the voltage applied to the inner wall, Q_{sheath} is the sheath flow (m^3 s^{-1}), R_{outer} is the outer cylinder radius (m), R_{inner} is the inner wall radius (m), L_{DMA} is the center rod length (m), and Zp is the particle electrical mobility (V m^{-2} s^{-1}). This method was developed and characterized in Sorooshian et al. 2008.[14]

Condensation Particle Counter

The condensation particle counter (CPC) is an optical particle counter. First, the sample aerosol enters the CPC at a flow rate of 0.36 LPM, where it enters the saturator, which is filled with butanol vapor. It then enters the condenser, where the butanol vapor can condense onto the particles. After the condenser, it passes through the optical block assembly, and as particles pass through this assembly, the beam light is scattered by the particles, and the number of times this scattering occurs is counted as the number of particles that have passed through. When combined with the DMA, where the particles are first separated by size, a size distribution of the sample aerosol is generated.

Data Output and Program Development in Igor Pro 8

To analyze the particle sizing data more efficiently, I developed a script and graphical user interface (GUI) written in Igor Pro 8 that converts the raw SEMS data outputs into user-friendly plots and tables of the aerosol size distribution properties. An example output is shown in Figure 2.3.

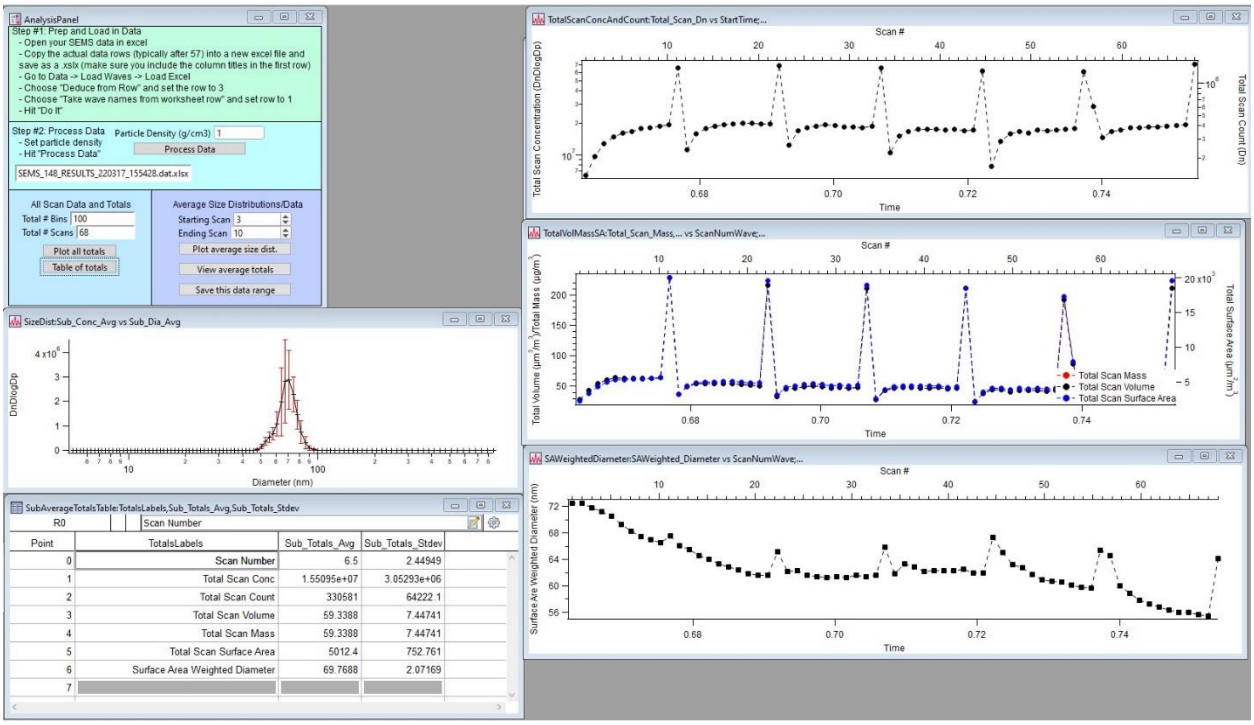

Figure 2.3 Image of SEMS Calculator V3.7

The primary output of the SEMS is bin data and concentration data, and each size distribution collected are referred to as "scans". In this context, "bins" are the midpoint diameters of the particles, and concentration is the log-normalized concentration (Dn/DlogDp) of particles. Depending on the data resolution desired, the number of bins can be changed to a higher number for higher resolution or vice versa, and the number of times spent at each bin size can also be changed, thus changing the overall scan time. Functionally, this means that any program written for this data needs to be able to adjust easily to changing dimensions. In this program, it first separates the matrix into the size bins measured and the concentrations for each bin. It then calculates the non-normalized concentrations (D_n) by multiplying the log-normalized concentrations by the logarithm of the bin size. Additional calculations were automated, including total number, volume, and mass concentrations, and mean-weighted diameter. It can also separate the data by scan number and generate a size distribution plot as well as an average of the bulk

information for individual time ranges. By developing this program, the processing time of particle size data was significantly reduced, from 20+ minutes in Excel to <5 minutes with this program. Furthermore, it ensured quality control in the processing of the SEMS data, because it does not require typing and retyping formulas in Excel.

2.3 Aerosol Aging and Kinetics Experiments with a Potential Aerosol Mass Oxidative Flow Reactor

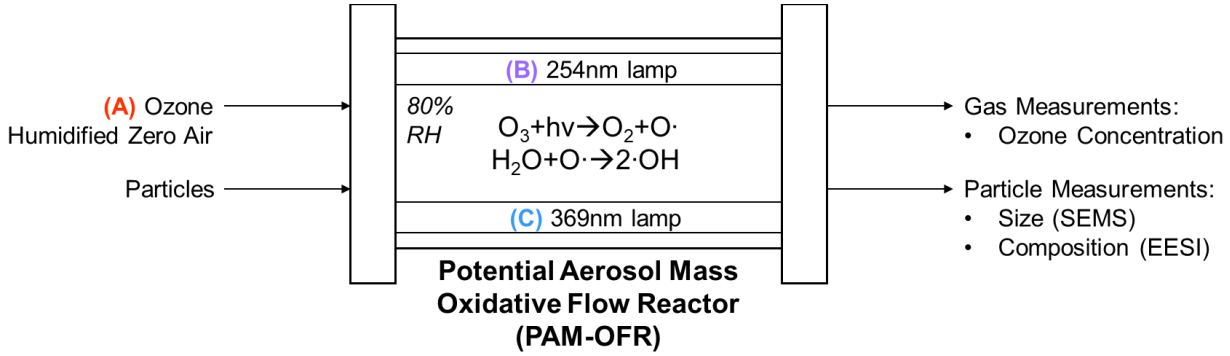

Figure 2.4 Example experimental setup for the PAM-OFR.

Oxidative Flow Reactors (OFRs) can be used for measuring reactive uptake kinetics between gases and particles at short residence times and over a range of oxidant levels.[17, 18] The potential aerosol mass oxidative flow reactor (PAM-OFR) is a commercially available OFR developed by Aerodyne Research Inc.[19, 20] The PAM-OFR is a 13.3L cylindrical aluminum tube equipped with four concentric lamps, protected by a quartz sleeve, to photochemically generate oxidants. As shown in Figure 2.4, the PAM-OFR was equipped with 254nm (GPH436T5L; Light Sources, Inc.) and 369nm (F436T5/BLC/4P-369; Aerodyne Research, Inc.) lamps. The PAM-OFR is different from typical larger-scale smog chambers in its internal volume and the concentrations of oxidants that are generated. Smog chambers operate under relatively lower oxidant concentrations and have a smaller surface area to volume ratio than the OFR, and experiments can last for several hours to days. The PAM-OFR exposes the sample gases and aerosols to relatively

high concentrations of oxidants on much shorter timescales, on the order of minutes, but the higher concentrations lead to exposure levels equivalent to days or weeks of exposure in the atmosphere, where oxidant exposure level = [oxidant]×time. Different oxidant concentrations can be accessed in the PAM-OFR by adjusting the lamp intensity with a ballast. For the experiments with 254 nm (setup B in **Error! Reference source not found.**) or 369 nm (setup C in **Error! Reference source not found.**) light only, and no gaseous oxidants, the light intensity was also modulated by varying the voltage sent to the lamps, and the flux from the lamps was monitored with a photodetector (TOCON-C6, sglux GmbH).

When equipped with 254nm lamps and either an external flow of ozone or the addition of 185nm lamps to generate ozone in situ from water vapor (setup A in **Error! Reference source not found.**), the PAM-OFR can generate OH radicals by the photodissociation of ozone and subsequent reaction with water vapor, following the reactions R 2.1 and R 2.2 below

$$O_3 + h\nu \rightarrow O_2 + O(^1D) \qquad \text{R 2.1}$$

$$O(^1D) + H_2O \rightarrow 2OH \qquad \text{R 2.2}$$

While the concentration of ozone can be monitored using an external ozone monitor (106-M, 2B technologies), OH radicals are difficult to measure due to their high reactivity and short lifetime. To determine the concentration of OH radicals, we measured it indirectly via reaction with CO, as done previously.[21] Here, a low concentration of CO gas (Airgas, 25 ppm ± 5% at 0.24 LPM), ultra-high purity nitrogen (Airgas, 4.76LPM), and ozone from an external ozone generator (Aerodyne, 1.2ppm at 1 LPM) are mixed within the OFR in the dark until a stable concentration of CO is reached, as measured by the CO monitor. Then, the 254 nm lamps are turned on while monitoring the output of the PAM with a CO monitor. During the experiment, the 254 nm lamps are set to a range of voltages (1.7-4V) to generate a calibration curve, as shown in Figure 2.5.

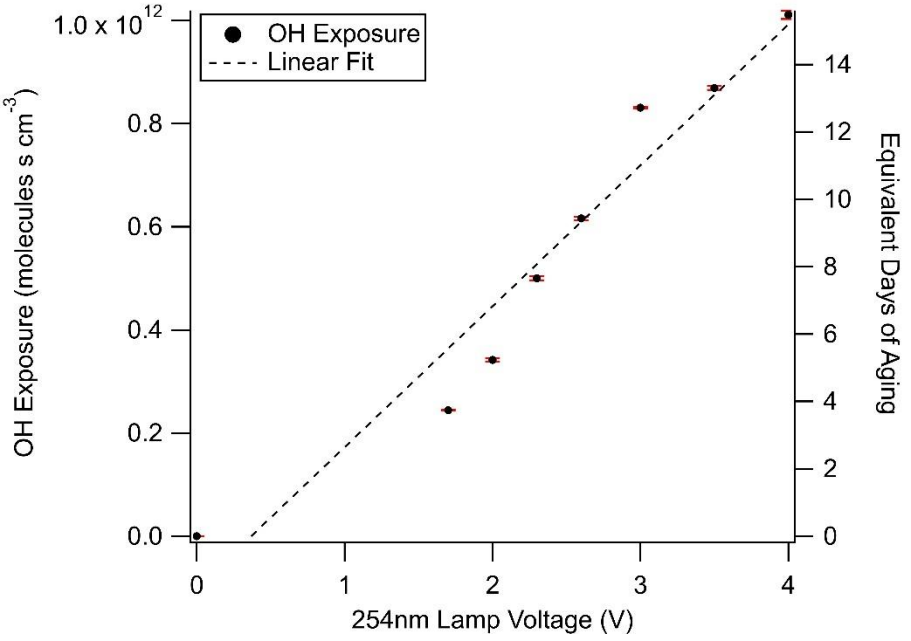

Figure 2.5 Calibration of OH Exposure (black circles) based on 254nm lamp voltage (error bars in red)

The reaction of OH and CO generates CO_2, as shown in R 2.3

$$OH + CO \rightarrow CO_2 + H \qquad \text{R 2.3}$$

To calculate the overall OH exposure (molecules s cm^{-3}), the following formula is used, which is the integrated differential rate equation for CO and assumes a pseudo-first order reaction between OH and CO ([OH]>>[CO]) shown in Eq. 2.3

$$OH\ Exposure = \frac{1}{k_{OH,CO}} * -\ln\left(\frac{[CO]_f}{[CO]_i}\right) \qquad \text{Eq. 2.3}$$

Where $k_{OH,CO}$=1.5×10^{-3} cm^3 molecules^{-1} s^{-1},[22] and $[CO]_i$ and $[CO]_f$ are the initial and final concentrations of CO, respectively. From the OH exposure, "days" of equivalent aging can be calculated using Eq. 2.4

$$Days = \frac{OH_{exp}}{[OH]_{amb}} * \frac{1}{t} \qquad \text{Eq. 2.4}$$

where OH_{exp} is the calculated OH exposure, $[OH]_{amb}$ is the average ambient concentration of OH, which is 1.5×10^6 molecules cm^{-3}, and t is 4.3×10^4, or the number of seconds in 12 hours, assuming a 12-hr sunlit day.

2.4 Extractive Electrospray Ionization Mass Spectrometry

The extractive electrospray ionization time-of-flight mass spectrometer (EESI-TOF) is an online aerosol composition measurement.[23-25] It has been used previously for measurements of ambient biogenic[26-31] and cooking-generated SOA,[32] biomass burning aerosol,[33] pharmaceuticals,[34] perfume,[35] and even gases.[36] The work in this thesis is the first time that EESI has been applied specifically to the measurements of plastics in aerosol and SSA. This section will cover (i) the operation of the inlet, (ii) the time-of-flight mass spectrometer, (iii) the data analysis procedure, and (iv) the advances made to the method by this work.

The EESI Inlet

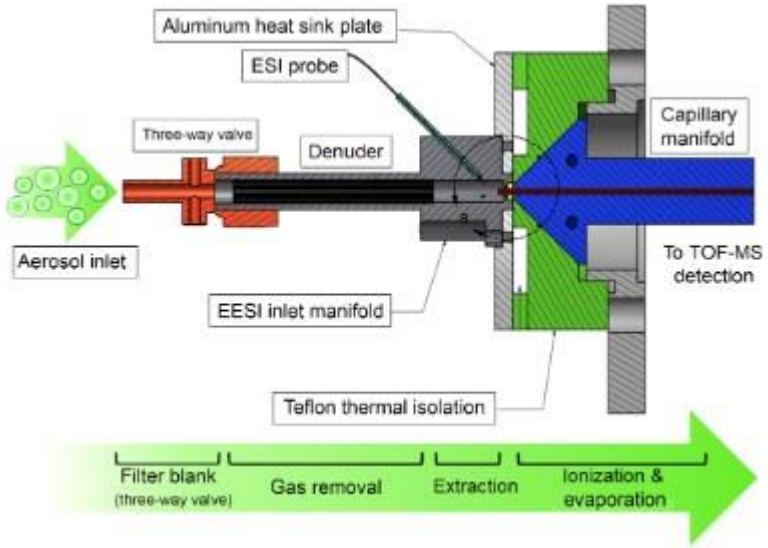

Figure 2.6 Diagram of the EESI inlet.[25]

A diagram of the EESI inlet is shown in Figure 2.6. The sample containing aerosols and gases first passes through a charcoal denuder (Aerodyne), which scrubs ambient gases from the sample, reducing the background noise level in the mass spectra. This denuder has a measured gas-phase hydrocarbon removal efficiency of > 99.999%, and a particle transmission efficiency of 75-90% for particles between 100-750 nm.[37] After scrubbing, it enters the inlet, where it can

interact with the reagent ion spray. The reagent ion spray is a solution consisting of 50/50 v/v organic solvent/water that is doped with 100ppm of salt (e.g., NaI) or acid (e.g., CH_3COOH) that dissociate in solution to Na^+ and I^- or CH_3COO^- and H^+, respectively. The solution gets charged to a maximum of +2500V/-2500V (positive/negative mode) from an external power supply and a source of pure nitrogen gas (from a liquid nitrogen dewar, Airgas) pushes the solution through a 360 μm OD and 50 μm ID fused silica capillary by 350mbar of pressure. The resulting fluid flow rate is adjusted between 0.1 and 10μL min^{-1}. The charged solution exiting the capillary forms electrospray droplets as the solution break apart, on the order of 1-10 μm.[25, 38, 39] These droplets then interact with the incoming aerosol sample, which can undergo several different forms of ionization, including coalescence, bounce, disruption, or fragmentation, as shown in Figure 2.7.[39] The relative ratios of these different interactions is still unknown, with one study finding no evidence of coalescence of the EESI spray and sample,[38] another showing evidence that EESI is a surface-mediated process exhibiting more of a bounce or disruption mechanism,[39] and others showing that the intensity of the sample ion peaks being proportional to the overall sample particle mass, and therefore exhibits coalescence.[25, 33] These discrepancies regarding the EESI method are explored further in Chapter 4.

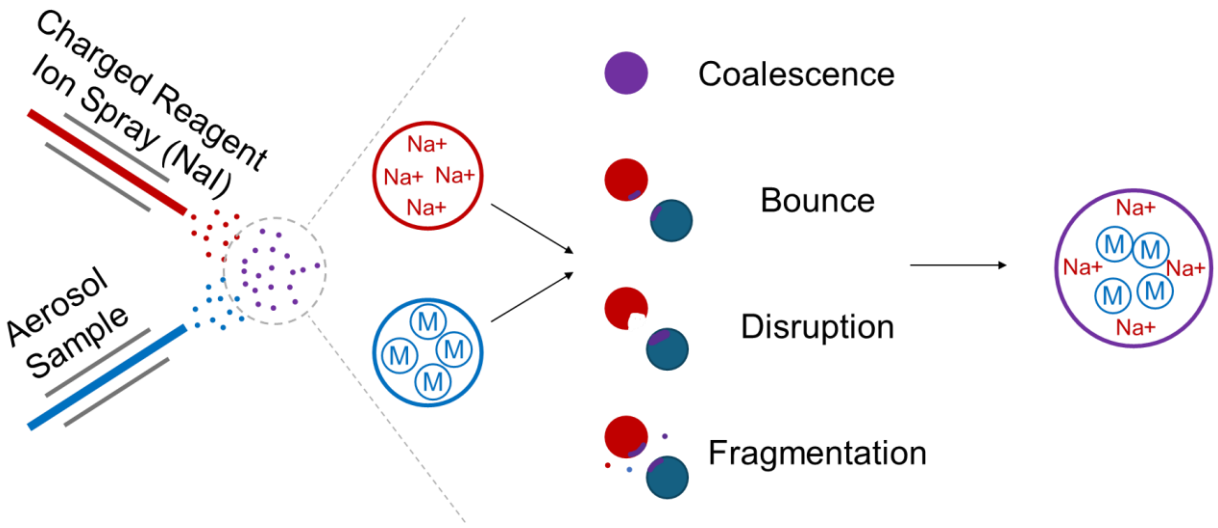

Figure 2.7 Diagram of a sample aerosol (blue) interacting with the EESI reagent spray (red) forming mixtures (purple). The four aerosol–droplet modes of interaction are shown for context.

Once the spray has interacted with the sample aerosol, it enters a stainless steel 0.5mm ID 1/16" OD 70mm long capillary that is heated to 220C. The particle then undergoes solvent evaporation, and then coulombic explosion where the sample ions become charged. In positive mode, the sample molecules (M) form Na^+-adducts and the sensitivity of adduct formation depends on the binding affinity between the analyte and Na^+, as shown in R 2.4.

$$Na^+ + M \rightarrow [M + Na]^+ \qquad \text{R 2.4}$$

Several classes of compounds except for organosulfates, nonoxygenated alkanes, alkenes, and aromatic hydrocarbons, can be detected by Na^+-adduct ionization.[25] This is the preferred ionization method for EESI because the organic sodium adducts are sufficiently stable that they do not fall apart while evaporating during transmission through the heated inlet. Na^+ also has no isotopes, leading to less complication in sample identification. Furthermore, it serves as an internal measure of the spray's stability and clusters between NaI and Na^+, or $[(NaI)_n]Na^+$, can serve as mass calibrants.

Atmospheric Pressure Inlet Time-of-Flight Mass Spectrometer

Time-of-flight mass spectrometry is based off the kinetic energy of a charged molecule, where after a pulsed acceleration voltage is applied, smaller molecules travel more quickly to the detector, and larger molecules travel more slowly, as shown in Eq. 2.5[40]

$$t = k\sqrt{\frac{m}{q}} \qquad \text{Eq. 2.5}$$

where k is a proportionality constant, m is the mass of the ion, and q is the charge of the ion. The mass spectrometer that the EESI inlet is attached to is an atmospheric pressure inlet time-of-flight mass spectrometer (APi-ToF), which is described in detail in Bertram et al. 2011 and shown in Figure 2.8.[41]

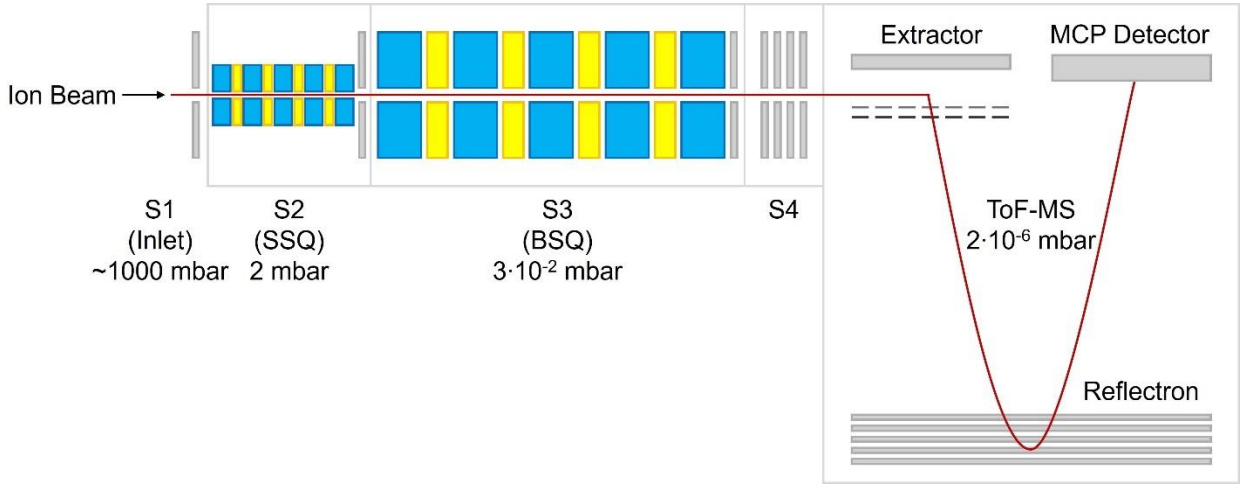

Figure 2.8 Diagram of the ToF-MS (adapted from Bertram et al. 2011)

The Api-TOF is divided into four primary segments. The first segment, S1, is the inlet, which is interchangeable depending on the type of measurements desired. When the EESI inlet is used, it is at atmospheric pressure. The second segment, S2, is a short, segmented RF-only quadrupole (SSQ) that acts as a collisional dissociation chamber and is held at ~2 mbar. This segment is primarily used to encourage strong and discourage weak adduct transmission into the rest of the mass spectrometer, while also focusing the incoming sample beam from the inlet.

Correct tuning of this segment is especially important for EESI, because while adduct formation is typically desired, larger ion clusters can also be formed, which will convolute the resulting spectra and make analysis additionally challenging. S3 is also an RF-only quadrupole (big segmented quadrupole, or BSQ) held at ~3×10^{-2} mbar, which further improves the focus of the ion beam, which generally improves the signal resolution. In S4, the ion beam is focused by a series of DC optics that focuses and accelerates the ion beam. This ion beam is then directed towards the orthogonal extraction reflectron ToF-MS, which is held at ~2×10^{-6} mbar.

EESI Data Analysis

Data analysis was conducted in Tofware (Aerodyne), a program which is described in more detail in Stark et al 2015 and will be described here briefly.[42] The mass spectrometer exports an .hdf5 file, or hierarchical data format version 5 file, which is a file format designed to hold large amounts of data. Once imported, the file is processed through a high-resolution workflow. This consists of mass calibration, baseline refinement, and peak width and shape refinement. Time-of-flight mass spectrometers are extremely susceptible to ambient temperature variations, because small fluctuations will cause slight changes in the ion beam path within the ToF-MS, thus changing the measured mass of the compound. To mitigate this, the measured masses are calibrated post-collection. During this process, a peak list of known ions that are present throughout the entire experiment are loaded, and the timings of each *m/z* between the known ions is slightly shifted to match the known values, with a target mass error of <5ppm in the known ions. For positive mode, these ions are listed below in

Table 2.1.

Table 2.1 List of mass calibrants used in positive mode EESI-TOF

Ion	*m/z*
Na^+	22.989221
$C_2H_4N^+$	42.033826
$C_2H_3NNa^+$	64.015770
$(C_2H_3N)_2Na_3^+$	151.022406
$NaNaI^+$	172.883462
$(C_2H_3N)_3Na_4^+$	215.038724
$Na_3I_2^+$	322.778252
$Na_4I_3^+$	472.672493
$Na_5I_4^+$	622.566734

Then, the baseline is refined, which defines the extent of the background noise. Finally, the peak shape and width are defined. The ideal peak shape would be a Gaussian curve, but typically there is some tailing on the left-hand side of the peak, which is accounted for within the peak shape processing. The peak width is also determined, which has a direct impact on peak resolution, as wider peaks will have a larger overlap at the same *m/z*, leading to less certainty in peak assignments.

Improvements to EESI

There are still many areas of improvement in the detection of different molecules that are underway with the EESI technique. This section will focus on the additional steps taken to examine chemical components of plastics in a SSA matrix, namely (i) detection in negative ionization mode

and (ii) optimization using Thuner. Improvements have also been made in our understanding of the effects of sample viscosity on the detectability with EESI as discussed in Chapter 4.

Advancements in Negative Mode EESI-TOF

While Na^+-adduct EESI is the type of ionization recommended by Aerodyne Research Inc. and is commonly used in the literature,[25] it was unable to detect certain analytes, including Bisphenol-A. To work around this challenge, the analysis was tested in negative mode. Initially, potassium acetate was used to deprotonate the sample molecules, as shown in R 2.5.

$$CH_3COO^- + M \rightarrow [M-H]^- + CH_3COOH \qquad \text{R 2.5}$$

This worked initially, and had clusters for mass calibration; however, it suffered from significant corona discharge caused by ionized air around the spray due to the high voltage applied to the spray. This effect has been seen in negative mode electrospray ionization (ESI-), leading to loss of spray stability and ultimately loss of signal.[43, 44] In EESI, this corona discharge led to extreme spray instability, where in some cases the spray could not be re-established. It was also correlated to a significant amount of O_2^- generation, which was observed in the mass spectra. The corona discharge made the use of potassium acetate in negative mode nearly impossible, because even if the spray was stable for periods of time, the source of the ionization was unclear when the O_2^- signal was significant, leading to potential drift in sensitivity that could not be accounted for.

To circumvent this issue, acetic acid was incorporated into the electrospray reagent solution. Acetic acid as an EESI reagent was first discussed in Law et al. 2010.[24] Figure 2.9 shows that potassium acetate (0% glacial acetic acid) had a ratio between O_2^- and CH_3COO^- of 54%, but upon switching the solution containing a greater fraction of glacial acetic acid, the ratio was reduced to 31-33%.

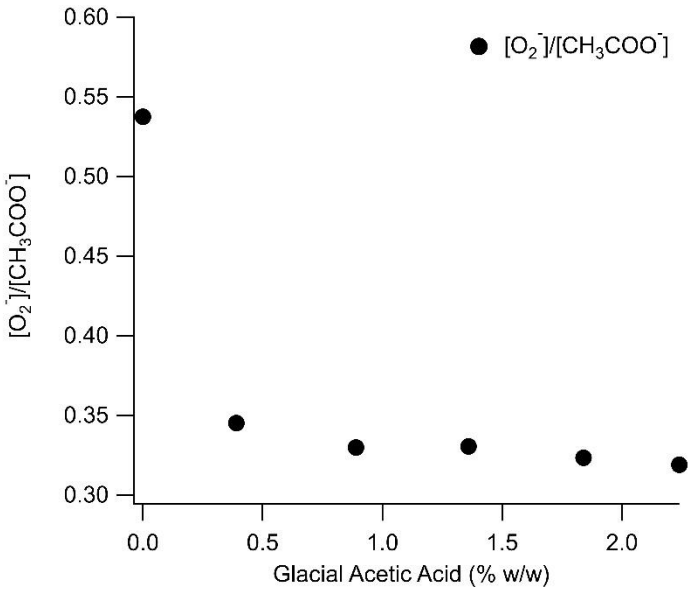

Figure 2.9 Ratio of O_2^- to acetate ion with varying percentage of acetic acid.

This improvement marked a significant advancement in our ability to use negative mode with EESI. However, the lack of molecular clusters from the reagent ion spray made it difficult to calibrate the mass accurately. The solution discovered was to incorporate 100ppm NaI to the reagent ion mixture, while tuning the instrument to detect deprotonated ions following the molecule's reaction with acetate ions (CH_3COO^-), as shown in R 2.6.

$$CH_3COO^- + M \rightarrow [M-H]^- + CH_3COOH \qquad \text{R 2.6}$$

The mass calibration list for negative mode is shown in

Table 2.2.

Table 2.2 List of mass calibrants used in negative mode EESI-TOF

Ion	m/z
O_2-	31.990378
CH_3COO-	59.013853
I-	126.90502
IO-	142.899935
IO_2-	158.89485
IO_3-	174.889764
I_2-	253.809492
$(CH_3COO)I_2$-	312.822797

Signal Improvement using Thuner

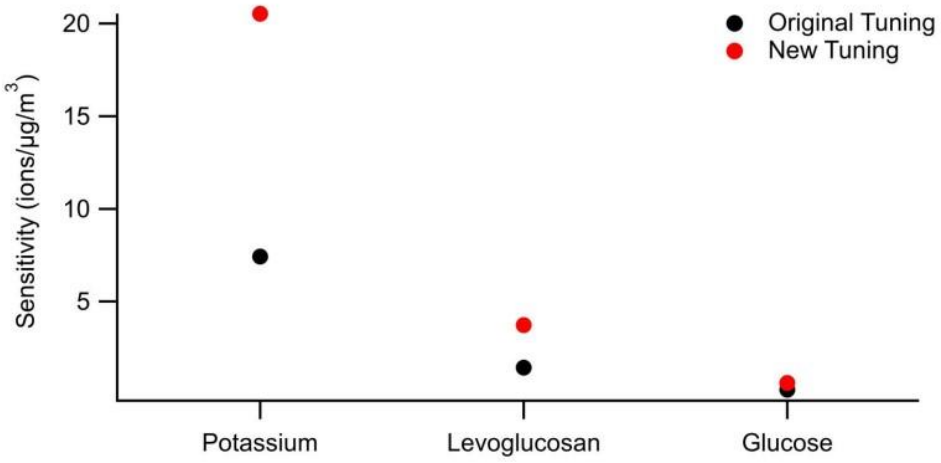

Figure 2.10 Tuning results of potassium, levoglucosan, and glucose, with the sensitivity of the old tuning (black) and new tuning (red)

One of the primary objectives during analysis with mass spectrometry is to enhance sensitivity and resolution. This is done by optimizing the voltages within the different mass spectrometer compartments that focus the ions into the detector and modulate the extent of clustering and fragmentation. This can be performed manually or automated. The automated program, Thuner (Tofwerk AG) was used to achieve this goal. Thuner can adjust all relevant voltages within the mass spectrometer (>40,000 combinations) to enhance sensitivity, resolution, and peak shape, as well as to determine the type of clustering desired between the reagent ion and the sample.[45] It does this iteratively until the peak resolution and shape are optimized. Figure 2.10 illustrates the outcomes of using Thuner with an aerosol sample that contains potassium, levoglucosan, and glucose. The results demonstrate that Thuner can improve sensitivity towards the target analyte by up to three times for K^+.

2.5 Theory

Reactive Uptake Coefficient Derivation

Reactive uptake coefficients (γ) describe the heterogeneous reaction kinetics between a gas and particle, and it is the ratio of reactive collisions with the particle that result in loss of the gas-phase molecule to the particle and the total number of particle collisions. This relationship is defined in Eq. 2.6

$$\gamma = \frac{J_{ads} - J_{des}}{J_{coll}} \qquad \text{Eq. 2.6}$$

Where J_{ads} is the adsorption flux, J_{des} is the desorption flux, and J_{coll} is the number of total collisions between the gas and the particle. Historically, γ has been determined by measuring the change in concentration of the gas-phase reactant with increasing residence time or particle surface area. γ can be described by either Eley–Rideal or Langmuir–Hinshelwood kinetics. In the Eley–Rideal mechanism, the gas immediately reacts with particle phase constituents on the particle surface before adsorbing.[46] Conversely, the Langmuir–Hinshelwood mechanism is based on the idea that the gas must first adsorb to the surface before reacting with the particle.[47] To isolate the mechanism, γ is often measured as a function of the reactant concentration. In Eley–Rideal kinetics, γ is unchanged with increasing concentration, whereas in Langmuir–Hinshelwood kinetics, γ decreases. To better understand the mechanism, γ can also be measured through the reactive decay of components in the condensed phase, expressed mathematically in Eq. 2.7.[48]

$$\ln\left(\frac{P}{P_0}\right) = -k_P[OH] \qquad \text{Eq. 2.7}$$

First, the experimentally determined second-order rate constant, k_p, is determined by the slope of the logarithmic decay of P (particle phase reactant) plotted against the concentration of OH.

The change in P with time is defined in Eq. 2.8,

$$\frac{d[P]}{dt} = -\gamma_{P,OH} \cdot f \cdot J_{coll} \cdot C_p \cdot A \quad \text{Eq. 2.8}$$

and depends on the reactive uptake rate of P and OH, $\gamma_{P,OH}$, the fraction of unreacted P molecules in the particle, *f*, the flux of OH at the surface of the particle, J_{coll}, the surface area of the particle, *A*, and the particle number concentration, C_p. Next, to solve for $\gamma_{P,OH}$, d[P]/dt is substituted with **Error! Reference source not found.**, f=[P]/[P_0], and J_{coll}= $\bar{c}$[OH]/4 to give Eq. 2.9

$$\gamma_{P,OH} = \frac{4 \cdot k_P \cdot [P]_0}{\bar{c} \cdot A \cdot C_P} \quad \text{Eq. 2.9}$$

where $\bar{c}$ is the mean speed of gas phase OH, equal to 661 m s^{-1}. $[P]_0$ can be simplified by incorporating the initial particle density ρ_0 using Eq. 2.10,

$$[P]_0 = \frac{C_p \cdot V \cdot \rho_0 \cdot N_A}{M_P} \quad \text{Eq. 2.10}$$

where *V* is particle volume, M_P is the molar mass of the particle-phase reactant, and N_A is Avogadro's number. Substituting this into **Error! Reference source not found.** we get the final formula for $\gamma_{P,OH}$ in Eq. 2.11

$$\gamma_{P,OH} = \frac{4 \cdot k_P \cdot D_{surf} \cdot \rho_0 \cdot N_A}{\bar{c} \cdot 6 \cdot M_P} \quad \text{Eq. 2.11}$$

where V/A is substituted for D_{surf}/6 and D_{surf} is the mean surface-weighted particle diameter of the sample aerosol.

One caveat of this approach is that it does not account for secondary reaction products due to radical intermediates reacting with the particle phase reactant. Secondary reactions in the particle or reactions with other gas-phase molecules would lead to an overestimation of γ.[49]

Gas-Particle Diffusion Correction

Another consideration for the calculation of γ is potential underestimation caused by concentration gradients close to the surface of the particle. This parametrization was defined by Fuchs and Sutugin 1970 and employed in the reactive uptake model from Smith et al. 2009.[48, 50] This is anticipated to be less of a problem in particle-based uptake studies rather than coated-wall

uptake studies, because the gas-particle collisions are driven by Brownian motion, but it still must be considered. This relationship is defined by Eq. 2.12

$$\frac{1}{\gamma} = \frac{1}{\gamma_{exp}} - \frac{0.75 + 0.286Kn}{Kn(Kn+1)} \quad \text{Eq. 2.12}$$

where γ is the true reactive uptake coefficient, γ_{exp} is the experimentally determined reactive uptake coefficient, and Kn is the Knudsen number, which is the ratio of the mean free path and the characteristic length. The Knudsen number for monodispersed particles can be defined by Eq. 2.13

$$Kn = \frac{3D_{OH}}{\omega r} \quad \text{Eq. 2.13}$$

where D_{OH} is the gas phase diffusion coefficient of OH, r is the particle radius, and ω is the average molecular speed of OH. For D_{OH}, a value of 0.26 $cm^2\ s^{-1}$ was used, which was determined by George et al. 2007 and employed in the Smith et al. 2009 work.[48, 51] ω was calculated to be 661 $m\ s^{-1}$ using Eq. 2.14

$$v_{avg} = \sqrt{\frac{3RT}{M}} \quad \text{Eq. 2.14}$$

where R is the gas constant (8.314 J mol^{-1} K^{-1}), T is the temperature (298 K), and M is the molar mass of the molecule (1.701×10-2 kg mol^{-1}). When fully calculated for a 100 nm particle, Kn is 2.36×10^{-2} (unitless) and results in <1% correction for a γ_{exp} of 0.1.

Glass Transition Temperature and Viscosity

The glass transition temperature, T_g, is the temperature interval at which amorphous organic particles transition from a liquid/semisolid to a glass upon cooling, and it is dependent on the rate of change in temperature and relative humidity, O:C ratio of the organics, and the mixing state of the particle.[52] The relationship between T_g and RH is that as RH increases, the greater liquid water content in the particle can act as a plasticizer, decreasing T_g.[52] When T_g decreases, the particle becomes more liquid-like, or less viscous, and therefore, is directly proportional to the

viscosity of the material. These definitions are important for Chapter 3 of this thesis, where the viscosity of BPA-containing aerosols is parametrized using T_g based upon the method described in Tumminello et al. 2021.[53, 54] T_g can be defined by Eq. 2.15

$$T_g = \frac{T_{g,w} k_{GT} + f(RH) T_g(RH = 0\%)}{k_{GT} + f(RH)} \quad \text{Eq. 2.15}$$

where $T_{g,w}$ is the glass transition of pure water and k_{GT} is the Gordon-Taylor constant for interactions between water and an organic solute. f(RH) is defined in Eq. 2.16

$$f(RH) = \frac{w_{org}}{w_w} = \frac{100 - RH}{RH} \frac{1}{\kappa_{org}} \frac{\rho_{org}}{\rho_w} \quad \text{Eq. 2.16}$$

where w_{org} and w_w are the mass fractions of organics and water within the particle, ρ_{org} and ρ_w are the density of the organics and water within the particle, and κ_{org} is the hygroscopicity parameter of the organic fraction, which is effectively how well the organics can take up water.

2.6 Acknowledgements

Dr. Paul Ryan Tumminello is acknowledged for assisting with the editing of this chapter.

2.7 References

(1) Stokes, M. D.; Deane, G. B.; Prather, K.; Bertram, T. H.; Ruppel, M. J.; Ryder, O. S.; Brady, J. M.; Zhao, D. A Marine Aerosol Reference Tank system as a breaking wave analogue for the production of foam and sea-spray aerosols. *Atmos. Meas. Tech.* **2013**, *6* (4), 1085-1094. DOI: 10.5194/amt-6-1085-2013.

(2) Prather, K. A.; Bertram, T. H.; Grassian, V. H.; Deane, G. B.; Stokes, M. D.; Demott, P. J.; Aluwihare, L. I.; Palenik, B. P.; Azam, F.; Seinfeld, J. H.; Moffet, R. C.; Molina, M. J.; Cappa, C. D.; Geiger, F. M.; Roberts, G. C.; Russell, L. M.; Ault, A. P.; Baltrusaitis, J.; Collins, D. B.; Corrigan, C. E.; Cuadra-Rodriguez, L. A.; Ebben, C. J.; Forestieri, S. D.; Guasco, T. L.; Hersey, S. P.; Kim, M. J.; Lambert, W. F.; Modini, R. L.; Mui, W.; Pedler, B. E.; Ruppel, M. J.; Ryder, O. S.; Schoepp, N. G.; Sullivan, R. C.; Zhao, D. Bringing the ocean into the laboratory to probe the chemical complexity of sea spray aerosol. *Proc. Natl. Acad. Sci. U. S. A.* **2013**, *110* (19), 7550-7555. DOI: 10.1073/pnas.1300262110.

(3) Jon S. Sauer; Kathryn J. Mayer; Christopher Lee; Michael R. Alves; Sarah Amiri; Cristina J. Bahaveolos; Emily B. Franklin; Daniel R. Crocker; Duyen Dang; Julie Dinasquet; Lauren A. Garofalo; Chathuri P. Kaluarachchi; Delaney B. Kilgour; Liora E. Mael; Brock A. Mitts; Daniel R. Moon; Alexia N. Moore; Clare K. Morris; Catherine A. Mullenmeister; Chi-Min Ni; Matthew A. Pendergraft; Daniel Petras; Rebecca M. C. Simpson; Stephanie Smith; Paul R. Tumminello; Joseph L. Walker; Paul J. DeMott; Delphine K. Farmer; Allen H. Goldstein; Vicki H. Grassian; Jules S. Jaffe; Francesca Malfatti; Todd R. Martz; Jonathan H. Slade; Alexei V. Tivanski; Timothy H. Bertram; Christopher D. Cappa; Prather, K. A. The Sea Spray Chemistry and Particle Evolution Study (SeaSCAPE): Overview and Experimental Methods. *Environ. Sci. Process. Impacts* **2022**. DOI: 10.1039/D1EM00260K.

(4) Wang, X.; Sultana, C. M.; Trueblood, J.; Hill, T. C. J.; Malfatti, F.; Lee, C.; Laskina, O.; Moore, K. A.; Beall, C. M.; McCluskey, C. S.; Cornwell, G. C.; Zhou, Y.; Cox, J. L.; Pendergraft, M. A.; Santander, M. V.; Bertram, T. H.; Cappa, C. D.; Azam, F.; DeMott, P. J.; Grassian, V. H.; Prather, K. A. Microbial Control of Sea Spray Aerosol Composition: A Tale of Two Blooms. *ACS Cent Sci* **2015**, *1* (3), 124-131. DOI: 10.1021/acscentsci.5b00148.

(5) Pham, D. Q.; O'Brien, R.; Fraund, M.; Bonanno, D.; Laskina, O.; Beall, C.; Moore, K. A.; Forestieri, S.; Wang, X.; Lee, C.; Sultana, C.; Grassian, V.; Cappa, C. D.; Prather, K. A.; Moffet, R. C. Biological Impacts on Carbon Speciation and Morphology of Sea Spray Aerosol. *ACS Earth Space Chem.* **2017**, *1* (9), 551-561. DOI: 10.1021/acsearthspacechem.7b00069.

(6) Ault, A. P.; Zhao, D.; Ebben, C. J.; Tauber, M. J.; Geiger, F. M.; Prather, K. A.; Grassian, V. H. Raman microspectroscopy and vibrational sum frequency generation spectroscopy as probes of the bulk and surface compositions of size-resolved sea spray aerosol particles. *Phys. Chem. Chem. Phys.* **2013**, *15* (17), 6206-6214. DOI: 10.1039/c3cp43899f.

(7) Wang, X.; Deane, G. B.; Moore, K. A.; Ryder, O. S.; Stokes, M. D.; Beall, C. M.; Collins, D. B.; Santander, M. V.; Burrows, S. M.; Sultana, C. M.; Prather, K. A. The role of jet and film drops in controlling the mixing state of submicron sea spray aerosol particles. *Proc. Natl. Acad. Sci. U. S. A.* **2017**, *114* (27), 6978-6983. DOI: 10.1073/pnas.1702420114.

(8) Guillard, R. R.; Ryther, J. H. Studies of marine planktonic diatoms. I. Cyclotella nana Hustedt, and Detonula confervacea (cleve) Gran. *Can. J. Microbiol.* **1962**, *8*, 229-239. DOI: 10.1139/m62-029.

(9) Lee, C.; Sultana, C. M.; Collins, D. B.; Santander, M. V.; Axson, J. L.; Malfatti, F.; Cornwell, G. C.; Grandquist, J. R.; Deane, G. B.; Stokes, M. D.; Azam, F.; Grassian, V. H.; Prather, K. A. Advancing Model Systems for Fundamental Laboratory Studies of Sea Spray Aerosol Using the Microbial Loop. *J. Phys. Chem. A* **2015**, *119* (33), 8860-8870. DOI: 10.1021/acs.jpca.5b03488.

(10) Liu, B. Y.; Lee, K. W. An aerosol generator of high stability. *Am. Ind. Hyg. Assoc. J.* **1975**, *36* (12), 861-865. DOI: 10.1080/0002889758507357.

(11) Dea, J. Y. Constant-output atomizer. NASA-CASE-MFS-25631-1|US-PATENT-4,413,784, 1983.

(12) May, K. R. The collison nebulizer: Description, performance and application. *J. Aerosol Sci.* **1973**, *4* (3), 235-243. DOI: 10.1016/0021-8502(73)90006-2.

(13) Model, T. S. I. 3076 Constant output atomizer instruction manual. *Revision J, June* **2005**.

(14) Sorooshian, A.; Hersey, S.; Brechtel, F. J.; Corless, A.; Flagan, R. C.; Seinfeld, J. H. Rapid, Size-Resolved Aerosol Hygroscopic Growth Measurements: Differential Aerosol Sizing and Hygroscopicity Spectrometer Probe (DASH-SP). *Aerosol Sci. Technol.* **2008**, *42* (6), 445-464. DOI: 10.1080/02786820802178506.

(15) Knutson, E. O.; Whitby, K. T. Aerosol classification by electric mobility: apparatus, theory, and applications. *J. Aerosol Sci.* **1975**, *6* (6), 443-451. DOI: 10.1016/0021-8502(75)90060-9.

(16) Intra, P.; Tippayawong, N. An overview of differential mobility analyzers for size classification of nanometer-sized aerosol particles. *Songklanakarin Journal of Science & Technology* **2008**, *30* (2).

(17) Kessler, S. H.; Nah, T.; Daumit, K. E.; Smith, J. D.; Leone, S. R.; Kolb, C. E.; Worsnop, D. R.; Wilson, K. R.; Kroll, J. H. OH-initiated heterogeneous aging of highly oxidized organic aerosol. *J. Phys. Chem. A* **2012**, *116* (24), 6358-6365. DOI: 10.1021/jp212131m.

(18) Peng, Z.; Jimenez, J. L. Radical chemistry in oxidation flow reactors for atmospheric chemistry research. *Chem. Soc. Rev.* **2020**, *49* (9), 2570-2616. DOI: 10.1039/c9cs00766k.

(19) Lambe, A. T.; Chhabra, P. S.; Onasch, T. B.; Brune, W. H.; Hunter, J. F.; Kroll, J. H.; Cummings, M. J.; Brogan, J. F.; Parmar, Y.; Worsnop, D. R.; Kolb, C. E.; Davidovits, P. Effect of oxidant concentration, exposure time, and seed particles on secondary organic aerosol chemical

composition and yield. *Atmos. Chem. Phys.* **2015**, *15* (6), 3063-3075. DOI: 10.5194/acp-15-3063-2015.

(20) A. T. Lambe; A. T. Ahern; L. R. Williams; J. G. Slowik; J. P. S. Wong; J. P. D. Abbatt; W. H. Brune; N. L. Ng; J. P. Wright; D. R. Croasdale; D. R. Worsnop; P. Davidovits; Onasch, T. B. Characterization of aerosol photooxidation flow reactors: heterogeneous oxidation, secondary organic aerosol formation and cloud condensation nuclei activity measurements. *Atmospheric Measurement Techniques* **2011**, *4* (3), 445-461. DOI: 10.5194/amt-4-445-2011.

(21) Li, R.; Palm, B. B.; Ortega, A. M.; Hlywiak, J.; Hu, W.; Peng, Z.; Day, D. A.; Knote, C.; Brune, W. H.; de Gouw, J. A.; Jimenez, J. L. Modeling the radical chemistry in an oxidation flow reactor: radical formation and recycling, sensitivities, and the OH exposure estimation equation. *J. Phys. Chem. A* **2015**, *119* (19), 4418-4432. DOI: 10.1021/jp509534k.

(22) Beno, M. F.; Jonah, C. D.; Mulac, W. A. Rate constants for the reaction OH + CO as functions of temperature and water concentration. *Int. J. Chem. Kinet.* **1985**, *17* (10), 1091-1101. DOI: 10.1002/kin.550171006.

(23) Gallimore, P. J.; Kalberer, M. Characterizing an extractive electrospray ionization (EESI) source for the online mass spectrometry analysis of organic aerosols. *Environ. Sci. Technol.* **2013**, *47* (13), 7324-7331. DOI: 10.1021/es305199h.

(24) Law, W. S.; Wang, R.; Hu, B.; Berchtold, C.; Meier, L.; Chen, H.; Zenobi, R. On the mechanism of extractive electrospray ionization. *Anal. Chem.* **2010**, *82* (11), 4494-4500. DOI: 10.1021/ac100390t.

(25) Felipe D. Lopez-Hilfiker; Veronika Pospisilova; Wei Huang; Markus Kalberer; Claudia Mohr; Giulia Stefenelli; Joel A. Thornton; Urs Baltensperger; Andre S. H. Prevot; Slowik, J. G. An extractive electrospray ionization time-of-flight mass spectrometer (EESI-TOF) for online measurement of atmospheric aerosol particles. *Atmospheric* **2019**. DOI: 10.5194/amt-12-4867-2019.

(26) Doezema, L. A.; Longin, T.; Cody, W.; Perraud, V.; Dawson, M. L.; Ezell, M. J.; Greaves, J.; Johnson, K. R.; Finlayson-Pitts, B. J. Analysis of secondary organic aerosols in air using extractive electrospray ionization mass spectrometry (EESI-MS). *RSC Adv.* **2012**, *2* (7), 2930-2938. DOI: 10.1039/C2RA00961G.

(27) Pospisilova, V.; Lopez-Hilfiker, F. D.; Bell, D. M.; Haddad, I. E.; Mohr, C.; Huang, W.; Heikkinen, L.; Xiao, M.; Dommen, J.; Prevot, A. S. H.; Baltensperger, U.; Slowik, J. G. On the fate of oxygenated organic molecules in atmospheric aerosol particles. *Science Advances* **2020**, *6* (11), eaax8922. DOI: 10.1126/sciadv.aax8922.

(28) Surdu, M.; Pospisilova, V.; Xiao, M.; Wang, M.; Mentler, B.; Simon, M.; Stolzenburg, D.; Hoyle, C. R.; Bell, D. M.; Lee, C. P.; Lamkaddam, H.; Lopez-Hilfiker, F.; Ahonen, L. R.; Amorim, A.; Baccarini, A.; Chen, D.; Dada, L.; Duplissy, J.; Finkenzeller, H.; He, X.-C.; Hofbauer, V.; Kim, C.; Kürten, A.; Kvashnin, A.; Lehtipalo, K.; Makhmutov, V.; Molteni, U.; Nie, W.; Onnela, A.; Petäjä, T.; Quéléver, L. L. J.; Tauber, C.; Tomé, A.; Wagner, R.; Yan, C.; Prevot, A. S. H.; Dommen, J.; Donahue, N. M.; Hansel, A.; Curtius, J.; Winkler, P. M.; Kulmala, M.; Volkamer,

R.; Flagan, R. C.; Kirkby, J.; Worsnop, D. R.; Slowik, J. G.; Wang, D. S.; Baltensperger, U.; El Haddad, I. Molecular characterization of ultrafine particles using extractive electrospray time-of-flight mass spectrometry. *Environ Sci Atmos* **2021**, *1* (6), 434-448. DOI: 10.1039/d1ea00050k.

(29) Tong, Y.; Qi, L.; Stefenelli, G.; Wang, D. S.; Canonaco, F.; Baltensperger, U.; Prévôt, A. S. H.; Slowik, J. G. Quantification of primary and secondary organic aerosol sources by combined factor analysis of extractive electrospray ionisation and aerosol mass spectrometer measurements (EESI-TOF and AMS). *Atmos. Meas. Tech.* **2022**, *15* (24), 7265-7291. DOI: 10.5194/amt-15-7265-2022.

(30) Kumar, V.; Giannoukos, S.; Haslett, S. L.; Tong, Y.; Singh, A.; Bertrand, A.; Lee, C. P.; Wang, D. S.; Bhattu, D.; Stefenelli, G.; Dave, J. S.; Puthussery, J. V.; Qi, L.; Vats, P.; Rai, P.; Casotto, R.; Satish, R.; Mishra, S.; Pospisilova, V.; Mohr, C.; Bell, D. M.; Ganguly, D.; Verma, V.; Rastogi, N.; Baltensperger, U.; Tripathi, S. N.; Prévôt, A. S. H.; Slowik, J. G. Highly time-resolved chemical speciation and source apportionment of organic aerosol components in Delhi, India, using extractive electrospray ionization mass spectrometry. *Atmos. Chem. Phys.* **2022**, *22* (11), 7739-7761. DOI: 10.5194/acp-22-7739-2022.

(31) Bell, D. M.; Zhang, J.; Top, J.; Bogler, S.; Surdu, M.; Slowik, J. G.; Prevot, A. S. H.; El Haddad, I. Sensitivity Constraints of Extractive Electrospray for a Model System and Secondary Organic Aerosol. *Anal. Chem.* **2023**. DOI: 10.1021/acs.analchem.3c00441.

(32) Brown, W. L.; Day, D. A.; Stark, H.; Pagonis, D.; Krechmer, J. E.; Liu, X.; Price, D. J.; Katz, E. F.; DeCarlo, P. F.; Masoud, C. G.; Wang, D. S.; Hildebrandt Ruiz, L.; Arata, C.; Lunderberg, D. M.; Goldstein, A. H.; Farmer, D. K.; Vance, M. E.; Jimenez, J. L. Real-time organic aerosol chemical speciation in the indoor environment using extractive electrospray ionization mass spectrometry. *Indoor Air* **2021**, *31* (1), 141-155. DOI: 10.1111/ina.12721.

(33) Pagonis, D.; Campuzano-Jost, P.; Guo, H.; Day, D. A.; Schueneman, M. K.; Brown, W. L.; Nault, B. A.; Stark, H.; Siemens, K.; Laskin, A.; Piel, F.; Tomsche, L.; Wisthaler, A.; Coggon, M. M.; Gkatzelis, G. I.; Halliday, H. S.; Krechmer, J. E.; Moore, R. H.; Thomson, D. S.; Warneke, C.; Wiggins, E. B.; Jimenez, J. L. Airborne extractive electrospray mass spectrometry measurements of the chemical composition of organic aerosol. *Atmos. Meas. Tech.* **2021**, *14* (2), 1545-1559. DOI: 10.5194/amt-14-1545-2021.

(34) Qin, M.; Qian, Y.; Huang, L.; Zhong, C.; Li, M.; Yu, J.; Chen, H. Extractive electrospray ionization mass spectrometry for analytical evaluation and synthetic preparation of pharmaceutical chemicals. *Front. Pharmacol.* **2023**, *14*, 1110900. DOI: 10.3389/fphar.2023.1110900.

(35) Chingin, K.; Gamez, G.; Chen, H.; Zhu, L.; Zenobi, R. Rapid classification of perfumes by extractive electrospray ionization mass spectrometry (EESI-MS). *Rapid Commun. Mass Spectrom.* **2008**, *22* (13), 2009-2014. DOI: 10.1002/rcm.3584.

(36) Lee, C. P.; Surdu, M.; Bell, D. M.; Dommen, J.; Xiao, M.; Zhou, X.; Baccarini, A.; Giannoukos, S.; Wehrle, G.; Schneider, P. A.; Prevot, A. S. H.; Slowik, J. G.; Lamkaddam, H.; Wang, D.; Baltensperger, U.; El Haddad, I. High-frequency gaseous and particulate chemical characterization using extractive electrospray ionization mass spectrometry (Dual-Phase-EESI-

TOF). *Atmospheric Measurement Techniques* **2022**, *15* (12), 3747-3760. DOI: 10.5194/amt-15-3747-2022.

(37) Eichler, P.; Müller, M.; D'Anna, B.; Wisthaler, A. A novel inlet system for online chemical analysis of semi-volatile submicron particulate matter. *Atmospheric Measurement Techniques* **2015**, *8* (3), 1353-1360. DOI: 10.5194/amt-8-1353-2015.

(38) Wang, R.; Gröhn, A. J.; Zhu, L.; Dietiker, R.; Wegner, K.; Günther, D.; Zenobi, R. On the mechanism of extractive electrospray ionization (EESI) in the dual-spray configuration. *Anal. Bioanal. Chem.* **2012**, *402* (8), 2633-2643. DOI: 10.1007/s00216-011-5471-8.

(39) Kumbhani, S.; Longin, T.; Wingen, L. M.; Kidd, C.; Perraud, V.; Finlayson-Pitts, B. J. New Mechanism of Extractive Electrospray Ionization Mass Spectrometry for Heterogeneous Solid Particles. *Anal. Chem.* **2018**, *90* (3), 2055-2062. DOI: 10.1021/acs.analchem.7b04164.

(40) Wiley, W. C.; McLaren, I. H. Time-of-Flight Mass Spectrometer with Improved Resolution. *Rev. Sci. Instrum.* **1955**, *26* (12), 1150-1157. DOI: 10.1063/1.1715212.

(41) Bertram, T. H.; Kimmel, J. R.; Crisp, T. A.; Ryder, O. S.; Yatavelli, R. L. N.; Thornton, J. A.; Cubison, M. J.; Gonin, M.; Worsnop, D. R. A field-deployable, chemical ionization time-of-flight mass spectrometer. *Atmos. Meas. Tech.* **2011**, *4* (7), 1471-1479. DOI: 10.5194/amt-4-1471-2011.

(42) Stark, H.; Yatavelli, R. L. N.; Thompson, S. L.; Kimmel, J. R.; Cubison, M. J.; Chhabra, P. S.; Canagaratna, M. R.; Jayne, J. T.; Worsnop, D. R.; Jimenez, J. L. Methods to extract molecular and bulk chemical information from series of complex mass spectra with limited mass resolution. *Int. J. Mass Spectrom.* **2015**, *389*, 26-38. DOI: 10.1016/j.ijms.2015.08.011.

(43) McClory, P. J.; Håkansson, K. Corona Discharge Suppression in Negative Ion Mode Nanoelectrospray Ionization via Trifluoroethanol Addition. *Anal. Chem.* **2017**, *89* (19), 10188-10193. DOI: 10.1021/acs.analchem.7b01225.

(44) Skalny, J. D.; Mikoviny, T.; Matejcik, S.; Mason, N. J. An analysis of mass spectrometric study of negative ions extracted from negative corona discharge in air. *Int. J. Mass Spectrom.* **2004**, *233* (1), 317-324. DOI: 10.1016/j.ijms.2004.01.012.

(45) Brophy, P.; Farmer, D. K. Clustering, methodology, and mechanistic insights into acetate chemical ionization using high-resolution time-of-flight mass spectrometry. *Atmospheric Measurement Techniques* **2016**, *9* (8), 3969-3986. DOI: 10.5194/amt-9-3969-2016.

(46) Eley, D. D.; Rideal, E. K. Parahydrogen Conversion on Tungsten. *Nature* **1940**, *146* (3699), 401-402. DOI: 10.1038/146401d0.

(47) Langmuir, I. The mechanism of the catalytic action of platinum in the reactions $2Co + O_2 = 2Co_2$ and $2H_2 + O_2 = 2H_2O$. *Trans. Faraday Soc.* **1922**, *17*, 621. DOI: 10.1039/tf9221700621.

(48) Smith, J. D.; Kroll, J. H.; Cappa, C. D.; Che, D. L.; Liu, C. L.; Ahmed, M.; Leone, S. R.; Worsnop, D. R.; Wilson, K. R. The heterogeneous reaction of hydroxyl radicals with sub-micron

squalane particles: a model system for understanding the oxidative aging of ambient aerosols. *Atmos. Chem. Phys.* **2009**, *9* (9), 3209-3222. DOI: 10.5194/acp-9-3209-2009.

(49) George, I. J.; Vlasenko, A.; Slowik, J. G.; Broekhuizen, K.; Abbatt, J. P. D. Heterogeneous oxidation of saturated organic aerosols by hydroxyl radicals: uptake kinetics, condensed-phase products, and particle size change. *Atmos. Chem. Phys.* **2007**, *7* (16), 4187-4201. DOI: 10.5194/acp-7-4187-2007.

(50) Fuchs, N. A.; Sutugin, A. G. High-Dispersed Aerosols. In *Topics in Current Aerosol Research*, Hidy, G. M., Brock, J. R. Eds.; Pergamon, 1971; p 1.

(51) George, I. J.; Abbatt, J. P. D. Heterogeneous oxidation of atmospheric aerosol particles by gas-phase radicals. *Nat. Chem.* **2010**, *2* (9), 713-722. DOI: 10.1038/nchem.806.

(52) Koop, T.; Bookhold, J.; Shiraiwa, M.; Pöschl, U. Glass transition and phase state of organic compounds: dependency on molecular properties and implications for secondary organic aerosols in the atmosphere. *Phys. Chem. Chem. Phys.* **2011**, *13* (43), 19238-19255. DOI: 10.1039/c1cp22617g.

(53) Tumminello, P. R.; James, R. C.; Kruse, S.; Kawasaki, A.; Cooper, A.; Guadalupe-Diaz, I.; Zepeda, K. L.; Crocker, D. R.; Mayer, K. J.; Sauer, J. S.; Lee, C.; Prather, K. A.; Slade, J. H. Evolution of Sea Spray Aerosol Particle Phase State Across a Phytoplankton Bloom. *ACS Earth Space Chem.* **2021**, *5* (11), 2995-3007. DOI: 10.1021/acsearthspacechem.1c00186.

(54) DeRieux, W.-S. W.; Li, Y.; Lin, P.; Laskin, J.; Laskin, A.; Bertram, A. K.; Nizkorodov, S. A.; Shiraiwa, M. Predicting the glass transition temperature and viscosity of secondary organic material using molecular composition. *Atmos. Chem. Phys.* **2018**, *18* (9), 6331-6351. DOI: 10.5194/acp-18-6331-2018.

Chapter 3 Heterogeneous and Photosensitized Oxidative Degradation Kinetics of the Plastic Additive Bisphenol-A in Sea Spray Aerosol Mimics

3.1 Abstract

Plastics have become ubiquitous in the world's oceans and recent work indicates they can transfer from the ocean to the atmosphere in sea spray aerosol (SSA). Hazardous chemical residues in plastics, including bisphenol-A (BPA), represents a sizable fraction of consumer plastics and has been measured consistently in air over both terrestrial and marine environments. However, the chemical lifetimes of BPA and mechanisms by which plastic residues degrade with respect to photochemical and heterogeneous oxidation processes in aerosols are unknown. Here, we present the photosensitized and OH-initiated heterogeneous oxidation kinetics of BPA in the aerosol phase consisting of pure-component BPA and internal mixtures of BPA, NaCl, and dissolved photosensitizing organic matter. We found that photosensitizers enhanced BPA degradation in binary-component BPA+photosensitizer aerosol mixtures when irradiated in the absence of OH. OH-initiated degradation of BPA was enhanced in the presence of NaCl with and without photosensitizing species. We attribute this enhanced degradation to greater mobility and thus reaction probability between BPA, OH, and reactive chlorine species (RCS) formed through reaction between OH and dissolved Cl- in the more liquid-like aerosol matrix in the presence of NaCl. Addition of the photosensitizers in the ternary-component BPA+NaCl+photosensitizer aerosol led to no enhancement in the degradation of BPA following light exposure compared to the binary-component BPA+NaCl aerosol. This was attributed to quenching of triplet state formation by dissolved Cl- in the less viscous aqueous aerosol mixtures containing NaCl. Based upon measured second-order heterogeneous reaction rates, the estimated lifetime of BPA with respect to heterogeneous oxidation by OH is one week in the presence of NaCl compared to 20 days in the absence of NaCl. This work highlights the important heterogeneous and

photosensitized reactions and the role of phase state, which affect the lifetimes of hazardous plastic pollutants in SSA with implications for understanding pollutant transport and exposure risks in coastal marine environments.

3.2 Introduction

An estimated 5% of the 275 million metric tons (MT) of annually produced plastics, 4.8 to 12.7 MT, accumulate in the world's oceans.[1] Epoxy resins and hardeners in plastics, including bisphenols such as bisphenol-A (BPA) represent 10 to 70% of the mass of additives in plastics and have known carcinogenic and teratogenic properties.[2, 3] BPA can leach from plastics into the surrounding water and due to its hydrophobicity and lipophilicity, accumulate at the ocean surface along with other organic material and inorganic salts. BPA concentrations in ocean water have been measured in the range of 0.04-17,000 µg/L depending on proximity to terrestrial inputs and are found to be more persistent in ocean water than in freshwater.[4-6] BPA is ubiquitous in the atmosphere with mass concentrations in the range of 1-17,400 pg m^{-3} in atmospheric aerosol sampled across urban, rural, marine, and polar regions.[7] A major source of atmospheric BPA is through plastic incineration, although a non-negligible portion (1-32 pg m^{-3}) has been measured in aerosol over the remote ocean.[7]

Non-volatile contaminants at the ocean surface can become airborne via selective transfer in sea spray aerosol (SSA), which is comprised of a complex mixture of inorganic salts, fatty acids, saccharides, and chromophoric (light-absorbing) dissolved organic matter that accumulate at the sea surface microlayer.[8-11] SSA contributes the largest aerosol flux by mass to the atmosphere per year. In recent work, SSA was found to be an important source of airborne plastics, with an estimated emission flux from the ocean of up to 22 megatons annually.[12] Due to its relatively high lipophilicity (logP=3.3), BPA is expected to selectively transfer into SSA following the rupture of films produced by bubbles at the ocean surface, which are enriched in surfactants and other

lipophilic material.[13, 14] Currently, the chemical lifetimes and pathways by which contaminant molecules such as BPA degrade in the presence of SSA constituents are unknown.

In the atmosphere, aerosols undergo chemical aging through photochemical and heterogeneous reaction pathways when exposed to sunlight and atmospheric oxidants including ozone, OH radicals, and Cl radicals.[15-17] Oxidation reactions can degrade organic components in aerosol and alter aerosol particle physicochemical properties, such as hygroscopicity, leading to greater wet depositional losses.[18-21] In addition to heterogeneous oxidation reactions, photosensitized reactions in atmospheric aerosols can promote further oxidative degradation via formation of transient reactive oxygen species[22, 23] or by enhancing the reactive uptake of atmospheric oxidants including ozone.[24] These reactions that alter the chemical composition of the aerosol can also modulate their toxicity, having implications for public health.[25] Photosensitizers play an important role in the marine-atmospheric environment and at the sea surface due to their accumulation at the sea surface and ability to transfer into SSA.[9, 26, 27] Prior work has shown that BPA can undergo enhanced degradation in the presence of photosensitizers in bulk water.[28] However, the photochemical and oxidative degradation pathways, reactive uptake kinetics by OH, and degradation kinetics of plastic additives including BPA in marine-relevant aerosol matrices have not been studied.

In this work, we examine the photochemical and heterogeneous oxidative degradation pathways and kinetics of BPA following OH reactive uptake to model SSA mixed with BPA. Lab-generated SSA "mimics" consisting of BPA, NaCl, and different photosensitizing organic material, including 4-benzoylbenzoic acid (4-BBA) and humic acid (HA), were irradiated in an oxidation flow reactor at varying exposure levels of light and OH. An extractive electrospray ionization time-of-flight mass spectrometer (EESI-TOF) was employed to measure aerosol

composition and the decay of BPA in real time following exposure to light and OH. This work highlights the importance of NaCl and photosensitizers as reactive species in the degradation of emerging contaminant molecules present in plastics that become airborne over the ocean with important implications regarding the persistence of organic contaminants in SSA.

3.3 Methods

An extractive electrospray ionization time-of-flight mass spectrometer (EESI-TOF; Aerodyne Research Inc and Tofwerk AG) was utilized to measure concentrations of BPA and its oxidation products in the aerosol phase. EESI-TOF was used in our previous analysis of SSA organic components and in other studies for the analysis of secondary organic aerosols.[18, 29-32] Briefly, a reagent ion spray was generated by passing the reagent solution through a 365 μm OD fused silica capillary (IDEX Health and Science, LLC) at a pressure of 350 mbar and charged at a voltage of -2500V. The EESI-TOF was operated in negative mode using a reagent solution of 2% (by mass) acetic acid (99.7%, Fisher Chemical), 48% H_2O (18mΩ, Millipore Synergy System), and 50% acetonitrile (≥99.95%, Fisher Chemical) spiked with 100 ppm sodium iodide (99%, Sigma-Aldrich) for the purposes of mass calibration. The aerosol was sampled through the EESI-TOF inlet at a rate of 1 liter per minute (LPM) and mixed orthogonally with the reagent ion spray. The mixed aerosol/reagent ion droplets were heated and volatilized at a temperature of 220°C.[29] Under these conditions, ionization occurred primarily via deprotonation as $C_{15}H_{15}O_2^-$.

Solutions of 25/75 (% by mass) water/methanol (≥99.9%, Fisher Chemical) were prepared with 100 ppm of BPA (≥99%, Sigma-Aldrich), 4-benzoylbenzoic acid (4-BBA; 99%, ACROS Organics), humic acid (HA; ≥95%, Alfa Aesar), and sodium chloride (99.5%, Fisher Chemical). Under these conditions, the pH of the atomizer solution was neutral for pure-component BPA and BPA+NaCl solutions and slightly more acidic when mixed with 4-BBA and HA. It is assumed because the pKa=10.6 for BPA that BPA remained in its molecular form for all experiments.

However, the predicted pKa=3.79 of 4-BBA indicates it would have been present in its carboxylate form. Particle- and hydrocarbon-free zero air (Airgas) was used as carrier flow. The solution was then atomized by zero air using a constant output atomizer (Model 3076, TSI Inc.) and sent through a silica bead diffusion dryer and an activated charcoal denuder to dry the aerosol particles and remove volatile species. The aerosol was then neutralized, and size selected by a differential mobility analyzer (Model 2100; Brechtel) to generate monodisperse aerosol with a nominal electrical mobility diameter of 100 nm to maintain size consistency across experiments.

The aerosol was exposed to differing levels of light, ozone, and OH in a potential aerosol mass oxidative flow reactor (PAM-OFR; Aerodyne Research Inc.).[33-36] The PAM-OFR was equipped with four interchangeable, narrowband lamps either operated at wavelengths of 254nm (GPH436T5L; Light Sources, Inc.) or 369nm (F436T5/BLC/4P-369; Aerodyne Research, Inc.) and arranged concentrically along the inner walls and protected by a quartz sheath tube and cooled with a gentle flow of nitrogen. The light intensity inside the PAM-OFR was adjusted with a ballast and measured with a photodetector (TOCON-C6, sglux GmbH). OH was generated via the photolysis of ozone in the presence of water vapor and 254 nm radiation in a mix with zero air (RH~80% and air flow rate of 3 LPM). Ozone was generated in an isolated external chamber via photolysis of O_2 in a flow of zero air (1 LPM) in the presence of 185 nm radiation. Ozone concentrations were measured with an ozone monitor (106-M, 2B Technologies) and were 1.2 (± 0.1) ppm for all experiments. OH concentrations in the PAM-OFR were calibrated by measuring the decay of CO with a CO monitor (Model APMA-370, Horiba) at the different lamp voltage settings and were varied from 1.5 to 5.0 $\times 10^9$ molecules cm^{-3}. This concentration range of OH is 2-3 orders of magnitude greater than ambient OH levels but chosen to achieve the equivalent of up to a week of aging in the atmosphere at the residence time in the PAM-OFR of 123 s. At higher

concentrations of OH, the rate of OH uptake by the aerosol may be affected, although other studies have shown that the elemental composition of aerosol is similar whether at low concentrations of OH over long exposure times or high concentrations of OH over short exposure times.[37, 38]

Losses of BPA resulting from exposure to ozone were insignificant and no further corrections were applied. While heterogeneous OH oxidation was conducted in the presence of 254 nm radiation, separate control experiments were conducted to determine the photodegradation rates of BPA by 254 nm light in the absence of OH. The additional losses of BPA resulting from photodegradation in the presence of 254 nm light alone were subtracted from the losses of BPA in the presence of OH. Studies of the photosensitized degradation kinetics of BPA were conducted in the presence of 369 nm light in the absence of OH and 254 nm light, representing more relevant conditions of irradiation in the troposphere.

All mass spectrometer datasets were processed in Tofware version 3.2.2 (Aerodyne LLC and Tofwerk AG), which ran in Igor Pro 8 (Wavemetrics). Mass spectral peaks were assigned based upon elemental formulae applying high-resolution peak fitting analysis at a nominal mass resolution ($m/\Delta m$) ~3000 for m/z 59 (CH_3COO^-) in negative mode. Signal intensities were corrected for drift applying a linear interpolation of the ion intensity of BPA measured prior to and after exposure to OH or light. Potential changes in sensitivity were accounted for by introducing an "internal standard" of BPA aerosol directly to the EESI-TOF inlet (bypassing the PAM-OFR) between different OH exposure levels. The intensity of the BPA signal measured at each OH exposure level was then normalized to the ratio of the internal standard signal measured before and after each OH exposure level as shown in Figure 3.6 and described in more detail in the SI. Background signal intensities (blanks) were acquired at the start and end of each trial after passing

the aerosol flow through a HEPA filter (99.99% removal efficiency at 0.1 μm) and were subtracted from the sample signal intensities of BPA.

Heterogeneous reactive uptake kinetics were assessed by measuring the diffusion-corrected reactive uptake coefficient (γ), defined here as the ratio of reactive collisions to total collisions between OH and the aerosol that result in the loss of BPA.[37, 39, 40] γ has been determined previously to evaluate such heterogeneous processes as the uptake kinetics of water onto acidic aqueous surfaces and the uptake of trace reactive gases by various organic aerosol compounds.[15, 37, 39, 41, 42] γ was calculated using Eq. 3.1:

$$\gamma = \frac{2D_0\rho_i N_a}{3c_{OH}M}k_{OH} \qquad \text{Eq. 3.1}$$

Here, D_0 is the mean surface area-weighted aerosol diameter, ρ_i is the density of BPA, N_A is Avogadro's number, c_{OH} is the average speed of OH in the gas phase, and M is the molecular weight of BPA. k_{OH} is the measured second-order heterogeneous loss rate, determined via the slope of the natural logarithm of the normalized BPA signal as a function of the OH exposure level measured in the PAM-OFR. γ was corrected for OH diffusion losses following the approach by Sutugin and Fuchs (1970),[43] resulting in less than 1% correction at 1 atm.

3.4 Results and Discussion

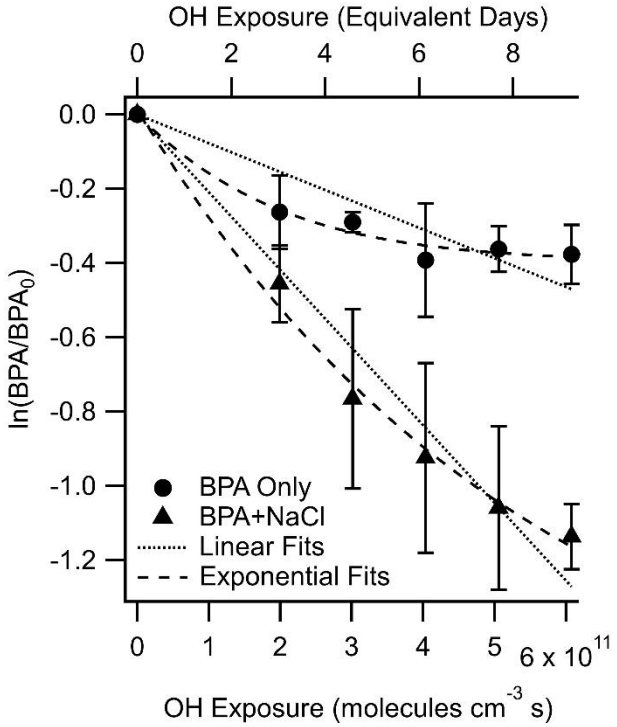

Figure 3.1 Natural logarithm of the decay of BPA as a function of OH exposure averaged over multiple experiments for BPA (circles) and BPA+NaCl (triangles). The slope of the exponential fit was a parameterization from Davies and Wilson et al. 2015 (large dashed line).[44] The slope of the linear fit (small dashed line) represents the second-order reaction rate constant.

Pure-Component BPA Degradation by OH.

Pure-component BPA aerosol was exposed to different OH exposure levels ranging from 0 to 6.1×10^{11} molecules s cm^{-3} corresponding to the equivalent of 0 to 9.4 days of aging in the atmosphere assuming an average daily OH concentration of 1.5×10^{6} molecules cm^{-3} (Figure 3.1). The heterogeneous oxidation kinetics of BPA were determined by plotting the natural logarithm of the normalized BPA signal (m/z=227.1077533 Th) as a function of OH exposure as shown in Figure 3.1. The slope of the fit to OH exposure is the effective second-order heterogeneous reaction rate constant (k_{OH}) expressed in cm^3 $molecule^{-1}$ s^{-1}, which is reported in Table 3.1 for all experiments.[39] As noted in the Methods, some of the BPA loss in the aerosol phase is attributed to direct photolysis by exposure to the 254 nm lamps in the PAM-OFR.[45] This loss, which was in addition to the reactive losses by OH, was subtracted from the measured decay when BPA was exposed to OH and 254 nm radiation. Following this correction and applying the linear fit as shown in Figure 3.1, the effective k_{OH}=0.773 (± 0.082) × 10^{-12} cm^3 $molecule^{-1}$ s^{-1}. This result is comparable with previous studies of OH heterogeneous oxidation of different organic aerosol compounds, which are on the order of 1.0 × 10^{-12} cm^3 $molecule^{-1}$ s^{-1}.[37]

Our calculated γ = 0.211 (± 0.002) is of the same magnitude but lower when compared to other reported γ values for OH uptake by single-component and mixed organic aerosol. In the case of water-soluble organic aerosol such as levoglucosan, γ = 0.65 (± 0.17) at 40% RH and γ = 0.21 (± 0.18) at 0% RH, while OH uptake by erythritol was measured to be γ = 0.77 (± 0.10).[19, 37] In contrast, sparingly soluble organic aerosol components including 4-methyl-5-nitrocatechol, exhibited slower OH uptake kinetics with γ = 0.07 (± 0.02) at RH = 26%.[19] The reactive uptake kinetics of OH have also been shown to depend on the concentration of OH via competitive reactions between co-adsorbed species, including OH with itself and reactions between OH and co-adsorbed O_3 or intermediate products, which occupy reactive sites for OH at the surface.[37, 46,

[47] In our experiments, it is likely that the relatively high [O_3] ~1 ppm affected the reactive uptake kinetics of OH, but not unlike in other studies of heterogeneous oxidation kinetics using the PAM-OFR, which employed similarly large [O_3] and [OH].[33] Furthermore, [O_3] and [OH] were the same for all experiments, therefore would not cause the relatively slower kinetics between OH and BPA compared to the other aerosol mixtures studied here. While the experiments presented here were performed at RH = 80%, the very low water solubility of BPA suggests the particles remained in a highly viscous or solid-like phase state, which conceivably could have slowed the rates of molecular diffusion and thus extent of reaction between OH and BPA in the particle phase. Evidence of this is demonstrated in Figure 3.1 for pure-component BPA, which did not significantly further degrade in the aerosol phase above an OH exposure level of ~4×10^{11} molecules s cm^{-3}, whereas the aqueous particle mixture with NaCl led to further degradation of BPA. In the work by Davies and Wilson 2015, reactive uptake of OH by citric acid decreased with increasing OH exposure level when RH<50%, whereas the reactive uptake of OH was enhanced when the RH was greater than 50% , attributed to better mixing of reactive components in the less viscous aqueous aerosol phase.[44] Based upon the applied parameterized fits in Figure 3.1, even at the high RH, apparent mixing lengths of BPA in the pure-component BPA aerosol were not considered well mixed. Further descriptions of this parameterization are provided in the SI but what this analysis indicated was that unreacted BPA was not readily replenished at the particle surface for reaction with OH.

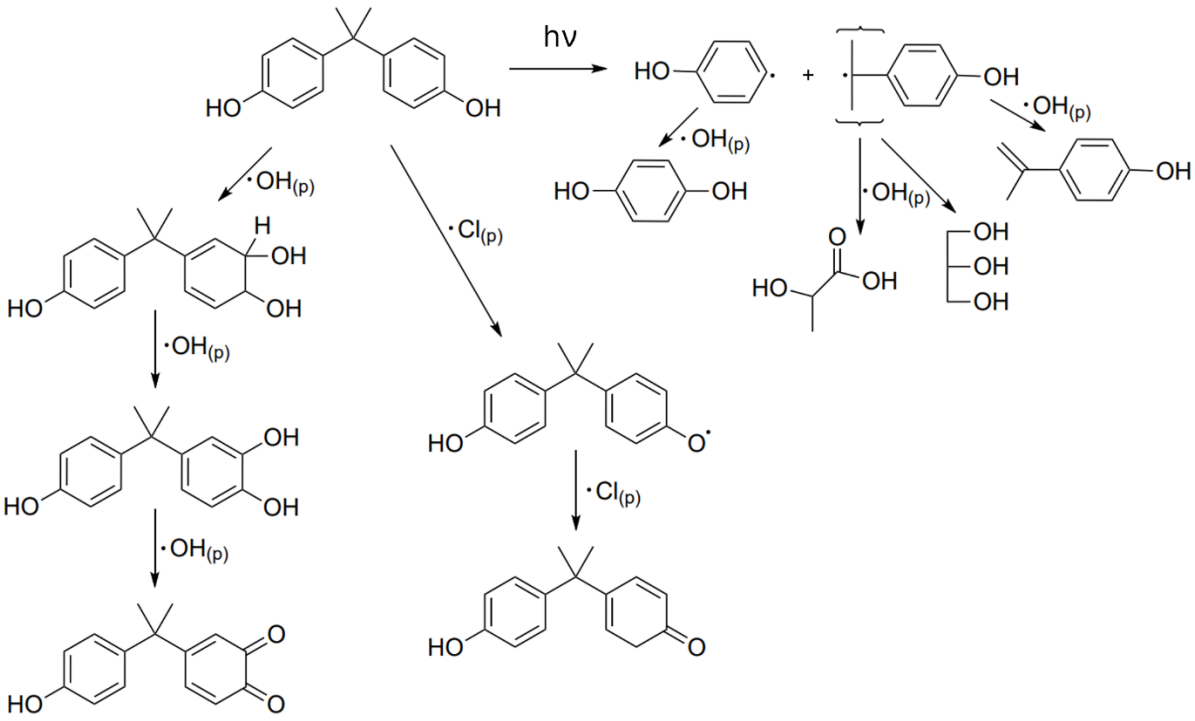

Figure 3.2 Dominant pathways of BPA degradation via OH and Cl radicals and light.[28, 48, 49]

The oxidative degradation of BPA by OH is expected to proceed via addition to the phenol ring generating a catechol.[49] Exposure to 254 nm radiation is known to decompose BPA by breaking the carbon-carbon bond between the quaternary carbon and carbon on the phenol group, and subsequent oxidation of these fragmented products by OH can form smaller molecular weight oxidation products.[28] These mechanisms are summarized in Figure 3.2. These products were not detected in the mass spectral data above the experimental background, which could result from the degradation of the first-generation oxidation products at the relatively high OH exposure levels in the PAM-OFR that subsequently fragment and volatilize from the aerosol surface, and therefore would not be detected in the aerosol phase by the EESI-TOF. As shown in Figure 3.7, ~3% of the particle mass was lost due to volatilization at the equivalent of 9.4 days of OH exposure. This indicates a shift in reaction pathways of BPA degradation by OH from functionalization at the lowest OH exposures (up to 3×10^{11} molecules s cm^{-3}) to fragmentation as the OH exposure was increased from 3×10^{11} to 6×10^{11} molecules s cm^{-3}.

Table 3.1 Experimentally-derived k_{OH}, k_{254nm}, k_{369nm}, γ, and atmospheric lifetime in days.

Experiment	k_{OH} (10^{-12} cm^3 $molecules^{-1}$ s^{-1})	k_{254nm} (10^{-3} s^{-1})	k_{369nm} (10^{-3} s^{-1})	γ	BPA lifetime by OH reaction (days)
BPA	0.773 ± 0.082	1.153 ± 0.398	1.457 ± 1.027	0.211 ± 0.022	20.0
BPA+NaCl	2.091 ± 0.098	1.928 ± 1.626	1.711 ± 1.418	0.398 ± 0.019	7.38
BPA+NaCl+ 4-BBA	2.016 ± 0.064	2.105 ± 0.772	0.545 ± 0.512	0.546 ± 0.017	7.66
BPA+NaCl+ HA	2.062 ± 0.069	1.801 ± 0.586	1.168 ± 0.843	0.580 ± 0.019	7.48
BPA+4-BBA	1.226 ± 0.047	5.381 ± 1.797	7.050 ± 3.821	0.313 ± 0.012	12.6
BPA+HA	0.791 ± 0.008	5.577 ± 1.373	3.478 ± 1.375	0.210 ± 0.002	19.5

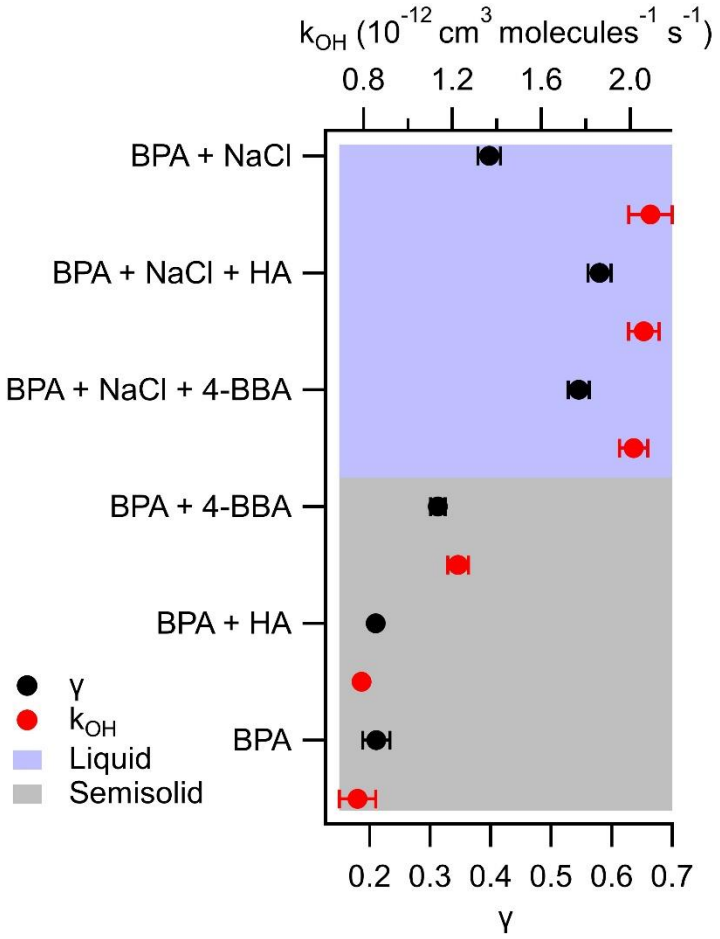

Figure 3.3 Experimentally-derived second-order rate constants of BPA degradation in aerosol by OH reactive uptake (k_{OH}; red) and the corresponding OH reactive uptake coefficients (γ; black) for all aerosol systems studied.

Degradation of BPA in the Presence of NaCl by OH and the Role of Phase State.

Sea salt (NaCl) was mixed with BPA (50:50 by wt.%) in the atomizer solution to mimic the bulk chemical composition of SSA. In the presence of NaCl, heterogeneous loss of BPA by reactive uptake of OH increased significantly in comparison to the pure-component BPA aerosol. The measured k_{OH}=2.091 (± 0.098) × 10^{-12} cm^3 $molecule^{-1}$ s^{-1}, and γ = 0.398 (± 0.019), a factor of 1.8 greater reactive loss of BPA when in the presence of NaCl, as shown in Figure 3.3. Previous work has also observed increased BPA degradation in aqueous systems containing NaCl, in which it is suggested that this is due to the generation of $HOCl^{\bullet-}$ and other reactive species that would otherwise not form in the absence of NaCl.[50] This is the first such observation of enhanced heterogeneous reactive loss of an organic component in the aerosol phase upon exposure to OH in the presence of NaCl. In Trueblood et al., 2019, heterogeneous OH oxidative aging of real SSA in a PAM-OFR led to a significant depletion in the fraction of the non-volatile organic components in the aerosol phase.[20] This was attributed to direct OH oxidation of the organic species in sea spray including amino acids that resulted from C-C bond scission. The effects of NaCl were not accounted for in that study. In Sakamoto et al. 2018, which measured the uptake of OH onto pure deliquesced NaCl aerosol, γ varied from 0.77 to 0.95, which is within the reported range of γ in this study for the aerosol mixtures containing NaCl measured above the deliquescence relative humidity (DRH~75%) of NaCl.[51] They attribute the greater uptake to greater diffusion and reaction in the aerosol bulk in the deliquesced state.

In the presence of NaCl, the degradation of BPA in the aerosol phase following OH uptake may be further impacted by the formation of reactive chlorine species (RCS), i.e., Cl radicals, Cl radical-ion species, and chlorine gas as shown in R 3.1-R 3.4, which subsequently could have reacted with neighboring BPA molecules in the aerosol phase**,** as shown in Figure 3.2.[52]

$$\bullet OH + Cl^- \leftrightarrow HOCl\bullet^- \quad \text{R 3.1}$$

$$HOCl\bullet^- + H^+ \leftrightarrow Cl\bullet + H_2O \quad \text{R 3.2}$$

$$Cl\bullet + Cl\bullet \leftrightarrow Cl_2 \quad \text{R 3.3}$$

$$Cl\bullet + Cl^- \leftrightarrow Cl_2\bullet^- \quad \text{R 3.4}$$

As shown in Figure 3.8, we observed depletion of the Cl^- signal (m/z= 34.969401) in the EESI-TOF following exposure to OH when NaCl was present in the aerosol phase. This depletion of Cl^- is indicative of heterogeneous reactions between OH and Cl^- and thus formation of RCS in the aerosol phase.

As shown in Figure 3.1, BPA continued to decay with increasing OH exposure levels above 4×10^{11} molecules s cm^{-3} in the binary component BPA+NaCl aerosol, unlike for the pure-component BPA decay, which did not decay further with increasing OH exposure. As described in Sakamoto et al., 2018, if we considered OH reactions as occurring only on the surface of the aerosol, OH reactive uptake (i.e., decay rate of BPA in this study) would slow with increasing OH exposure. In contrast, no apparent limitations to OH reactive uptake exist when bulk reactions are considered. This highlights the potential importance of phase state in the reactive uptake kinetics of OH and degradation of contaminant species in aerosol in general. NaCl is hygroscopic, and the high RH of the PAM-OFR (80%) was above its DRH. Here, the binary-component BPA+NaCl aerosol would hydrate, which would encourage mixing of reactive components in the aerosol phase. In contrast, BPA is hydrophobic and sparingly soluble in water, thus no appreciable water uptake is expected in the pure-component BPA aerosol experiments even at this RH. To investigate this further, we performed theoretical calculations of the viscosity of pure-component BPA aerosol at RH=80% and contrasted with the estimated viscosity of binary-component BPA+NaCl aerosol at RH=80% (full details included in SI).[53] We considered two different conditions, one whereby

the hygroscopicity parameter of BPA was set to κ=0.01 (characteristic of sparingly water-soluble organic matter), and one whereby κ=0.1 (often used for parameterizing the hygroscopicity of organic aerosol).[54] In the case of κ=0.01 for BPA, the viscosity of pure-component BPA aerosol at RH=80% and temperature of 295 K was a factor of two more viscous compared to the binary-component BPA+NaCl aerosol at the same temperature and RH. Assuming κ=0.1 for BPA, pure-component BPA aerosol was nearly a factor of ten more viscous compared to the binary-component BPA+NaCl aerosol. This indicates that the bulk diffusivity and mixing timescales of BPA, OH, and RCS were approximately two to ten times faster in the presence of NaCl than in the pure-component BPA aerosol, which could explain the factor of four enhancement in the reactive uptake and degradation rates of BPA in the presence of NaCl. In addition to these viscosity calculations, we also applied the parameterization from Davies and Wilson described in the BPA only section to the BPA+NaCl case and shown in Figure 3.1 (further details in SI).[44] In this case, the k_{OH} values for the linear and parameterized exponential fits were within error of each other, further indicating that in the presence of NaCl, the particle was well-mixed, which can lead to greater replenishment of unreacted BPA at the surface and thus greater fractional loss of BPA in the aerosol phase. In other mixed organic/inorganic aerosol systems, phase state and RH are shown to regulate heterogeneous oxidation.[55] This suggests further that uptake and reactions between OH and BPA were enhanced and more likely driven by both surface and bulk reactions in the binary-component BPA+NaCl aerosol with lower viscosity, whereas OH oxidation of BPA was limited to the surface in the more viscous pure-component BPA aerosol.

The Setschenow (salting-out) coefficient of BPA in NaCl has been measured as 0.174 M^{-1}.[56] The polarity of the di-substituted phenyl rings suggests that BPA may have a propensity for both the bulk and the surface of the particles even with high ionic strength. Given the increased

ionic strength of the particles with NaCl, however, some BPA is likely to be promoted to the particle surface. In addition to the greater mixing of BPA in the less viscous aqueous aerosol matrix containing NaCl, the effect of salting out could accelerate reactions between OH and BPA as reactions with OH are expected to occur within the near-surface layer of the particle (predicted reacto-diffusive length of OH is ≤1 nm).[19] This effect by salting out has been observed in other aerosol systems, e.g., in the accelerated oxidation of sulfur by O_3 in the presence of optically-trapped sodium thiosulfate/sucrose/aqueous droplets.[57] Furthermore, the larger surface area-to-volume ratio (SA/V) of BPA in the mixed BPA/NaCl aerosol compared to pure BPA could lead to greater reactive loss of BPA as observed in the heterogeneous oxidation of squalane by reaction with OH on squalene-coated ammonium sulfate particles compared to pure squalane particles.[46]

Degradation of BPA in the Presence of NaCl and Photosensitizers by OH.

Mimicking the complexity of SSA, we added to the mixture of BPA and NaCl two photosensitizing molecules as substitutes for the chromophoric dissolved organic matter found in SSA: 4-benzoylbenzoic acid (4-BBA) and more complex humic acid (HA). Both 4-BBA and HA have been employed in previous work as representative photosensitizing molecules but notably may lack some of the key photosensitizing properties and chemical features of real chromophoric material present at the ocean surface, which includes enriched levels of nitrogen.[9, 58] These experiments were performed in the absence and in the presence of NaCl to elucidate possible additive effects on the degradation of BPA by NaCl and the photosensitizers. The decay rates of BPA in the ternary-component aerosol comprised of either photosensitizer were considerably higher than the binary-component BPA+NaCl aerosol. k_{OH} for the BPA+NaCl aerosol mixture was 2.091 (± 0.098) × 10^{-12} cm^3 $molecule^{-1}$ s^{-1} while k_{OH} for the BPA+NaCl+4-BBA aerosol mixture was 2.016 (± 0.064) × 10^{-12} cm^3 $molecule^{-1}$ s^{-1} and k_{OH} for the BPA+NaCl+HA aerosol mixture was 2.062 (± 0.069) × 10^{-12} cm^3 $molecule^{-1}$ s^{-1}, which are all within error of each other. These

corresponded to uptake rates of 0.546 (± 0.017) for BPA+NaCl+4-BBA and 0.580 (± 0.019) for BPA+NaCl+HA. This is expected, as there is the impact of the lowered viscosity with the addition of NaCl, which can lead to increased photodegradation by better mixing of the photosensitizer molecules, allowing more photosensitizer molecules to be activated by light at the surface of the particle. k_{OH} = 1.226 (± 0.047) × 10^{-12} cm^3 $molecule^{-1}$ s^{-1} in the presence of 4-BBA and k_{OH} = 0.791 (± 0.008) × 10^{-12} cm^3 $molecule^{-1}$ s^{-1} in the presence of HA. This corresponded to γ = 0.313 (± 0.012) and γ = 0.210 (± 0.002), respectively, which was an enhancement of up to 49% in γ for the BPA mixture with 4-BBA. Interestingly, the photosensitizers behave quite differently without NaCl present. Analogous to our findings, Trueblood et al., 2019 reported that HA was a less efficient photosensitizer than 4-BBA with respect to the degradation of nonanoic acid thin films, although a mechanism was not provided. However, the larger molecular weight and predicted viscosity of HA in comparison with 4-BBA and BPA could lead to morphology changes at the high RH in this study, including phase separation between organic components with different solubilities, in analogy to the liquid-liquid phase separation as observed for mixed aqueous organic-inorganic aerosol.[59] If phase separation occurred, we speculate that the slower degradation of BPA in the aerosol mixture with HA was due to less interaction of reactive species formed by HA under light exposure.

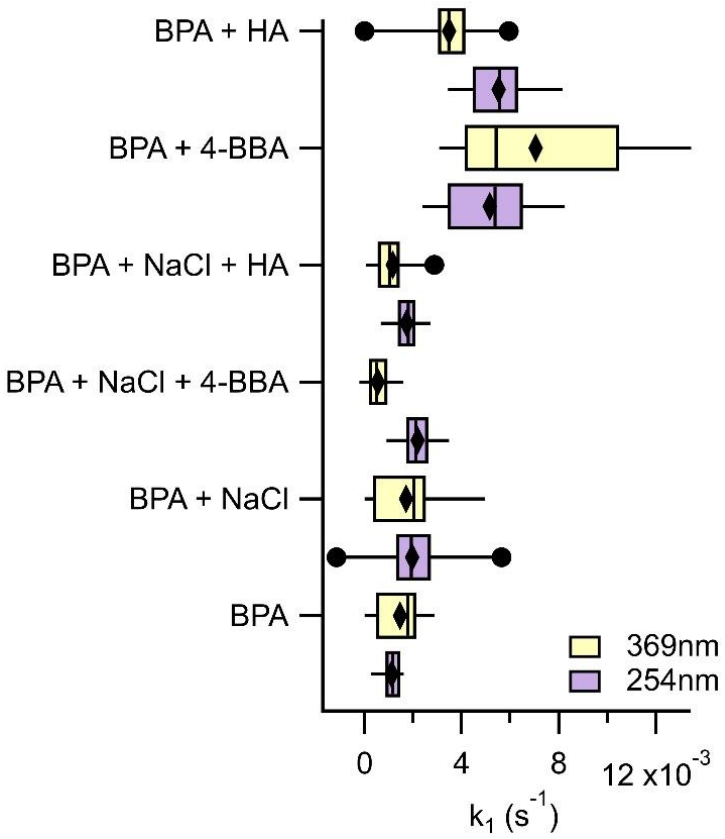

Figure 3.4 First-order loss rates of BPA for the different aerosol systems following exposure to 369 nm light (yellow boxes) and 254 nm light (purple boxes).

Degradation of BPA in the Presence of 254 nm and 369 nm Light.

In a separate set of experiments, BPA was exposed to either 254 nm light or 369 nm light inside the PAM-OFR in the absence of OH and ozone but with the same RH and flow rates as in all experiments. In the 254 nm experiments, the irradiance was adjusted systematically from 24 to 171 W/m^2, which corresponded to the same levels in the OH experiments. In the 369 nm experiments, the irradiance was adjusted from 30 to 267 W/m^2. First-order loss rate constants, k_{254} and k_{369}, were calculated from the slope of the natural logarithm of the fractional decay of BPA (before and after irradiance) as a function of the residence time (123 s) in the PAM-OFR. The results for the different aerosol systems are displayed in Figure 3.4. k_{369} for the pure-component BPA was 1.457 (± 1.027) × 10^{-3} s^{-1} and k_{254} = 1.153 (± 0.398) × 10^{-3} s^{-1}. In the binary-component BPA+NaCl aerosol mixture, mean k_{369} = 1.711 (± 1.418) × 10^{-3} s^{-1} and k_{254} = 1.928 (± 1.626) × 10^{-3} s^{-1}, which was not statistically different from the first-order decay rate of pure-component BPA aerosol upon irradiation. Irradiation of the ternary-component BPA+NaCl+photosensitizer aerosol by 369 nm light led to a slight but insignificant decrease in the degradation of BPA compared to the binary-component BPA+NaCl aerosol. Here, k_{369} = 0.545 (± 0.512) × 10^{-3} s^{-1} and k_{254} = 2.105 (± 0.772) × 10^{-3} s^{-1} for the BPA+NaCl+4-BBA aerosol mixture and k_{369} = 1.168 (± 0.843) × 10^{-3} s^{-1} and k_{254} = 1.801 (± 0.586) × 10^{-3} s^{-1} for the BPA+NaCl+HA aerosol mixture. In contrast, in the absence of NaCl, the addition of the photosensitizers to BPA led to a significant enhancement in the degradation of BPA following exposure to 369 nm light, increasing to k_{369} = 7.050 (± 3.821) × 10^{-3} s^{-1} and k_{254} = 5.381 (± 1.797) × 10^{-3} s^{-1} for the binary-component BPA+4-BBA and k_{369} = 3.478 (± 1.375) × 10^{-3} s^{-1} and k_{254} = 5.577 (± 1.373) × 10^{-3} s^{-1} for the binary-component BPA+HA aerosol mixtures. Zhan et al. 2006 found similarly that the rate of BPA degradation in bulk aqueous solutions under solar-simulated light was insignificant with BPA alone but increased in the presence of humic acids.[28]

It is possible that BPA degradation in the ternary-component aerosol mixtures was suppressed due to quenching of the excited triplet state of the photosensitizer by halide ions. As discussed in Tinel et al. 2014 and shown in R 3.5, the excited triplet state of the photosensitizer, imidazole-2-carboxaldehyde (IC), which has been shown in other work by Tinel to exhibit similar photosensitizing capabilities as 4-BBA, gets quenched in the presence of halides:[60, 61]

$$IC^* + X^- \rightarrow IC^{\bullet -} + X^{\bullet} \qquad \text{R 3.5}$$

In the absence of NaCl, the photosensitizers can access the excited triplet state and upon energy transfer can degrade neighboring organic molecules via formation of reactive oxygen species. The greater loss rates measured for BPA in the binary-component BPA+photosensitizer aerosol mixtures following exposure to 254 nm and 369 nm radiation are attributed to photosensitized degradation processes. Singlet oxygen can be produced in the presence of UV/VIS radiation due to an electronic energy transfer between the excited triplet state of the photosensitizer and the ground triplet state of molecular oxygen, which could readily react with BPA.[23, 62] Alternatively, direct interactions between the triplet state of the photosensitizer and BPA can promote the formation of radicals such as HO_2, accelerating the loss of BPA when irradiated.[63] Notably, there is little difference between the first-order loss rates of BPA mixed with the photosensitizers when exposed to 254 nm light compared to irradiation at 369 nm, which is indicative that these photosensitized processes do not require absorption of highly energetic light to proceed, and could proceed under more relevant daylight conditions in the atmosphere. Using the Atmospheric Chemistry Observations & Modeling tool from the National Center for Atmospheric Research, it is estimated that during an average summertime afternoon, San Diego, CA would receive roughly 2.02×10^{13} photons s^{-1} cm^{-2} of 369 nm light.[64] While the lowest light exposure in the 369 nm experiments was still an order of magnitude greater than that predicted by

the model, light exposures are expected to increase with altitude to ~1×10^{14} photons s^{-1} cm^{-2} at 369 nm and 6 km in the atmosphere. Additionally, integrated light exposure across all UV and VIS wavelengths of the solar spectrum could lead to even greater photosensitized degradation rates of BPA than what was reported here at only 369 nm. Furthermore, longitude and solar zenith angle (or time of day) will affect the intensity and wavelength of light absorbed by the aerosol.

3.5 Conclusions

In this study, we demonstrated that OH-initiated heterogeneous reactivity and photodegradation kinetics of aerosol-phase BPA, representative of the toxic additives in airborne micro- and nano-plastics, are greatly impacted by the presence of sea salt (NaCl) and photosensitizing species. The heterogeneous and photosensitized processes that promote the decay of BPA depend on the particle viscosity or phase state. Aerosol mixtures comprised of BPA and NaCl, the least viscous phase states, exhibited the greatest loss of BPA following exposure to OH due to greater diffusive mixing of reactive species in the particle bulk. Calculated uptake coefficients based on the decay of BPA were a factor of four greater in the presence of NaCl compared to pure-component BPA aerosol and bulk diffusion mixing timescales of reactants in the particle phase were shown to be a factor of two to ten faster in the presence of NaCl. The addition of a photosensitizer to BPA promoted the loss of BPA following light exposure to 369 nm radiation in the absence of OH. No significant enhancements in the reactive losses of BPA by OH or light exposure were observed when a photosensitizer was added to the BPA+NaCl aerosol mixtures. These differences were attributed to surface-enhanced photosensitized reactions in the case of the more viscous BPA+photosensitizer aerosol and quenching of the excited triplet state of the photosensitizer in the more liquid-like aqueous-phase NaCl aerosol.

In the context of SSA in the real atmosphere, particularly in the marine boundary layer where the RH is ~85% or greater, photosensitized reactions between chromophores emitted in SSA

and plastic contaminant molecules such as BPA may be limited due to quenching of the triplet state by halide ions, whereas heterogeneous oxidation via OH could promote the formation of reactive halogen radicals. The more liquid-like phase states of SSA in the marine boundary layer[18] could increase the probability of reaction with BPA as OH, BPA, and RCS diffuse more readily in the particle bulk in the presence of aqueous sea salt, promoting the degradation of BPA. As contaminated SSA becomes lofted over land and mixed in the vertical to higher altitudes above the marine boundary layer to regions of lower RH and exposure to more intense solar radiation, the particles dry and BPA and chromophoric organic molecules get salted out and promoted to the particle surface wherein photosensitized reactions may become more prevalent.

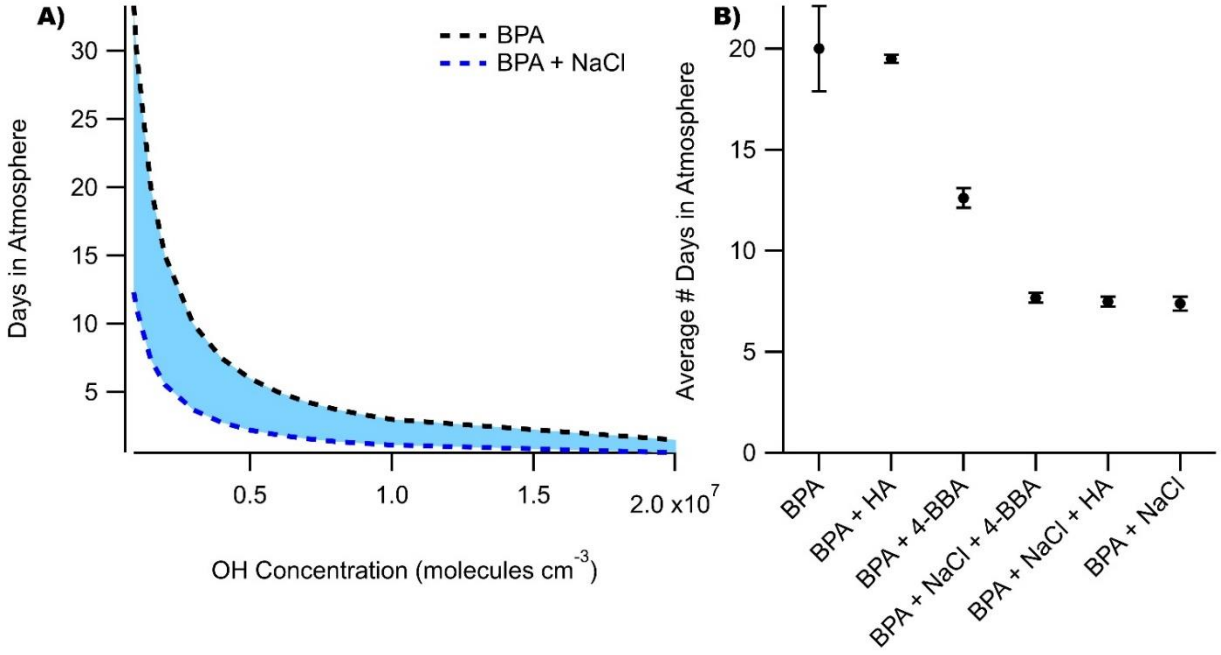

Figure 3.5 (A) Chemical lifetimes of BPA with respect to heterogeneous OH oxidation as a function of OH concentration. (B) Averaged chemical lifetimes of BPA in the different aerosol mixtures based on [OH]=1.5×10^{6} molecules cm^{-3}.

The e-folding lifetimes (τ) of BPA following exposure to OH in the different aerosol mixtures studied here are shown in Figure 3.5 and were calculated from Eq. 3.2:

$$\tau = 1/k_{OH}[OH] \quad \text{Eq. 3.2}$$

The e-folding lifetime is equivalent to the average time that BPA would remain chemically viable in aerosol and calculated assuming [OH] = 1.5×10^6 molecules cm^{-3}. BPA alone is expected to decay due to heterogeneous reaction with OH with a τ equivalent to about three weeks in the atmosphere, which is longer than the physical lifetime of the aerosol of around a week due to wet deposition. In the presence of NaCl, the lifetime of BPA is reduced by more than half to 7.4 days, competitive with wet depositional lifetimes. In drier areas like the Pacific Southwest where rain events are infrequent, heterogeneous and photo-initiated oxidation processes could thus serve as the major sinks for airborne particulate BPA. In the absence of NaCl but presence of a photosensitizer, the chemical lifetime of BPA is reduced with respect to pure-component BPA to 12.6 days in the presence of 4-BBA and 19.5 days in the presence of HA. These timescales are important as they suggest BPA and other additives in plastics that become airborne can remain in appreciable amounts in the aerosol phase for up to a week following their emission.

Future work could aim to increase the complexity of the aerosol to understand how BPA degrades in real SSA matrices, e.g., by generating SSA from bubble-bursting in real seawater employing a marine aerosol reference tank.[65] The composition of the chromophores in the dissolved organic matter in real SSA can differ from 4-BBA and HA studied here, potentially leading to different photosensitized degradation rates.[9] In addition, photosensitized reactions and degradation rates are known to differ depending on if the organic matter is in its anionic or neutral (zwitterionic) forms and shown to increase with increasing pH.[66] In Angle et al., 2021, the pH of SSA was shown to vary with particle size and differ from the pH of seawater at the ocean–air

interface.[67] Although the pH of the atomizer solutions (neutral to slightly acidic) indicated that BPA was in its molecular form and 4-BBA was in its carboxylate form, pH of the aerosol could be important in dictating the photosensitized kinetics, requiring further study beyond the scope of this work. Overall, this study provides a basis for understanding the different heterogeneous and photochemical degradation pathways of a key atmospheric plastic additive present in microplastics, which is an emerging concern for air quality in coastal marine environments.

3.6 Supplemental Information

Bisphenol-A (BPA) Signal Correction Method

We applied a single-point standardization of the EESI-TOF during the experiment to monitor potential drifts in sensitivity. Here, atomized BPA aerosol periodically bypassed (byp) the PAM-OFR. The adjusted (I_{adj}) BPA signal was calculated using formula Eq. 3.3:

$$I_{adj} = I_N - (I_N \left(\frac{I_{byp,2}}{I_{byp,N}}\right)) \quad \text{Eq. 3.3}$$

Here, I_N represents the BPA signal (ions s^{-1}) while the aerosol is flowing through the PAM-OFR during OH exposure (red shaded regions in Figure 3.6), $I_{byp,2}$ is the signal of the second single point standard (the second grey shaded region in Figure 3.6), and $I_{byp,N}$ is the signal of the single point standard that correlates to I_N. The first grey shaded region in Figure 3.6 is not utilized for correction because everything is normalized to the signal of aerosol flow through the PAM-OFR with no OH exposure (region in Figure 3.6 with no shading) and is only used to ensure proper instrument function after the filter blank (green shaded region in Figure 3.6) before starting the experiment.

Radial Reaction Depth Modeling for BPA Only and BPA+NaCl

To investigate the nonlinearity of the BPA only system, we chose to incorporate the parameterization from Davies and Wilson 2015.[44] In this model, we used Eq. 3.4 to determine the effective second order rate constant, k_{OH}, radial reaction depth, L, and the radial probing depth, d:

$$\ln\left(\frac{[BPA]}{[BPA_0]}\right) = \ln\left(\frac{D^3-(D-2L)^3}{D^3-(D-2d)^3}exp(-k_{OH}x) + \frac{(D-2L)^3-(D-2d)^3}{D^3-(D-2d)^3}\right) \quad \text{Eq. 3.4}$$

In this equation, D is the diameter of the particle, and [BPA]/[BPA_0] is the concentration as determined from the EESI-MS. Initially, k_{OH} was allowed to vary, and in the case of BPA and NaCl, this k_{OH} value was within that of the linear fit, indicating that the particles were well-mixed. However, in the case of BPA only, the values varied significantly, so the data was fit again, allowing k, L, and d to vary. In the case of EESI-MS, d is not defined, as it is dependent on the RH and solubility of the sample molecules in the reagent spray, so it was also determined by the fitting procedure. In this fitting, L was determined to be 2.5 (± 1) nm, k_{OH} was determined to be 5.93 (± 1.23) × 10^{-12} cm^3 $molecule^{-1}$ s^{-1}, and d was determined to be 9 (± 5) nm. After these parameters were determined, the new gamma was calculated using Eq. 3.5 from Davies and Wilson 2015:

$$\gamma = \frac{2 * \rho_{aq} * m_f * N_A}{3 * c * M_{org} * k_{OH}} * \frac{D^3-(D-2L)^3}{D^2} \quad \text{Eq. 3.5}$$

Where m_f is the mass fraction of BPA, ρ_{aq} is the density of BPA, N_A is Avogadro's number, c is the mean velocity of OH, M_{org} is the molar mass of BPA, and k_{OH} is the effective second order rate constant determined in the fitting procedure. This gives us gamma of 0.268 (± 0.056), which is within error of the gamma calculated based off the linear fit, 0.247 (± 0.026).

Estimated Glass Transition Temperature and Viscosity Calculations for Pure Component and Salt-Containing BPA Aerosol

The methods shown here closely follow those from Tumminello et al 2021.[18] Viscosity of the BPA aerosol was estimated from the aerosol's glass transition temperature (T_g), defined as the approximate range of temperatures over which a transition between semi-solid to amorphous solid (glassy) states occur.[68, 69] Here, we estimate the dry T_g of BPA ($T_{g,org}$) applying the formulations described in DeRieux et al.[53] $T_{g,org}$ was calculated using Eq. 3.6, where M and O:C are the molar mass and O:C of BPA with M=227 g mol^{-1}, O:C=0.13, and A, B, C, D, and E are best fit parameters.[53]

$$T_{g,org} = A + BM + CM^2 + D(O:C) + EM(O:C) \quad \text{Eq. 3.6}$$

To account for the impact of aerosol liquid water content on the $T_{g,org}$ of BPA, we calculated the volume of liquid water associated with BPA ($V_{w,org}$) in equilibrium with the relative humidity (assuming the water activity, a_w, is equal to relative humidity) applying Eq. 3.7:[54]

$$V_{w,org} = \frac{a_w}{1 - a_w} V_{org} \varepsilon_{org} \kappa_{org} \quad \text{Eq. 3.7}$$

The volume of the organic component in SSA (V_{org}) was determined based on the mean surface-area weighted diameter of 100 nm and the organic volume fraction (ε_{org}) from Eq. 3.8:

$$\varepsilon_{org} = \frac{f_{org}}{(f_{org} + (1 - f_{org})\left(\frac{\rho_{org}}{\rho_{org}}\right))} \quad \text{Eq. 3.8}$$

Here, f_{org} is the mass fraction of BPA, and ρ_{org} and ρ_{inorg} refer to the densities of the organic material (1.2 g cm^{-3}) and inorganic material (2.2 g cm^{-3}),[70] respectively. The volume mixing rule[54] was applied to solve for κ_{org} based two κ assumptions of 0.1 and 0.01 and assuming κ_{inorg}=1.51 for NaCl.[71] Note that there are certain assumptions in the calculated κ_{org} applying the volume mixing rule, including (1) that the aerosol population is considered homogeneous and contains both salt

and organic material as an internal mixture, (2) the hygroscopicity parameter of the inorganic component is known, and (3) aerosol water uptake behaves as a linear combination of the organic and inorganic components. $V_{w,org}$ was converted to mass of water ($m_{w,org}$) from the density of water of 1.0 g cm^{-3}. The Gordon-Taylor equation Eq. 3.9 was applied to calculate the average T_g of the organic-water mixture, $T_{g,org,w}$, where $f_{ALW}= m_{w,org}/(m_{org}+m_{w,org})$ and $T_{g,w}$ is the glass transition of pure water (136 K).[53]

$$T_{g,org,w} = \frac{T_{g,w}(f_{ALW}) + \frac{1}{k_{GT}} f_{org} T_{g,org}}{(f_{ALW}) + \frac{1}{k_{GT}} f_{org}} \quad \text{Eq. 3.9}$$

Finally, $T_{g,org,w}$ values were converted to viscosity, η_{org} (Pa·s) utilizing Eq. 3.10 and Eq. 3.11, where z, the fragility parameter was set to 12, a value used for organic compounds in previous studies.[53, 69]

$$T_0 = \frac{39.17 T_{g,org,w}}{z + 39.17} \quad \text{Eq. 3.10}$$

$$\log \eta = -5 + 0.434 \frac{T_0 z}{T - T_0} \quad \text{Eq. 3.11}$$

The viscosities of BPA and NaCl were calculated separately and then combined to estimate the viscosity of the mixture, which assumes the organic and inorganic components are homogeneous and internally-mixed, so we caution the following calculations are only appropriate for homogeneous internally-mixed organic/inorganic salt particles. To determine the viscosity of the aqueous salt solution, we first calculated the volume fraction of the inorganic portion (assuming an equal atomization efficiency of 0.5 for NaCl and 0.5 for BPA) (ε_{inorg}) as $\varepsilon_{inorg} = 1 - \varepsilon_{org}$, where ε_{org} was derived from Eq. S4. We then estimated the aerosol liquid water derived from the inorganic components in analogy to that for the organic components using Eq. S4 and applying a

κ_{inorg}=1.51 for NaCl.[71] The viscosity of the aqueous salt solution, η_{inorg}, was calculated adapting the formulations described in Goldsack and Franchetto, 1977.[72] In its simplest form, the η_{inorg} can be calculated using Eq. 3.12:

$$\eta_{inorg} = \frac{\eta_w e^{X_c E}}{1 + X_c V} \qquad \text{Eq. 3.12}$$

Here, η_w is the viscosity of water at 25°C, 0.8904 cP, X_c is the mole fraction of cations in solution, defined as $X_c=m_c/(55.51+2m)$, which applies to an aqueous solution on the molal scale given there are 55.51 moles of water per kg of water and 2m moles of salt (anion plus cation) for an m molal solution of a 1:1 salt, which we apply here for NaCl. E is the free energy based on the relationship, $E=(\Delta G_c^* + \Delta G_a^* - 2\Delta G_1^* \ 116)/RT$, determined from a data table (Table 3 in Goldsack and Franchetto, 1977)[72] for NaCl. V is the molar volume of the hole in the liquid created by the cations and anions moving in the liquid, also determined from the same data table. Assuming the organic components and salt are well mixed in the aerosol, the component viscosities of each were combined to calculate the viscosity of the BPA/NaCl aerosol based on the following classic mixing rules for liquids[73] Eq. 3.13:

$$\ln(\eta_{mix}) = \sum_{i=1}^{N} x_i \ln(\eta_i) \qquad \text{Eq. 3.13}$$

Here, x_i is the mole fraction and η_i is the viscosity of the component, i=organic or inorganic salt.

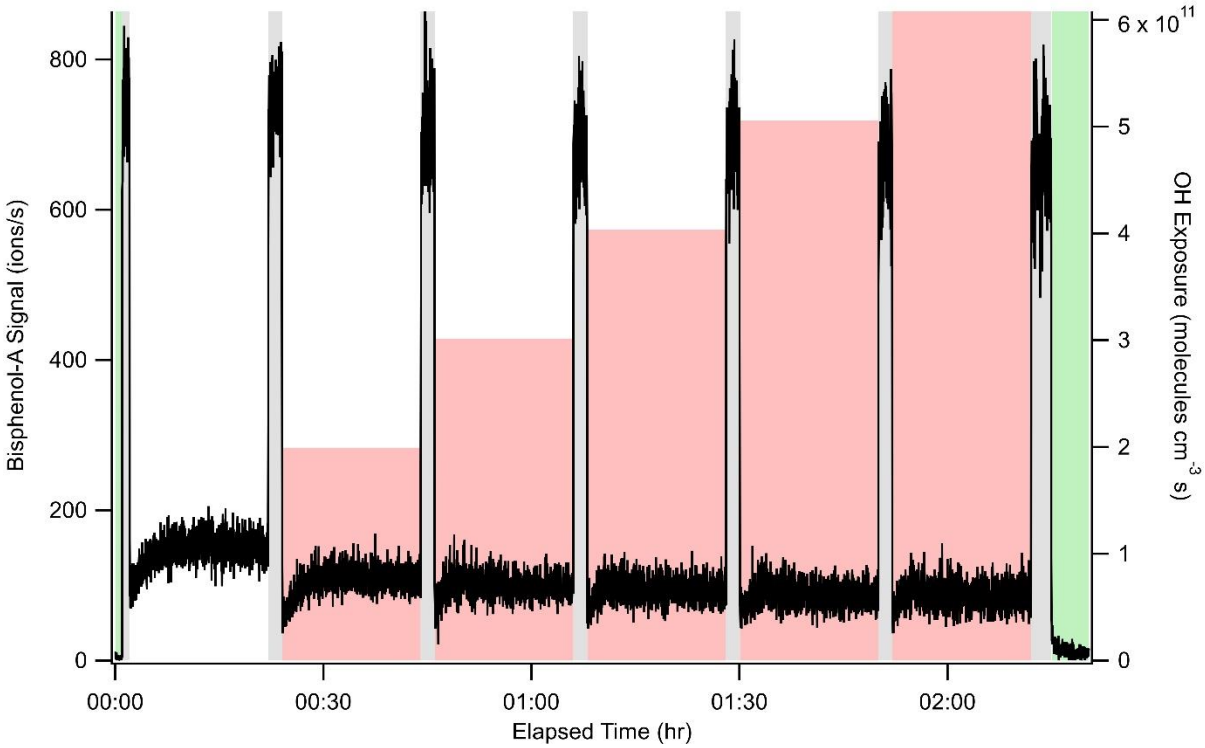

Figure 3.6 Full time series of BPA signal for one experiment. The green shaded regions indicate filter blanks, the grey shaded regions indicate the internal standards, and the red shaded regions indicate the OH exposures, corresponding to the right y-axis.

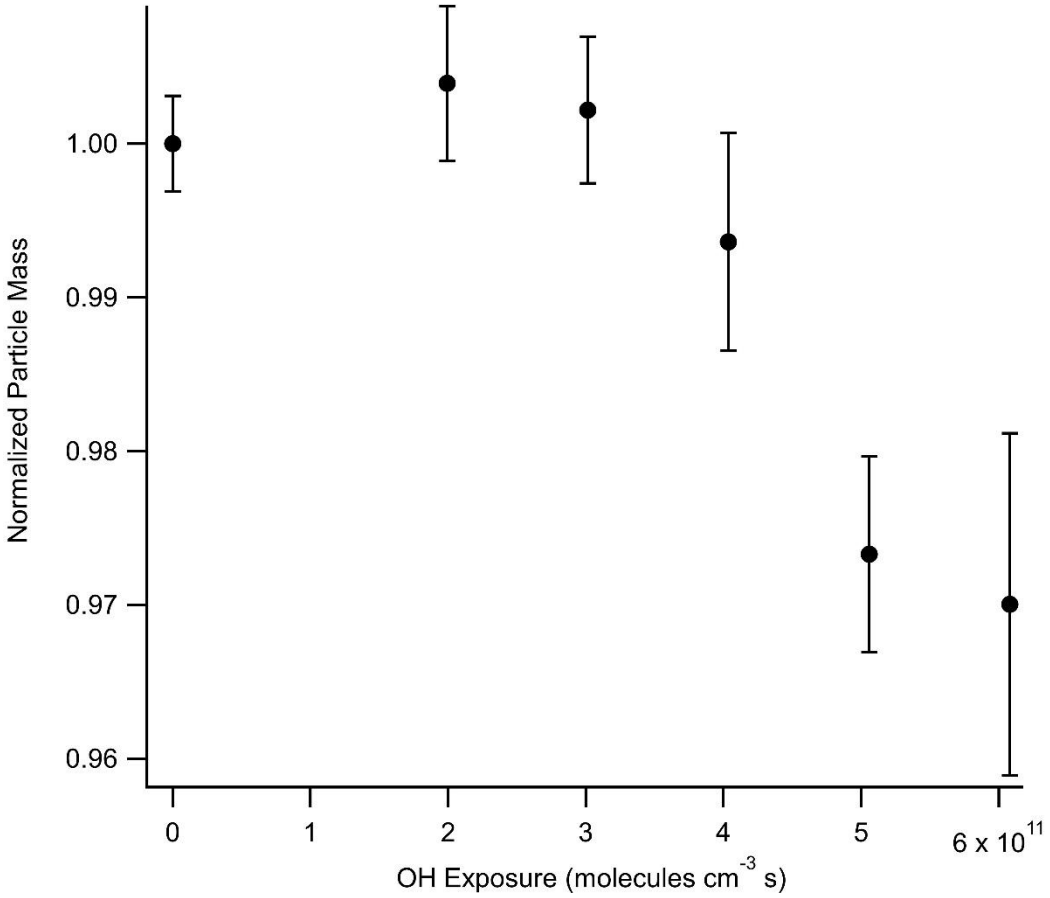

Figure 3.7 Normalized pure-component BPA aerosol mass concentrations as a function of OH exposure in the PAM-OFR.

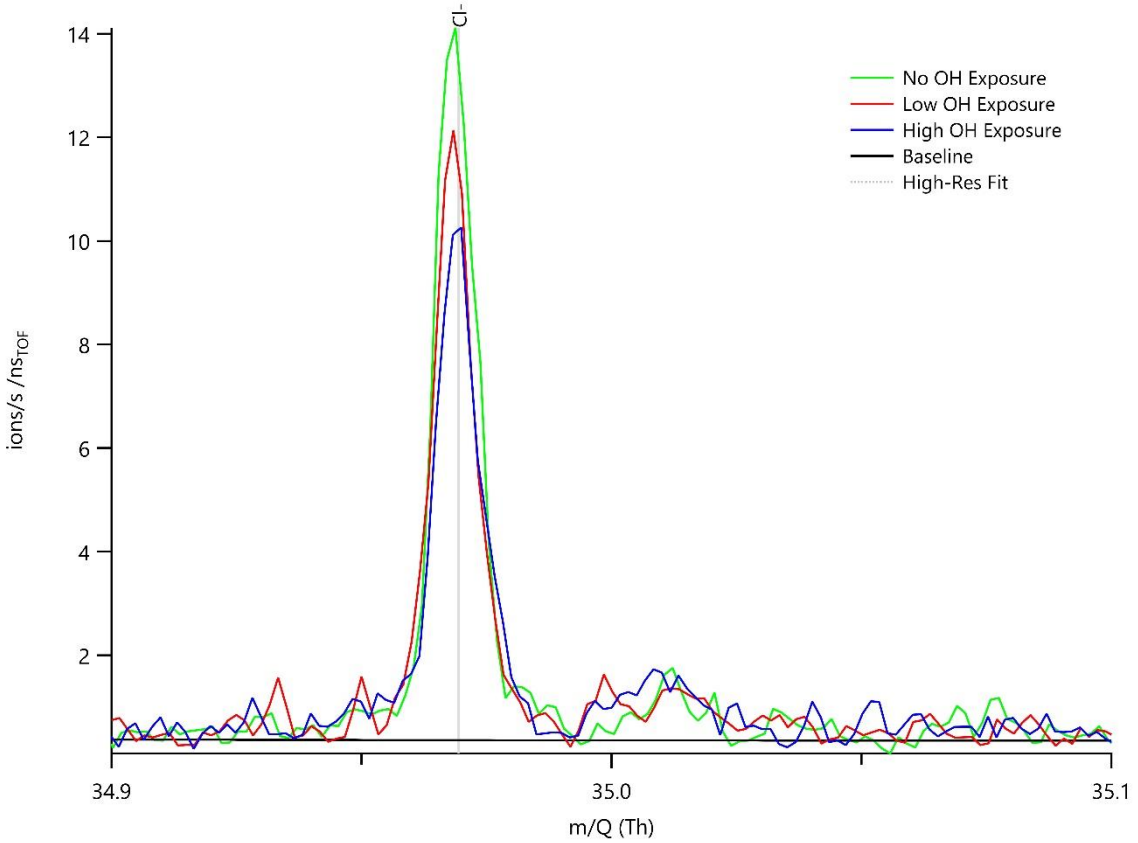

Figure 3.8 Chloride signal (m/z= 34.969401 Th) at no OH exposure (green), the lowest OH exposure (red), and the highest OH exposure (blue). Black represents the fitted spectrum baseline, and the light grey line represents the high-resolution fit for the no OH exposure signal.

3.7 Acknowledgements

Chapter 3, in full, is a reprint of the material as it appears in the Journal of Physical Chemistry A. “Heterogeneous and Photosensitized Oxidative Degradation Kinetics of the Plastic Additive Bisphenol-A in Sea Spray Aerosol Mimics” Kruse, Samantha M., Slade, Jonathan H., 2023. The dissertation author was the primary researcher and author of this paper.

The authors would like to thank Paul R. Tumminello for assistance with the viscosity calculations in this work and Prof. David Dehaan for helpful insights. The authors would also like to thank their funding source, National Science Foundation – Atmospheric and Geospace Sciences (NSF-AGS) grant #2135218

3.8 References

(1) Jambeck, J. R.; Geyer, R.; Wilcox, C.; Siegler, T. R.; Perryman, M.; Andrady, A.; Narayan, R.; Law, K. L. Plastic waste inputs from land into the ocean. *Science* **2015**, *347* (6223), 768-771. DOI: 10.1126/science.1260352.

(2) Seachrist, D. D.; Bonk, K. W.; Ho, S.-M.; Prins, G. S.; Soto, A. M.; Keri, R. A. A review of the carcinogenic potential of bisphenol A. *Reprod. Toxicol.* **2016**, *59*, 167-182. DOI: 10.1016/j.reprotox.2015.09.006.

(3) Moreman, J.; Lee, O.; Trznadel, M.; David, A.; Kudoh, T.; Tyler, C. R. Acute toxicity, teratogenic, and estrogenic effects of bisphenol A and its alternative replacements bisphenol S, bisphenol F, and bisphenol AF in zebrafish embryo-larvae. *Environ. Sci. Technol.* **2017**, *51* (21), 12796-12805. DOI: 10.1021/acs.est.7b03283.

(4) Kang, J.-H.; Kondo, F. Bisphenol A degradation in seawater is different from that in river water. *Chemosphere* **2005**, *60* (9), 1288-1292. DOI: 10.1016/j.chemosphere.2005.01.058.

(5) Kawahata, H.; Ohta, H.; Inoue, M.; Suzuki, A. Endocrine disrupter nonylphenol and bisphenol A contamination in Okinawa and Ishigaki Islands, Japan—within coral reefs and adjacent river mouths. *Chemosphere* **2004**, *55* (11), 1519-1527. DOI: 10.1016/j.chemosphere.2004.01.032.

(6) Yamamoto, T.; Yasuhara, A.; Shiraishi, H.; Nakasugi, O. Bisphenol A in hazardous waste landfill leachates. *Chemosphere* **2001**, *42* (4), 415-418. DOI: 10.1016/s0045-6535(00)00079-5.

(7) Fu, P.; Kawamura, K. Ubiquity of bisphenol A in the atmosphere. *Environ. Pollut.* **2010**, *158* (10), 3138-3143. DOI: 10.1016/j.envpol.2010.06.040.

(8) Cochran, R. E.; Laskina, O.; Jayarathne, T.; Laskin, A.; Laskin, J.; Lin, P.; Sultana, C.; Lee, C.; Moore, K. A.; Cappa, C. D.; Bertram, T. H.; Prather, K. A.; Grassian, V. H.; Stone, E. A.

Analysis of Organic Anionic Surfactants in Fine and Coarse Fractions of Freshly Emitted Sea Spray Aerosol. *Environ. Sci. Technol.* **2016**, *50* (5), 2477-2486. DOI: 10.1021/acs.est.5b04053.

(9) Trueblood, J. V.; Alves, M. R.; Power, D.; Santander, M. V.; Cochran, R. E.; Prather, K. A.; Grassian, V. H. Shedding Light on Photosensitized Reactions within Marine-Relevant Organic Thin Films. *ACS Earth Space Chem.* **2019**, *3* (8), 1614-1623. DOI: 10.1021/acsearthspacechem.9b00066.

(10) Bertram, T. H.; Cochran, R. E.; Grassian, V. H.; Stone, E. A. Sea spray aerosol chemical composition: elemental and molecular mimics for laboratory studies of heterogeneous and multiphase reactions. *Chem. Soc. Rev.* **2018**, *47* (7), 2374-2400. DOI: 10.1039/c7cs00008a.

(11) Glicker, H. S.; Lawler, M. J.; Chee, S.; Resch, J.; Garofalo, L. A.; Mayer, K. J.; Prather, K. A.; Farmer, D. K.; Smith, J. N. Chemical Composition of an Ultrafine Sea Spray Aerosol during the Sea Spray Chemistry and Particle Evolution Experiment. *ACS Earth Space Chem.* **2022**. DOI: 10.1021/acsearthspacechem.2c00127.

(12) Allen, D.; Allen, S.; Abbasi, S.; Baker, A.; Bergmann, M.; Brahney, J.; Butler, T.; Duce, R. A.; Eckhardt, S.; Evangeliou, N.; Jickells, T.; Kanakidou, M.; Kershaw, P.; Laj, P.; Levermore, J.; Li, D.; Liss, P.; Liu, K.; Mahowald, N.; Masque, P.; Materić, D.; Mayes, A. G.; McGinnity, P.; Osvath, I.; Prather, K. A.; Prospero, J. M.; Revell, L. E.; Sander, S. G.; Shim, W. J.; Slade, J.; Stein, A.; Tarasova, O.; Wright, S. Microplastics and nanoplastics in the marine-atmosphere environment. *Nat Rev Earth Environ* **2022**. DOI: 10.1038/s43017-022-00292-x.

(13) Mathieu-Denoncourt, J.; Wallace, S. J.; de Solla, S. R.; Langlois, V. S. Influence of Lipophilicity on the Toxicity of Bisphenol A and Phthalates to Aquatic Organisms. *Bull. Environ. Contam. Toxicol.* **2016**, *97* (1), 4-10. DOI: 10.1007/s00128-016-1812-9.

(14) Wang, X.; Deane, G. B.; Moore, K. A.; Ryder, O. S.; Stokes, M. D.; Beall, C. M.; Collins, D. B.; Santander, M. V.; Burrows, S. M.; Sultana, C. M.; Prather, K. A. The role of jet and film drops in controlling the mixing state of submicron sea spray aerosol particles. *Proc. Natl. Acad. Sci. U. S. A.* **2017**, *114* (27), 6978-6983. DOI: 10.1073/pnas.1702420114.

(15) Kroll, J. H.; Lim, C. Y.; Kessler, S. H.; Wilson, K. R. Heterogeneous Oxidation of Atmospheric Organic Aerosol: Kinetics of Changes to the Amount and Oxidation State of Particle-Phase Organic Carbon. *J. Phys. Chem. A* **2015**, *119* (44), 10767-10783. DOI: 10.1021/acs.jpca.5b06946.

(16) Kaluarachchi, C. P.; Or, V. W.; Lan, Y.; Hasenecz, E. S.; Kim, D.; Madawala, C. K.; Dorcé, G. P.; Mayer, K. J.; Sauer, J. S.; Lee, C.; Cappa, C. D.; Bertram, T. H.; Stone, E. A.; Prather, K. A.; Grassian, V. H.; Tivanski, A. V. Effects of Atmospheric Aging Processes on Nascent Sea Spray Aerosol Physicochemical Properties. *ACS Earth Space Chem.* **2022**, *6* (11), 2732-2744. DOI: 10.1021/acsearthspacechem.2c00258.

(17) Ravishankara, A. R. Heterogeneous and Multiphase Chemistry in the Troposphere. *Science* **1997**, *276* (5315), 1058-1065. DOI: 10.1126/science.276.5315.1058.

(18) Tumminello, P. R.; James, R. C.; Kruse, S.; Kawasaki, A.; Cooper, A.; Guadalupe-Diaz, I.; Zepeda, K. L.; Crocker, D. R.; Mayer, K. J.; Sauer, J. S.; Lee, C.; Prather, K. A.; Slade, J. H. Evolution of Sea Spray Aerosol Particle Phase State Across a Phytoplankton Bloom. *ACS Earth Space Chem.* **2021**, *5* (11), 2995-3007. DOI: 10.1021/acsearthspacechem.1c00186.

(19) Slade, J. H.; Knopf, D. A. Multiphase OH oxidation kinetics of organic aerosol: The role of particle phase state and relative humidity. *Geophys. Res. Lett.* **2014**, *41* (14), 5297-5306. DOI: 10.1002/2014gl060582.

(20) Trueblood, J. V.; Wang, X.; Or, V. W.; Alves, M. R.; Santander, M. V.; Prather, K. A.; Grassian, V. H. The Old and the New: Aging of Sea Spray Aerosol and Formation of Secondary Marine Aerosol through OH Oxidation Reactions. *ACS Earth Space Chem.* **2019**, *3* (10), 2307-2314. DOI: 10.1021/acsearthspacechem.9b00087.

(21) Rosati, B.; Christiansen, S.; Dinesen, A.; Roldin, P.; Massling, A.; Nilsson, E. D.; Bilde, M. The impact of atmospheric oxidation on hygroscopicity and cloud droplet activation of inorganic sea spray aerosol. *Sci. Rep.* **2021**, *11* (1), 10008. DOI: 10.1038/s41598-021-89346-6.

(22) Tsui, W. G.; McNeill, V. F. Modeling Secondary Organic Aerosol Production from Photosensitized Humic-like Substances (HULIS). *Environ. Sci. Technol. Lett.* **2018**, *5* (5), 255-259. DOI: 10.1021/acs.estlett.8b00101.

(23) Corral Arroyo, P.; Bartels-Rausch, T.; Alpert, P. A.; Dumas, S.; Perrier, S.; George, C.; Ammann, M. Particle-Phase Photosensitized Radical Production and Aerosol Aging. *Environ. Sci. Technol.* **2018**, *52* (14), 7680-7688. DOI: 10.1021/acs.est.8b00329.

(24) Forrester, S. M.; Knopf, D. A. Photosensitised heterogeneous oxidation kinetics of biomass burning aerosol surrogates by ozone using an irradiated rectangular channel flow reactor. *Atmos. Chem. Phys.* **2013**, *13* (13), 6507-6522. DOI: 10.5194/acp-13-6507-2013.

(25) Liu, Q.; Liggio, J.; Wu, D.; Saini, A.; Halappanavar, S.; Wentzell, J. J. B.; Harner, T.; Li, K.; Lee, P.; Li, S.-M. Experimental Study of OH-Initiated Heterogeneous Oxidation of Organophosphate Flame Retardants: Kinetics, Mechanism, and Toxicity. *Environ. Sci. Technol.* **2019**, *53* (24), 14398-14408. DOI: 10.1021/acs.est.9b05327.

(26) Martins-Costa, M. T. C.; Anglada, J. M.; Francisco, J. S.; Ruiz-López, M. F. Photosensitization mechanisms at the air-water interface of aqueous aerosols. *Chem. Sci.* **2022**, *13* (9), 2624-2631. DOI: 10.1039/d1sc06866k.

(27) Medeiros, P. M.; Seidel, M.; Powers, L. C.; Dittmar, T.; Hansell, D. A.; Miller, W. L. Dissolved organic matter composition and photochemical transformations in the northern North Pacific Ocean. *Geophys. Res. Lett.* **2015**, *42* (3), 863-870. DOI: 10.1002/2014gl062663.

(28) Zhan, M.; Yang, X.; Xian, Q.; Kong, L. Photosensitized degradation of bisphenol A involving reactive oxygen species in the presence of humic substances. *Chemosphere* **2006**, *63* (3), 378-386. DOI: 10.1016/j.chemosphere.2005.08.046.

(29) Felipe D. Lopez-Hilfiker; Veronika Pospisilova; Wei Huang; Markus Kalberer; Claudia Mohr; Giulia Stefenelli; Joel A. Thornton; Urs Baltensperger; Andre S. H. Prevot; Slowik, J. G. An extractive electrospray ionization time-of-flight mass spectrometer (EESI-TOF) for online measurement of atmospheric aerosol particles. *Atmospheric* **2019**. DOI: 10.5194/amt-12-4867-2019.

(30) Brown, W. L.; Day, D. A.; Stark, H.; Pagonis, D.; Krechmer, J. E.; Liu, X.; Price, D. J.; Katz, E. F.; DeCarlo, P. F.; Masoud, C. G.; Wang, D. S.; Hildebrandt Ruiz, L.; Arata, C.; Lunderberg, D. M.; Goldstein, A. H.; Farmer, D. K.; Vance, M. E.; Jimenez, J. L. Real-time organic aerosol chemical speciation in the indoor environment using extractive electrospray ionization mass spectrometry. *Indoor Air* **2021**, *31* (1), 141-155. DOI: 10.1111/ina.12721.

(31) Pospisilova, V.; Lopez-Hilfiker, F. D.; Bell, D. M.; Haddad, I. E.; Mohr, C.; Huang, W.; Heikkinen, L.; Xiao, M.; Dommen, J.; Prevot, A. S. H.; Baltensperger, U.; Slowik, J. G. On the fate of oxygenated organic molecules in atmospheric aerosol particles. *Science Advances* **2020**, *6* (11), eaax8922. DOI: 10.1126/sciadv.aax8922.

(32) Doezema, L. A.; Longin, T.; Cody, W.; Perraud, V.; Dawson, M. L.; Ezell, M. J.; Greaves, J.; Johnson, K. R.; Finlayson-Pitts, B. J. Analysis of secondary organic aerosols in air using extractive electrospray ionization mass spectrometry (EESI-MS). *RSC Adv.* **2012**, *2* (7), 2930-2938. DOI: 10.1039/C2RA00961G.

(33) A. T. Lambe; A. T. Ahern; L. R. Williams; J. G. Slowik; J. P. S. Wong; J. P. D. Abbatt; W. H. Brune; N. L. Ng; J. P. Wright; D. R. Croasdale; D. R. Worsnop; P. Davidovits; Onasch, T. B. Characterization of aerosol photooxidation flow reactors: heterogeneous oxidation, secondary organic aerosol formation and cloud condensation nuclei activity measurements. *Atmospheric Measurement Techniques* **2011**, *4* (3), 445-461. DOI: 10.5194/amt-4-445-2011.

(34) Tkacik, D. S.; Lambe, A. T.; Jathar, S.; Li, X.; Presto, A. A.; Zhao, Y.; Blake, D.; Meinardi, S.; Jayne, J. T.; Croteau, P. L.; Robinson, A. L. Secondary organic aerosol formation from in-use motor vehicle emissions using a potential aerosol mass reactor. *Environ. Sci. Technol.* **2014**, *48* (19), 11235-11242. DOI: 10.1021/es502239v.

(35) Xu, W.; Li, Z.; Lambe, A. T.; Li, J.; Liu, T.; Du, A.; Zhang, Z.; Zhou, W.; Sun, Y. Secondary organic aerosol formation and aging from ambient air in an oxidation flow reactor during wintertime in Beijing, China. *Environmental Research* **2022**, *209*, 112751. DOI: 10.1016/j.envres.2022.112751.

(36) Chen, S.; Brune, W. H.; Lambe, A. T.; Davidovits, P.; Onasch, T. B. Modeling organic aerosol from the oxidation of α-pinene in a Potential Aerosol Mass (PAM) chamber. *Atmos. Chem. Phys.* **2013**, *13* (9), 5017-5031. DOI: 10.5194/acp-13-5017-2013.

(37) Slade, J. H.; Knopf, D. A. Heterogeneous OH oxidation of biomass burning organic aerosol surrogate compounds: assessment of volatilisation products and the role of OH concentration on the reactive uptake kinetics. *Phys. Chem. Chem. Phys.* **2013**, *15* (16), 5898-5915. DOI: 10.1039/c3cp44695f.

(38) Lambe, A. T.; Chhabra, P. S.; Onasch, T. B.; Brune, W. H.; Hunter, J. F.; Kroll, J. H.; Cummings, M. J.; Brogan, J. F.; Parmar, Y.; Worsnop, D. R.; Kolb, C. E.; Davidovits, P. Effect of oxidant concentration, exposure time, and seed particles on secondary organic aerosol chemical composition and yield. *Atmos. Chem. Phys.* **2015**, *15* (6), 3063-3075. DOI: 10.5194/acp-15-3063-2015.

(39) Kessler, S. H.; Smith, J. D.; Che, D. L.; Worsnop, D. R.; Wilson, K. R.; Kroll, J. H. Chemical sinks of organic aerosol: kinetics and products of the heterogeneous oxidation of erythritol and levoglucosan. *Environ. Sci. Technol.* **2010**, *44* (18), 7005-7010. DOI: 10.1021/es101465m.

(40) Kessler, S. H.; Nah, T.; Daumit, K. E.; Smith, J. D.; Leone, S. R.; Kolb, C. E.; Worsnop, D. R.; Wilson, K. R.; Kroll, J. H. OH-initiated heterogeneous aging of highly oxidized organic aerosol. *J. Phys. Chem. A* **2012**, *116* (24), 6358-6365. DOI: 10.1021/jp212131m.

(41) C. E. Kolb; R. A. Cox; J. P. D. Abbatt; M. Ammann; E. J. Davis; D. J. Donaldson; B. C. Garrett; C. George; P. T. Griffiths; D. R. Hanson; M. Kulmala; G. McFiggans; U. Pöschl; I. Riipinen; M. J. Rossi; Y. Rudich; P. E. Wagner; P. M. Winkler; D. R. Worsnop; Dowd, C. D. O. An overview of current issues in the uptake of atmospheric trace gases by aerosols and clouds. *Atmos. Clim. Sci.* **2010**, *10* (21), 10561-10605. DOI: 10.5194/acp-10-10561-2010.

(42) George, I. J.; Abbatt, J. P. D. Heterogeneous oxidation of atmospheric aerosol particles by gas-phase radicals. *Nat. Chem.* **2010**, *2* (9), 713-722. DOI: 10.1038/nchem.806.

(43) Sutugin, A. G.; Fuchs, N. A. Formation of condensation aerosols under rapidly changing environmental conditions: Theory and method of calculation. *J. Aerosol Sci.* **1970**, *1* (4), 287-293. DOI: 10.1016/0021-8502(70)90002-9.

(44) Davies, J. F.; Wilson, K. R. Nanoscale interfacial gradients formed by the reactive uptake of OH radicals onto viscous aerosol surfaces. *Chem. Sci.* **2015**, *6* (12), 7020-7027. DOI: 10.1039/c5sc02326b.

(45) Abo, R.; Kummer, N. A.; Merkel, B. J. Optimized photodegradation of Bisphenol A in water using ZnO, TiO_2 and SnO_2 photocatalysts under UV radiation as a decontamination procedure. *Drink. Water Eng. Sci.* **2016**, *9*, 27-35. DOI: 10.5194/dwes-9-27-2016.

(46) Lim, C. Y.; Browne, E. C.; Sugrue, R. A.; Kroll, J. H. Rapid heterogeneous oxidation of organic coatings on submicron aerosols. *Geophys. Res. Lett.* **2017**, *44* (6), 2949-2957. DOI: 10.1002/2017gl072585.

(47) Renbaum, L. H.; Smith, G. D. Artifacts in measuring aerosol uptake kinetics: the roles of time, concentration and adsorption. *Atmos. Chem. Phys.* **2011**, *11* (14), 6881-6893. DOI: 10.5194/acp-11-6881-2011.

(48) Lei, Y.; Cheng, S.; Luo, N.; Yang, X.; An, T. Rate Constants and Mechanisms of the Reactions of Cl• and $Cl_2^{\bullet-}$ with Trace Organic Contaminants. *Environ. Sci. Technol.* **2019**, *53* (19), 11170-11182. DOI: 10.1021/acs.est.9b02462.

(49) Zhou, D.; Wu, F.; Deng, N.; Xiang, W. Photooxidation of bisphenol A (BPA) in water in the presence of ferric and carboxylate salts. *Water Res.* **2004**, *38* (19), 4107-4116. DOI: 10.1016/j.watres.2004.07.021.

(50) Sajiki, J.; Yonekubo, J. Degradation of bisphenol-A (BPA) in the presence of reactive oxygen species and its acceleration by lipids and sodium chloride. *Chemosphere* **2002**, *46* (2), 345-354. DOI: 10.1016/s0045-6535(01)00093-5.

(51) Sakamoto, Y.; Zhou, J.; Kohno, N.; Nakagawa, M.; Hirokawa, J.; Kajii, Y. Kinetics Study of OH Uptake onto Deliquesced NaCl Particles by Combining Laser Photolysis and Laser-Induced Fluorescence. *J. Phys. Chem. Lett.* **2018**, *9* (14), 4115-4119. DOI: 10.1021/acs.jpclett.8b01725.

(52) Oum, K. W.; Lakin, M. J.; DeHaan, D. O.; Brauers, T.; Finlayson-Pitts, B. J. Formation of molecular chlorine from the photolysis of ozone and aqueous sea-salt particles. *Science* **1998**, *279* (5347), 74-77. DOI: 10.1126/science.279.5347.74.

(53) DeRieux, W.-S. W.; Li, Y.; Lin, P.; Laskin, J.; Laskin, A.; Bertram, A. K.; Nizkorodov, S. A.; Shiraiwa, M. Predicting the glass transition temperature and viscosity of secondary organic material using molecular composition. *Atmos. Chem. Phys.* **2018**, *18* (9), 6331-6351. DOI: 10.5194/acp-18-6331-2018.

(54) Petters, M. D.; Kreidenweis, S. M. A single parameter representation of hygroscopic growth and cloud condensation nucleus activity. *Atmos. Chem. Phys.* **2007**, *7* (8), 1961-1971. DOI: 10.5194/acp-7-1961-2007.

(55) Shen, C.; Zhang, W.; Choczynski, J.; Davies, J. F.; Zhang, H. Phase State and Relative Humidity Regulate the Heterogeneous Oxidation Kinetics and Pathways of Organic-Inorganic Mixed Aerosols. *Environ. Sci. Technol.* **2022**, *56* (22), 15398-15407. DOI: 10.1021/acs.est.2c04670.

(56) Endo, S.; Pfennigsdorff, A.; Goss, K.-U. Salting-out effect in aqueous NaCl solutions: trends with size and polarity of solute molecules. *Environ. Sci. Technol.* **2012**, *46* (3), 1496-1503. DOI: 10.1021/es203183z.

(57) Hsu, S.-H.; Lin, F.-Y.; Huang, G. G.; Chang, Y.-P. Accelerated Sulfur Oxidation by Ozone on Surfaces of Single Optically Trapped Aerosol Particles. *J. Phys. Chem. C* **2023**. DOI: 10.1021/acs.jpcc.2c06831.

(58) Alves, M. R.; Coward, E. K.; Gonzales, D.; Sauer, J. S.; Mayer, K. J.; Prather, K. A.; Grassian, V. H. Changes in light absorption and composition of chromophoric marine-dissolved organic matter across a microbial bloom. *Environ. Sci. Process. Impacts* **2022**, *24* (10), 1923-1933. DOI: 10.1039/d2em00150k.

(59) You, Y.; Bertram, A. K. Effects of molecular weight and temperature on liquid–liquid phase separation in particles containing organic species and inorganic salts. *Atmos. Chem. Phys.* **2015**, *15* (3), 1351-1365. DOI: 10.5194/acp-15-1351-2015.

(60) Tinel, L.; Dumas, S.; George, C. A time-resolved study of the multiphase chemistry of excited carbonyls: Imidazole-2-carboxaldehyde and halides. *C. R. Chim.* **2014**, *17* (7), 801-807. DOI: 10.1016/j.crci.2014.03.008.

(61) Tinel, L.; Rossignol, S.; Bianco, A.; Passananti, M.; Perrier, S.; Wang, X.; Brigante, M.; Donaldson, D. J.; George, C. Mechanistic Insights on the Photosensitized Chemistry of a Fatty Acid at the Air/Water Interface. *Environ. Sci. Technol.* **2016**, *50* (20), 11041-11048. DOI: 10.1021/acs.est.6b03165.

(62) Aguer, J. P.; Richard, C. Reactive species produced on irradiation at 365 nm of aqueous solutions of humic acids. *J. Photochem. Photobiol. A Chem.* **1996**, *93* (2-3), 193-198. DOI: 10.1016/1010-6030(95)04183-4.

(63) Canonica, S.; Jans, U.; Stemmler, K.; Hoigne, J. Transformation kinetics of phenols in water: photosensitization by dissolved natural organic material and aromatic ketones. *Environ. Sci. Technol.* **1995**, *29* (7), 1822-1831. DOI: 10.1021/es00007a020.

(64) *NCAR/tuv-x: Version 0.2.0*; Zenodo: 2022. (accessed.

(65) Stokes, M. D.; Deane, G. B.; Prather, K.; Bertram, T. H.; Ruppel, M. J.; Ryder, O. S.; Brady, J. M.; Zhao, D. A Marine Aerosol Reference Tank system as a breaking wave analogue for the production of foam and sea-spray aerosols. *Atmos. Meas. Tech.* **2013**, *6* (4), 1085-1094. DOI: 10.5194/amt-6-1085-2013.

(66) Wenk, J.; Graf, C.; Aeschbacher, M.; Sander, M.; Canonica, S. Effect of Solution pH on the Dual Role of Dissolved Organic Matter in Sensitized Pollutant Photooxidation. *Environ. Sci. Technol.* **2021**, *55* (22), 15110-15122. DOI: 10.1021/acs.est.1c03301.

(67) Angle, K. J.; Crocker, D. R.; Simpson, R. M. C.; Mayer, K. J.; Garofalo, L. A.; Moore, A. N.; Mora Garcia, S. L.; Or, V. W.; Srinivasan, S.; Farhan, M.; Sauer, J. S.; Lee, C.; Pothier, M. A.; Farmer, D. K.; Martz, T. R.; Bertram, T. H.; Cappa, C. D.; Prather, K. A.; Grassian, V. H. Acidity across the interface from the ocean surface to sea spray aerosol. *Proc. Natl. Acad. Sci. U. S. A.* **2021**, *118* (2), e2018397118. DOI: 10.1073/pnas.2018397118.

(68) Koop, T.; Bookhold, J.; Shiraiwa, M.; Pöschl, U. Glass transition and phase state of organic compounds: dependency on molecular properties and implications for secondary organic aerosols in the atmosphere. *Phys. Chem. Chem. Phys.* **2011**, *13* (43), 19238-19255. DOI: 10.1039/c1cp22617g.

(69) Shiraiwa, M.; Li, Y.; Tsimpidi, A. P.; Karydis, V. A.; Berkemeier, T.; Pandis, S. N.; Lelieveld, J.; Koop, T.; Pöschl, U. Global distribution of particle phase state in atmospheric secondary organic aerosols. *Nat. Commun.* **2017**, *8* (1), 15002. DOI: 10.1038/ncomms15002.

(70) Collins, D. B.; Zhao, D. F.; Ruppel, M. J.; Laskina, O.; Grandquist, J. R.; Modini, R. L.; Stokes, M. D.; Russell, L. M.; Bertram, T. H.; Grassian, V. H.; Deane, G. B.; Prather, K. A. Direct aerosol chemical composition measurements to evaluate the physicochemical differences between controlled sea spray aerosol generation schemes. *Atmos. Meas. Tech. Discuss.* **2014**, *7* (7), 6457-6499. DOI: 10.5194/amtd-7-6457-2014.

(71) Topping, D.; Barley, M.; Bane, M. K.; Higham, N.; Aumont, B.; Dingle, N.; McFiggans, G. UManSysProp v1.0: an online and open-source facility for molecular property prediction and atmospheric aerosol calculations. *Geosci. Model Dev.* **2016**, *9* (2), 899-914. DOI: 10.5194/gmd-9-899-2016.

(72) Goldsack, D. E.; Franchetto, R. The viscosity of concentrated electrolyte solutions. I. Concentration dependence at fixed temperature. *Can. J. Chem.* **1977**, *55* (6), 1062-1072. DOI: 10.1139/v77-148.

(73) Grunberg, L.; Nissan, A. H. Mixture law for viscosity. *Nature* **1949**, *164* (4175), 799. DOI: 10.1038/164799b0.

Chapter 4 Effects of Relative Humidity and Phase on the Molecular Detection of Nascent Sea Spray Aerosol using Extractive Electrospray Ionization

4.1 Abstract

Online mass spectrometry techniques, such as extractive electrospray ionization time-of-flight mass spectrometry (EESI-TOF), present an attractive alternative for analyzing aerosol molecular composition due to reduced aerosol sample collection and handling times and improved time resolution. Recent studies show a dependence of EESI-TOF sensitivity on particle size and mixing state. This study measured authentic sea spray aerosol (SSA) components generated during a phytoplankton bloom, specifically glycerol, palmitic acid, and potassium ions. We demonstrate temporal variability and trends dependent on specific biological processes occurring in seawater. We found that the EESI-TOF sensitivity, after adjusting for pressure variations at the inlet and normalizing to the reagent ion, critically depends on the sample's relative humidity. Relevant SSA species exhibited heightened sensitivity at an elevated relative humidity near the deliquescence relative humidity of sea salt and poorer sensitivity with sparse detection below the efflorescence relative humidity. Modeling the reagent ion's diffusive depth demonstrates the sample aerosol particle viscosity governs the relative humidity dependence because it modulates the distance the reagent ion diffuses and reacts with components in the particle bulk. Furthermore, the particle's stickiness and coagulation efficiency with the electrospray droplets increase at higher relative humidity. The effects of particle size and mixing state are discussed, revealing improved sensitivity of phase-separated components present along the particle surface. This work highlights the importance of the particle phase state in detecting and quantifying molecular components within authentic and complex aerosol particles and the utility of EESI-TOF for measuring SSA composition.

4.2 Introduction

Sea spray aerosols (SSA) play a crucial role in the climate system by influencing the global radiative budget through the direct and indirect scattering and absorption of solar and terrestrial radiation.[1-6] SSA constitutes the most abundant aerosol by mass in the atmosphere alongside mineral dust,[7, 8] with an estimated global production rate ranging from 3 to 70 Pg yr^{-1}.[8, 9] This mass significantly surpasses anthropogenic aerosols and contributes substantially to the global aerosol burden, providing a considerable amount of cloud condensation nuclei (CCN).[10] Atmospheric models commonly parameterize SSA as pure sea salt.[11, 12] Yet, they are far more chemically and physically complex, encompassing varying mixtures of dissolved and crystalline inorganic salts,[13] dissolved and particulate organic carbon,[14, 15] and whole cells.[16] The proportions of these components vary with particle diameter due primarily to their production method via bubble bursting.[17-19] Though organic matter may not dominate the total SSA mass, it can constitute a significant portion of SSA particles smaller than 1 μm in the ambient marine atmosphere, with film droplets that are primarily organic carbon constituting ~57% of the number concentration of submicron SSA.[17, 18, 20] Moreover, studies show a higher organic carbon mass fraction in ultrafine (<0.1 μm) SSA, with purely organic SSA particles exceeding the SSA particles comprised only of sea salts or sea salts mixed with organic carbon.[17, 18, 21, 22] Identified organic molecules in SSA include free and polysaccharides,[23] lipids and fatty acids,[24, 25] and amino acids.[26, 27] Organic matter can modulate water uptake and the CCN activity of SSA.[4, 28, 29] Therefore, characterizing the molecular composition of SSA and factors such as biological activity altering the organic carbon proportion of SSA particles is crucial for better understanding their indirect radiative effects, the least understood aspect of global radiative forcing.[30]

Several techniques have contributed to the growing knowledge of SSA composition. For example, liquid chromatography coupled with high-resolution mass spectrometry (HRMS) can

detect individual organic molecules and elemental ratios in SSA.[31-33] While highly sensitive, these measurements face challenges such as long sample collection times (between 5 and 12 hours)[34] needed to obtain sufficient particulate mass for detection, storage, incubation, sample extraction, and derivatization.[35, 36] Techniques like Raman[37, 38] and IR spectroscopy[39, 40] focus on identifying specific functional groups and compound classes. These methods can be coupled with microscopy to determine inter- and intra-particle chemical variability with high chemical specificity for the particle's surface,[40, 41] but they focus on a single particle at a time. While such measurements have been critical to understanding SSA composition, in dynamic marine environments with rapidly changing conditions such as variations in water biological activity, air temperature, relative humidity, air mass history, and wave break conditions occurring on short timescales, online methods become indispensable for accurately capturing the temporal variability in SSA composition. Currently, online techniques, such as aerosol mass spectrometry (AMS) and aerosol time-of-flight mass spectrometry (ATOFMS), have been employed for size-dependent chemical composition analysis of SSA particles,[42, 43] but extensive molecular fragmentation prevents unambiguous detection of individual molecules in SSA, necessitating softer ionization approaches.

Extractive electrospray ionization time-of-flight mass spectrometry (EESI-TOF)[44] is a promising yet untested online technique for analyzing SSA chemical composition. During EESI, aerosol components are extracted following collision and coalescence between the aerosol and a charged solvent spray (electrospray). Sample molecules are ionized based on their binding affinity with a reagent ion in the electrospray droplet (commonly Na^+), and the ionized sample molecules are then detected downstream after being heated and evaporated into the gas phase.[45] With the entire EESI process occurring in a fraction of a second, this technique enables high temporal resolution aerosol chemical composition measurements. Operating in positive mode ionization

with Na^+, EESI-TOF has achieved detection limits of 1-10 ng m^{-3} or even lower for some organic molecules.[44-46] While applied in various field studies,[47-51] its application to SSA has been limited, with only one study from this lab conducted thus far.[52]

The exact EESI mechanism is still debated, and although there have been a few studies employing single-component organic aerosols and internally mixed binary-component organic/inorganic aerosols generated in the lab that examined the effects of particle size,[53] component volatility,[54] relative humidity (RH),[44] and particle organic coating thickness[55] on EESI extraction efficiency, none have considered such effects on aerosols sampled in the field or authentic SSA. SSA particles adopt different phase states (viscosities), morphologies, and mixing states that change with RH and biological activity.[22, 52, 56-58] Changes in RH can induce complex multistep phase transitions in SSA.[56] Such changes likely affect the extraction and ionization efficiencies of EESI, e.g., by altering the coagulation efficiency between the aerosol sample and electrospray droplets and the bulk diffusion rates of ions and molecules within the droplet-aerosol mixture. To our knowledge, factors such as particle viscosity and RH-induced phase transitions have not been characterized in how they affect EESI.

This study investigates the effects of sample RH (spanning a range of 20% to 75% near the sea salt efflorescence and deliquescence RH, respectively) and subsequent changes to particle viscosity on the molecular detection of components in authentic SSA produced while inducing a phytoplankton bloom in natural seawater in a wave flume. The study also aims to provide insights into the temporal variations in specific SSA molecular components during the bloom, emphasizing the method's capability to detect and track SSA compositional changes with higher temporal resolution and softer ionization than previous techniques throughout a bloom cycle. This work underscores the importance of the particle phase state in the molecular detection of components

by EESI in authentic SSA, which needs to be considered in other ambient aerosol measurements that use EESI.

4.3 Experimental Section

SSA Generation and Biological Activity Measurements

This study was conducted as part of the Sea Spray Chemistry and Particle Evolution (SeaSCAPE) study in 2019 with the National Science Foundation Center for Aerosol Impacts on Chemistry of the Environment (NSF-CAICE). Comprehensive details of the study can be referred to in previous works,[32, 34, 40, 41, 52, 59-61]with a brief overview provided here. Water was sampled from the Scripps Pier in La Jolla, CA (32° 52' 01.0" N, 117° 15' 25.7" W) on 7/23. The water was filtered using 50 µm Nitex nylon mesh (Flystuff; Cat # 57-106) to remove larger biological species. This water was placed into the 11,800 L, 33 m-long glass tank equipped with fluorescent lamps along the outer walls and a moving paddle to simulate a diurnal solar cycle and generate SSA through wave breaking. A phytoplankton bloom was induced by spiking the water with f/2 growth media and sodium metasilicate. This work focuses explicitly on SSA measurements during the third bloom between 7/31 and 8/9, which generated the largest biomass. Biological activity was monitored by measuring chlorophyll-a concentration via continuous fluorescence (ESP),[62] an indication of algal biomass, bacterial cell counts with a Liquid Spot Sampler (SS110A, Aerosol Devices Inc) and flow cytometry, and dissolved organic carbon (DOC) concentrations with a Shimadzu TOC-V_{CSH} catalytic combustion oxidation instrument.

Sampling Apparatus and Conditions

The sampling apparatus and conditions followed the details outlined in Tumminello et al., 2021.[52] Briefly, filtered air was supplied to the wave flume's headspace to prevent outside contamination, and the headspace air was drawn through one silica gel diffusion dryer and into our sampling setup at a flow rate of 5 L min^{-1}. A Pyrex flow tube (inner diameter of 5 cm and 50 cm

long) facilitated the mixing and equilibration of particles at the tube's RH, adjusted by varying zero air (747-30, AADCO) flows through a bubbler containing pure water or a "dry" bypass sampling line. These RH values were measured by an inline RH/temperature sensor (Sensirion AG). The sample flow was split for particle size and composition analysis, passing through a honeycomb-type activated charcoal denuder to remove volatile hydrocarbons before entering the mass spectrometer inlet, as shown in Figure 4.1. Two two-way valves directed the flow either directly into the inlet or through two particle filters connected in series (HEPA Capsule Versapor, 99.97% efficiency for 0.3 μm) for a background, or "blank" measurement. Filter blanks were taken at the start of every measurement period at four flow settings to modulate RH (20 min total, 5 min each). Then the sampling and long RH cycles began (1 hr at each setting, four settings total), also shown in Figure 4.6. SSA size distributions were measured every two minutes with a Brechtel scanning electrical mobility sizer (SEMS; Model 2100; size range of 5 nm to 850 nm across 100 size bins). Measurements occurred in approximately three to four (dependent on start time) subsequent 4-hour cycles overnight (8-11 P.M. to 7-8:30 A.M. local time), systematically adjusting between four RH regimes within a cycle from a maximum RH of ~75% to a minimum RH of ~20%, covering a range that extended to the deliquescence RH (DRH) (~75%) and below the efflorescence RH (ERH) (~44%) of NaCl. We categorized RH into four regimes depending on the wet-to-dry flow ratio: 20-35%, 35-50%, 50-65%, and 65-75%.

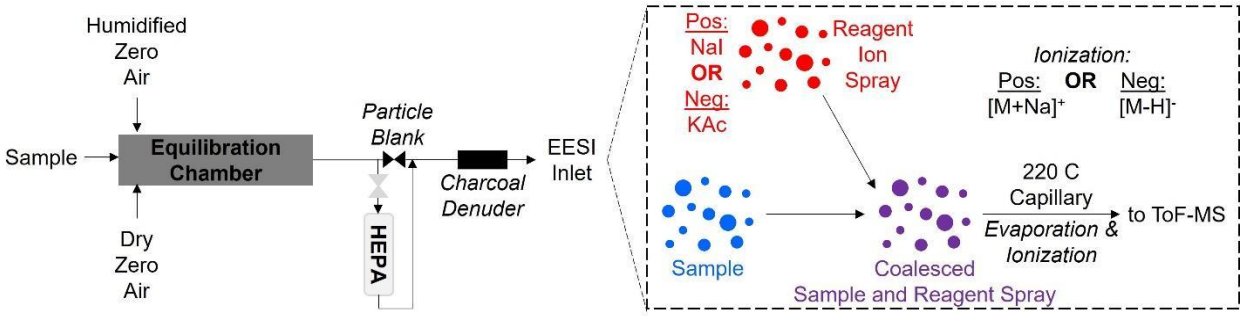

Figure 4.1 EESI-TOF sampling apparatus and visualization of the ionization mechanism

EESI-TOF Description

The nascent SSA molecular composition was measured using an extractive electrospray ionization time-of-flight mass spectrometer (EESI-TOF; Aerodyne Research Inc. and Tofwerk AG). EESI involves exposure of the aerosol sample to suspended electrospray droplets, resulting in a signal proportional to the mass concentration of components in the aerosol phase.[44, 47, 48, 50, 52, 63, 64]The reagent ion spray was generated by passing the reagent solution through a 365 μm OD fused silica capillary (IDEX Health and Science, LLC) at a pressure of 350 mbar. It was charged at −2500V in negative mode and +2500V in positive mode. The reagent solution for negative mode consisted of 50% (by mass) H_2O (18 mΩ, Millipore Synergy System) and 50% acetonitrile (≥99.95%, Fisher Chemical) spiked with 100 ppm potassium acetate (99%, Sigma-Aldrich), resulting primarily in ionization by deprotonation $[M-H]^-$. In positive mode, the reagent solution consisted of 50% acetonitrile (≥99.95%, Fisher Chemical) and 50% H_2O spiked with 100 ppm sodium iodide (99%, Sigma-Aldrich), which ionized the sample by clustering with sodium $[M+Na]^+$. Negative and positive mode EESI-TOF measurements were conducted, but only positive mode results are described here because of their broader coverage throughout the measurement period. The aerosol was sampled at 1 liter per minute (LPM), mixed with the reagent ion spray, and heated to 220 °C before detection by the TOF mass analyzer.[46]

Mass Spectra Data Processing

The mass spectra were processed using Tofware (Version 3.3.0, Aerodyne Research Inc. and Tofwerk AG) in IGOR 9 (Wavemetrics). Files with 1-second time resolution were averaged in 60-second increments before further high-resolution analysis. After data processing, there was <10 ppm error in the mass calibration and a resolution of ~5000 m/Δm in negative mode for *m/z*=59.013853 (CH_3COO^-) and ~5500 in positive mode for *m/z*=22.989221 (Na^+). Chemical formulae were determined using a pre-determined peak list based on compounds previously identified in SSA (Table S1) and the formula generator developed by Stark et al. 2015.[65] The generator allowed for all combinations of C, H, O, and N with *m/z* in the range from 50 to 400, with maximum oxygen-to-carbon ratios (O:C) of 2, double bond equivalences (DBE) from 0 to 1, and minimum hydrogen-to-carbon ratios (H:C) of 0.5.[65, 66] Due to some clustering between molecular ions and the acetonitrile organic solvent, which could flag as false positives for CHON compounds when they are possibly CHO compounds clustered with acetonitrile, all nitrogen-containing elemental formulae were omitted from the peak list, except for those with the same formulae as amino acids previously measured in SSA.[27]

Peaks were identified as present if their mass accuracy was within 15 ppm and intensities were above the limit of detection, determined by the area near the peak, as done in Lopez-Hilfiker et al. 2019.[44] It is important to note that some volatile components that transmit through the charcoal denuder and break through the particle filters used for blank measurements can dissolve into or become solvated in the electrospray and lead to elevated background levels.[48] The filters and denuder were new as of the start of the study and regularly cleaned by flushing with dry zero air and, for the charcoal denuder, baking it in an oven at 150 °C. Detected molecular ions were filter-blank subtracted and normalized to the background Na^+ reagent ion intensity at the

corresponding RH without further corrections, mitigating interferences from gas breakthrough, Na^+ in SSA, and accounting for potential sensitivity differences with varying RH.

4.4 Results and Discussion

Temporal Trends and Variability in Measured SSA Components with Changing Seawater Biology

This section elucidates the temporal trends and variability in tracer components within nascent SSA measured by EESI-TOF. We focus on the temporal behavior and enrichment during a controlled phytoplankton bloom of K^+, palmitic acid, and glycerol, which are representative components in nascent SSA that depend on seawater biological activity.[23, 24, 67, 68]

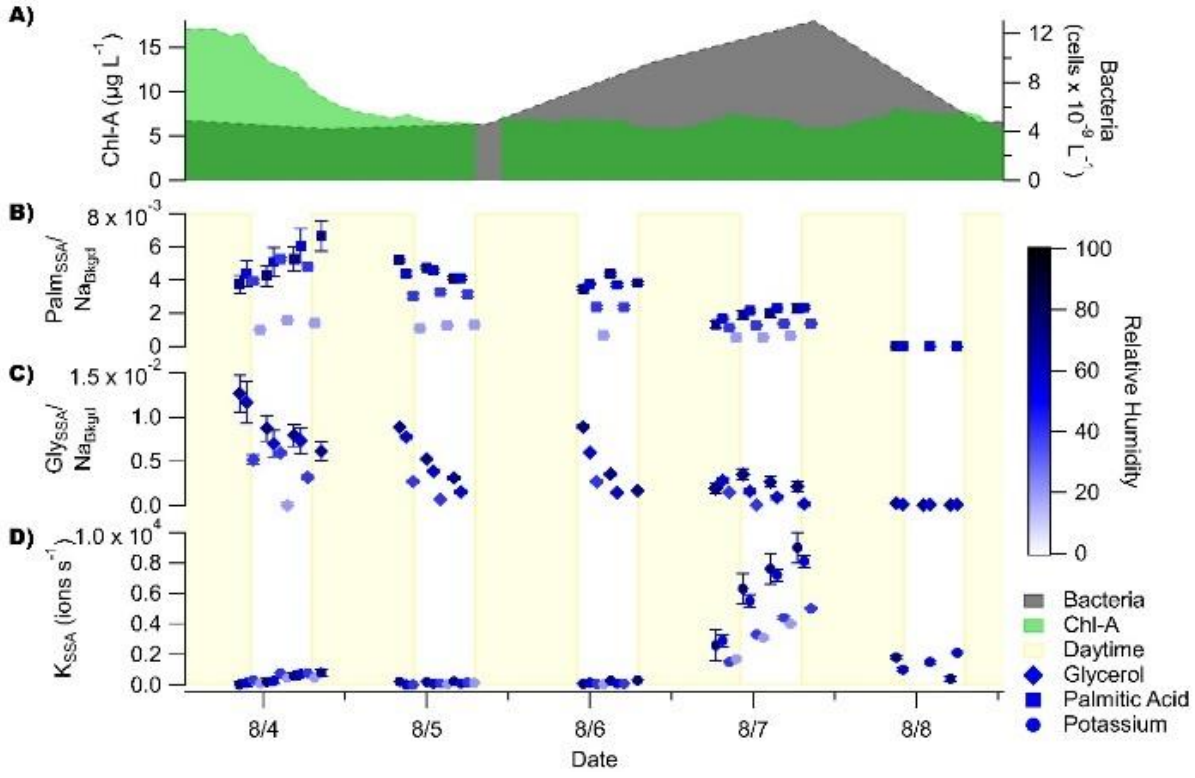

Figure 4.2 Time series of (A) chlorophyll-a concentrations in μg L^{-1} (green) and bacterial cell counts in cells x 10^{-9} L^{-1} (gray). Hourly-averaged normalized intensities of (B) palmitic acid (squares) (C) glycerol (diamonds), and (D) potassium (circles).

Marine biological activity can be assessed through various biological markers, as depicted in Figure 4.2A. This section provides a brief overview of the results concerning these markers, with a more comprehensive analysis in Sauer et al. 2022.[34] Chlorophyll-a is the primary marker

for monitoring phytoplankton growth, as they produce chlorophyll-a to capture sunlight energy. While phytoplankton can generate different types of chlorophyll, measurements of chlorophyll-a remain the most reliable indicator of overall phytoplankton growth.[69] Diatoms (mainly *Skeletonema* sp. and *Cylindrotheca* sp.) and diatom aggregates (mostly *Cylindrotheca* sp. and *Navicula* sp.) dominated the phytoplankton communities in this study.[34] Following the phytoplankton bloom, there was an extended period of senescence after 8/5, succeeded by a surge in bacteria, as confirmed by bacterial cell counts, a characteristic feature of post-bloom conditions established in prior research.[34, 70] Table 1 shows the r^2 values for each identified compound versus the chlorophyll-a concentration and bacterial cell counts, with the correlation plots in Figure 4.10.

Table 4.1 Correlation coefficients (R^2 values) for the linear regression analysis of chlorophyll-a and bacteria cell counts with palmitic acid, glycerol, and potassium.

	Palmitic Acid	Glycerol	Potassium
Chlorophyll-A	0.06	0.48	0.11
Bacteria	0.05	0.11	0.62

Figure 4.2B shows the temporal variability in $C_{16}H_{32}O_2Na^+$ (*m/z*=279.229451), tentatively identified as palmitic acid, the predominant saturated fatty acid in nascent SSA at concentrations between 20 and 214 ng m^{-3}.[14, 24] The highest palmitic acid levels in SSA coincided with the end of the chlorophyll-a peak on 8/4, diminishing as the bacterial levels increased. It is unclear if the palmitic acid levels in nascent SSA were greater in earlier stages of the phytoplankton bloom before the positive mode EESI-TOF measurements, but studies show an increase in fatty acid concentration within SSA after nutrients are exhausted during a phytoplankton bloom.[24, 25] In a diatom-dominated bloom, palmitic acid and other 16-carbon fatty acids are produced by the phytoplankton,[71] potentially increasing palmitic acid levels in SSA near the chlorophyll-a peak's end. Following the peak, palmitic acid levels decreased, then decreased more rapidly as the

bacteria grew on 8/6 and 8/7. This decline may result from its usage by bacteria, as all bacteria can incorporate exogenous fatty acids for use in the β-oxidation cycle to yield acetyl-coenzyme A, which the bacteria can then use to make phospholipids to build the cell membrane.[72] The decreasing trend in palmitic acid across the bloom did not align with the total SSA volume, surface area, or number concentration trends, which remained relatively stable except when the lamps were on (Figure 4.11). Additionally, the concentrations of palmitic acid did not strongly correlate with chlorophyll-a or bacteria (r^2=0.06 and 0.05, respectively). Although previous work suggests a diel cycle in SSA production,[73-76] our study lacked sufficient measurements during lamp-on periods to identify any diurnal trend in SSA composition.

Figure 4.2C shows the temporal variability in $C_3H_8O_3Na^+$ (*m/z*=115.036565), tentatively identified as glycerol due to it having no naturally occurring structural isomers, its prevalence in marine biota,[77] and SSA.[78] Glycerol, a small saccharide and the backbone of triglycerides and phospholipids, showed decreasing levels in nascent SSA from 8/4 to 8/8. However, unlike palmitic acid, glycerol exhibited consistently higher signals at the start of the night, decreasing through the night during all five nighttime measurement periods. Glycerol, a byproduct of photosynthesis,[79] can be exuded by phytoplankton into surrounding water, varying in quantity with phytoplankton type.[80-83] As photosynthesis stops once the wave flume lights are turned off, glycerol levels decrease. This could explain the glycerol signal decay throughout the nighttime sampling period and the better correlation between glycerol and chlorophyll-a (r^2=0.48), as chlorophyll-a reflects the photosynthetically active phytoplankton abundance. Additionally, bacteria can metabolize glycerol for energy, potentially explaining the near-zero glycerol signal by the end of the bloom following the bacterial spike on 8/7.[84]

Figure 4.2D presents temporal variability and trends in K^+ in SSA (detected at *m/z*=38.963158), with K^+ confirmed by its isotopic abundance in the mass spectra (Figure 4.12). K^+ is known to be enriched relative to Na^+ in SSA compared to seawater.[17, 23] The signal remained relatively low and stable immediately following the bloom but subsequently increased, coinciding with gradual bacterial growth after 8/5 (r^2=0.62). A similar trend in K^+ enrichment relative to Na^+ was observed in Jayarathne et al. 2016,[23] coinciding with the maxima in chlorophyll-a and bacterial cell counts. This enrichment was attributed to the complexation of cations with dissolved organic carbon components at the sea surface, including oligo/polysaccharides selectively transferred in SSA. Such cation enrichment has been observed in other studies.[85, 86] While Mg^{2+} and Ca^{2+} in SSA are expected to be enhanced alongside K^+, they were not detected in this study, possibly because the TOF mass analyzer was tuned to Na^+-ion adducts and not to doubly charged species like Mg^{2+} and Ca^{2+}.

Local changes in water pH could influence these observations, as pH can affect complexation.[87, 88] Flynn and Mitra et al., 2023, demonstrated that phytoplankton activity can impact local pH, where growth leads to increased pH due to CO_2 uptake, and subsequent heterotrophic consumption results in decreased pH.[89] Throughout this phytoplankton bloom, the average pH of the bulk water increased from ~7.9 on 7/31 to as high as ~8.3 at peak chlorophyll-a concentration on 8/4 and 8/5, followed by a subsequent decrease in pH, as shown in Figure 4.8. The pH of the sea surface microlayer (SSML) remained relatively stable between 7/31 and 8/5, decreasing following the bloom from a high of ~8.0 on 8/5 to a low of ~7.7 as the bacteria grew in. Hakim et al. 2019 indicated that pH can influence the complexation of cations with DOM, where an increase in pH, especially above the pKa of DOM, enhances binding between anionic forms of the organic carbon and divalent cations.[90] Considering that previous work shows 60% of

marine DOM exhibits carboxylic-like pKa values of 3.6 and 4.8,[87] we conjecture that the increase in K^+ in SSA coinciding with the peak in bacteria cell counts could be due to a smaller proportion of K^+ bound to anionic forms of DOM in the SSML at the lower pH, effectively "releasing" the carbon-bound K^+ and forming free K^+ in SSA, which becomes detectable by EESI.

Relative Humidity Effects

Substantial variations in the EESI-TOF intensity for specific ions (normalized to the background reagent Na^+) were noted in response to changes in the sample RH, as shown in the color scale of Figure 4.2. We illustrate this further in Figure 4.3A for palmitic acid during a representative measurement cycle, showing a significant decrease in the reagent ion-normalized signal as the RH was stepped down from ~70% to ~20%. As shown in Figure 4.9, changes in intensity were evident in nearly all signals associated with SSA with varying RH, with less signal variability (i.e., relative error) for ions at lower m/z and elevated RH. For the majority, though not all, of the identified MS peaks, intensities were prominent under elevated RH, while most approached background levels or were undetected (i.e., below background) at RH < 40%.

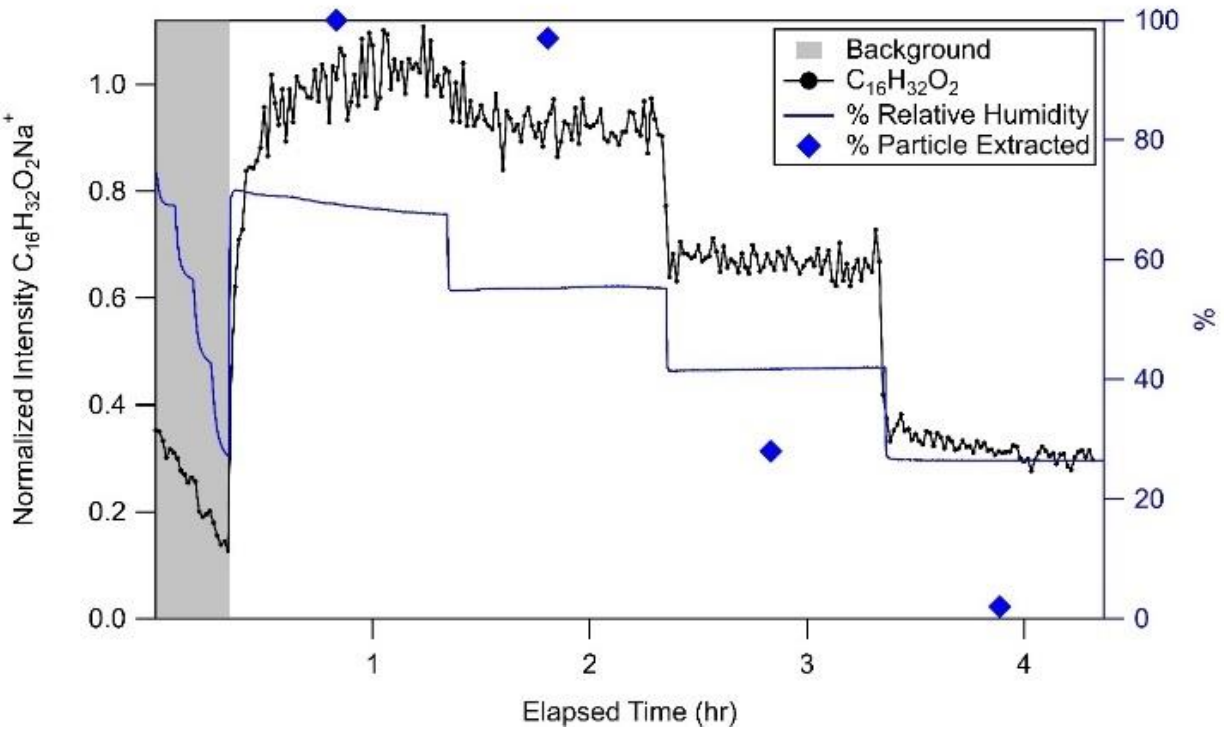

Figure 4.3 (A) Example temporal profile of the normalized $C_{16}H_{32}O_2Na^+$ (palmitic acid) intensity with changing relative humidity (black). The background measurement period is highlighted in the gray-shaded region. The measured relative humidity is indicated in the blue trace. The blue diamonds show the calculated particle extraction (%) from Eq. 2

Figure 4.4 shows an intercomparison of the detection frequencies and normalized signal intensities from the hourly-averaged palmitic acid, glycerol, and K^+ data presented in Figure 4.2 for each RH range, considering the full measurement period. Despite the effects on their signal intensities due to changing biological activity, the most significant and reproducible impact was due to sample RH. In Figure 4.4A, we present the fraction of the hourly-averaged samples detected above background. Detection frequencies increased for all three ions with increasing RH, with glycerol demonstrating the most substantial increase from ~0% detection frequency at 20% RH to 100% detection frequency at 70% RH. In contrast to glycerol, K^+ and palmitic acid were still detected in about half of the measurements at 20% RH. These trends also held in terms of their normalized signal intensities shown as averages at the different RH ranges in Figure 4.4B. Both glycerol and palmitic acid exhibited significantly greater average ion intensities with increasing

RH across the bloom. In comparison, K^+ showed some but insignificant enhancement in signal with increasing RH.

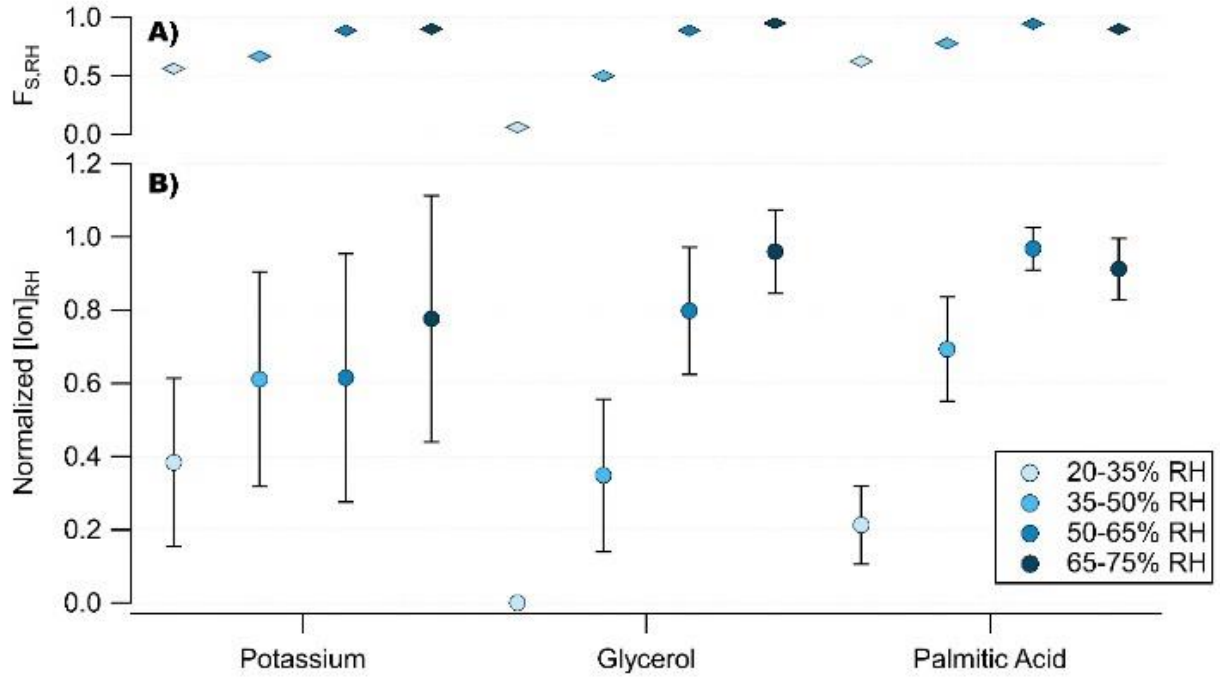

Figure 4.4 Variations in (A) detection frequency and (B) average normalized intensities of potassium, glycerol, and palmitic acid at different sample relative humidity ranges.

In the study by Lopez-Hilfiker et al. 2019 using EESI-TOF, insignificant perturbations in the MS intensities were observed for homogeneously nucleated alpha-pinene secondary organic aerosol (SOA) components in the RH range between 0% and 80%, with most showing no perturbation at all.[44] We hypothesize that the change in RH can influence EESI-TOF sensitivity primarily in two ways: (1) the change in RH modulates the particle size of mostly water-soluble or hygroscopic aerosol particles, i.e., "shrinking" the particles with decreasing RH and "growing" the particles with increasing RH, affecting the coagulation efficiency between the sample aerosol particles and electrospray droplets, and (2) RH-induced phase transitions that modulate the aerosol's sticking probability or coagulation efficiency with the droplets and distance that

components in the sample aerosol and the reagent ion (e.g., Na^+) in the electrospray droplet must diffuse before they interact. These two pathways are explored further in the following sections.

Particle Size Effects

As depicted in Figure 4.11, throughout the study, the surface area-weighted diameter varied with RH, ranging from 180(±10) nm to 239(±15) nm across the phytoplankton bloom, generally exhibiting a stepwise decrease in diameter between the highest and lowest RH. In Gallimore and Kalberer, 2013, the EESI-TOF response to components in purely organic aerosol particles was linear for particles with mobility diameters ranging from 70 nm to 200 nm.[46] In contrast, Lee et al. 2021 reported a significant and non-linear increase in the EESI-TOF sensitivity as the particle diameter decreased from 300 nm to 30 nm for organic-coated NH_4NO_3 particles.[53] They attributed the heightened sensitivity for smaller particles to differences in the coagulation rates between the sample aerosol particles and electrospray droplets, estimated from the Brownian coagulation coefficient,[91] calculating a coefficient of ~1 for 100 nm particles and ~10 for 30 nm particles. This translated to a 30x increase in sensitivity for the 30 nm particles compared to the 100 nm particles in that study. Furthermore, the coagulation coefficient varies dramatically and decreases above 100 nm. It is proposed that this variation is due to a reduced coagulation rate between the electrospray droplets (ranging from 0.5 to 5 μm) with larger sample aerosol and that a decrease in the difference between the size of the electrospray and the aerosol sample leads to a reduced coagulation rate. Without direct measurement of the electrospray droplet size distribution, these impacts remain unknown for other EESI-TOF measurements. However, based on the results in Lee et al. 2021, 200 nm particles, approximately the size of the peak number-weighted SSA particles measured here, have one to three times lower coagulation efficiency than 100 nm particles.[53] In this study, the decrease in the sample aerosol particle size at the lower RH is expected to enhance sensitivity because of the greater anticipated coagulation efficiency between smaller

aerosol particles and larger electrospray droplets. Despite the anticipated increase in sensitivity with decreasing particle size with lower RH, the opposite is observed – a marked decrease in sensitivity for most aerosol components at the lower RH. This suggests that the change in particle size with RH was either too small to influence coagulation rates significantly or that another RH-dependent mechanism is responsible.

Viscosity effects

A different explanation is the increased mobility of reactants resulting from the reduced SSA particle viscosity at higher RH.[22, 40, 52] This would heighten diffusive mixing and facilitate interactions between Na^+ at the particle surface and the molecular components in nascent SSA, akin to the enhanced reaction probabilities between molecules at the particle interface and in the bulk of lower viscosity aerosols at higher RH.[63, 92-94]

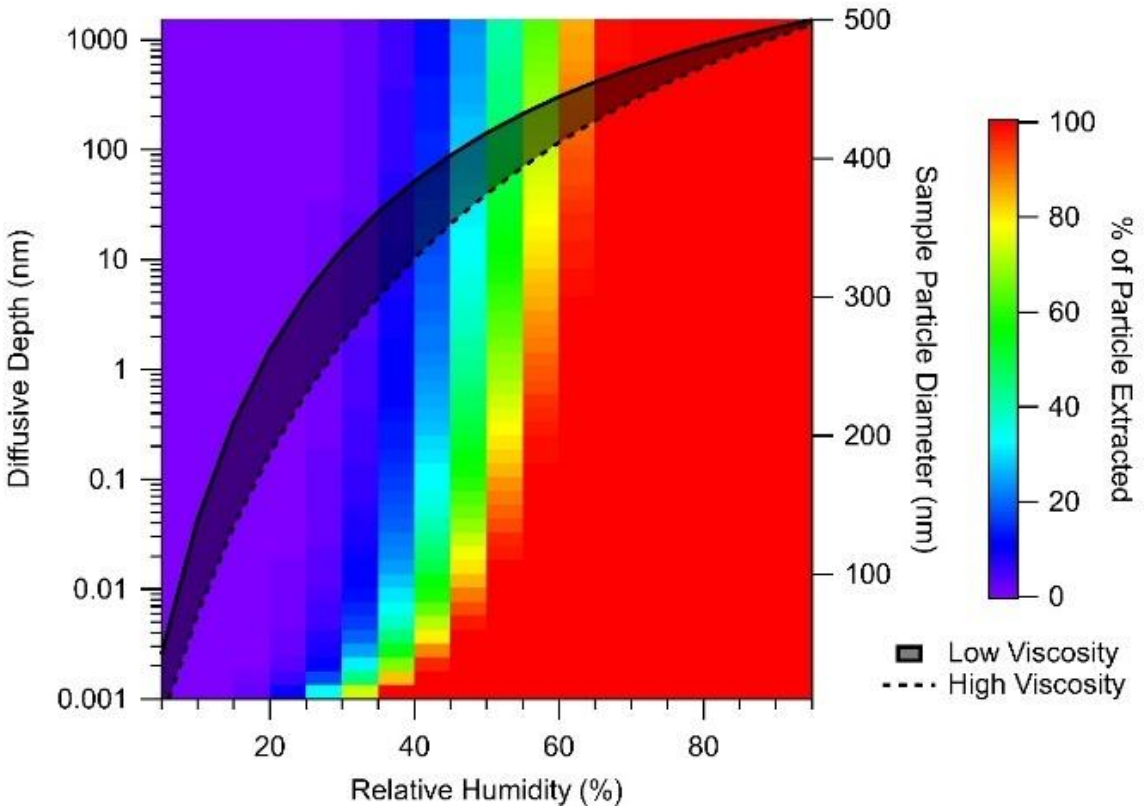

Figure 4.5 Modeled diffusive depths of the reagent ion, Na^+, in SSA particles at different particle diameters and as a function of relative humidity according to the relative humidity-dependent SSA viscosities reported in Tumminello et al., 2021, which was conducted jointly with this study. The color scale is the estimated percent particle volume extracted according to Eq. 2.

To examine the influence of RH-dependent viscosities on the diffusion and reaction between the Na^+ reagent ion and components in the particle phase, we modeled the "diffusive depth" of Na^+ entering an SSA particle between an RH of 5% to 95% in Figure 4.5. The modeled diffusive depth represents the solution to the Stokes-Einstein equation under the assumption of atomic radii for Na^+ and the maximum residence time of a particle within the EESI-TOF inlet, as shown in Eq. 4.1:

$$Depth = \sqrt{t * \frac{k_b T}{6\pi\eta r}} \qquad \text{Eq. 4.1}$$

Here, t represents the residence time inside the EESI-TOF inlet (16.96 milliseconds), k_b is the Boltzmann constant, T is the ambient temperature (K), η is the particle viscosity (Pa·s)

estimated from Tumminello et al. 2021 for SSA, and r is the ionic radius of Na^+ of 1.02×10^{-10} m. η of SSA was taken directly from the estimated η for the organic carbon reported in Tumminello et al. 2021.[52] On the higher end, the η of SSA was estimated to range from 9.14×10^{10} Pa·s at 5% RH to 1.88×10^{-3} Pa·s at 95% RH, coinciding with the peak in chlorophyll-a, and between 5.58×10^{9} Pa·s at 5% RH to 1.55×10^{-2} Pa·s at 95% RH on the lower end, during a period of low biological activity. Other particle properties, e.g., solubility, surface tension, morphology, mixing state, and localized differences in pH and concentration of other reactants between the particle surface and bulk might also play a role in the mass transfer of components.[95] Therefore, the reported diffusive depths are treated as estimates to demonstrate viscosity's effects on mass transfer. If components at the particle surface dissolve into the electrospray droplet upon collision with the droplet, the Na^+ ion will likely interact with and diffuse to greater depths in the particle than predicted by this model. The reported mixing depths may serve as a lower limit in such cases. Figure 4.5 illustrates these outcomes as a function of RH. At a relatively low RH of 20%, Na^+ is estimated to penetrate the particle only to within 1 nm from the surface (black curve), while at a relatively high RH of 70%, the depth is around 200 nm, i.e., diffusing completely through the sample particle in the time the particles spend in the EESI inlet. While the modeled diffusive depth is independent of the sample's particle size, fewer molecules in larger particles will interact with Na^+ than in smaller ones with the same viscosity. To illustrate these different size-related effects, we can estimate the percentage of the sample aerosol particle volume extracted for spherical particles (Eq. 4.2), approximating the thickness of the particle layer extracted as the diffusive depth.

$$\%\, Volume\ Extracted = \frac{r_s^3 - (r_s - d)^3}{r_s^3} * 100 \qquad \text{Eq. 4.2}$$

In Eq. 4.2, r_s is the sample particle radius (nm), and d is the diffusive depth (nm). For a nascent SSA particle with a mobility diameter of 211.5±15.4 nm, the estimated percent volume of

the particle extracted and ionized by Na^+ is ~1.8% at 25% RH and 100% at 70% RH. This closely follows the relative palmitic acid signal intensity trends with RH shown in Figure 4.3A (blue diamonds). This implies that in this study's sample RH range and the size range of SSA, increasingly smaller volume fractions of the nascent SSA were extracted and measured by the EESI-TOF with decreasing RH and that the extraction depends on the viscosity.

Potential Combined Effects of Viscosity and Particle Morphology on the Coagulation Efficiency and Extraction of Palmitic Acid, Glycerol, and K^+ in SSA

The ionization of glycerol and palmitic acid in SSA by EESI necessitated Na^+-adduct formation. Due to the lower η of SSA at elevated RH, we attribute the heightened detection frequencies at the higher RH to greater diffusivity and mixing of Na^+ with glycerol and palmitic acid. In addition, the less viscous, or stickier, SSA particles are expected to exhibit less bounce off and, thus, greater coagulation efficiency with the electrospray droplets with increasing RH,[96-98] promoting interactions between the molecules and reagent ion during EESI. As shown in Figure 4.13, within the post-bloom period (between 8/5 and 8/9), the measured SSA particle bounce fractions, a proxy for particle viscosity,[52] were inversely proportional to the normalized intensities of all three ions. Within the peak bloom period (8/2 to 8/5), the highest normalized intensities coincided with the minimum bounce fraction and the smallest with the maximum bounce fraction. Although no clear or robust dependence between signal intensity and bounce fraction absolute values could be made, these results further indicate that less bouncy or stickier SSA particles yield higher detection frequencies and signal intensities with EESI-TOF compared to their bouncier counterparts at a lower RH.

Furthermore, particle morphologies were investigated with atomic force microscopy during SeaSCAPE for the same bloom, demonstrating an increasing number of larger core-shell SSA particles with solid-like organic shells across the bloom at the lower RH of 20% compared to

an RH of 60%.[40] Such phase separation is common in SSA[22, 40, 56, 99] and may facilitate interactions between molecules at the particle surface and the EESI reagent ion. The observation that EESI demonstrates greater specificity for extracting and ionizing molecular components at the particle surface is not novel. Kumbhani et al. 2018 found minimal signal for $NaNO_3$ in the particle core and mostly glutaric acid from the particle surface for $NaNO_3$ particles coated with glutaric acid.[55] However, a substantial sampling of malonic acid and the glutaric acid core occurred, with malonic acid coating on glutaric acid particles.[55] As a surfactant, palmitic acid has a greater surface activity than glycerol, which could explain the higher detection frequencies for palmitic acid than glycerol at the lower RH. By a different mechanism, K^+ can be enriched at the surface of nascent SSA.[24, 100] Because K^+ is already ionized and does not require Na^+ ions to diffuse within the particle and react, less change in the K^+ signal intensity with RH was observed.

4.5 Conclusions

This study demonstrates the capability of the EESI-TOF method for measuring components in nascent SSA, namely palmitic acid, glycerol, and K^+. The finer temporal resolution enabled key new findings in our understanding of SSA molecular composition: (1) K^+ in SSA correlated with bacteria levels in seawater, possibly from complexation with anions in the DOC, and did not correlate with chlorophyll-a, (2) palmitic acid did not strongly correlate with either chlorophyll-a or bacterial cell counts but generally decreased in intensity as the chlorophyll-a concentrations in seawater decreased, and (3) glycerol correlated with chlorophyll-a, decreasing with time after the lamps were turned off. The different K^+, palmitic acid, and glycerol levels in SSA at different bloom periods could be important for understanding the evolution of SSA CCN activity throughout the bloom. Glycerol and other polyols are relatively hygroscopic organic compounds.[101] While palmitic acid is poorly soluble in water, it is surface active and, hence, expected to increase CCN activity via the Kelvin effect by suppressing the droplet's surface tension. In Tumminello et al.,

2021, we observed this effect where the SSA CCN activity remained elevated even with a greater organic carbon mass fraction during the peak of the phytoplankton bloom.[6]

The impact of RH on sample extraction via the EESI-TOF method is significant, depending on the sample aerosol's size, viscosity, and morphology. Within the context of SSA, imaging of different authentic SSA particles has demonstrated that phase separation occurs in SSA in as many as six multistep phase transitions upon changes in RH.[22, 56] EESI extraction depends upon the ambient RH as shown here, and particle properties such as viscosity, and processes such as phase separation that depend on RH could critically impact the ability to detect molecular components by EESI-TOF, emphasizing the need for understanding the EESI extraction mechanism more precisely for different particle phases and multiple phases together. Phase-separated or core-shell-type particles, like the mixed glutaric acid/$NaNO_3$ particles studied in Kumbhani et al., 2018, and those common to SSA at a low RH,[22, 40, 52, 56] favor the extraction of components from the particle surface. On the other hand, well-mixed and deliquesced organic carbon/aqueous electrolyte particles with low viscosity, such as the nascent SSA near the deliquescence RH of sea salt,[52] favor complete extraction and ionization of the particles. Future work should also focus on the role of phase in other aerosol systems, e.g., in SOA, which undergoes liquid-liquid and liquid-solid phase transitions depending on the aerosol's composition and ambient RH.[95, 102]

The impact of phase on EESI is expected to be more relevant in detecting components in larger particles when the particle diameter is greater than the diffusive depth of the reagent ion. In the case of SSA, this suggests that the components in film droplets, which are smaller than jet droplets,[18] potentially have a higher probability of complete extraction based on their smaller size, contingent on particle viscosity. Our results suggest that studies quantifying molecular components in ambient aerosols with EESI-TOF could be underestimated, mainly if the ambient RH is lower

(or the particles are more viscous) than when calibrated. These results highlight the importance of knowing the aerosol sample's physicochemical properties (i.e., phase state, viscosity, and morphology) for meaningful analysis of the results.

4.6 Supplemental Information

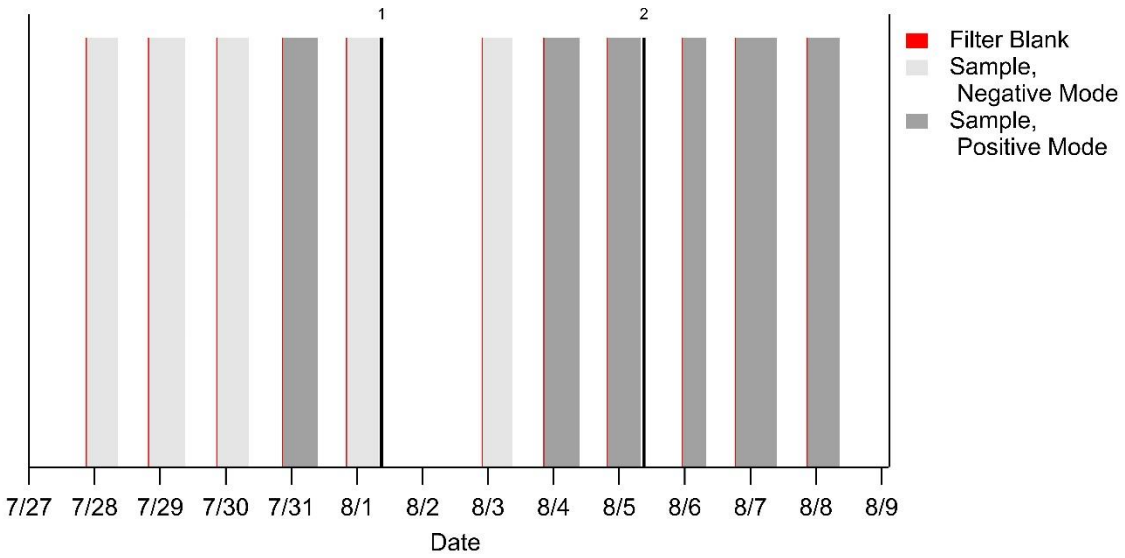

Figure 4.6 Time series of the sampling periods for positive (dark grey) and negative (light grey) mode, including filter blanks (red). The times of three major events (black lines) during the bloom are included.[34] Line 1 corresponds to the outdoor tank being added to the waveflume. Line 2 corresponds to the scraping of the waveflume walls.

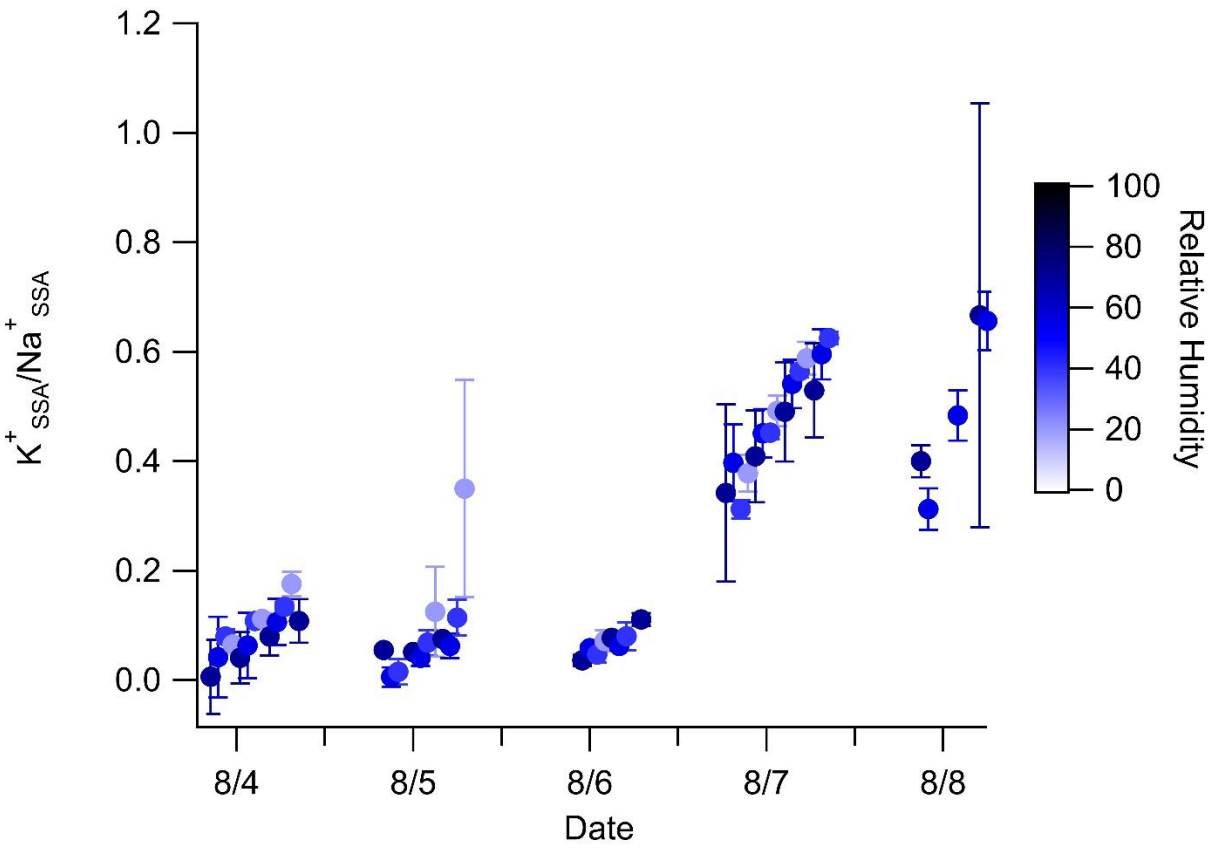

Figure 4.7 Time series of background-subtracted potassium signal normalized to the background-subtracted sodium signal. The blue color scale (white at 0% and black at 100%) represents the relative humidity (%).

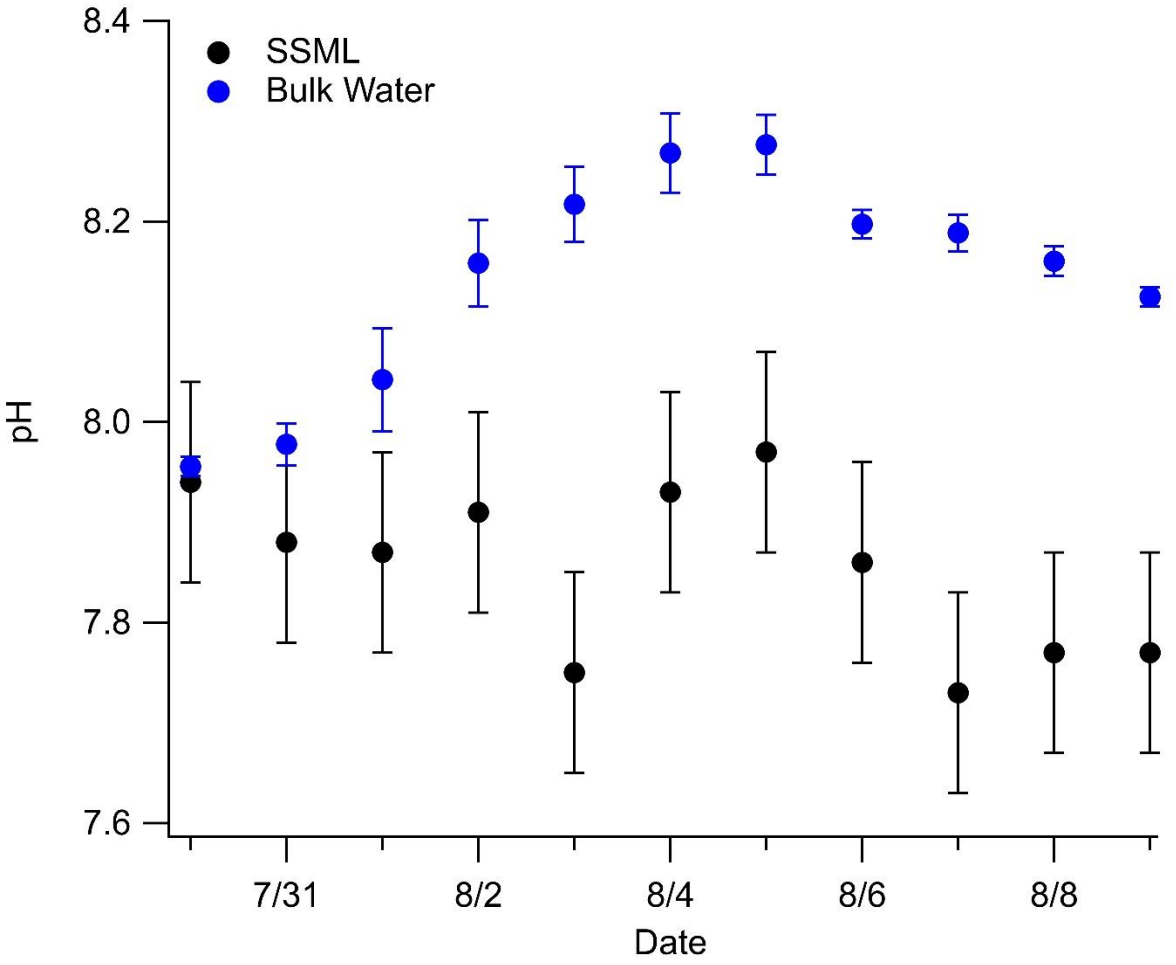

Figure 4.8 Time series of the daily average pH for the bulk water of the flume (blue circles) and the SSML (black circles).

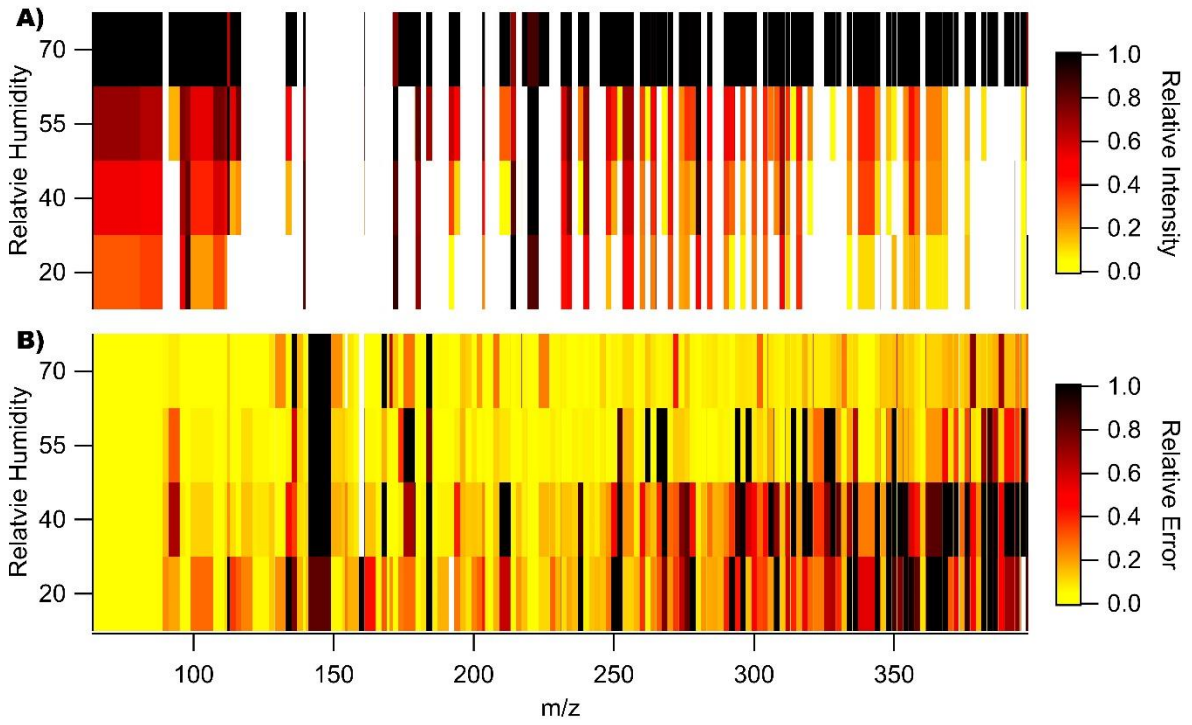

Figure 4.9 (A) Heat map of the relative intensity (yellow at zero and black at one) for each m/z identified during the same period as Figure 3, normalized to the maximum for each m/z. (B) Heat map of the relative error (yellow at zero and black at one) m/z identified during the same period as Figure 3.

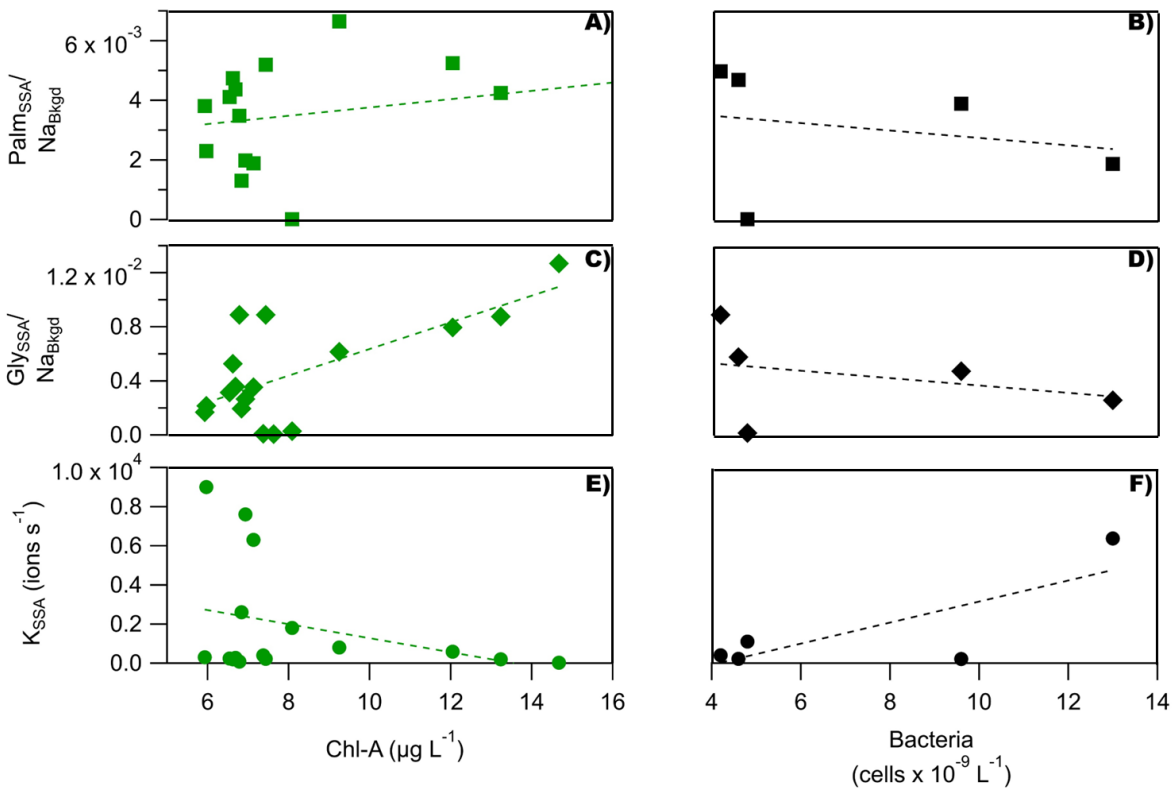

Figure 4.10 Correlation plots between normalized palmitic acid signal and (A) chlorophyll-a (green squares) and (B) bacteria (black squares), normalized glycerol signal and (C) chlorophyll-a (green diamonds) and (D) bacteria (black diamonds), and potassium signal and (E) chlorophyll-a (green circles) and (F) bacteria (black circles)

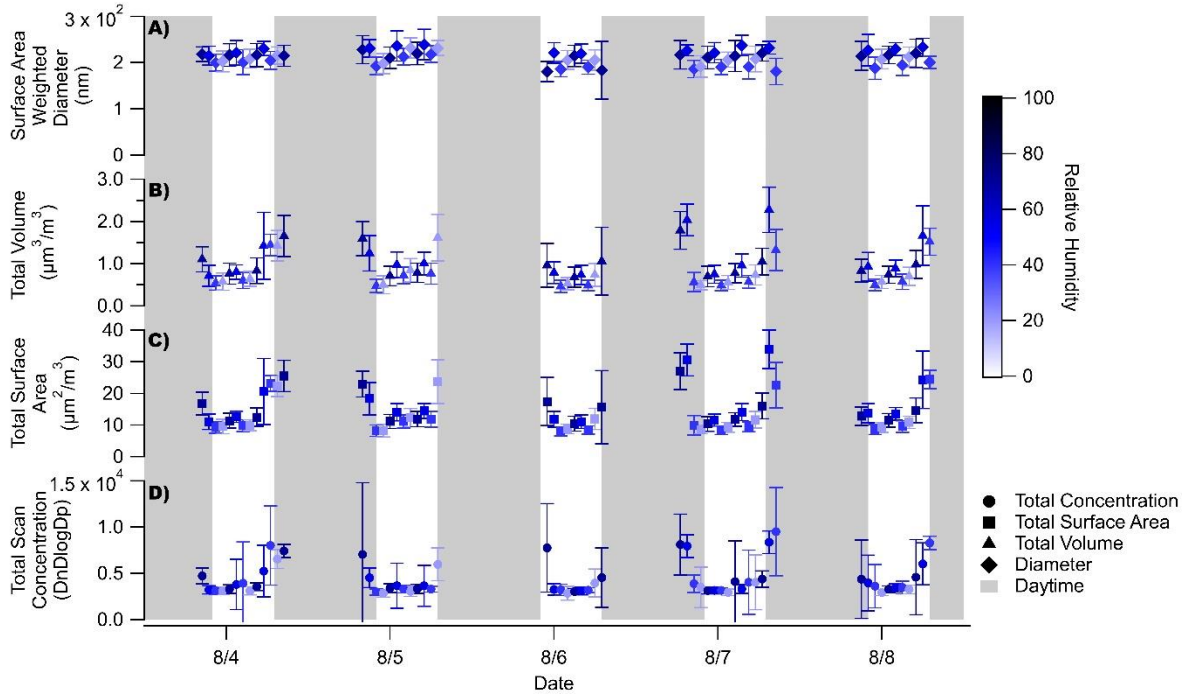

Figure 4.11 Time series of the hourly average (a) total scan concentration (circles), (b) total surface area (squares), (c) total volume (triangles), and (d) surface area weighted diameter (diamonds). The blue color scale (white at 0% and black at 100%) represents the relative humidity during each period. The grey shading represents daytime.

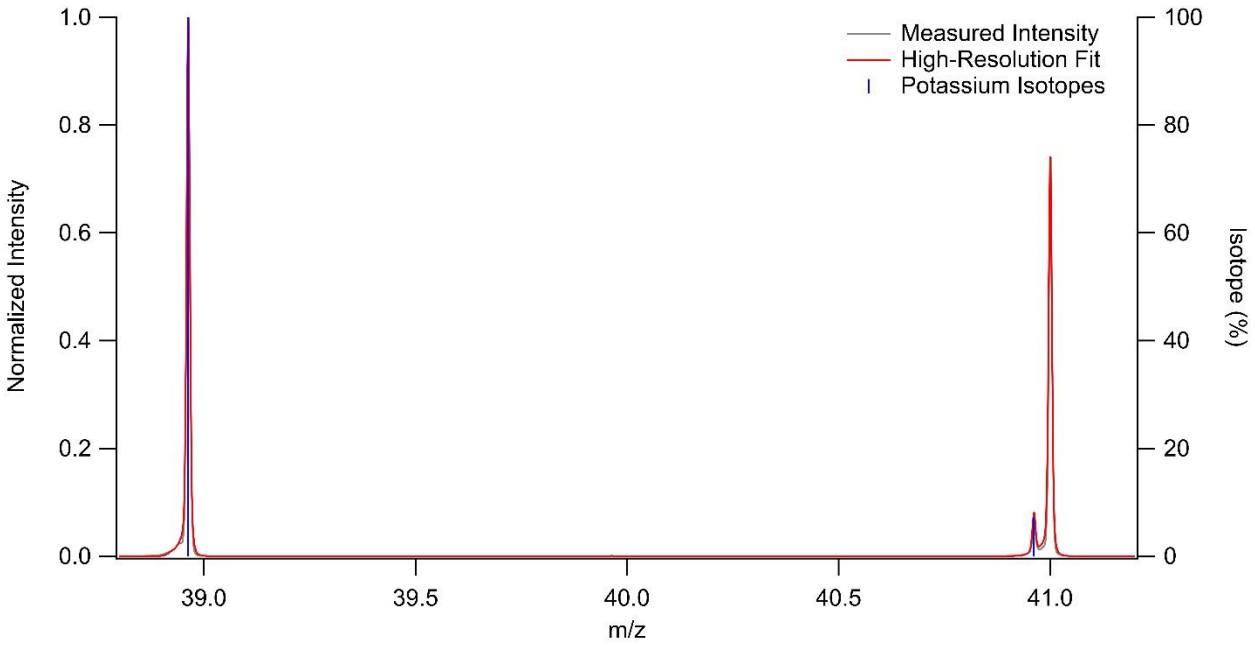

Figure 4.12 The mass spectra of the normalized intensity (grey), high-resolution fit (red), and isotopic abundance for potassium (blue lines). The second peak at 41 m/z is a sodium water cluster (H_2ONa^+).

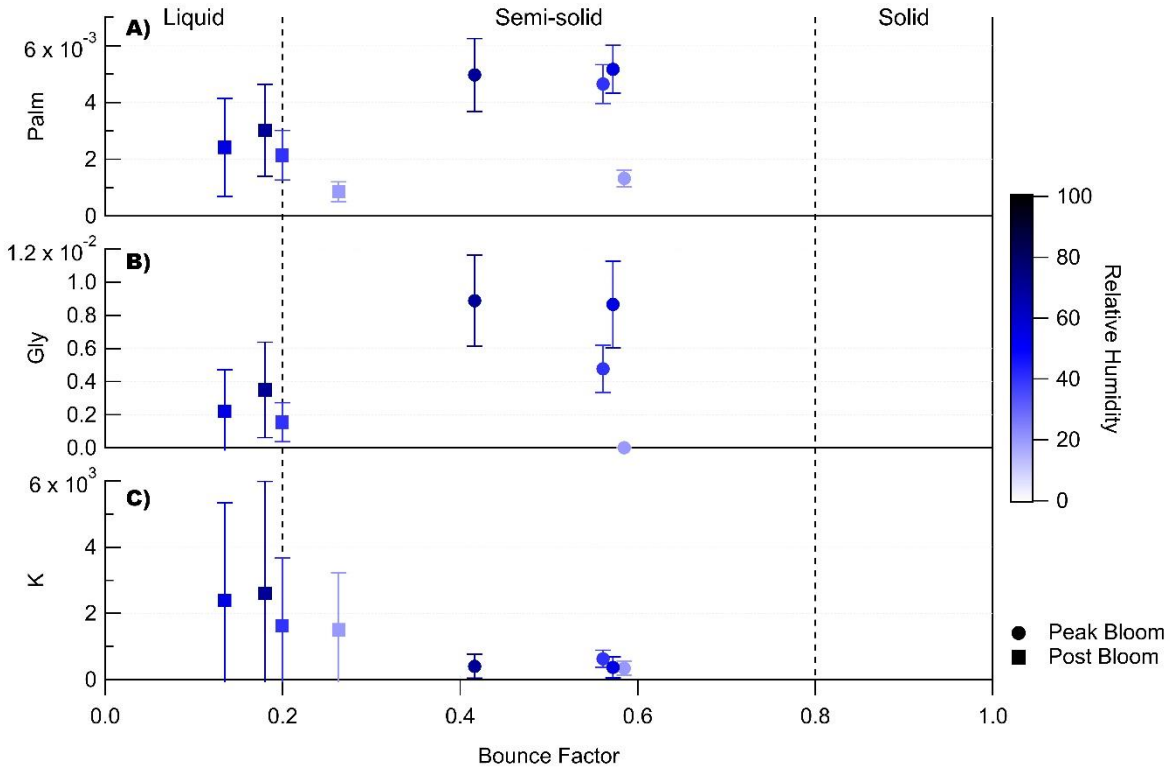

Figure 4.13 Bounce factor from Tumminello et al. 2021 during the peak bloom (circles) and post bloom (squares)[52] plotted against the intensity of palmitic acid (A), glycerol (B), and potassium (C). The blue color scale (white at 0% and black at 100%) represents the relative humidity during each period.

Table 4.2 List of compounds previously identified in SSA from Mandalakis et al. 2011,[103] Decesari et al. 2020,[67] Cochran et al. 2016,[24] Triesch et al. 2021,[104] and Jayarathne et al. 2016[23]

Chemical Formula	Molecular Weight (g/mol)	Chemical Name	Reference
$C_2H_5NO_2$	75.032028	glycine	Mandalakis et al. 2011
$C_3H_7NO_2$	89.047678	alanine	Decesari et al. 2020
$C_3H_8O_3$	92.046796	glycerol	Decesari et al. 2020
$C_3H_4O_4$	104.010959	propanedioic acid	Cochran et al. 2016
$C_3H_7NO_3$	105.042593	serine	Mandalakis et al. 2011
$C_4H_7N_3O$	113.058363	creatinine	Decesari et al. 2020
$C_5H_9NO_2$	115.063329	proline	Mandalakis et al. 2011
$C_5H_8O_3$	116.047344	oxopentanoic acid	Cochran et al. 2016
$C_6H_{12}O_2$	116.08373	hexanoic acid	Cochran et al. 2016
$C_5H_{11}NO_2$	117.078979	valine	Mandalakis et al. 2011
$C_4H_6O_4$	118.026609	butanedioic acid	Cochran et al. 2016
$C_5H_{10}O_3$	118.062994	hydroxy-pentanoic acid	Cochran et al. 2016
$C_4H_9NO_3$	119.058243	threonine	Mandalakis et al. 2011
$C_6H_{10}O_3$	130.062994	oxohexanoic acid	Cochran et al. 2016
$C_5H_9NO_3$	131.058243	hydroxyproline	Mandalakis et al. 2011
$C_6H_{13}NO_2$	131.094629	leucine	Mandalakis et al. 2011
$C_5H_8O_4$	132.042259	pentanedioic acid	Cochran et al. 2016
$C_4H_8N_2O_3$	132.053492	asparagine	Mandalakis et al. 2011
$C_6H_{12}O_3$	132.078644	hydroxy-hexanoic acid	Cochran et al. 2016
$C_4H_7NO_4$	133.037508	aspartic acid	Triesch et al. 2021
$C_3H_8SO_4$	140.01433	monopropylsulfate	Cochran et al. 2016
$C_7H_{12}O_3$	144.078644	oxoheptanoic acid	Cochran et al. 2016
$C_8H_{16}O_2$	144.11503	octanoic acid	Cochran et al. 2016
$C_6H_{10}O_4$	146.057909	hexanedioic acid	Cochran et al. 2016
$C_5H_{10}N_2O_3$	146.069142	glutamine	Mandalakis et al. 2011
$C_7H_{14}O_3$	146.094294	hydroxy-heptanoic acid	Cochran et al. 2016
$C_5H_9NO_4$	147.053158	glutamic acid	Triesch et al. 2021
$C_5H_{11}NSO_2$	149.05105	methionine	Mandalakis et al. 2011
$C_4H_{10}SO_4$	154.02998	monotetrasulfate	Cochran et al. 2016
$C_6H_9N_3O_2$	155.069477	histidine	Mandalakis et al. 2011
$C_8H_{14}O_3$	158.094294	oxooctanoic acid	Cochran et al. 2016
$C_9H_{18}O_2$	158.13068	nonanoic acid	Cochran et al. 2016
$C_7H_{12}O_4$	160.073559	heptanedioic acid	Cochran et al. 2016
$C_8H_{16}O_3$	160.109944	hydroxy-octanoic acid	Cochran et al. 2016
$C_9H_{11}NO_2$	165.078979	phenylalanine	Mandalakis et al. 2011
$C_5H_{12}SO_4$	168.04563	monopentasulfate	Cochran et al. 2016
$C_9H_{16}O_3$	172.109944	oxononanoic acid	Cochran et al. 2016

Table 4.2 List of compounds previously identified in SSA from Mandalakis et al. 2011,[103] Decesari et al. 2020,[67] Cochran et al. 2016,[24] Triesch et al. 2021,[104] and Jayarathne et al. 2016[23] (continued)

Chemical Formula	Molecular Weight (g/mol)	Chemical Name	Reference
$C_{10}H_{20}O_2$	172.14633	decanoic acid	Cochran et al. 2016
$C_8H_{14}O_4$	174.089209	octanedioic acid	Cochran et al. 2016
$C_6H_{14}N_4O_2$	174.111676	arginine	Mandalakis et al. 2011
$C_9H_{18}O_3$	174.125594	hydroxy-nonanoic acid	Cochran et al. 2016
$C_{11}H_{14}O_2$	178.09938	undecatetraenoic acid	Cochran et al. 2016
$C_6H_{12}O_6$	180.063388	glucose	Jayarathne et al. 2016
$C_9H_{11}NO_3$	181.073893	tyrosine	Mandalakis et al. 2011
$C_6H_{14}SO_4$	182.06128	monohexylsulfate	Cochran et al. 2016
$C_{10}H_{18}O_3$	186.125594	oxodecanoic acid	Cochran et al. 2016
$C_{11}H_{22}O_2$	186.16198	undecanoic acid	Cochran et al. 2016
$C_9H_{16}O_4$	188.104859	nonanedioic acid	Cochran et al. 2016
$C_{10}H_{20}O_3$	188.141245	hydroxy-decanoic acid	Cochran et al. 2016
$C_{12}H_{16}O_2$	192.11503	dodecatetraenoic acid	Cochran et al. 2016
$C_7H_{16}SO_4$	196.07693	monoheptasulfate	Cochran et al. 2016
$C_{12}H_{20}O_2$	196.14633	dodecadienoic acid	Cochran et al. 2016
$C_{12}H_{22}O_2$	198.16198	dodecenoic acid	Cochran et al. 2016
$C_{11}H_{20}O_3$	200.141245	oxoundecanoic acid	Cochran et al. 2016
$C_{12}H_{24}O_2$	200.17763	dodecanoic acid	Cochran et al. 2016
$C_{10}H_{18}O_4$	202.120509	decanedioic acid	Cochran et al. 2016
$C_{11}H_{22}O_3$	202.156895	hydroxy-undecanoic acid	Cochran et al. 2016
$C_8H_{18}SO_4$	210.09258	monooctylsulfate	Cochran et al. 2016
$C_{13}H_{22}O_2$	210.16198	tridecadienoic acid	Cochran et al. 2016
$C_{13}H_{24}O_2$	212.17763	tridecenoic acid	Cochran et al. 2016
$C_{12}H_{22}O_3$	214.156895	oxododecanoic acid	Cochran et al. 2016
$C_{13}H_{26}O_2$	214.19328	tridecanoic acid	Cochran et al. 2016
$C_{11}H_{20}O_4$	216.136159	undecanedioic acid	Cochran et al. 2016
$C_{12}H_{24}O_3$	216.172545	hydroxy-dodecanoic acid	Cochran et al. 2016
$C_{14}H_{22}O_2$	222.16198	tetradecatrienoic acid	Cochran et al. 2016
$C_9H_{20}SO_4$	224.10823	monononasulfate	Cochran et al. 2016
$C_{14}H_{24}O_2$	224.17763	tetradecadienoic acid	Cochran et al. 2016
$C_{14}H_{26}O_2$	226.19328	tetradecenoic acid	Cochran et al. 2016
$C_{13}H_{24}O_3$	228.172545	oxotridecanoic acid	Cochran et al. 2016
$C_{14}H_{28}O_2$	228.20893	tetradecanoic acid	Cochran et al. 2016
$C_{12}H_{22}O_4$	230.151809	dodecanedioic acid	Cochran et al. 2016
$C_{13}H_{26}O_3$	230.188195	hydroxy-tridecanoic acid	Cochran et al. 2016
$C_{10}H_{22}SO_4$	238.12388	monodecylsulfate	Cochran et al. 2016

Table 4.2 List of compounds previously identified in SSA from Mandalakis et al. 2011,[103] Decesari et al. 2020,[67] Cochran et al. 2016,[24] Triesch et al. 2021,[104] and Jayarathne et al. 2016[23] (continued)

Chemical Formula	Molecular Weight (g/mol)	Chemical Name	Reference
$C_{15}H_{26}O_2$	238.19328	pentadecadienoic acid	Cochran et al. 2016
$C_{15}H_{28}O_2$	240.20893	pentadecenoic acid	Cochran et al. 2016
$C_{14}H_{26}O_3$	242.188195	oxotetradecanoic acid	Cochran et al. 2016
$C_{15}H_{30}O_2$	242.22458	pentadecanoic acid	Cochran et al. 2016
$C_{13}H_{24}O_4$	244.167459	tridecanedioic acid	Cochran et al. 2016
$C_{14}H_{28}O_3$	244.203845	hydroxy-tetradecanoic acid	Cochran et al. 2016
$C_{16}H_{24}O_2$	248.17763	hexadecatetraenoic acid	Cochran et al. 2016
$C_{16}H_{26}O_2$	250.19328	hexadecatrienoic acid	Cochran et al. 2016
$C_{11}H_{24}SO_4$	252.13953	monoundecylsulfate	Cochran et al. 2016
$C_{16}H_{28}O_2$	252.20893	hexadecadienoic acid	Cochran et al. 2016
$C_{16}H_{30}O_2$	254.22458	hexadecenoic acid	Cochran et al. 2016
$C_{15}H_{28}O_3$	256.203845	oxopentadecanoic acid	Cochran et al. 2016
$C_{16}H_{32}O_2$	256.24023	hexadecanoic acid	Cochran et al. 2016
$C_{14}H_{26}O_4$	258.183109	tetradecanedioic acid	Cochran et al. 2016
$C_{15}H_{30}O_3$	258.219495	hydroxy-pentadecanoic acid	Cochran et al. 2016
$C_{12}H_{26}SO_4$	266.15518	monododecylsulfate	Cochran et al. 2016
$C_{17}H_{30}O_2$	266.22458	heptadecadienoic acid	Cochran et al. 2016
$C_{17}H_{32}O_2$	268.24023	heptadecenoic acid	Cochran et al. 2016
$C_{16}H_{30}O_3$	270.219495	oxohexadecanoic acid	Cochran et al. 2016
$C_{17}H_{34}O_2$	270.25588	heptadecanoic acid	Cochran et al. 2016
$C_{15}H_{28}O_4$	272.198759	pentadecanedioic acid	Cochran et al. 2016
$C_{16}H_{32}O_3$	272.235145	hydroxy-hexadecanoic acid	Cochran et al. 2016
$C_{18}H_{26}O_2$	274.19328	octadecapentaenoic acid	Cochran et al. 2016
$C_{18}H_{28}O_2$	276.20893	octadecatetraenoic acid	Cochran et al. 2016
$C_{18}H_{30}O_2$	278.22458	octadecatrienoic acid	Cochran et al. 2016
$C_{13}H_{28}SO_4$	280.170831	monotridecylsulfate	Cochran et al. 2016
$C_{18}H_{34}O_2$	282.25588	octadecenoic acid	Cochran et al. 2016
$C_{17}H_{32}O_3$	284.235145	oxoheptadecanoic acid	Cochran et al. 2016
$C_{18}H_{36}O_2$	284.27153	octadecanoic acid	Cochran et al. 2016
$C_{16}H_{30}O_4$	286.214409	hexadecanedioic acid	Cochran et al. 2016
$C_{17}H_{34}O_3$	286.250795	hydroxy-heptadecanoic acid	Cochran et al. 2016
$C_{14}H_{30}SO_4$	294.186481	monotetradecylsulfate	Cochran et al. 2016
$C_{16}H_{26}SO_3$	298.160266	decylbenzenesulfonate	Cochran et al. 2016
$C_{18}H_{34}O_3$	298.250795	oxooctadecanoic acid	Cochran et al. 2016
$C_{19}H_{38}O_2$	298.28718	nonadecanoic acid	Cochran et al. 2016
$C_{18}H_{36}O_3$	300.266445	hydroxy-octadecanoic acid	Cochran et al. 2016

Table 4.2 List of compounds previously identified in SSA from Mandalakis et al. 2011,[103] Decesari et al. 2020,[67] Cochran et al. 2016,[24] Triesch et al. 2021,[104] and Jayarathne et al. 2016[23] (continued)

Chemical Formula	Molecular Weight (g/mol)	Chemical Name	Reference
$C_{20}H_{30}O_2$	302.22458	eicosapentaenoic acid	Cochran et al. 2016
$C_{20}H_{32}O_2$	304.24023	eicosatetraenoic acid	Cochran et al. 2016
$C_{15}H_{32}SO_4$	308.202131	monopentadecylsulfate	Cochran et al. 2016
$C_{17}H_{28}SO_3$	312.175916	undecylbenzenesulfonate	Cochran et al. 2016
$C_{20}H_{40}O_2$	312.302831	eicosanoic acid	Cochran et al. 2016
$C_{18}H_{34}O_4$	314.24571	octadecanedioic acid	Cochran et al. 2016
$C_{21}H_{34}O_2$	318.25588	uneicosatetraenoic acid	Cochran et al. 2016
$C_{16}H_{34}SO_4$	322.217781	monohexadecylsulfate	Cochran et al. 2016
$C_{18}H_{30}SO_3$	326.191566	dodecylbenzenesulfonate	Cochran et al. 2016
$C_{21}H_{42}O_2$	326.318481	uneicosanoic acid	Cochran et al. 2016
$C_{22}H_{32}O_2$	328.24023	doeicosahexaenoic acid	Cochran et al. 2016
$C_{19}H_{36}O_4$	328.26136	nonadecanedioic acid	Cochran et al. 2016
$C_{22}H_{34}O_2$	330.25588	doeicosapentaenoic acid	Cochran et al. 2016
$C_{17}H_{36}SO_4$	336.233431	monoheptadecylsulfate	Cochran et al. 2016
$C_{19}H_{32}SO_3$	340.207216	tridecylbenzenesulfonate	Cochran et al. 2016
$C_{22}H_{44}O_2$	340.334131	dodeicosanoic acid	Cochran et al. 2016
$C_{12}H_{22}O_{11}$	342.116212	sucrose	Decesari et al. 2020
$C_{20}H_{38}O_4$	342.27701	eicosanedioic acid	Cochran et al. 2016
$C_{20}H_{34}SO_3$	354.222866	tetradecylbenzenesulfonate	Cochran et al. 2016
$C_{23}H_{46}O_2$	354.349781	trieicosanoic acid	Cochran et al. 2016
$C_{24}H_{48}O_2$	368.365431	tetracosanoic acid	Cochran et al. 2016
$C_{22}H_{42}O_4$	370.30831	doeicosanedioic acid	Cochran et al. 2016

4.7 Acknowledgements

Chapter 4, in full, has been submitted to Analytical Chemistry. Kruse, Samantha M., Tumminello, Paul R. Slade, Jonathan H. The dissertation author was the primary researcher and author of this paper.

This work was funded by the NSF through NSF-CAICE under Grant CHE-1801971. The authors thank the entire SeaSCAPE team for their efforts in making the wave flume study possible.

4.8 References

(1) A.-I. Partanen; E. M. Dunne; T. Bergman; A. Laakso; H. Kokkola; J. Ovadnevaite; L. Sogacheva; D. Baisnée; J. Sciare; A. Manders; C. O'Dowd; G. de Leeuw; Korhonen, H. Global modelling of direct and indirect effects of sea spray aerosol using a source function encapsulating wave state. *Atmos. Chem. Phys.* **2014**, *14* (21), 11731-11752. DOI: 10.5194/acp-14-11731-2014.

(2) Antti-Ilari Partanen; Harri Kokkola; Sami Romakkaniemi; Veli-Matti Kerminen; Kari E. J. Lehtinen; Tommi Bergman; Antti Arola; Korhonen, H. Direct and indirect effects of sea spray geoengineering and the role of injected particle size. *Journal of* **2012**. DOI: 10.1029/2011JD016428.

(3) Ayash, T.; Gong, S.; Jia, C. Q. Direct and Indirect Shortwave Radiative Effects of Sea Salt Aerosols. *J. Clim.* **2008**, *21* (13), 3207-3220. DOI: 10.1175/2007JCLI2063.1.

(4) Moore, M. J. K.; Furutani, H.; Roberts, G. C.; Moffet, R. C.; Gilles, M. K.; Palenik, B.; Prather, K. A. Effect of organic compounds on cloud condensation nuclei (CCN) activity of sea spray aerosol produced by bubble bursting. *Atmos. Environ.* **2011**, *45* (39), 7462-7469. DOI: 10.1016/j.atmosenv.2011.04.034.

(5) DeMott, P. J.; Hill, T. C. J.; McCluskey, C. S.; Prather, K. A.; Collins, D. B.; Sullivan, R. C.; Ruppel, M. J.; Mason, R. H.; Irish, V. E.; Lee, T.; Hwang, C. Y.; Rhee, T. S.; Snider, J. R.; McMeeking, G. R.; Dhaniyala, S.; Lewis, E. R.; Wentzell, J. J. B.; Abbatt, J.; Lee, C.; Sultana, C. M.; Ault, A. P.; Axson, J. L.; Diaz Martinez, M.; Venero, I.; Santos-Figueroa, G.; Stokes, M. D.; Deane, G. B.; Mayol-Bracero, O. L.; Grassian, V. H.; Bertram, T. H.; Bertram, A. K.; Moffett, B. F.; Franc, G. D. Sea spray aerosol as a unique source of ice nucleating particles. *Proc. Natl. Acad. Sci. U. S. A.* **2016**, *113* (21), 5797-5803. DOI: 10.1073/pnas.1514034112.

(6) Collins, D. B.; Bertram, T. H.; Sultana, C. M.; Lee, C.; Axson, J. L.; Prather, K. A. Phytoplankton blooms weakly influence the cloud forming ability of sea spray aerosol. *Geophys. Res. Lett.* **2016**, *43* (18), 9975-9983. DOI: 10.1002/2016gl069922.

(7) de Leeuw, G.; Andreas, E. L.; Anguelova, M. D.; Fairall, C. W.; Lewis, E. R.; O'Dowd, C.; Schulzl, M.; Schwartz, S. E. Production Flux Of Sea Spray Aerosol. *Reviews of Geophysics* **2011**, *49*, 1-39. DOI: 10.1029/2010RG000349.

(8) Lewis, E. R.; Schwartz, S. E. *Sea Salt Aerosol Production: Mechanisms, Methods, Measurements, and Models*; American Geophysical Union, 2004.

(9) Grythe, H.; Ström, J.; Krejci, R.; Quinn, P.; Stohl, A. A review of sea-spray aerosol source functions using a large global set of sea salt aerosol concentration measurements. *Atmos. Chem. Phys.* **2014**, *14* (3), 1277-1297. DOI: 10.5194/acp-14-1277-2014.

(10) Xu, W.; Ovadnevaite, J.; Fossum, K. N.; Lin, C.; Huang, R.-J.; Ceburnis, D.; O'Dowd, C. Sea spray as an obscured source for marine cloud nuclei. *Nat. Geosci.* **2022**, *15* (4), 282-286. DOI: 10.1038/s41561-022-00917-2.

(11) Tsigaridis, K.; Koch, D.; Menon, S. Uncertainties and importance of sea spray composition on aerosol direct and indirect effects. *JGR Atmospheres* **2013**, *118*, 220-235. DOI: 10.1029/2012JD018165.

(12) Ma, X.; Salzen, K.; Li, J. Modelling sea salt aerosol and its direct and indirect effects on climate. *Atmos. Chem. Phys.* **2007**, *8*, 1311-1327. DOI: 10.5194/ACP-8-1311-2008.

(13) Quinn, P. K.; Bates, T. S.; Miller, T. L.; Coffman, D. J.; Johnson, J. E.; Harris, J. M.; Ogren, J. A.; Forbes, G.; Anderson, T. L.; Covert, D. S.; Rood, M. J. Surface submicron aerosol chemical composition: What fraction is not sulfate? *J. Geophys. Res.* **2000**, *105* (D5), 6785-6805. DOI: 10.1029/1999jd901034.

(14) Bertram, T. H.; Cochran, R. E.; Grassian, V. H.; Stone, E. A. Sea spray aerosol chemical composition: elemental and molecular mimics for laboratory studies of heterogeneous and multiphase reactions. *Chem. Soc. Rev.* **2018**, *47* (7), 2374-2400. DOI: 10.1039/c7cs00008a.

(15) Quinn, P. K.; Collins, D. B.; Grassian, V. H.; Prather, K. A.; Bates, T. S. Chemistry and related properties of freshly emitted sea spray aerosol. *Chem. Rev.* **2015**, *115* (10), 4383-4399. DOI: 10.1021/cr500713g.

(16) Patterson, J. P.; Collins, D. B.; Michaud, J. M.; Axson, J. L.; Sultana, C. M.; Moser, T.; Dommer, A. C.; Conner, J.; Grassian, V. H.; Stokes, M. D.; Deane, G. B.; Evans, J. E.; Burkart, M. D.; Prather, K. A.; Gianneschi, N. C. Sea Spray Aerosol Structure and Composition Using Cryogenic Transmission Electron Microscopy. *ACS Cent Sci* **2016**, *2* (1), 40-47. DOI: 10.1021/acscentsci.5b00344.

(17) Ault, A. P.; Moffet, R. C.; Baltrusaitis, J.; Collins, D. B.; Ruppel, M. J.; Cuadra-Rodriguez, L. A.; Zhao, D.; Guasco, T. L.; Ebben, C. J.; Geiger, F. M.; Bertram, T. H.; Prather, K. A.; Grassian, V. H. Size-dependent changes in sea spray aerosol composition and properties with different seawater conditions. *Environ. Sci. Technol.* **2013**, *47* (11), 5603-5612. DOI: 10.1021/es400416g.

(18) Wang, X.; Deane, G. B.; Moore, K. A.; Ryder, O. S.; Stokes, M. D.; Beall, C. M.; Collins, D. B.; Santander, M. V.; Burrows, S. M.; Sultana, C. M.; Prather, K. A. The role of jet and film drops in controlling the mixing state of submicron sea spray aerosol particles. *Proc. Natl. Acad. Sci. U. S. A.* **2017**, *114* (27), 6978-6983. DOI: 10.1073/pnas.1702420114.

(19) Prather, K. A.; Bertram, T. H.; Grassian, V. H.; Deane, G. B.; Stokes, M. D.; Demott, P. J.; Aluwihare, L. I.; Palenik, B. P.; Azam, F.; Seinfeld, J. H.; Moffet, R. C.; Molina, M. J.; Cappa, C. D.; Geiger, F. M.; Roberts, G. C.; Russell, L. M.; Ault, A. P.; Baltrusaitis, J.; Collins, D. B.; Corrigan, C. E.; Cuadra-Rodriguez, L. A.; Ebben, C. J.; Forestieri, S. D.; Guasco, T. L.; Hersey, S. P.; Kim, M. J.; Lambert, W. F.; Modini, R. L.; Mui, W.; Pedler, B. E.; Ruppel, M. J.; Ryder, O. S.; Schoepp, N. G.; Sullivan, R. C.; Zhao, D. Bringing the ocean into the laboratory to probe the chemical complexity of sea spray aerosol. *Proc. Natl. Acad. Sci. U. S. A.* **2013**, *110* (19), 7550-7555. DOI: 10.1073/pnas.1300262110.

(20) O'Dowd, C. D.; Facchini, M. C.; Cavalli, F.; Ceburnis, D.; Mircea, M.; Decesari, S.; Fuzzi, S.; Yoon, Y. J.; Putaud, J.-P. Biogenically driven organic contribution to marine aerosol. *Nature* **2004**, *431* (7009), 676-680. DOI: 10.1038/nature02959.

(21) Crocker, D. R.; Hernandez, R. E.; Huang, H. D.; Pendergraft, M. A.; Cao, R.; Dai, J.; Morris, C. K.; Deane, G. B.; Prather, K. A.; Thiemens, M. H. Biological Influence on δ13C and Organic Composition of Nascent Sea Spray Aerosol. *ACS Earth Space Chem.* **2020**, *4* (9), 1686-1699. DOI: 10.1021/acsearthspacechem.0c00072.

(22) Lee, H. D.; Morris, H. S.; Laskina, O.; Sultana, C. M.; Lee, C.; Jayarathne, T.; Cox, J. L.; Wang, X.; Hasenecz, E. S.; DeMott, P. J.; Bertram, T. H.; Cappa, C. D.; Stone, E. A.; Prather, K. A.; Grassian, V. H.; Tivanski, A. V. Organic Enrichment, Physical Phase State, and Surface Tension Depression of Nascent Core–Shell Sea Spray Aerosols during Two Phytoplankton Blooms. *ACS Earth Space Chem.* **2020**, *4* (4), 650-660. DOI: 10.1021/acsearthspacechem.0c00032.

(23) Jayarathne, T.; Sultana, C. M.; Lee, C.; Malfatti, F.; Cox, J. L.; Pendergraft, M. A.; Moore, K. A.; Azam, F.; Tivanski, A. V.; Cappa, C. D.; Bertram, T. H.; Grassian, V. H.; Prather, K. A.; Stone, E. A. Enrichment of Saccharides and Divalent Cations in Sea Spray Aerosol During Two Phytoplankton Blooms. *Environ. Sci. Technol.* **2016**, *50* (21), 11511-11520. DOI: 10.1021/acs.est.6b02988.

(24) Cochran, R. E.; Laskina, O.; Jayarathne, T.; Laskin, A.; Laskin, J.; Lin, P.; Sultana, C.; Lee, C.; Moore, K. A.; Cappa, C. D.; Bertram, T. H.; Prather, K. A.; Grassian, V. H.; Stone, E. A. Analysis of Organic Anionic Surfactants in Fine and Coarse Fractions of Freshly Emitted Sea Spray Aerosol. *Environ. Sci. Technol.* **2016**, *50* (5), 2477-2486. DOI: 10.1021/acs.est.5b04053.

(25) Kattner, G.; Gercken, G.; Eberlein, K. Development of lipids during a spring plankton bloom in the northern North Sea: I. Particulate fatty acids. *Mar. Chem.* **1983**, *14* (2), 149-162. DOI: 10.1016/0304-4203(83)90038-5.

(26) Angle, K. J.; Nowak, C. M.; Davasam, A.; Dommer, A. C.; Wauer, N. A.; Amaro, R. E.; Grassian, V. H. Amino Acids Are Driven to the Interface by Salts and Acidic Environments. *J. Phys. Chem. Lett.* **2022**, *13* (12), 2824-2829. DOI: 10.1021/acs.jpclett.2c00231.

(27) Triesch, N.; van Pinxteren, M.; Salter, M.; Stolle, C.; Pereira, R.; Zieger, P.; Herrmann, H. Sea Spray Aerosol Chamber Study on Selective Transfer and Enrichment of Free and Combined Amino Acids. *ACS Earth Space Chem.* **2021**, *5* (6), 1564-1574. DOI: 10.1021/acsearthspacechem.1c00080.

(28) Ovadnevaite, J.; Ceburnis, D.; Martucci, G.; Bialek, J.; Monahan, C.; Rinaldi, M.; Facchini, M. C.; Berresheim, H.; Worsnop, D. R.; O'Dowd, C. Primary marine organic aerosol: A dichotomy of low hygroscopicity and high CCN activity. *Geophys. Res. Lett.* **2011**, *38* (21). DOI: 10.1029/2011gl048869.

(29) Westervelt, D. M.; Moore, R. H.; Nenes, A.; Adams, P. J. Effect of primary organic sea spray emissions on cloud condensation nuclei concentrations. *Atmos. Chem. Phys.* **2012**, *12* (1), 89-101. DOI: 10.5194/acp-12-89-2012.

(30) Lee, H.; Romero, J. IPCC, 2023: Climate Change 2023: Synthesis Report. **2023**, 35-115. DOI: 10.59327/IPCC/AR6-9789291691647.

(31) Glicker, H. S.; Lawler, M. J.; Chee, S.; Resch, J.; Garofalo, L. A.; Mayer, K. J.; Prather, K. A.; Farmer, D. K.; Smith, J. N. Chemical Composition of an Ultrafine Sea Spray Aerosol during the Sea Spray Chemistry and Particle Evolution Experiment. *ACS Earth Space Chem.* **2022**. DOI: 10.1021/acsearthspacechem.2c00127.

(32) Franklin, E. B.; Amiri, S.; Crocker, D.; Morris, C.; Mayer, K.; Sauer, J. S.; Weber, R. J.; Lee, C.; Malfatti, F.; Cappa, C. D.; Bertram, T. H.; Prather, K. A.; Goldstein, A. H. Anthropogenic and Biogenic Contributions to the Organic Composition of Coastal Submicron Sea Spray Aerosol. *Environ. Sci. Technol.* **2022**. DOI: 10.1021/acs.est.2c04848.

(33) Cochran, R. E.; Jayarathne, T.; Stone, E. A.; Grassian, V. H. Selectivity Across the Interface: A Test of Surface Activity in the Composition of Organic-Enriched Aerosols from Bubble Bursting. *J. Phys. Chem. Lett.* **2016**, *7* (9), 1692-1696. DOI: 10.1021/acs.jpclett.6b00489.

(34) Jon S. Sauer; Kathryn J. Mayer; Christopher Lee; Michael R. Alves; Sarah Amiri; Cristina J. Bahaveolos; Emily B. Franklin; Daniel R. Crocker; Duyen Dang; Julie Dinasquet; Lauren A. Garofalo; Chathuri P. Kaluarachchi; Delaney B. Kilgour; Liora E. Mael; Brock A. Mitts; Daniel R. Moon; Alexia N. Moore; Clare K. Morris; Catherine A. Mullenmeister; Chi-Min Ni; Matthew A. Pendergraft; Daniel Petras; Rebecca M. C. Simpson; Stephanie Smith; Paul R. Tumminello; Joseph L. Walker; Paul J. DeMott; Delphine K. Farmer; Allen H. Goldstein; Vicki H. Grassian; Jules S. Jaffe; Francesca Malfatti; Todd R. Martz; Jonathan H. Slade; Alexei V. Tivanski; Timothy H. Bertram; Christopher D. Cappa; Prather, K. A. The Sea Spray Chemistry and Particle Evolution Study (SeaSCAPE): Overview and Experimental Methods. *Environ. Sci. Process. Impacts* **2022**. DOI: 10.1039/D1EM00260K.

(35) Petras, D.; Koester, I.; Da Silva, R.; Stephens, B. M.; Haas, A. F.; Nelson, C. E.; Kelly, L. W.; Aluwihare, L. I.; Dorrestein, P. C. High-Resolution Liquid Chromatography Tandem Mass Spectrometry Enables Large Scale Molecular Characterization of Dissolved Organic Matter. *Frontiers in Marine Science* **2017**, *4*. DOI: 10.3389/fmars.2017.00405.

(36) Pendergraft, M. A.; Belda-Ferre, P.; Petras, D.; Morris, C. K.; Mitts, B. A.; Aron, A. T.; Bryant, M.; Schwartz, T.; Ackermann, G.; Humphrey, G.; Kaandorp, E.; Dorrestein, P. C.; Knight, R.; Prather, K. A. Bacterial and Chemical Evidence of Coastal Water Pollution from the Tijuana River in Sea Spray Aerosol. *Environ. Sci. Technol.* **2023**. DOI: 10.1021/acs.est.2c02312.

(37) Ault, A. P.; Zhao, D.; Ebben, C. J.; Tauber, M. J.; Geiger, F. M.; Prather, K. A.; Grassian, V. H. Raman microspectroscopy and vibrational sum frequency generation spectroscopy as probes of the bulk and surface compositions of size-resolved sea spray aerosol particles. *Phys. Chem. Chem. Phys.* **2013**, *15* (17), 6206-6214. DOI: 10.1039/c3cp43899f.

(38) Trueblood, J. V.; Wang, X.; Or, V. W.; Alves, M. R.; Santander, M. V.; Prather, K. A.; Grassian, V. H. The Old and the New: Aging of Sea Spray Aerosol and Formation of Secondary Marine Aerosol through OH Oxidation Reactions. *ACS Earth Space Chem.* **2019**, *3* (10), 2307-2314. DOI: 10.1021/acsearthspacechem.9b00087.

(39) Lewis, S. L.; Russell, L. M.; Saliba, G.; Quinn, P. K.; Bates, T. S.; Carlson, C. A.; Baetge, N.; Aluwihare, L. I.; Boss, E.; Frossard, A. A.; Bell, T. G.; Behrenfeld, M. J. Characterization of Sea Surface Microlayer and Marine Aerosol Organic Composition Using STXM-NEXAFS Microscopy and FTIR Spectroscopy. *ACS Earth Space Chem.* **2022**. DOI: 10.1021/acsearthspacechem.2c00119.

(40) Kaluarachchi, C. P.; Or, V. W.; Lan, Y.; Madawala, C. K.; Hasenecz, E. S.; Crocker, D. R.; Morris, C. K.; Lee, H. D.; Mayer, K. J.; Sauer, J. S.; Lee, C.; Dorce, G.; Malfatti, F.; Stone, E. A.; Cappa, C. D.; Grassian, V. H.; Prather, K. A.; Tivanski, A. V. Size-Dependent Morphology, Composition, Phase State, and Water Uptake of Nascent Submicrometer Sea Spray Aerosols during a Phytoplankton Bloom. *ACS Earth Space Chem.* **2022**, *6* (1), 116-130. DOI: 10.1021/acsearthspacechem.1c00306.

(41) Kaluarachchi, C. P.; Or, V. W.; Lan, Y.; Hasenecz, E. S.; Kim, D.; Madawala, C. K.; Dorcé, G. P.; Mayer, K. J.; Sauer, J. S.; Lee, C.; Cappa, C. D.; Bertram, T. H.; Stone, E. A.; Prather, K. A.; Grassian, V. H.; Tivanski, A. V. Effects of Atmospheric Aging Processes on Nascent Sea Spray Aerosol Physicochemical Properties. *ACS Earth Space Chem* **2022**, *6* (11), 2732-2744. DOI: 10.1021/acsearthspacechem.2c00258.

(42) Collins, D. B.; Zhao, D. F.; Ruppel, M. J.; Laskina, O.; Grandquist, J. R.; Modini, R. L.; Stokes, M. D.; Russell, L. M.; Bertram, T. H.; Grassian, V. H.; Deane, G. B.; Prather, K. A. Direct aerosol chemical composition measurements to evaluate the physicochemical differences between controlled sea spray aerosol generation schemes. *Atmos. Meas. Tech. Discuss.* **2014**, *7* (7), 6457-6499. DOI: 10.5194/amtd-7-6457-2014.

(43) Sultana, C. M.; Collins, D. B.; Prather, K. A. Effect of Structural Heterogeneity in Chemical Composition on Online Single-Particle Mass Spectrometry Analysis of Sea Spray Aerosol Particles. *Environ. Sci. Technol.* **2017**, *51* (7), 3660-3668. DOI: 10.1021/acs.est.6b06399.

(44) Felipe D. Lopez-Hilfiker; Veronika Pospisilova; Wei Huang; Markus Kalberer; Claudia Mohr; Giulia Stefenelli; Joel A. Thornton; Urs Baltensperger; Andre S. H. Prevot; Slowik, J. G. An extractive electrospray ionization time-of-flight mass spectrometer (EESI-TOF) for online measurement of atmospheric aerosol particles. *Atmospheric* **2019**. DOI: 10.5194/amt-12-4867-2019.

(45) Law, W. S.; Wang, R.; Hu, B.; Berchtold, C.; Meier, L.; Chen, H.; Zenobi, R. On the mechanism of extractive electrospray ionization. *Anal. Chem.* **2010**, *82* (11), 4494-4500. DOI: 10.1021/ac100390t.

(46) Gallimore, P. J.; Kalberer, M. Characterizing an extractive electrospray ionization (EESI) source for the online mass spectrometry analysis of organic aerosols. *Environ. Sci. Technol.* **2013**, *47* (13), 7324-7331. DOI: 10.1021/es305199h.

(47) Surdu, M.; Pospisilova, V.; Xiao, M.; Wang, M.; Mentler, B.; Simon, M.; Stolzenburg, D.; Hoyle, C. R.; Bell, D. M.; Lee, C. P.; Lamkaddam, H.; Lopez-Hilfiker, F.; Ahonen, L. R.; Amorim, A.; Baccarini, A.; Chen, D.; Dada, L.; Duplissy, J.; Finkenzeller, H.; He, X.-C.; Hofbauer, V.; Kim, C.; Kürten, A.; Kvashnin, A.; Lehtipalo, K.; Makhmutov, V.; Molteni, U.; Nie, W.; Onnela, A.; Petäjä, T.; Quéléver, L. L. J.; Tauber, C.; Tomé, A.; Wagner, R.; Yan, C.; Prevot, A. S. H.; Dommen, J.; Donahue, N. M.; Hansel, A.; Curtius, J.; Winkler, P. M.; Kulmala, M.; Volkamer, R.; Flagan, R. C.; Kirkby, J.; Worsnop, D. R.; Slowik, J. G.; Wang, D. S.; Baltensperger, U.; El Haddad, I. Molecular characterization of ultrafine particles using extractive electrospray time-of-flight mass spectrometry. *Environ Sci Atmos* **2021**, *1* (6), 434-448. DOI: 10.1039/d1ea00050k.

(48) Brown, W. L.; Day, D. A.; Stark, H.; Pagonis, D.; Krechmer, J. E.; Liu, X.; Price, D. J.; Katz, E. F.; DeCarlo, P. F.; Masoud, C. G.; Wang, D. S.; Hildebrandt Ruiz, L.; Arata, C.; Lunderberg, D. M.; Goldstein, A. H.; Farmer, D. K.; Vance, M. E.; Jimenez, J. L. Real-time organic aerosol chemical speciation in the indoor environment using extractive electrospray ionization mass spectrometry. *Indoor Air* **2021**, *31* (1), 141-155. DOI: 10.1111/ina.12721.

(49) Chen, H.; Venter, A.; Cooks, R. G. Extractive electrospray ionization for direct analysis of undiluted urine, milk and other complex mixtures without sample preparation. *Chem. Commun.* **2006**, (19), 2042-2044. DOI: 10.1039/b602614a.

(50) Doezema, L. A.; Longin, T.; Cody, W.; Perraud, V.; Dawson, M. L.; Ezell, M. J.; Greaves, J.; Johnson, K. R.; Finlayson-Pitts, B. J. Analysis of secondary organic aerosols in air using extractive electrospray ionization mass spectrometry (EESI-MS). *RSC Adv.* **2012**, *2* (7), 2930-2938. DOI: 10.1039/C2RA00961G.

(51) Pagonis, D.; Campuzano-Jost, P.; Guo, H.; Day, D. A.; Schueneman, M. K.; Brown, W. L.; Nault, B. A.; Stark, H.; Siemens, K.; Laskin, A.; Piel, F.; Tomsche, L.; Wisthaler, A.; Coggon, M. M.; Gkatzelis, G. I.; Halliday, H. S.; Krechmer, J. E.; Moore, R. H.; Thomson, D. S.; Warneke, C.; Wiggins, E. B.; Jimenez, J. L. Airborne extractive electrospray mass spectrometry measurements of the chemical composition of organic aerosol. *Atmos. Meas. Tech.* **2021**, *14* (2), 1545-1559. DOI: 10.5194/amt-14-1545-2021.

(52) Tumminello, P. R.; James, R. C.; Kruse, S.; Kawasaki, A.; Cooper, A.; Guadalupe-Diaz, I.; Zepeda, K. L.; Crocker, D. R.; Mayer, K. J.; Sauer, J. S.; Lee, C.; Prather, K. A.; Slade, J. H. Evolution of Sea Spray Aerosol Particle Phase State Across a Phytoplankton Bloom. *ACS Earth Space Chem.* **2021**, *5* (11), 2995-3007. DOI: 10.1021/acsearthspacechem.1c00186.

(53) Chuan Ping Lee; Mihnea Surdu; David M. Bell; Houssni Lamkaddam; Mingyi Wang; Farnoush Ataei; Victoria Hofbauer; Brandon Lopez; Neil M. Donahue; Josef Dommen; Andre S. H. Prevot; Jay G. Slowik; Dongyu Wang; Urs Baltensperger; Haddad, I. E. Effects of aerosol size and coating thickness on the molecular detection using extractive electrospray ionization. *Atmospheric Measurement Techniques* **2021**, *14* (9), 5913-5923. DOI: 10.5194/amt-14-5913-2021.

(54) Lee, C. P.; Surdu, M.; Bell, D. M.; Dommen, J.; Xiao, M.; Zhou, X.; Baccarini, A.; Giannoukos, S.; Wehrle, G.; Schneider, P. A.; Prevot, A. S. H.; Slowik, J. G.; Lamkaddam, H.; Wang, D.; Baltensperger, U.; El Haddad, I. High-frequency gaseous and particulate chemical characterization using extractive electrospray ionization mass spectrometry (Dual-Phase-EESI-TOF). *Atmospheric Measurement Techniques* **2022**, *15* (12), 3747-3760. DOI: 10.5194/amt-15-3747-2022.

(55) Kumbhani, S.; Longin, T.; Wingen, L. M.; Kidd, C.; Perraud, V.; Finlayson-Pitts, B. J. New Mechanism of Extractive Electrospray Ionization Mass Spectrometry for Heterogeneous Solid Particles. *Anal. Chem.* **2018**, *90* (3), 2055-2062. DOI: 10.1021/acs.analchem.7b04164.

(56) Nandy, L.; Liu, S.; Gunsbury, C.; Wang, X.; Pendergraft, M. A.; Prather, K. A.; Dutcher, C. S. Multistep Phase Transitions in Sea Surface Microlayer Droplets and Aerosol Mimics using Microfluidic Wells. *ACS Earth Space Chem.* **2019**, *3* (7), 1260-1267. DOI: 10.1021/acsearthspacechem.9b00121.

(57) You, Y.; Smith, M. L.; Song, M.; Martin, S. T.; Bertram, A. K. Liquid–liquid phase separation in atmospherically relevant particles consisting of organic species and inorganic salts. *Int. Rev. Phys. Chem.* **2014**, *33* (1), 43-77. DOI: 10.1080/0144235X.2014.890786.

(58) Richards, D. S.; Trobaugh, K. L.; Hajek-Herrera, J.; Price, C. L.; Sheldon, C. S.; Davies, J. F.; Davis, R. D. Ion-molecule interactions enable unexpected phase transitions in organic-inorganic aerosol. *Sci Adv* **2020**, *6* (47). DOI: 10.1126/sciadv.abb5643.

(59) Franklin, E. B.; Alves, M. R.; Moore, A. N.; Kilgour, D. B.; Novak, G. A.; Mayer, K.; Sauer, J. S.; Weber, R. J.; Dang, D.; Winter, M.; Lee, C.; Cappa, C. D.; Bertram, T. H.; Prather, K. A.; Grassian, V. H.; Goldstein, A. H. Atmospheric Benzothiazoles in a Coastal Marine Environment. *Environ. Sci. Technol.* **2021**, *55* (23), 15705-15714. DOI: 10.1021/acs.est.1c04422.

(60) Alves, M. R.; Coward, E. K.; Gonzales, D.; Sauer, J. S.; Mayer, K. J.; Prather, K. A.; Grassian, V. H. Changes in light absorption and composition of chromophoric marine-dissolved organic matter across a microbial bloom. *Environ. Sci. Process. Impacts* **2022**, *24* (10), 1923-1933. DOI: 10.1039/d2em00150k.

(61) DeMott, P. J.; Hill, T. C. J.; Moore, K. A.; Perkins, R. J.; Mael, L. E.; Busse, H. L.; Lee, H.; Kaluarachchi, C. P.; Mayer, K. J.; Sauer, J. S.; Mitts, B. A.; Tivanski, A. V.; Grassian, V. H.; Cappa, C. D.; Bertram, T. H.; Prather, K. A. Atmospheric oxidation impact on sea spray produced ice nucleating particles. *Environ. Sci.: Atmos.* **2023**. DOI: 10.1039/D3EA00060E.

(62) Wang, X.; Sultana, C. M.; Trueblood, J.; Hill, T. C. J.; Malfatti, F.; Lee, C.; Laskina, O.; Moore, K. A.; Beall, C. M.; McCluskey, C. S.; Cornwell, G. C.; Zhou, Y.; Cox, J. L.; Pendergraft, M. A.; Santander, M. V.; Bertram, T. H.; Cappa, C. D.; Azam, F.; DeMott, P. J.; Grassian, V. H.; Prather, K. A. Microbial Control of Sea Spray Aerosol Composition: A Tale of Two Blooms. *ACS Cent Sci* **2015**, *1* (3), 124-131. DOI: 10.1021/acscentsci.5b00148.

(63) Kruse, S. M.; Slade, J. H. Heterogeneous and Photosensitized Oxidative Degradation Kinetics of the Plastic Additive Bisphenol-A in Sea Spray Aerosol Mimics. *J. Phys. Chem. A* **2023**, *127* (21), 4724-4733. DOI: 10.1021/acs.jpca.3c00127.

(64) Pospisilova, V.; Lopez-Hilfiker, F. D.; Bell, D. M.; Haddad, I. E.; Mohr, C.; Huang, W.; Heikkinen, L.; Xiao, M.; Dommen, J.; Prevot, A. S. H.; Baltensperger, U.; Slowik, J. G. On the fate of oxygenated organic molecules in atmospheric aerosol particles. *Science Advances* **2020**, *6* (11), eaax8922. DOI: 10.1126/sciadv.aax8922.

(65) Stark, H.; Yatavelli, R. L. N.; Thompson, S. L.; Kimmel, J. R.; Cubison, M. J.; Chhabra, P. S.; Canagaratna, M. R.; Jayne, J. T.; Worsnop, D. R.; Jimenez, J. L. Methods to extract molecular and bulk chemical information from series of complex mass spectra with limited mass resolution. *Int. J. Mass Spectrom.* **2015**, *389*, 26-38. DOI: 10.1016/j.ijms.2015.08.011.

(66) Cochran, R. E.; Laskina, O.; Trueblood, J. V.; Estillore, A. D.; Morris, H. S.; Jayarathne, T.; Sultana, C. M.; Lee, C.; Lin, P.; Laskin, J.; Laskin, A.; Dowling, J. A.; Qin, Z.; Cappa, C. D.; Bertram, T. H.; Tivanski, A. V.; Stone, E. A.; Prather, K. A.; Grassian, V. H. Molecular Diversity of Sea Spray Aerosol Particles: Impact of Ocean Biology on Particle Composition and Hygroscopicity. *Chem* **2017**, *2* (5), 655-667. DOI: 10.1016/j.chempr.2017.03.007.

(67) Decesari, S.; Paglione, M.; Rinaldi, M.; Dall'Osto, M.; Simó, R.; Zanca, N.; Volpi, F.; Facchini, M. C.; Hoffmann, T.; Götz, S.; Kampf, C. J.; O'Dowd, C.; Ceburnis, D.; Ovadnevaite, J.; Tagliavini, E. Shipborne measurements of Antarctic submicron organic aerosols: an NMR perspective linking multiple sources and bioregions. *Atmos. Chem. Phys.* **2020**, *20* (7), 4193-4207. DOI: 10.5194/acp-20-4193-2020.

(68) Facchini, M. C.; Rinaldi, M.; Decesari, S.; Carbone, C.; Finessi, E.; Mircea, M.; Fuzzi, S.; Ceburnis, D.; Flanagan, R.; Nilsson, E. D.; de Leeuw, G.; Martino, M.; Woeltjen, J.; O'Dowd, C. D. Primary submicron marine aerosol dominated by insoluble organic colloids and aggregates. *Geophys. Res. Lett.* **2008**, *35* (17). DOI: 10.1029/2008gl034210.

(69) Huot, Y.; Babin, M.; Bruyant, F.; Grob, C.; Twardowski, M. S.; Claustre, H. Does chlorophyll a provide the best index of phytoplankton biomass for primary productivity studies? *Biogeosci. Discuss.* **2007**, *4* (2), 707-745.

(70) Buchan, A.; LeCleir, G. R.; Gulvik, C. A.; González, J. M. Master recyclers: features and functions of bacteria associated with phytoplankton blooms. *Nat. Rev. Microbiol.* **2014**, *12* (10), 686-698. DOI: 10.1038/nrmicro3326.

(71) Budge, S. M.; Devred, E.; Forget, M.-H.; Stuart, V.; Trzcinski, M. K.; Sathyendranath, S.; Platt, T. Estimating concentrations of essential omega-3 fatty acids in the ocean: supply and demand. *ICES J. Mar. Sci.* **2014**, *71* (7), 1885-1893. DOI: 10.1093/icesjms/fsu003.

(72) Yao, J.; Rock, C. O. Exogenous fatty acid metabolism in bacteria. *Biochimie* **2017**, *141*, 30-39. DOI: 10.1016/j.biochi.2017.06.015.

(73) Flores, J. M.; Bourdin, G.; Kostinski, A. B.; Altaratz, O.; Dagan, G.; Lombard, F.; Haëntjens, N.; Boss, E.; Sullivan, M. B.; Gorsky, G.; Lang-Yona, N.; Trainic, M.; Romac, S.; Voolstra, C. R.; Rudich, Y.; Vardi, A.; Koren, I. Diel cycle of sea spray aerosol concentration. *Nat. Commun.* **2021**, *12* (1), 5476. DOI: 10.1038/s41467-021-25579-3.

(74) Keene, W. C.; Long, M. S.; Reid, J. S.; Frossard, A. A.; Kieber, D. J.; Maben, J. R.; Russell, L. M.; Kinsey, J. D.; Quinn, P. K.; Bates, T. S. Factors That Modulate Properties of Primary Marine Aerosol Generated From Ambient Seawater on Ships at Sea. *Journal of Geophysical Research: Atmospheres* **2017**, *122* (21), 11,961-911,990. DOI: 10.1002/2017JD026872.

(75) Long, M. S.; Keene, W. C.; Kieber, D. J.; Frossard, A. A.; Russell, L. M.; Maben, J. R.; Kinsey, J. D.; Quinn, P. K.; Bates, T. S. Light-enhanced primary marine aerosol production from biologically productive seawater. *Geophys. Res. Lett.* **2014**, *41* (7), 2661-2670. DOI: 10.1002/2014gl059436.

(76) Liu, S.; Liu, C.-C.; Froyd, K. D.; Schill, G. P.; Murphy, D. M.; Bui, T. P.; Dean-Day, J. M.; Weinzierl, B.; Dollner, M.; Diskin, G. S.; Chen, G.; Gao, R.-S. Sea spray aerosol concentration modulated by sea surface temperature. *Proc. Natl. Acad. Sci. U. S. A.* **2021**, *118* (9). DOI: 10.1073/pnas.2020583118.

(77) Lü, X.; Liu, X.; Xu, C.; Song, J.; Li, X.; Yuan, H.; Li, N.; Wang, D.; Yuan, H.; Ye, S. The origins and implications of glycerol ether lipids in China coastal wetland sediments. *Sci. Rep.* **2019**, *9* (1), 18529. DOI: 10.1038/s41598-019-55104-y.

(78) Fu, P.; Kawamura, K.; Miura, K. Molecular characterization of marine organic aerosols collected during a round-the-world cruise. *J. Geophys. Res.* **2011**, *116* (D13). DOI: 10.1029/2011jd015604.

(79) Savakis, P.; Tan, X.; Du, W.; Branco dos Santos, F.; Lu, X.; Hellingwerf, K. J. Photosynthetic production of glycerol by a recombinant cyanobacterium. *J. Biotechnol.* **2015**, *195*, 46-51. DOI: 10.1016/j.jbiotec.2014.12.015.

(80) Hellebust, J. A. Excretion of some organic compounds by marine phytoplankton1. *Limnol. Oceanogr.* **1965**, *10* (2), 192-206. DOI: 10.4319/lo.1965.10.2.0192.

(81) Suescún-Bolívar, L. P.; Iglesias-Prieto, R.; Thomé, P. E. Induction of glycerol synthesis and release in cultured Symbiodinium. *PLoS One* **2012**, *7* (10), e47182. DOI: 10.1371/journal.pone.0047182.

(82) Yao, Y.; Lu, Y.; Peng, K.-T.; Huang, T.; Niu, Y.-F.; Xie, W.-H.; Yang, W.-D.; Liu, J.-S.; Li, H.-Y. Glycerol and neutral lipid production in the oleaginous marine diatom Phaeodactylum tricornutum promoted by overexpression of glycerol-3-phosphate dehydrogenase. *Biotechnol. Biofuels* **2014**, *7* (1), 110. DOI: 10.1186/1754-6834-7-110.

(83) Ben-Amotz, A.; Sussman, I.; Avron, M. Glycerol production by Dunaliella. In *New Trends in Research and Utilization of Solar Energy through Biological Systems*, Mislin, H., Bachofen, R. Eds.; Birkhäuser Basel, 1982; pp 55-58.

(84) Poblete-Castro, I.; Wittmann, C.; Nikel, P. I. Biochemistry, genetics and biotechnology of glycerol utilization in Pseudomonas species. *Microb. Biotechnol.* **2020**, *13* (1), 32-53. DOI: 10.1111/1751-7915.13400.

(85) Tang, C. Y.; Allen, H. C. Ionic binding of Na^+ versus K^+ to the carboxylic acid headgroup of palmitic acid monolayers studied by vibrational sum frequency generation spectroscopy. *J. Phys. Chem. A* **2009**, *113* (26), 7383-7393. DOI: 10.1021/jp9000434.

(86) Salter, M. E.; Hamacher-Barth, E.; Leck, C.; Werner, J.; Johnson, C. M.; Riipinen, I.; Nilsson, E. D.; Zieger, P. Calcium enrichment in sea spray aerosol particles. *Geophys. Res. Lett.* **2016**, *43* (15), 8277-8285. DOI: 10.1002/2016gl070275.

(87) Louis, Y.; Garnier, C.; Lenoble, V.; Omanović, D.; Mounier, S.; Pizeta, I. Characterisation and modelling of marine dissolved organic matter interactions with major and trace cations. *Mar. Environ. Res.* **2009**, *67* (2), 100-107. DOI: 10.1016/j.marenvres.2008.12.002.

(88) Lu, Y.; Allen, H. E. Characterization of copper complexation with natural dissolved organic matter (DOM)--link to acidic moieties of DOM and competition by Ca and Mg. *Water Res.* **2002**, *36* (20), 5083-5101. DOI: 10.1016/s0043-1354(02)00240-3.

(89) Flynn, K. J.; Mitra, A. Feeding in mixoplankton enhances phototrophy increasing bloom-induced pH changes with ocean acidification. *J. Plankton Res.* **2023**, *45* (4), 636-651. DOI: 10.1093/plankt/fbad030.

(90) Hakim, A.; Suzuki, T.; Kobayashi, M. Strength of Humic Acid Aggregates: Effects of Divalent Cations and Solution pH. *ACS Omega* **2019**, *4* (5), 8559-8567. DOI: 10.1021/acsomega.9b00124.

(91) Davies, C. N. Coagulation of aerosols by brownian motion. *J. Aerosol Sci.* **1979**, *10* (2), 151-161. DOI: 10.1016/0021-8502(79)90064-8.

(92) Slade, J. H.; Knopf, D. A. Multiphase OH oxidation kinetics of organic aerosol: The role of particle phase state and relative humidity. *Geophys. Res. Lett.* **2014**, *41* (14), 5297-5306. DOI: 10.1002/2014gl060582.

(93) Rasool, Q. Z.; Shrivastava, M.; Liu, Y.; Gaudet, B.; Zhao, B. Modeling the Impact of the Organic Aerosol Phase State on Multiphase OH Reactive Uptake Kinetics and the Resultant Heterogeneous Oxidation Timescale of Organic Aerosol in the Amazon Rainforest. *ACS Earth Space Chem.* **2023**. DOI: 10.1021/acsearthspacechem.2c00366.

(94) Davies, J. F.; Wilson, K. R. Nanoscale interfacial gradients formed by the reactive uptake of OH radicals onto viscous aerosol surfaces. *Chem. Sci.* **2015**, *6* (12), 7020-7027. DOI: 10.1039/c5sc02326b.

(95) Schervish, M.; Donahue, N. M.; Shiraiwa, M. Effects of volatility, viscosity, and non-ideality on particle–particle mixing timescales of secondary organic aerosols. *Aerosol Sci. Technol.* **2023**, *58* (4), 411-426. DOI: 10.1080/02786826.2023.2256827.

(96) Rim, D.; Green, M.; Wallace, L.; Persily, A.; Choi, J.-I. Evolution of Ultrafine Particle Size Distributions Following Indoor Episodic Releases: Relative Importance of Coagulation, Deposition and Ventilation. *Aerosol Sci. Technol.* **2012**, *46* (5), 494-503. DOI: 10.1080/02786826.2011.639317.

(97) Wang, Y.; Chen, L.; Chen, R.; Tian, G.; Li, D.; Chen, C.; Ge, X.; Ge, G. Effect of relative humidity on the deposition and coagulation of aerosolized SiO2 nanoparticles. *Atmos. Res.* **2017**, *194*, 100-108. DOI: 10.1016/j.atmosres.2017.04.030.

(98) Yu, M.; Koivisto, A. J.; Hämeri, K.; Seipenbusch, M. Size Dependence of the Ratio of Aerosol Coagulation to Deposition Rates for Indoor Aerosols. *Aerosol Sci. Technol.* **2013**, *47* (4), 427-434. DOI: 10.1080/02786826.2012.759640.

(99) Xiao, H.-S.; Dong, J.-L.; Wang, L.-Y.; Zhao, L.-J.; Wang, F.; Zhang, Y.-H. Spatially Resolved Micro-Raman Observation on the Phase Separation of Effloresced Sea Salt Droplets. *Environ. Sci. Technol.* **2008**, *42* (23), 8698-8702. DOI: 10.1021/es801181f.

(100) Ault, A. P.; Guasco, T. L.; Ryder, O. S.; Baltrusaitis, J.; Cuadra-Rodriguez, L. A.; Collins, D. B.; Ruppel, M. J.; Bertram, T. H.; Prather, K. A.; Grassian, V. H. Inside versus outside: ion redistribution in nitric acid reacted sea spray aerosol particles as determined by single particle analysis. *J. Am. Chem. Soc.* **2013**, *135* (39), 14528-14531. DOI: 10.1021/ja407117x.

(101) Ekström, S.; Noziére, B.; Hansson, H. C. CCN Properties of Water-soluble Organic Compounds Produced by Common Bioaerosols. In Nucleation and Atmospheric Aerosols, 2007.

(102) Chen, Y.; Pei, X.; Liu, H.; Meng, Y.; Xu, Z.; Zhang, F.; Xiong, C.; Preston, T. C.; Wang, Z. Influence of acidity on liquid–liquid phase transitions of mixed secondary organic aerosol (SOA) proxy–inorganic aerosol droplets. *Atmos. Chem. Phys.* **2023**, *23* (17), 10255-10265. DOI: 10.5194/acp-23-10255-2023.

(103) Mandalakis, M.; Apostolaki, M.; Tziaras, T.; Polymenakou, P.; Stephanou, E. G. Free and combined amino acids in marine background atmospheric aerosols over

the Eastern Mediterranean. *Atmospheric Environment* **2011**, *45* (4), 1003-1009. DOI: 10.1016/j.atmosenv.2010.10.046.

(104) Triesch, N.; van Pinxteren, M.; Engel, A.; Herrmann, H. Concerted measurements of free amino acids at the Cabo Verde islands: high enrichments in submicron sea spray aerosol particles and cloud droplets. *Atmos. Chem. Phys.* **2021**, *21* (1), 163-181. DOI: 10.5194/acp-21-163-2021.

Chapter 5 Impacts of pH on the Photoinitiated Degradation Kinetics of Aerosol-Phase Bisphenol-A in the Presence of a Photosensitizer and NaCl

5.1 Abstract

Plastics are a rapidly growing concern in the Earth's oceans, and plastics and their leachates can become airborne in sea spray aerosol (SSA). Bisphenol-A (BPA), a significant component of plastics, is ubiquitous in ocean water and aerosol globally. BPA photodegradation is an expected major loss pathway in aerosol, but only one study by this group has measured its photodegradation rates in SSA laboratory mimics, while previous studies have focused on its photodegradation in surface waters. SSA is chemically and physically distinct from the sea surface, exhibiting different pH, ionic strength, surface tension, and mixing states. These properties can affect the photodegradation of organic molecules. In this study, BPA, 4-benzoyl benzoic acid (4-BBA) as a photosensitizer, and NaCl were prepared in 1:0:0, 1:1:0, 1:0:1, and 1:1:1 (w:w:w) solutions and atomized as 100 nm monodispered aerosols and exposed to 369 nm light in an irradiated flow reactor. The BPA photodegradation and photosensitized kinetics were monitored in the aerosol phase using extractive electrospray ionization time-of-flight mass spectrometry (EESI-TOF). We contrast the BPA photodegradation kinetics with and without a photosensitizer between acidic (pH=3.0), slightly acidic (pH=5.8), and basic (pH=11.0) conditions, spanning below and above the pKa of BPA and 4-BBA. The findings indicate that photodegradation is inhibited at pH=3.0 and pH=11.0 compared to pH=5.8. At pH=5.8, BPA photodegradation was enhanced in the presence of 4-BBA and suppressed when BPA was mixed with 4-BBA and NaCl, attributed to quenching of ^{3}4-BBA* by Cl^{-}. While BPA photodegradation rates were slower by a factor of five to ten at pH=3.0, adding 4-BBA did not enhance BPA photodegradation. No change in BPA photodegradation rates were detected under basic conditions with or without a photosensitizer within error, although the EESI-TOF signals of BPA were close to the background noise. We

conjecture no BPA photodegradation at pH=11.0 because of Coulomb repulsion between ionic forms of BPA and 4-BBA. In contrast, in the presence of NaCl, BPA photodegradation rates were faster at pH=11.0 compared to pH=3.0. Compared to bulk solution studies, the first-order rate constants determined here in the aerosol phase are about 10 times faster. We attribute this relatively enhanced BPA photosensitized degradation in aerosol to less of a "solvent cage" effect than bulk solutions. Additionally, the sensitivity influence of particle pH on EESI-TOF detection is discussed. Modeled lifetimes of BPA are 0.4-10.4 days with respect to the lowest and highest rates of degradation.

5.2 Introduction

As of 2023, there is an estimated total of 82-358 trillion plastic pieces in the ocean, weighing 1.1-4.9 million tonnes, which is increasing daily.[1, 2] Plastics contain various chemical additives that increase the durability and longevity of plastics. However, weathering can lead to increasing fragmentation of larger macroplastics into smaller microscopic and nano-sized plastics over time. The increasing plastic surface area-to-volume ratios enhance the leaching of chemical additives in the plastic.[3] Some of these additives are harmful to organisms, accumulate in the environment, and are regulated by the US Food and Drug Administration (FDA) and Environmental Protection Agency (EPA).[4-6] Bisphenol-A (BPA) is one of these harmful additives and is of significant concern due to its ubiquity in the environment and impacts on humans.[6] BPA is used in the production of plastics, primarily as a co-polymer, as well as in epoxy resins and as a plastic additive.[7] BPA is a known endocrine disruptor in the body,[8, 9] and can have both carcinogenic[10] and teratogenic[11] effects. Among other endocrine-disrupting chemicals (EDCs) also found in plastics, BPA has been found to leach from the microplastics in the marine environment at rates up to 6x higher than other EDCs studied.[4] BPA in its molecular form is known to persist

for up to 25 days[12] in seawater at concentrations of up to 17 mg/L [12-15] and has been identified in aerosol globally at concentrations up to 17.4 ng/m^3.[16]

Sea spray aerosol (SSA) is a potential source of airborne BPA. The production mechanism of SSA leads to enhanced aerosol concentrations of compounds that reside at the ocean–air interface, including surface active and hydrophobic molecules.[17, 18] Due to BPA's relatively high lipophilicity (logP = 3.3),[19] it is expected to transfer preferentially into SSA along with other lipophilic material.[20] This lipophilic enhancement has been observed previously for both biogenic[21] and anthropogenic compounds[22, 23] including perfluoroalkyl acids. However, there hasn't been prior motivation demonstrating SSA as a source of atmopheric BPA.

Photosensitizers are compounds that absorb light and due to extensive pi networks, through promotion to an excited triplet state, transfer energy and react directly or indirectly with neighboring molecules. Photosensitizers interacting with oxygen occur as either Type I or Type II. This is shown in R 5.1 and R 5.2:

$$^3Ph^* + M \rightarrow {}^0Ph + P \qquad \text{R 5.1}$$

$$^3Ph^* + {}^1O_2 \rightarrow {}^0Ph + {}^3O_2 + M \rightarrow P \qquad \text{R 5.2}$$

Where *Ph* is a photosensitizer, *M* is the molecule being reacted, and *P* is the photoproduct. Photosensitizers include chromophoric dissolved organic matter (CDOM), which is broadly defined as DOM that absorbs light. Photosensitizers are an important source of reactive oxygen species (ROS) in aerosols. Studies have shown that marine CDOM is present in atmospheric aerosols,[24, 25] and that it can perform the same types of photosensitized chemistry as in bulk solutions.[26, 27] There have been multiple studies showing that the presence of photosensitizers and salt increase the photodegradation of anthropogenic compounds in bulk water, including BPA.[28-32] Prior work in this group has investigated the photochemical degradation of BPA in different SSA-mimicking aerosol systems, including photosensitizers (4-benzoylbenzoic acid (4-BBA) and

humic acid (HA)) and salt (NaCl). 4-BBA and HA have been used as proxies for real marine CDOM; however, they differ chemically in their elemental ratios, with marine CDOM containing more nitrogen associated with amino acids, which was found to lead to less photosensitized degradation of nonanoic acid compared to HA and 4-BBA.[33] Kruse and Slade, 2023 found that 4-BBA and HA can enhance BPA photodegradation by a factor of three compared to pure BPA in the presence of 369 nm light.[34] However, NaCl inhibited photosensitized degradation of BPA when mixed with either 4-BBA or HA, attributed to quenching of the photosensitizers triplet state.[34]

One of the factors regulating the photolytic and photosensitized lifetimes of BPA in bulk water[28, 30, 35] that has not yet been investigated in the aerosol phase is pH. As reported in Angle et al., 2021, the pH of nascent, or freshly-emitted, SSA is significantly more acidic than the bulk ocean water and the sea surface microlayer, from a pH of 8.1 in bulk water to a pH as low as 2 in SSA between 0.1-1µm.[36] In this work, the photodegradation of pure BPA, BPA in the presence of the photosensitizer 4-BBA, and BPA in the presence of 4-BBA and NaCl is explored at a bulk atomizer solution pH of 3 and 11.

5.3 Methods

An extractive electrospray ionization time-of-flight mass spectrometer (EESI-TOF; Aerodyne Research Inc and Tofwerk AG)[34, 37, 38] was utilized to measure the concentrations of BPA and its transformation products in the aerosol phase. Briefly, a reagent ion spray was generated by passing the reagent solution through a 365 μm OD fused silica capillary (IDEX Health and Science, LLC) at a pressure of 350 mbar and charged at a voltage of -2500V. The EESI-TOF was operated in negative mode using a reagent solution of 2% (by mass) acetic acid (99.7%, Fisher Chemical), 48% H2O (18mΩ, Millipore Synergy System), and 50% acetonitrile (≥99.95%, Fisher Chemical) spiked with 100 ppm sodium iodide (99%, Sigma-Aldrich) for mass calibration purposes. The aerosol was sampled through the EESI-TOF inlet at a rate of 1 liter per minute

(LPM) and mixed orthogonally with the reagent ion spray. The mixed aerosol/reagent ion droplets were then heated and volatilized at a temperature of 220°C. Under these conditions, ionization occurred primarily via deprotonation and BPA was detected at *m/z*=227.107753 with an elemental formula of $C_{15}H_{15}O_2^-$. BPA has two different pKas at 9.59 and 10.2 as shown in Figure 5.1.

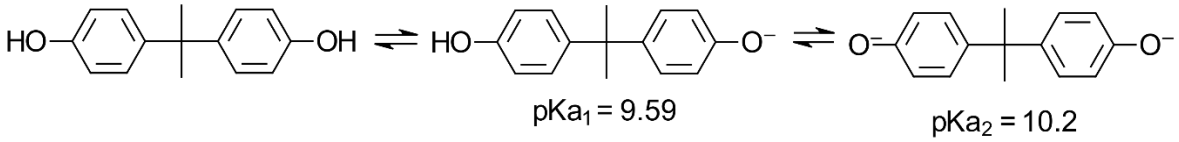

Figure 5.1 Two-dimensional chemical structure of BPA in its neutral, anionic, and dianionic forms[35]

Solutions of 25/75 (% by mass) water/methanol (≥99.9%, Fisher Chemical) were prepared with 100 ppm of BPA (≥99%, Sigma-Aldrich), 4-benzoylbenzoic acid (4-BBA; 99%, ACROS Organics), and sodium chloride (99.5%, Fisher Chemical). To modulate the pH of the solutions, 37% HCl in H_2O (>97% purity, Fisher Scientific) and NaOH (≥97%, Sigma-Aldrich) were added to the solutions, and the pH of the solutions was confirmed with a pH meter (Model IQ 150, I.Q. Scientific Instruments). These conditions resulted in an average pH of 3.0±0.1 and 11.2±0.2 for the low and high pH experiments, respectively, for all systems. The pH for the data from Kruse at Slade et al. 2023 is 5.8±0.1.[34] For ease of reading, the systems will be referred to as pH 3, 6, and 11 respectively. It is assumed because the pKa_1=9.59 and pKa_2=10.6 for BPA that BPA remained in its molecular form for the low pH experiments and its dianionic form for the higher pH experiments (Figure 5.1).[35, 39] For 4-BBA with a predicted pKa=3.79, it is anticipated to be in its molecular form during the low pH experiments and its anionic form for the high pH experiments. Particle- and hydrocarbon-free zero air (Airgas) was used as carrier flow. The solution was then atomized by zero air using a constant output atomizer (Model 3076, TSI Inc.) and directed through a silica bead diffusion dryer and an activated charcoal denuder to dry the aerosol particles and remove volatile species. A secondary activated charcoal denuder scrubbed MeOH and other

volatile hydrocarbons. The aerosol was then neutralized, and size selected by a differential mobility analyzer (Model 2100; Brechtel) to generate monodisperse aerosol with a nominal electrical mobility diameter of 100 nm to maintain size consistency across experiments.

The aerosol was exposed to 369nm light in a potential aerosol mass oxidative flow reactor (PAM-OFR; Aerodyne Research Inc.). The PAM-OFR was equipped with four interchangeable, narrowband lamps operated at wavelengths of 369nm (F436T5/BLC/4P-369; Aerodyne Research, Inc.) and arranged concentrically along the inner walls and protected by a quartz sheath tube and cooled with a gentle flow of nitrogen. The residence time inside the PAM-OFR was adjusted by adjusting the dilution flow rate, with three residence time settings of 219s, 253s, and 301s. The light intensity inside the PAM-OFR was adjusted with a ballast and measured with a photodetector (TOCON-C6, sglux GmbH).

All mass spectrometer datasets were processed in Tofware version 3.3.0 (Aerodyne LLC and Tofwerk AG), which ran in Igor Pro 9 (Wavemetrics). Mass spectral peaks were assigned based upon elemental formulae applying high-resolution peak fitting analysis at a nominal mass resolution ($m/\Delta m$) ~4000 for *m/z* 59 (CH_3COO^-) in negative mode. Once the aerosol concentration stabilized in the PAM-OFR, the lights were turned on and off in seven-minute intervals. Background signal intensities (blanks) were acquired at the start and end of each trial after passing the aerosol flow through a HEPA filter (99.99% removal efficiency at 0.1 μm), which was subtracted from the BPA sample signal intensity. The BPA intensity was normalized to the CH_3COO^- intensity before further manipulation. Because each run had a t_0 concentration of BPA, no further correction was applied.

5.4 Results and Discussion

Influence of aerosol pH on EESI Sensitivity

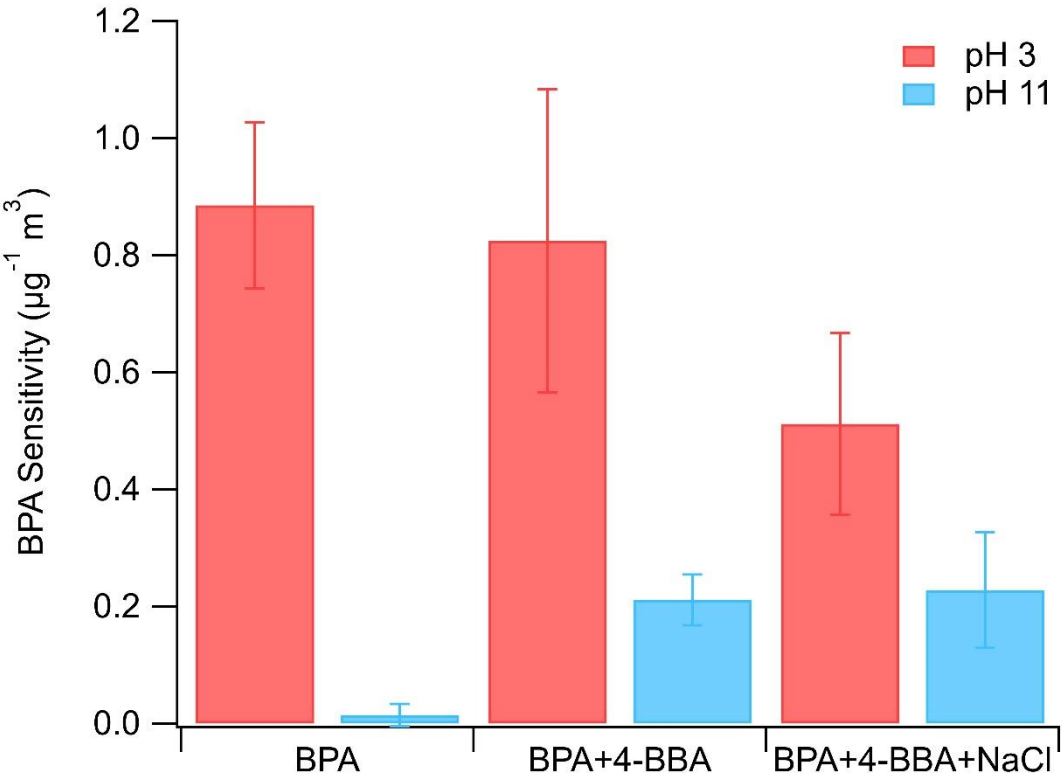

Figure 5.2 BPA sensitivity is presented as a function of the three aerosol systems at pH 3 (red bars) and pH 11 (blue bars). The error bars represent the standard deviation of three trials.

pH is an important consideration for detection of different small molecules in standard electrospray ionization (ESI), but their effects on EESI sensitivity, to our knowledge, have not been investigated. Figure 5.2 shows the sensitivity of BPA in all three aerosol systems with pH 3 and pH 11. BPA sensitivity was calculated as the slope of the linear fit of normalized BPA intensity versus total aerosol mass. In the low pH experiments, EESI-TOF sensitivity to BPA decreased from 0.885(±0.142) μg^{-1} m^3 for pure BPA aerosol to 0.824(±0.259) μg^{-1} m^3 in BPA+4-BBA and 0.511(±0.155) μg^{-1} m^3 in BPA+4-BBA+NaCl. These sensitivities have been adjusted for changing quantities of BPA in each particle system. In other words, we expect that when two components are well mixed as in the 1:1 BPA:4-BBA mixture, the relative BPA mass concentration to the total

aerosol mass concentration reduces by half and the sensitivity would also decrease by half. To amend this, the sensitivity of BPA presented here is x2 and x3 the original values in the BPA+4-BBA and BPA+4-BBA+NaCl cases respectively. Interestingly, there is a decrease in sensitivity when NaCl is added to the system. This could be due to peak splitting from adduct formation. In ESI, one of the driving reasons that the presence of salt causes signal suppression of different analytes is because the analytes can form adducts with the salt ions.[40] However, because the EESI-TOF in negative mode is tuned for the transmission of deprotonated ions, these formed adducts may not be effectively transmitted to the TOF, as these adducts are not observed in the mass spectra.

At pH 11, the sensitivity decreases significantly compared to pH 3. For pure-component BPA aerosols, the sensitivity is 0.014(±0.019) μg^{-1} m^3 or about 63x less than in pH 3 solution. The sensitivities for the BPA+4-BBA and BPA+4-BBA+NaCl systems improved slightly, increasing to 0.211(± 0.043) μg^{-1} m^3 and 0.228(±0.099) μg^{-1} m^3 respectively. Prior EESI work has shown that sensitivity depends on the sample particle size.[41, 42] In this study, the sample particle size was held constant at 100 nm and did not vary significantly between the outlet of the monodisperse aerosol generator and the inlet of the SEMS, as shown in Figure 5.4. Therefore, these sensitivity changes are not due to changes in particle size. In the pH 11 solution, BPA is likely to be doubly deprotonated (as shown in Figure 5.1), which could change the *m/z* where BPA is detected. However, there is no discernable change in the mass spectra at the doubly deprotonated mass (*m/z* 113) or any potential clusters. It is also possible that this decrease in detection could be due to the incoming aerosol neutralizing the reagent ion spray. Considering that acetic acid, the ion within the reagent ion spray, is a weak acid whereas the sample droplets contained a strong base, if this were the case, the reaction would proceed as follows in R 5.3:

CH_3COOH (spray) + NaOH (sample) → CH_3COONa (coalesced droplet) + H_2O R 5.3

While the difference between the sample aerosol and reagent ion spray particle mass is significant (1000x assuming a reagent ion spray of 1μm diameter), atomized aerosols are also significantly more concentrated than the bulk solution they sample from due to evaporation of the solvent. The neutralization of the reagent ion spray due to an acidic reagent spray and basic particle sample has also been seen in Law et al. 2010, where a pH sensitive dye showed less fluoresence when the droplets coalesced.[43] If this reaction dominates upon collision between the aerosol sample and the electrospray droplet, Na^+ would compete with neutral and anionic forms of BPA for CH_3COO^- leaving less CH_3COO^- to react with BPA. A similar process involving reaction of Na^+ with anionic forms of BPA could form neutral salt clusters with BPA as shown in R 5.4, and since NaOH is a strong base, the salt clusters may be more energetically favorable than deprotonation of the BPA molecules in these conditions.

$$Na^+ + C_{15}H_{15}O_2^- \rightarrow C_{15}H_{15}O_2Na \qquad \text{R 5.4}$$

Beyond the solution ionization mechanism, it is also important to consider the droplet dynamics of EESI and how they are dissimilar from ESI. Work by Liu et al. 2011 found that contrary to what would be expected for particles coalescing, droplets of different pH oppose each other and do not coalesce.[44] They worked with emulsions, which are a type of colloidal suspension. Coalesence of droplets in an emulsion (through electrostatic attraction of the droplets) would lead to the destruction of the suspension, which was anticipated with the oppositely charged droplets. In this work, they conclude that electrostatic attraction is not a full explanation for how these droplets behave, but that the full mechanism is not fully understood and needs to be investigated further.

BPA Photodecomposition Rates at Different pH in Pure-, Binary-, and Ternary-Component Aerosol Mixtures

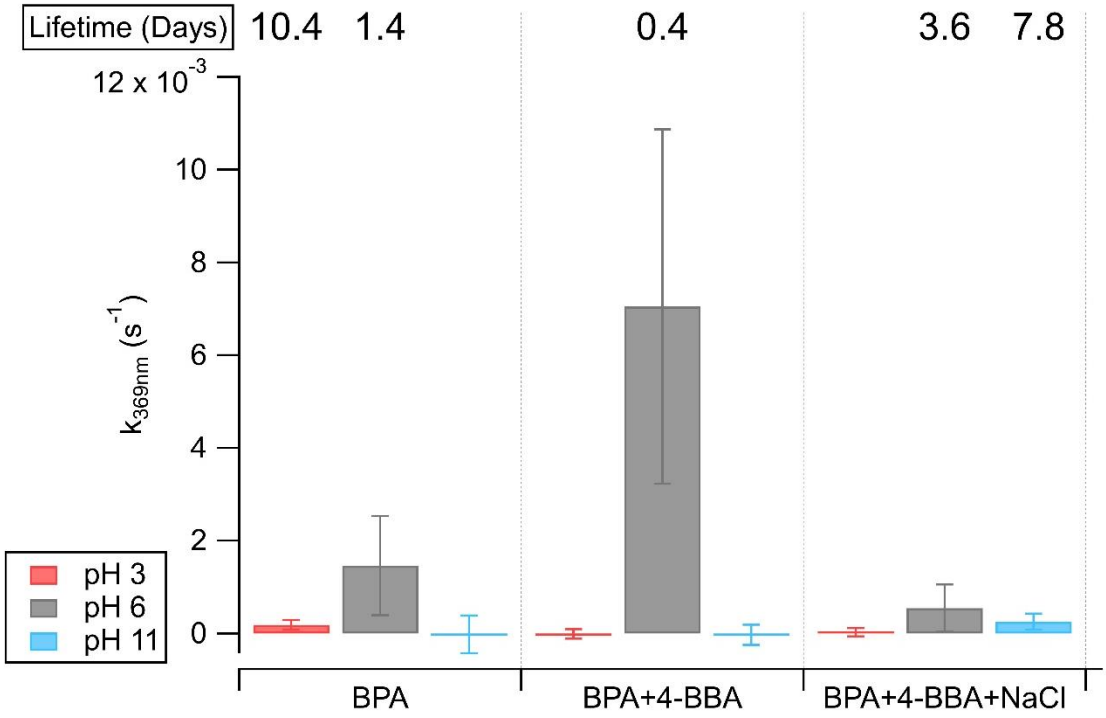

Figure 5.3 Bar chart of the measured first-order rate constants (y-axis) of the three different aerosol systems at pH 3.0±0.1 (red), pH 5.8±0.1 (grey, Kruse and Slade et al. 2023)[34], and pH 11.2±0.2 (blue). Estimated atmospheric lifetimes are presented on the top axis for systems that had statistically significant (at least 1σ) k_{369nm} values.

Figure 5.3 shows the first-order rate constant of BPA degraded by 369nm light, k_{369nm}, for all three aerosol systems (BPA, BPA+4-BBA, and BPA+4-BBA+NaCl) at three different pH (3, 6, and 11). The pH 6 data was published in Kruse and Slade et al. 2023.[34] The data used for the calculation of k_{369nm} are presented in Figure 5.5. In the pH 3 experiments, the only system which had statistically significant (at least 1σ) degradation of BPA was BPA alone ($1.83\times10^{-4} \pm 1.05\times10^{-4}$ s^{-1}), and in the pH 11 experiments, only the BPA+4-BBA+NaCl had statistically significant degradation of BPA ($2.52\times10^{-4} \pm 1.71\times10^{-4}$ s^{-1}).

For the BPA system at the three pH settings, the degradation increases between pH 3 and pH 6, from $1.83\times10^{-4} \pm 1.05\times10^{-4}$ s^{-1} to $1.46\times10^{-4} \pm 1.07\times10^{-4}$ s^{-1} and is not observed at pH 11.

Wang et al. 2007 demonstrated that in bulk solution when irradiated with 254nm light, BPA degradation increases significantly with increasing pH.[28] This was attributed to the deprotonation of BPA at the high pH, leading to increased light absorbance in the 240nm to 260nm range. Increased degradation at higher pH has also been seen for other bisphenols, such as bisphenol-s, which was also attributed to deprotonation of the bisphenol at higher pH enabling more extensive absorption of incoming light.[29] Wang et al. 2007 also demonstrated that under irradiation by 365nm light at pH 7, BPA has a degradation rate of 2.9×10^{-4} s^{-1}, which is slightly higher than seen here for pH 3, and an order of magnitude lower than at pH 6.[28] These discrepancies may be due to differences in phase. In Nissenson et al 2006, there was an enhancement observed in the photolysis of a molybdenum complex in the aerosol compared to the bulk phase.[45] Their conclusion was that in the bulk solution phase, there is an effect called the "solvent cage", where photoproducts are temporarily stabilized by surrounding solvent, and can recombine with the original molecule. This is not expected in aerosols because of the smaller amount of solvent remaining in the particle phase and some partitioning of the photoproducts into the gas phase. This effect has also been seen for the photodissociation of OClO at the liquid-gas interface when compared to the bulk of solution.[46]

In the BPA+4-BBA system, degradation was only observed at pH 6, at $7.05\times10^{-3} \pm 3.82\times10^{-3}$ s^{-1}. Multiple studies have found that BPA degradation increases in the presence of photosensitizing material.[12, 31] However, few have investigated the influence of pH. Tsai et al. found that when using TiO_2 as a photocatalyst at pH 3, photodegradation of BPA is slower than at pH 6, and then decreases again at pH 11, which is quite similar to the results seen here, and it is possible that with a longer residence time, degradation would be seen at pH 3 and 11.[30] Work from Bilski et al found that the quantum yield of $^1O_2$ (type II photosensitization) by the photosensitizer norfloxacin is highly pH dependent, with a sharp increase in yield at pH 3.4 and a subsequent

decrease at pH 7.4.[47] In contrast, work by Horiuchi et al. 2016 found that for amino-substituted tetraphenylporphorins, the type II photosensitization pathway is very weak when the molecule is in its neutral form, and it is the acidic moieties that allow the porphorins to behave as photosensitizers.[48] Comparing the results in Kruse and Slade 2023, pure BPA will degrade on its own under irradiation by 369nm light, but there is a clear increase in the degradation with the addition of the photosensitizer, which may indicate that the pH influence of the mechanism would follow those for either type I or II photosensitizers rather than photolysis. However, it is still unclear which pathway would be dominant.

In the BPA+4-BBA+NaCl system, the rates of degradation are within error of each other for the pH 5 and pH 11 system (k_{369nm}= $5.45\times10^{-4} \pm 5.12\times10^{-4}$ s^{-1} and $2.52\times10^{-4} \pm 1.71\times10^{-4}$ s^{-1}), and degradation is not observed in the pH 3 system. Zhang et al. 2019 found that in solutions with high ionic strength from NaCl, photodegradation of oxytetracycline was diminished,[49] with the same conclusion from Kruse and Slade 2023, that the energized triplet state photosensitizer is being quenched by the chloride anions present in the solution, which was discovered by Tinel et al. 2014.[50]

It is suspected that the lack of degradation rate for the organic pH 11 systems but observed degradation for the BPA+4-BBA+NaCl system may be due to the poor sensitivity of BPA at pH 11, and not due to a lack of photosensitized reactions. As shown in our lab's prior work, even at 80% RH, the pure organic systems have semisolid viscosities, and the organic/inorganic systems are liquid.[50, 51] The reason that the BPA+4-BBA+NaCl system was not negatively influenced by the pH effects as discussed in the previous section is potentially because BPA in its dianionic form (nonpolar) will likely be enhanced at the surface of that aerosol system due to the salting out

effect,[51, 52] mitigating the decrease in sensitivity, coupled with the lower viscosity of the particle system.

For the systems with observed degradation of BPA, the estimated atmospheric lifetime was calculated using Eq. 5.1:

$$\tau = \frac{1}{k_{369nm}} * \frac{F_{San\ Diego}}{F_{PAM-OFR}} * \frac{1}{43{,}200} \quad \text{Eq. 5.1}$$

Where t is the characteristic lifetime, k_{369nm} is the pseudo first order rate constant, $F_{San\ Diego}$ is the average photon flux of 369nm light in San Diego during the summertime afternoon (2.02×10^{13} photons s^{-1} cm^{-2}), $F_{PAM\text{-}OFR}$ is the photon flux inside the PAM-OFR at the voltage setting used in these experiments (1.78×10^{15} photons s^{-1} cm^{-2}), and 43,200 is the number of seconds in 12 hours, so that the lifetime accounts for nighttime. In the BPA+4-BBA+NaCl system, which is the closest approximation to real SSA in this study, the lifetime of BPA is approximated to be between 3.6-7.8 days in the atmosphere.

5.5 Conclusions

In this work, we demonstrate that at low pH, BPA photodegradation is inhibited with and without the presence of a photosensitizer. The results are less clear for the high pH condition, but in the BPA+4-BBA+NaCl system, it appears to be in the same range as the neutral condition. The calculated first-order photodegradation rate constants were on the order of 10^{-4} s^{-1} for all the aerosol mixtures in this work. Putting these results in a broader context, this may indicate that BPA found in real SSA would have a longer atmospheric lifetime than BPA in other systems, such as plastic-burning aerosol. While studies on the pH of plastic-burning aerosols are limited, Balasubramanian et al. 1999 found that the pH of rain after the Indonesian forest fires of 1997 had pH values between 3.79 to 6.20, with a volume-weighted mean of 4.35.[53] It is important to consider that each unit of pH represents a ten-fold change in concentration of H^+, so in the comparison of the pH of SSA from Angle et al. 2021 of 2 versus even the low value from Balasubramanian et al.

1999 of 3.79, this is a 190x change in the concentration of H^+.[36] In the results shown here, that difference could mean nearly (1.9x) halving the lifetime of BPA in plastic-burning aerosols vs SSA.

This work also underscores the complexity of the EESI measurement, and the further steps that need to be taken by the community to make quantitative measurements. In the case of BPA being measured in negative mode, based on the results shown here, the quantitation of BPA in SSA versus a lab generated aerosol at a pH of 6 would underestimate the total concentration of BPA by roughly 60%. These considerations are especially important in EESI quantitation, where lab-generated calibration aerosols may or may not be within the relevant pH range for the ambient aerosol sample. For example, levoglucosan, a common tracer for biomass burning, has a pKa of 12.21. If the lab-based calibrations are performed at a neutral pH, but the pH of the ambient aerosol is the same as in Balasubramanian et al. 1999 of 3.79, this could result in serious discrepancies between the actual and measured quantity of levoglucosan and other common aerosol tracers. While this is less of an issue when EESI is paired with more traditionally quantitative methods such as the FIGAERO-CIMS, it is a major issue for EESI to be used as an independent measurement tool without further characterization.

5.6 Supplemental Information

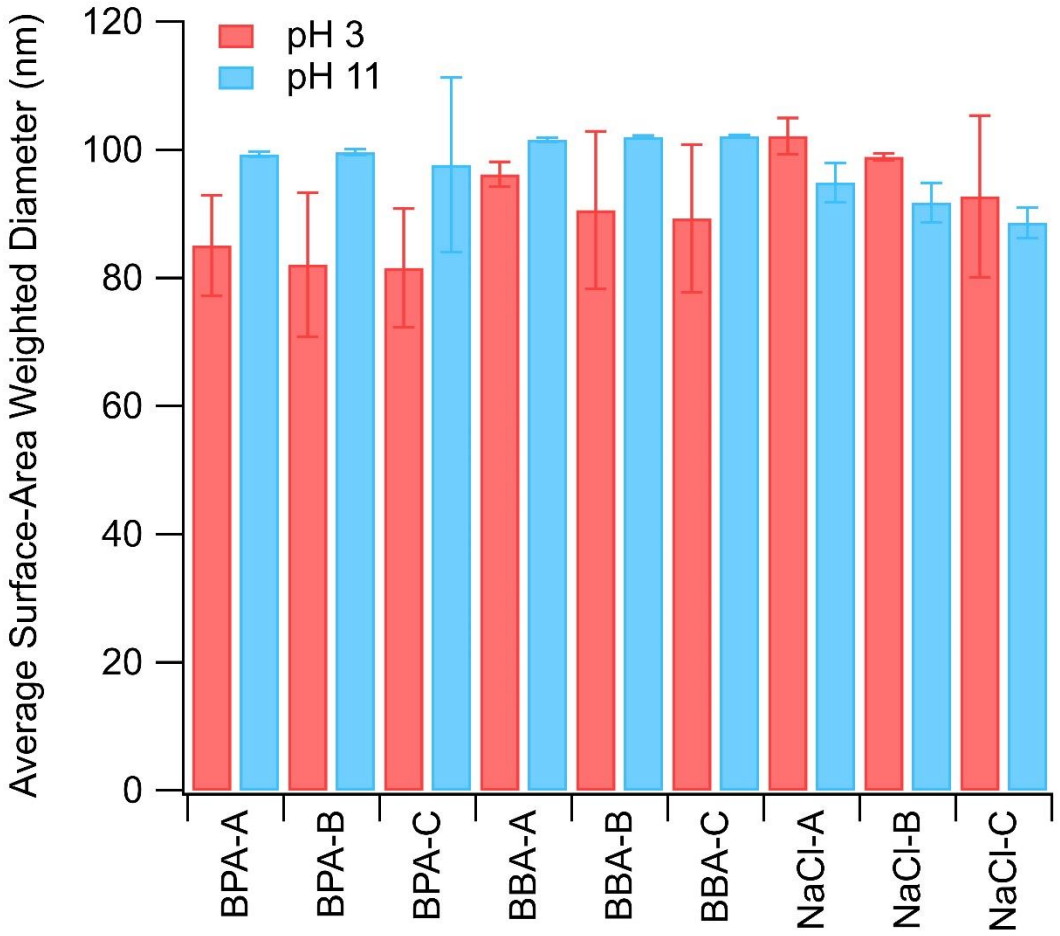

Figure 5.4 Average surface-area weighted diameter for each aerosol system at all three residence times (A=219s, B=253s, C=301s) for the pH 3 (red) and pH 11 (blue) systems. Error bars represent the standard deviation of three runs at each residence time.

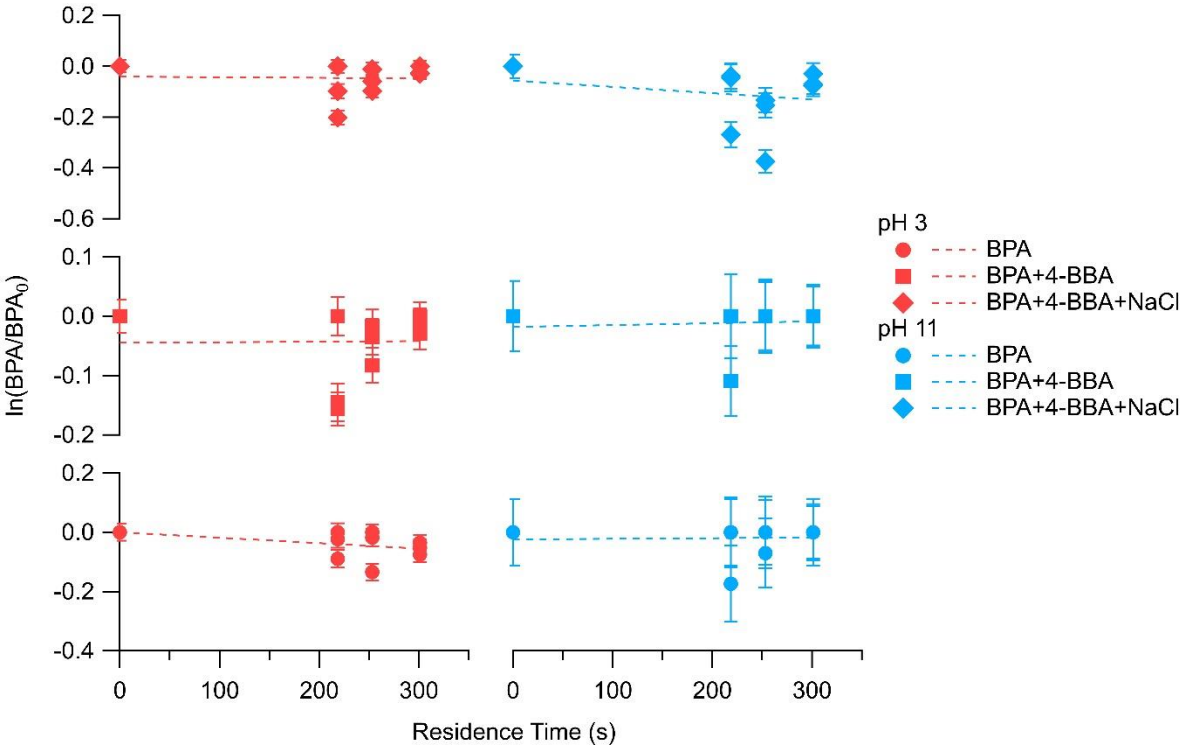

Figure 5.5 Linear fits to the first order decays for the six different aerosol systems.

5.7 Acknowledgements

Chapter 5, in full, is currently being prepared for submission for publication in American Chemical Society Environmental Science & Technology Air. Kruse, Samantha M., Slade, Jonathan H. The dissertation author was the primary researcher and author of this paper.

5.8 References

(1) Wright, S. L.; Kelly, F. J. Plastic and Human Health: A Micro Issue? *Environ. Sci. Technol.* **2017**, *51* (12), 6634-6647. DOI: 10.1021/acs.est.7b00423.

(2) Eriksen, M.; Cowger, W.; Erdle, L. M.; Coffin, S.; Villarrubia-Gómez, P.; Moore, C. J.; Carpenter, E. J.; Day, R. H.; Thiel, M.; Wilcox, C. A growing plastic smog, now estimated to be over 170 trillion plastic particles afloat in the world's oceans-Urgent solutions required. *PLoS One* **2023**, *18* (3), e0281596. DOI: 10.1371/journal.pone.0281596.

(3) Luo, H.; Zhao, Y.; Li, Y.; Xiang, Y.; He, D.; Pan, X. Aging of microplastics affects their surface properties, thermal decomposition, additives leaching and interactions in simulated fluids. *Sci. Total Environ.* **2020**, *714*, 136862. DOI: 10.1016/j.scitotenv.2020.136862.

(4) Chen, Q.; Allgeier, A.; Yin, D.; Hollert, H. Leaching of endocrine disrupting chemicals from marine microplastics and mesoplastics under common life stress conditions. *Environ. Int.* **2019**, *130*, 104938. DOI: 10.1016/j.envint.2019.104938.

(5) Romera-Castillo, C.; Birnstiel, S.; Álvarez-Salgado, X. A.; Sebastián, M. Aged Plastic Leaching of Dissolved Organic Matter Is Two Orders of Magnitude Higher Than Virgin Plastic Leading to a Strong Uplift in Marine Microbial Activity. *Frontiers in Marine Science* **2022**, *9*. DOI: 10.3389/fmars.2022.861557.

(6) Haffner, D.; Schecter, A. Persistent Organic Pollutants (POPs): A Primer for Practicing Clinicians. *Current Environmental Health Reports* **2014**, *1* (2), 123-131. DOI: 10.1007/s40572-014-0009-9.

(7) Pakalin, S. A., K.; Munn, S. Updated European Union risk assessment report 4,4'-isopropylidenediphenol (bisphenol-A)

Human health addendum of February 2008. **2010**. DOI: 10.2788/40195.

(8) Fenichel, P.; Chevalier, N.; Brucker-Davis, F. Bisphenol A: an endocrine and metabolic disruptor. *Ann. Endocrinol.* **2013**, *74* (3), 211-220. DOI: 10.1016/j.ando.2013.04.002.

(9) Rubin, B. S. Bisphenol A: an endocrine disruptor with widespread exposure and multiple effects. *J. Steroid Biochem. Mol. Biol.* **2011**, *127* (1-2), 27-34. DOI: 10.1016/j.jsbmb.2011.05.002.

(10) Seachrist, D. D.; Bonk, K. W.; Ho, S.-M.; Prins, G. S.; Soto, A. M.; Keri, R. A. A review of the carcinogenic potential of bisphenol A. *Reprod. Toxicol.* **2016**, *59*, 167-182. DOI: 10.1016/j.reprotox.2015.09.006.

(11) Moreman, J.; Lee, O.; Trznadel, M.; David, A.; Kudoh, T.; Tyler, C. R. Acute toxicity, teratogenic, and estrogenic effects of bisphenol A and its alternative replacements bisphenol S, bisphenol F, and bisphenol AF in zebrafish embryo-larvae. *Environ. Sci. Technol.* **2017**, *51* (21), 12796-12805. DOI: 10.1021/acs.est.7b03283.

(12) Kang, J.-H.; Kondo, F. Bisphenol A degradation in seawater is different from that in river water. *Chemosphere* **2005**, *60* (9), 1288-1292. DOI: 10.1016/j.chemosphere.2005.01.058.

(13) Xie, J.; Zhao, N.; Zhang, Y.; Hu, H.; Zhao, M.; Jin, H. Occurrence and partitioning of bisphenol analogues, triclocarban, and triclosan in seawater and sediment from East China Sea. *Chemosphere* **2022**, *287* (Pt 2), 132218. DOI: 10.1016/j.chemosphere.2021.132218.

(14) Kawahata, H.; Ohta, H.; Inoue, M.; Suzuki, A. Endocrine disrupter nonylphenol and bisphenol A contamination in Okinawa and Ishigaki Islands, Japan—within coral reefs and adjacent river mouths. *Chemosphere* **2004**, *55* (11), 1519-1527. DOI: 10.1016/j.chemosphere.2004.01.032.

(15) Yamamoto, T.; Yasuhara, A.; Shiraishi, H.; Nakasugi, O. Bisphenol A in hazardous waste landfill leachates. *Chemosphere* **2001**, *42* (4), 415-418. DOI: 10.1016/s0045-6535(00)00079-5.

(16) Fu, P.; Kawamura, K. Ubiquity of bisphenol A in the atmosphere. *Environ. Pollut.* **2010**, *158* (10), 3138-3143. DOI: 10.1016/j.envpol.2010.06.040.

(17) Stefan, R. L.; Szeri, A. J. Surfactant Scavenging and Surface Deposition by Rising Bubbles. *J. Colloid Interface Sci.* **1999**, *212* (1), 1-13. DOI: 10.1006/jcis.1998.6037.

(18) Jayarathne, T.; Sultana, C. M.; Lee, C.; Malfatti, F.; Cox, J. L.; Pendergraft, M. A.; Moore, K. A.; Azam, F.; Tivanski, A. V.; Cappa, C. D.; Bertram, T. H.; Grassian, V. H.; Prather, K. A.; Stone, E. A. Enrichment of Saccharides and Divalent Cations in Sea Spray Aerosol During Two Phytoplankton Blooms. *Environ. Sci. Technol.* **2016**, *50* (21), 11511-11520. DOI: 10.1021/acs.est.6b02988.

(19) Mathieu-Denoncourt, J.; Wallace, S. J.; de Solla, S. R.; Langlois, V. S. Influence of Lipophilicity on the Toxicity of Bisphenol A and Phthalates to Aquatic Organisms. *Bull. Environ. Contam. Toxicol.* **2016**, *97* (1), 4-10. DOI: 10.1007/s00128-016-1812-9.

(20) Wang, X.; Deane, G. B.; Moore, K. A.; Ryder, O. S.; Stokes, M. D.; Beall, C. M.; Collins, D. B.; Santander, M. V.; Burrows, S. M.; Sultana, C. M.; Prather, K. A. The role of jet and film drops in controlling the mixing state of submicron sea spray aerosol particles. *Proc. Natl. Acad. Sci. U. S. A.* **2017**, *114* (27), 6978-6983. DOI: 10.1073/pnas.1702420114.

(21) Van Acker, E.; Huysman, S.; De Rijcke, M.; Asselman, J.; De Schamphelaere, K. A. C.; Vanhaecke, L.; Janssen, C. R. Phycotoxin-Enriched Sea Spray Aerosols: Methods, Mechanisms, and Human Exposure. *Environ. Sci. Technol.* **2021**, *55* (9), 6184-6196. DOI: 10.1021/acs.est.1c00995.

(22) Johansson, J. H.; Salter, M. E.; Acosta Navarro, J. C.; Leck, C.; Nilsson, E. D.; Cousins, I. T. Global transport of perfluoroalkyl acids via sea spray aerosol. *Environ. Sci. Process. Impacts* **2019**, *21* (4), 635-649. DOI: 10.1039/c8em00525g.

(23) Sha, B.; Johansson, J. H.; Tunved, P.; Bohlin-Nizzetto, P.; Cousins, I. T.; Salter, M. E. Sea Spray Aerosol (SSA) as a Source of Perfluoroalkyl Acids (PFAAs) to the Atmosphere: Field Evidence from Long-Term Air Monitoring. *Environ. Sci. Technol.* **2022**, *56* (1), 228-238. DOI: 10.1021/acs.est.1c04277.

(24) Kieber, R. J.; Whitehead, R. F.; Reid, S. N.; Willey, J. D.; Seaton, P. J. Chromophoric Dissolved Organic Matter (CDOM) In Rainwater, Southeastern North Carolina, USA. *J. Atmos. Chem.* **2006**, *54* (1), 21-41. DOI: 10.1007/s10874-005-9008-4.

(25) Chen, Q.; Miyazaki, Y.; Kawamura, K.; Matsumoto, K.; Coburn, S.; Volkamer, R.; Iwamoto, Y.; Kagami, S.; Deng, Y.; Ogawa, S.; Ramasamy, S.; Kato, S.; Ida, A.; Kajii, Y.; Mochida, M. Characterization of chromophoric water-soluble organic matter in urban, forest, and marine aerosols by HR-ToF-AMS analysis and excitation-emission matrix spectroscopy. *Environ. Sci. Technol.* **2016**, *50* (19), 10351-10360. DOI: 10.1021/acs.est.6b01643.

(26) Kaur, R.; Anastasio, C. First Measurements of Organic Triplet Excited States in Atmospheric Waters. *Environ. Sci. Technol.* **2018**, *52* (9), 5218-5226. DOI: 10.1021/acs.est.7b06699.

(27) Corral Arroyo, P.; Bartels-Rausch, T.; Alpert, P. A.; Dumas, S.; Perrier, S.; George, C.; Ammann, M. Particle-Phase Photosensitized Radical Production and Aerosol Aging. *Environ. Sci. Technol.* **2018**, *52* (14), 7680-7688. DOI: 10.1021/acs.est.8b00329.

(28) Wang, B.; Wu, F.; Li, P.; Deng, N. UV-light induced photodegradation of bisphenol a in water: Kinetics and influencing factors. *React. Kinet. Catal. Lett.* **2007**, *92* (1), 3-9. DOI: 10.1007/s11144-007-5045-0.

(29) Cao, G.; Lu, J.; Wang, G. Photolysis kinetics and influencing factors of bisphenol S in aqueous solutions. *J. Environ. Sci.* **2012**, *24* (5), 846-851. DOI: 10.1016/s1001-0742(11)60809-7.

(30) Tsai, W.-T.; Lee, M.-K.; Su, T.-Y.; Chang, Y.-M. Photodegradation of bisphenol-A in a batch TiO_2 suspension reactor. *J. Hazard. Mater.* **2009**, *168* (1), 269-275. DOI: 10.1016/j.jhazmat.2009.02.034.

(31) Zhan, M.; Yang, X.; Xian, Q.; Kong, L. Photosensitized degradation of bisphenol A involving reactive oxygen species in the presence of humic substances. *Chemosphere* **2006**, *63* (3), 378-386. DOI: 10.1016/j.chemosphere.2005.08.046.

(32) Gmurek, M.; Olak-Kucharczyk, M.; Ledakowicz, S. Photochemical decomposition of endocrine disrupting compounds – A review. *Chem. Eng. J.* **2017**, *310*, 437-456. DOI: 10.1016/j.cej.2016.05.014.

(33) Trueblood, J. V.; Alves, M. R.; Power, D.; Santander, M. V.; Cochran, R. E.; Prather, K. A.; Grassian, V. H. Shedding Light on Photosensitized Reactions within Marine-Relevant Organic Thin Films. *ACS Earth Space Chem.* **2019**, *3* (8), 1614-1623. DOI: 10.1021/acsearthspacechem.9b00066.

(34) Kruse, S. M.; Slade, J. H. Heterogeneous and Photosensitized Oxidative Degradation Kinetics of the Plastic Additive Bisphenol-A in Sea Spray Aerosol Mimics. *J. Phys. Chem. A* **2023**, *127* (21), 4724-4733. DOI: 10.1021/acs.jpca.3c00127.

(35) Staples, C. A.; Dome, P. B.; Klecka, G. M.; Oblock, S. T.; Harris, L. R. A review of the environmental fate, effects, and exposures of bisphenol A. *Chemosphere* **1998**, *36* (10), 2149-2173. DOI: 10.1016/S0045-6535(97)10133-3.

(36) Angle, K. J.; Crocker, D. R.; Simpson, R. M. C.; Mayer, K. J.; Garofalo, L. A.; Moore, A. N.; Mora Garcia, S. L.; Or, V. W.; Srinivasan, S.; Farhan, M.; Sauer, J. S.; Lee, C.; Pothier, M. A.; Farmer, D. K.; Martz, T. R.; Bertram, T. H.; Cappa, C. D.; Prather, K. A.; Grassian, V. H. Acidity across the interface from the ocean surface to sea spray aerosol. *Proc. Natl. Acad. Sci. U. S. A.* **2021**, *118* (2), e2018397118. DOI: 10.1073/pnas.2018397118.

(37) Tumminello, P. R.; James, R. C.; Kruse, S.; Kawasaki, A.; Cooper, A.; Guadalupe-Diaz, I.; Zepeda, K. L.; Crocker, D. R.; Mayer, K. J.; Sauer, J. S.; Lee, C.; Prather, K. A.; Slade, J. H. Evolution of Sea Spray Aerosol Particle Phase State Across a Phytoplankton Bloom. *ACS Earth Space Chem.* **2021**, *5* (11), 2995-3007. DOI: 10.1021/acsearthspacechem.1c00186.

(38) Felipe D. Lopez-Hilfiker; Veronika Pospisilova; Wei Huang; Markus Kalberer; Claudia Mohr; Giulia Stefenelli; Joel A. Thornton; Urs Baltensperger; Andre S. H. Prevot; Slowik, J. G. An extractive electrospray ionization time-of-flight mass spectrometer (EESI-TOF) for online measurement of atmospheric aerosol particles. *Atmospheric* **2019**. DOI: 10.5194/amt-12-4867-2019.

(39) Corrales, J.; Kristofco, L. A.; Steele, W. B.; Yates, B. S.; Breed, C. S.; Williams, E. S.; Brooks, B. W. Global Assessment of Bisphenol A in the Environment: Review and Analysis of Its Occurrence and Bioaccumulation. *Dose Response* **2015**, *13* (3), 1559325815598308. DOI: 10.1177/1559325815598308.

(40) Metwally, H.; McAllister, R. G.; Konermann, L. Exploring the mechanism of salt-induced signal suppression in protein electrospray mass spectrometry using experiments and molecular dynamics simulations. *Anal. Chem.* **2015**, *87* (4), 2434-2442. DOI: 10.1021/ac5044016.

(41) Surdu, M.; Pospisilova, V.; Xiao, M.; Wang, M.; Mentler, B.; Simon, M.; Stolzenburg, D.; Hoyle, C. R.; Bell, D. M.; Lee, C. P.; Lamkaddam, H.; Lopez-Hilfiker, F.; Ahonen, L. R.; Amorim, A.; Baccarini, A.; Chen, D.; Dada, L.; Duplissy, J.; Finkenzeller, H.; He, X.-C.; Hofbauer, V.; Kim, C.; Kürten, A.; Kvashnin, A.; Lehtipalo, K.; Makhmutov, V.; Molteni, U.; Nie, W.; Onnela, A.; Petäjä, T.; Quéléver, L. L. J.; Tauber, C.; Tomé, A.; Wagner, R.; Yan, C.; Prevot, A. S. H.; Dommen, J.; Donahue, N. M.; Hansel, A.; Curtius, J.; Winkler, P. M.; Kulmala, M.; Volkamer, R.; Flagan, R. C.; Kirkby, J.; Worsnop, D. R.; Slowik, J. G.; Wang, D. S.; Baltensperger, U.; El Haddad, I. Molecular characterization of ultrafine particles using extractive electrospray time-of-flight mass spectrometry. *Environ Sci Atmos* **2021**, *1* (6), 434-448. DOI: 10.1039/d1ea00050k.

(42) Lee, C. P.; Surdu, M.; Bell, D. M.; Dommen, J.; Xiao, M.; Zhou, X.; Baccarini, A.; Giannoukos, S.; Wehrle, G.; Schneider, P. A.; Prevot, A. S. H.; Slowik, J. G.; Lamkaddam, H.; Wang, D.; Baltensperger, U.; El Haddad, I. High-frequency gaseous and particulate chemical characterization using extractive electrospray ionization mass spectrometry (Dual-Phase-EESI-

TOF). *Atmospheric Measurement Techniques* **2022**, *15* (12), 3747-3760. DOI: 10.5194/amt-15-3747-2022.

(43) Law, W. S.; Wang, R.; Hu, B.; Berchtold, C.; Meier, L.; Chen, H.; Zenobi, R. On the mechanism of extractive electrospray ionization. *Anal. Chem.* **2010**, *82* (11), 4494-4500. DOI: 10.1021/ac100390t.

(44) Liu, T.; Seiffert, S.; Thiele, J.; Abate, A. R.; Weitz, D. A.; Richtering, W. Non-coalescence of oppositely charged droplets in pH-sensitive emulsions. *Proc. Natl. Acad. Sci. U. S. A.* **2012**, *109* (2), 384-389. DOI: 10.1073/pnas.1019196109.

(45) Nissenson, P.; Knox, C. J. H.; Finlayson-Pitts, B. J.; Phillips, L. F.; Dabdub, D. Enhanced photolysis in aerosols: evidence for important surface effects. *Phys. Chem. Chem. Phys.* **2006**, *8* (40), 4700-4710. DOI: 10.1039/b609219e.

(46) Chorny, I.; Vieceli, J.; Benjamin, I. Photodissociation and Vibrational Relaxation of OClO at Liquid Surfaces. *J. Phys. Chem. B* **2003**, *107* (1), 229-236. DOI: 10.1021/jp021796m.

(47) Bilski, P.; Martinez, L. J.; Koker, E. B.; Chignell, C. F. Photosensitization by norfloxacin is a function of pH. *Photochem. Photobiol.* **1996**, *64* (3), 496-500. DOI: 10.1111/j.1751-1097.1996.tb03096.x.

(48) Horiuchi, H.; Kuribara, R.; Hirabara, A.; Okutsu, T. pH-Response Optimization of Amino-Substituted Tetraphenylporphyrin Derivatives as pH-Activatable Photosensitizers. *J. Phys. Chem. A* **2016**, *120* (28), 5554-5561. DOI: 10.1021/acs.jpca.6b05019.

(49) Zhang, Y.-N.; Zhao, J.; Zhou, Y.; Qu, J.; Chen, J.; Li, C.; Qin, W.; Zhao, Y.; Peijnenburg, W. J. G. M. Combined effects of dissolved organic matter, pH, ionic strength and halides on photodegradation of oxytetracycline in simulated estuarine waters. *Environ. Sci. Process. Impacts* **2019**, *21* (1), 155-162. DOI: 10.1039/c8em00473k.

(50) Tinel, L.; Dumas, S.; George, C. A time-resolved study of the multiphase chemistry of excited carbonyls: Imidazole-2-carboxaldehyde and halides. *C. R. Chim.* **2014**, *17* (7), 801-807. DOI: 10.1016/j.crci.2014.03.008.

(51) Fu, H.; Sun, Y.; Teng, H.; Zhang, D.; Xiu, Z. Salting-out extraction of carboxylic acids. *Sep. Purif. Technol.* **2015**, *139*, 36-42. DOI: 10.1016/j.seppur.2014.11.001.

(52) El Haber, M.; Ferronato, C.; Giroir-Fendler, A.; Fine, L.; Nozière, B. Salting out, non-ideality and synergism enhance surfactant efficiency in atmospheric aerosols. *Sci. Rep.* **2023**, *13* (1), 20672. DOI: 10.1038/s41598-023-48040-5.

(53) Balasubramanian, R.; Victor, T.; Begum, R. Impact of biomass burning on rainwater acidity and composition in Singapore. *J. Geophys. Res.* **1999**, *104* (D21), 26881-26890. DOI: 10.1029/1999jd900247.

Chapter 6 Conclusions

6.1 Synopsis

This thesis focused on probing the composition, heterogeneous oxidation kinetics, and photosensitized kinetics of SSA components with EESI-TOF. Chapter 3 targeted the oxidative degradation of BPA, an important plastic additive and environmental pollutant, in the aerosol phase via heterogeneous OH oxidation and photosensitized reactions in SSA mimics. Chapter 4 focused on high-temporal measurements of SSA molecular composition with EESI-TOF, the influence of biological activity on SSA molecular composition, and how varying relative humidity impacted the EESI efficiency. Lastly, Chapter 5 targeted the influence of pH on the degradation of aerosolized BPA in the presence of a photosensitizer, NaCl, and light. The main conclusions from each chapter and suggested future directions of related study are provided in the following sections.

6.2 Conclusions

Heterogeneous and Photosensitized Oxidative Degradation Kinetics of the Plastic Additive Bisphenol-A in Sea Spray Aerosol Mimics

Chapter 3, published in the *ACS Journal of Physical Chemistry A*,[1] reports the heterogeneous oxidation kinetics of BPA by OH and photochemical degradation of BPA by light in different aerosol mixtures, including salt and photosensitizers to mimic real SSA. The results show BPA degradation rates in the aerosol phase increase when mixed with photosensitizers and exposed to 254nm and 369nm light. Adding NaCl to the aerosol enhanced the heterogeneous OH oxidation kinetics of BPA, attributed to enhanced surface reactivity by salting out and greater diffusive mixing of reactive components in the lower viscosity particles containing hygroscopic NaCl and water. However, adding NaCl inhibited the photosensitized degradation of BPA, which was attributed to the quenching of the photosensitizer's triplet state by Cl^-. Based on the results, it is hypothesized that heterogeneous oxidative degradation of plastic additives by OH is likely

enhanced in SSA. In aerosols with less salt mixed with chromophores, photosensitized degradation may play a more significant role in BPA degradation.

Effects of Relative Humidity and Phase on the Molecular Detection of Nascent Sea Spray Aerosol Using Extractive Electrospray Ionization

Chapter 4, submitted to *Analytical Chemistry*, discussed the temporal variability of three different SSA constituents during a phytoplankton bloom using EESI-TOF. The work showed that glycerol, a polyol related to photosynthesis, in SSA, was correlated with phytoplankton biomass, as monitored by chlorophyll-a. The relatively high temporal resolution of the EESI method assisted in elucidating an apparent diurnal cycle in glycerol coincident with chlorophyll-a. There was also a strong correlation observed for K^+ with the peak in bacteria during the senescent phase of the phytoplankton bloom. This was proposed to result from the enrichment of cations complexed with marine-derived organic matter at the sea surface. Significant differences in the ionization efficiency of all measured SSA molecular components were observed with changing RH. This was attributed to enhanced coagulation and "sticking" between less viscous SSA and the electrospray droplets with elevated RH. Employing a simple theoretical framework, the diffusive depth of the reagent ion (i.e., Na^+) in the particle phase at different particle viscosities was modeled. The model results showed, consistent with the measurement data, that most SSA particles with a geometric mean diameter of 200 nm could be fully extracted at the deliquescence RH of sea salt, whereas there was only sporadic detection near the efflorescence RH.

Impacts of pH on the Photoinitiated Degradation Kinetics of Aerosol-Phase Bisphenol-A in the Presence of a Photosensitizer and NaCl

Chapter 5, which is in preparation for submission to *ACS Environmental Science & Technology Air*, demonstrated that pH is critical in the photoinitiated degradation (at 369nm) of aerosol-phase BPA. In these results, statistically significant BPA degradation was observed for all particle mixtures at pH 6 (Kruse and Slade 2023),[1] whereas significant BPA degradation was only

observed for the pure BPA aerosol at pH 3, and for BPA+4-BBA+NaCl at pH 11. This work demonstrated that BPA photodegradation when mixed with 4-BBA at pH 3 (i.e., both in neutral form) or at pH 11 (i.e., both in anionic form) were slower by about a factor of ten compared to pH 6. The measured first-order rate constants at pH 6 were about ten times faster than previously measured in bulk solutions. It is argued that differences in pH contribute to different degrees of protonation, altering the molecule's electronic state and absorption properties. The slower degradation at pH 11 may result from Coulomb repulsion between ionic forms of BPA and 4-BBA. It was also poorly detected by EESI-TOF, potentially due to neutralization by electrospray. The enhanced reactions in the particle phase compared to bulk may be attributed to less solvent caging due to greater solvent evaporation in the aerosol phase compared to bulk solutions. Similarly to Chapter 3, this has important implications for the source of BPA and other plastic additives to ambient aerosols, where plastic-burning aerosol may degrade BPA in the presence of other photosensitizers faster than in SSA, but further work is needed to make these conclusions.

6.3 Future Work

Increased complexity of SSA "Mimics"

Future work with respect to the plastic additives focused on in this thesis should aim to increase the complexity of the aerosol systems being studied. For example, the presence of different surfactants in SSA may "protect" plastic additives from degradation by enhancing more at the surface of the aerosol and forming a well-organized layer.[2] Furthermore, Chapter 3 only explored the influence of NaCl. $CaCl_2$ and other salts are relevant in SSA and vary in their ratios with particle size and some cations are enhanced relative to Na^+ in SSA compared to seawater.[3-5] These other cations may form complexes with either the plastic additives or dissolved organic matter.[6] Ca^{2+} can also encourage the formation of microgels that may otherwise inhibit degradation of plastic additives in SSA.[7] Another area to probe specific to BPA is the influence of different

types of photosensitizers on BPA degradation. One area this could be applied in is testing photosensitizers that exhibit primarily Type 1 photosensitization vs Type II, potentially incorporating furfuryl alcohol or some other chemical trap to observe the change in singlet oxygen over time.[8] This could then be applied to real samples of marine CDOM to better understand the mechanism of photosensitized degradation.

There is also the general perspective of performing these same kinds of studies on different plastic additives or anthropogenic contaminants. Work from this lab has demonstrated that for the antimicrobial triclosan, direct photolysis is competitive with OH degradation in the presence of 254 nm light, which was not the case for BPA. New additives for plastics are constantly being created and used with little to no federal restriction. As of 2020, there were over 400 unique chemical compounds being added to plastics,[9] which demonstrates the need for more studies like this one, to rapidly determine the lifetimes and degradation products of these additives in order to write effective legislation that serve to protect the health and safety of the public.

EESI Mechanism Determination

There is significant disagreement and variability in the scientific literature on the exact EESI mechanism. Some EESI studies suggest that the reagent ion spray does not coalesce with the aerosol sample and extraction happens only at the surface,[10, 11] whereas others insist that it captures the entire particle.[12, 13] Two complementary approaches to clarify the mechanism are proposed in the following section and include lab-based aerosol studies and particle interaction modeling.

Lab-Based EESI Mechanism Determination

Some of the EESI mechanism work that has been done previously utilizes different spray configurations and fluorescence to determine the degree of particle coalescence. However, this could be done in a more standardized way that is more relevant to the way the EESI inlet works. By detaching the inlet of the EESI and hooking it up to a filter sampling stage at the same flow

rate as the TOF, one could take samples of the real coalesced (or not) EESI spray and perform imaging studies using microscopy. This could be coupled with pH-sensitive dyes added to the incoming sample aerosol to identify the degree of coalescence. To this end, RH could be modulated while sampling to determine the influence of particle viscosity. The role of morphology and phase-separation on EESI sensitivity also needs more research. Systematic studies could be carried out inducing different aerosol phases by modulating the RH or temperature of the flow tube and varying the mixture of aerosol phase components based on their solubility in water and volatility.

KM-GAP Particle Modeling

Recent work by Schervish et al. 2023 demonstrated the newest development of the kinetic multilayer model of gas-particle interactions (KM-GAP).[14] In this newer model, particle-particle interactions can be determined based on properties of both the aerosol surface and the aerosol bulk. This probes the influence of both aerosol properties, such as viscosity and mass fraction, as well as interactions between the two particles such as solvation. I propose that this model be applied to a representative EESI extraction process. As in the lab-based studies, this could be approached from the SOA perspective of a predominantly organic aerosol system with consistent viscosity compared to SSA with different viscosities between the core and the shell of the particle.

6.4 References

(1) Kruse, S. M.; Slade, J. H. Heterogeneous and Photosensitized Oxidative Degradation Kinetics of the Plastic Additive Bisphenol-A in Sea Spray Aerosol Mimics. *J. Phys. Chem. A* **2023**, *127* (21), 4724-4733. DOI: 10.1021/acs.jpca.3c00127.

(2) Faust, J. A.; Abbatt, J. P. D. Organic Surfactants Protect Dissolved Aerosol Components against Heterogeneous Oxidation. *J. Phys. Chem. A* **2019**, *123* (10), 2114-2124. DOI: 10.1021/acs.jpca.9b00167.

(3) Cochran, R. E.; Jayarathne, T.; Stone, E. A.; Grassian, V. H. Selectivity Across the Interface: A Test of Surface Activity in the Composition of Organic-Enriched Aerosols from Bubble Bursting. *J. Phys. Chem. Lett.* **2016**, *7* (9), 1692-1696. DOI: 10.1021/acs.jpclett.6b00489.

(4) Salter, M. E.; Hamacher-Barth, E.; Leck, C.; Werner, J.; Johnson, C. M.; Riipinen, I.; Nilsson, E. D.; Zieger, P. Calcium enrichment in sea spray aerosol particles. *Geophys. Res. Lett.* **2016**, *43* (15), 8277-8285. DOI: 10.1002/2016gl070275.

(5) Jayarathne, T.; Sultana, C. M.; Lee, C.; Malfatti, F.; Cox, J. L.; Pendergraft, M. A.; Moore, K. A.; Azam, F.; Tivanski, A. V.; Cappa, C. D.; Bertram, T. H.; Grassian, V. H.; Prather, K. A.; Stone, E. A. Enrichment of Saccharides and Divalent Cations in Sea Spray Aerosol During Two Phytoplankton Blooms. *Environ. Sci. Technol.* **2016**, *50* (21), 11511-11520. DOI: 10.1021/acs.est.6b02988.

(6) Hering, J. G.; Morel, F. M. Humic acid complexation of calcium and copper. *Environ. Sci. Technol.* **1988**, *22* (10), 1234-1237. DOI: 10.1021/es00175a018.

(7) Chin, W.-C.; Orellana, M. V.; Verdugo, P. Spontaneous assembly of marine dissolved organic matter into polymer gels. *Nature* **1998**, *391* (6667), 568-572. DOI: 10.1038/35345.

(8) Eugene, A. J.; Guzman, M. I. Production of Singlet Oxygen ($^1O_2$) during the Photochemistry of Aqueous Pyruvic Acid: The Effects of pH and Photon Flux under Steady-State O_2(aq) Concentration. *Environ. Sci. Technol.* **2019**, *53* (21), 12425-12432. DOI: 10.1021/acs.est.9b03742.

(9) Gunaalan, K.; Fabbri, E.; Capolupo, M. The hidden threat of plastic leachates: A critical review on their impacts on aquatic organisms. *Water Res.* **2020**, *184*, 116170. DOI: 10.1016/j.watres.2020.116170.

(10) Kumbhani, S.; Longin, T.; Wingen, L. M.; Kidd, C.; Perraud, V.; Finlayson-Pitts, B. J. New Mechanism of Extractive Electrospray Ionization Mass Spectrometry for Heterogeneous Solid Particles. *Anal. Chem.* **2018**, *90* (3), 2055-2062. DOI: 10.1021/acs.analchem.7b04164.

(11) Wang, R.; Gröhn, A. J.; Zhu, L.; Dietiker, R.; Wegner, K.; Günther, D.; Zenobi, R. On the mechanism of extractive electrospray ionization (EESI) in the dual-spray configuration. *Anal. Bioanal. Chem.* **2012**, *402* (8), 2633-2643. DOI: 10.1007/s00216-011-5471-8.

(12) Felipe D. Lopez-Hilfiker; Veronika Pospisilova; Wei Huang; Markus Kalberer; Claudia Mohr; Giulia Stefenelli; Joel A. Thornton; Urs Baltensperger; Andre S. H. Prevot; Slowik, J. G.

An extractive electrospray ionization time-of-flight mass spectrometer (EESI-TOF) for online measurement of atmospheric aerosol particles. *Atmospheric* **2019**. DOI: 10.5194/amt-12-4867-2019.

(13) Pagonis, D.; Campuzano-Jost, P.; Guo, H.; Day, D. A.; Schueneman, M. K.; Brown, W. L.; Nault, B. A.; Stark, H.; Siemens, K.; Laskin, A.; Piel, F.; Tomsche, L.; Wisthaler, A.; Coggon, M. M.; Gkatzelis, G. I.; Halliday, H. S.; Krechmer, J. E.; Moore, R. H.; Thomson, D. S.; Warneke, C.; Wiggins, E. B.; Jimenez, J. L. Airborne extractive electrospray mass spectrometry measurements of the chemical composition of organic aerosol. *Atmos. Meas. Tech.* **2021**, *14* (2), 1545-1559. DOI: 10.5194/amt-14-1545-2021.

(14) Schervish, M.; Donahue, N. M.; Shiraiwa, M. Effects of volatility, viscosity, and non-ideality on particle–particle mixing timescales of secondary organic aerosols. *Aerosol Sci. Technol.* **2023**, *58* (4), 411-426. DOI: 10.1080/02786826.2023.2256827.